

ZZ PRODUCTION IN PROTON-PROTON COLLISIONS AT  
 $\sqrt{s} = 13$  TeV IN FOUR-LEPTON EVENTS USING THE  
CMS DETECTOR AT THE LHC

*by*

Nathaniel Woods

A dissertation submitted in partial fulfillment of  
the requirements for the degree of

Doctor of Philosophy  
(Physics)

*at the*  
UNIVERSITY OF WISCONSIN – MADISON  
2017

Defended on 25 October 2017

Dissertation approved by the following members of the Final Oral Committee:

Wesley Smith · Bjorn Wiik Professor of Physics  
Sridhara Dasu · Professor of Physics  
Matthew Herndon · Professor of Physics  
Lisa Everett · Professor of Physics  
Pupa Gilbert · Professor of Physics

## Abstract

Several studies of four-lepton production in proton-proton collisions are presented. The dataset used corresponds to an integrated luminosity  $35.9 \text{ fb}^{-1}$  at a center-of-mass energy of  $13 \text{ TeV}$ , collected by the CMS detector at the LHC. All reported measurements use the  $2\ell 2\ell'$  final states, where  $\ell, \ell' = e$  or  $\mu$ . The total ZZ cross section for all events with two Z bosons in the mass range  $60$ – $120 \text{ GeV}$  is measured and found to be  $\sigma(\text{pp} \rightarrow \text{ZZ}) = 17.2 \pm 0.5 \text{ (stat)} \pm 0.7 \text{ (syst)} \pm 0.4 \text{ (theo)} \pm 0.4 \text{ (lumi)} \text{ pb}$ . The Z branching fraction to four leptons is found to be  $\mathcal{B}(Z \rightarrow 4\ell) = 4.8 \pm 0.2 \text{ (stat)} \pm 0.2 \text{ (syst)} \pm 0.1 \text{ (theo)} \pm 0.1 \text{ (lumi)} \times 10^{-6}$  for events with  $80 < m_{4\ell} < 100 \text{ GeV}$  and  $m_{\ell\ell} > 4 \text{ GeV}$  for all opposite-sign, same-flavor lepton pairs. Differential cross sections are measured as functions of a number of kinematic and jet-related observables. All these results agree with standard model predictions. A search for fully electroweak ZZ + 2jets production is performed, and an excess consistent with standard model vector boson scattering is found at the  $2.7\sigma$  level. Searches for anomalous triple and quartic gauge couplings are performed, and the four-lepton invariant mass distributions are used to set the most stringent limits to date on a number of parameters affecting neutral gauge boson interactions.

## Acknowledgements

They say it takes a village to raise a child, and a grad student is just a toddler whose grape juice has fermented, so I have many people to thank. I am indebted to too many advisors, colleagues, friends, and family members to name them all here, so I will highlight just a few for particular appreciation; the many omissions are solely for the purpose of keeping this document under 200 pages.

I must first thank the members of the Wisconsin CMS group, who have, understandably, played a central role in my life over the past five and a half years. The professors, Wesley Smith, Sridhara Dasu, and Matt Herndon, are great physicists and master tacticians, and their clear-eyed advice has been extremely valuable throughout my time in research. Sascha Savin has been a great guide to the day-to-day business of being a physicist, and he has taught me an enormous amount about physics, data analysis, work habits, intracollaboration politics, and just about everything else. The postdocs, Evan Friis, Maria Cepeda, Senka Duric, Isobel Ojalvo, Bhawna Gomber, and Cécile Caillol, are uniformly brilliant and endlessly helpful. Everything would grind to a halt and nothing would ever get done if not for Dan Bradley, Ajit Mohapatra, Carl Vuosalo, and the rest of the computing team, whom I should both thank and apologize to for all the times I completely broke everything. Pam Klabbers and Aleš Svetek are founts of knowledge about the CMS trigger, and are fully responsible for any competence I appeared to display while on shift. I would never have accomplished anything without the other UW CMS grad students. Tom Perry, Aaron Levine, Laura Dodd, Devin Taylor, Tyler Ruggles, Nick Smith, Kenneth Long, James Buchanan, and Usama Hussain, and others with whom I overlapped more briefly, have been great friends and comrades-in-arms. The intelligence, collective knowledge, and snark on continuous display in the group chat and in our office chats were invaluable

to both my work and my mental health.

Ivan Furic and Darin Acosta helped me get my foot in the door during my REU at the University of Florida and taught me a lot when I had essentially no knowledge base to work from.

The friends I made in Madison and Geneva are far too numerous to mention individually, but they are wonderful people and I'm lucky to have them in my life. A special shout-out goes to my flatmates, Laser Kaplan, Svet Hristozkov, Heather Russell, and Tessa Carver, for not just putting up with my idiosyncrasies but actively making home a place I wanted to go.

I never would have gone anywhere in life without my smart, funny, supportive family: my parents Anne and David, my siblings Julia and Peter, a small army of extended family and a clowder of cats led by The Boss, Gadget. I could not ask for a stronger foundation on which to build my future.

# Contents

Abstract . . . . .	i
Acknowledgements . . . . .	ii
<b>Contents</b>	iv
<b>List of Figures</b>	ix
<b>List of Tables</b>	xiii
<b>1 The Standard Model</b>	1
1.1 Introduction . . . . .	3
1.2 Matter and Forces . . . . .	3
1.3 Electroweak Unification and Symmetry Breaking, and the Higgs Boson	10
1.4 Diboson and Multiboson Physics . . . . .	13
1.4.1 Vector Boson Scattering . . . . .	16
1.5 Limitations and Possible Extensions . . . . .	17
1.5.1 Anomalous Gauge Couplings . . . . .	18
1.6 Proton-Proton Collisions . . . . .	21
1.7 ZZ Measurements in Context . . . . .	23
<b>2 ZZ Phenomenology and Previous Results</b>	24
2.1 Nonresonant ZZ/Z $\gamma^*$ Production and Decay . . . . .	25

2.1.1	Vector Boson Scattering . . . . .	27
2.1.2	Prior Measurements . . . . .	28
2.2	Resonant $ZZ^*/Z\gamma^*$ Production . . . . .	34
2.2.1	$Z$ Boson Decays to Four Leptons . . . . .	35
2.2.2	Higgs Boson Production . . . . .	35
2.2.2.1	Prior Measurements . . . . .	36
2.3	Anomalous Gauge Couplings . . . . .	38
2.3.1	Previous Limits . . . . .	40
2.4	Background Processes . . . . .	42
<b>3</b>	<b>The CMS Experiment and the CERN LHC</b>	<b>44</b>
3.1	The CERN Large Hadron Collider . . . . .	44
3.1.1	Accelerator Chain, Layout, and Detectors . . . . .	46
3.1.2	Operating Parameters . . . . .	49
3.1.2.1	Design . . . . .	50
3.1.2.2	Run I . . . . .	51
3.1.2.3	Run II . . . . .	52
3.2	The Compact Muon Solenoid Detector . . . . .	53
3.2.1	Terminology and Geometry . . . . .	54
3.2.2	Magnet and Inner Tracking System . . . . .	55
3.2.2.1	Pixel Detector . . . . .	58
3.2.2.2	Strip Tracker . . . . .	59
3.2.3	Electromagnetic Calorimeter . . . . .	59
3.2.4	Hadronic Calorimeter . . . . .	61
3.2.5	Muon Spectrometer . . . . .	63
3.2.5.1	Drift Tubes . . . . .	64

3.2.5.2	Cathode Strip Chambers . . . . .	65
3.2.5.3	Resistive Plate Chambers . . . . .	66
3.2.6	Data Acquisition and Trigger . . . . .	67
3.2.6.1	Level-1 Trigger . . . . .	68
3.2.6.2	High-Level Trigger . . . . .	70
3.2.7	Luminosity Determination . . . . .	71
<b>4</b>	<b>Simulation</b>	<b>74</b>
4.1	Monte Carlo Event Generation . . . . .	74
4.1.1	Matrix Element and Hard Process Generation . . . . .	75
4.1.2	Parton Shower, Hadronization, and Underlying Event . . . . .	76
4.1.3	Pileup Simulation . . . . .	78
4.1.4	Samples Used in this Analysis . . . . .	78
4.2	Detector Simulation . . . . .	79
<b>5</b>	<b>Object Reconstruction and Selection</b>	<b>82</b>
5.1	Track Reconstruction and Vertex Identification . . . . .	83
5.2	Particle Flow Reconstruction . . . . .	85
5.2.1	PF Candidates . . . . .	86
5.2.1.1	Muons . . . . .	87
5.2.1.2	Electrons and Prompt Photons . . . . .	88
5.2.1.3	Charged and Neutral Hadrons . . . . .	88
5.2.2	Jets . . . . .	89
5.2.3	Missing Transverse Energy . . . . .	91
5.3	Object Identification and Selection . . . . .	91
5.3.1	Electrons . . . . .	92
5.3.2	Muons . . . . .	95

5.3.3	Final State Photon Radiation . . . . .	96
5.3.4	Jets . . . . .	97
5.3.5	Misidentified Objects . . . . .	97
5.4	ZZ Candidate and Event Selection . . . . .	98
5.4.1	$Z/\gamma^*$ Candidate Selection . . . . .	99
5.4.2	ZZ Candidate Selection . . . . .	100
5.4.3	Dijet and VBS Signal Selection . . . . .	102
<b>6</b>	<b>Analysis Strategy</b>	<b>103</b>
6.1	Background Estimation . . . . .	104
6.2	Systematic Uncertainties . . . . .	106
6.3	Fiducial and Total Cross Section Calculation . . . . .	109
6.3.1	Signal Strength Extraction . . . . .	111
6.3.2	$Z \rightarrow 4\ell$ Branching Fraction . . . . .	112
6.4	Differential Cross Sections . . . . .	112
6.4.1	Unfolding . . . . .	113
6.4.2	Uncertainties . . . . .	114
6.5	VBS Signal Extraction . . . . .	115
6.6	Anomalous Gauge Coupling Searches . . . . .	117
<b>7</b>	<b>Results</b>	<b>119</b>
7.1	Four-Lepton Yields and Inclusive Cross Sections . . . . .	120
7.1.1	Full Spectrum . . . . .	120
7.1.2	$Z \rightarrow 4\ell$ Resonance . . . . .	120
7.1.3	Higgs Resonance . . . . .	125
7.1.4	ZZ Production . . . . .	126
7.2	Differential Cross Sections . . . . .	136

7.3	Vector Boson Scattering . . . . .	138
7.4	Anomalous Coupling Limits . . . . .	138
<b>8</b>	<b>Conclusions</b>	<b>156</b>
8.1	Summary . . . . .	156
8.2	Outlook . . . . .	158
	<b>Bibliography</b>	<b>160</b>

# List of Figures

1.1	Triple gauge boson coupling vertex . . . . .	13
1.2	Quartic gauge boson coupling vertex . . . . .	14
1.3	Higgs couplings to the gauge bosons . . . . .	14
1.4	Higgs self couplings . . . . .	15
1.5	Tree level Feynman diagrams for diboson production in fermion-anti-fermion collisions . . . . .	16
1.6	Gluon-gluon fusion box diagram for general diboson production . . .	16
1.7	Unitarity violation in vector boson scattering without a Higgs boson	17
1.8	Neutral anomalous gauge coupling vertices . . . . .	19
1.9	Neutral anomalous triple gauge coupling vertex . . . . .	20
1.10	Parton distribution functions . . . . .	22
2.1	Leading order $ZZ \rightarrow 4\ell$ production . . . . .	26
2.2	Next-to-leading order $ZZ \rightarrow 4\ell$ production . . . . .	27
2.3	Gluon-gluon fusion box diagram for $ZZ \rightarrow 4\ell$ production . . . . .	28
2.4	Vector boson scattering diagrams . . . . .	29
2.5	Measured $e^+e^- \rightarrow ZZ$ cross sections from OPAL. . . . .	30
2.6	Measured four-lepton mass spectrum from D0. . . . .	31
2.7	Measured four-lepton mass spectrum from CMS at $\sqrt{s} = 8$ TeV. . . . .	32

2.8	Measured four-lepton mass spectrum from ATLAS at $\sqrt{s} = 8$ TeV. . . . .	33
2.9	Feynman diagram for $Z \rightarrow 4\ell$ production . . . . .	35
2.10	Higgs production mechanisms . . . . .	37
2.11	Higgs boson SM cross section and branching ratio, as a function of $m_H$ .	38
2.12	Enhancements in $p_T^Z$ and $p_T^\mu$ resulting from nonzero aTGCs . . . . .	39
2.13	Lepton angular correlations resulting from nonzero aTGCs . . . . .	40
2.14	Previous two-dimensional aTGC limits from CMS. . . . .	41
2.15	Example background diagrams . . . . .	43
3.1	LHC dipole schematic . . . . .	47
3.2	LHC accelerator and experiment layout . . . . .	48
3.3	Integrated luminosity delivered to CMS in each LHC run period . . .	52
3.4	CMS cutout schematic . . . . .	54
3.5	Inner tracker layout . . . . .	57
3.6	Tracker material budget in radiation lengths . . . . .	58
3.7	ECAL geometry . . . . .	60
3.8	HCAL geometry . . . . .	62
3.9	Total material budget in nuclear interaction lengths . . . . .	63
3.10	Muon system geometry . . . . .	64
3.11	Trigger data flow . . . . .	71
4.1	Comparison of data and simulation in $e^+e^-$ events around the $Z$ resonance . . . . .	81
5.1	Lepton vertex compatibility . . . . .	93
5.2	Lepton isolation distributions . . . . .	95
6.1	Misidentification rates for electrons and muons . . . . .	105

6.2	Differential cross section shape uncertainty sources . . . . .	115
7.1	Full four-lepton mass spectrum . . . . .	121
7.2	Mass of all $Z/\gamma^*$ candidates in the full spectrum selection . . . . .	122
7.3	Mass of $Z_1$ candidates in the full spectrum selection . . . . .	123
7.4	Scatter plot of $m_{Z_2}$ vs. $m_{Z_1}$ for data events in the full spectrum selection	124
7.5	Four-lepton mass in the $Z \rightarrow 4\ell$ selection . . . . .	125
7.6	Scatter plot of $m_{Z_2}$ vs. $m_{Z_1}$ for data events in the $Z \rightarrow 4\ell$ selection .	126
7.7	Four-lepton mass spectrum around the Higgs resonance . . . . .	127
7.8	Mass of $Z_1$ candidates in events near the Higgs resonance . . . . .	128
7.9	Mass of $Z_2$ candidates in events near the Higgs resonance . . . . .	129
7.10	Scatter plot of $m_{Z_2}$ vs. $m_{Z_1}$ for data events near the Higgs resonance	130
7.11	Four-lepton mass spectrum for events with both $Z$ candidates on-shell	131
7.12	Mass of all $Z/\gamma^*$ candidates in the on-shell selection . . . . .	132
7.13	Jet multiplicity . . . . .	133
7.14	Transverse momentum of the leading and subleading jets . . . . .	134
7.15	Pseudorapidity of the leading and subleading jets . . . . .	134
7.16	Dijet invariant mass . . . . .	135
7.17	Dijet pseudorapidity separation . . . . .	136
7.18	Total ZZ cross section as a function of center-of-mass energy . . . . .	137
7.19	Normalized differential ZZ cross section as a function of four-lepton invariant mass . . . . .	139
7.20	Normalized differential ZZ cross section as a function of four-lepton system $p_T$ . . . . .	140
7.21	Normalized differential ZZ cross section as a function of Z boson candidate $p_T$ . . . . .	141

7.22	Normalized differential ZZ cross section as a function of leading lepton $p_T$	142
7.23	Normalized differential ZZ cross section as a function of $\Delta R$ between the Z bosons	143
7.24	Normalized differential ZZ cross section as a function of $\Delta\phi$ between the Z bosons	144
7.25	Normalized differential ZZ cross section as a function of jet multiplicity	145
7.26	Normalized differential ZZ cross section as a function of dijet invariant mass	146
7.27	Normalized differential ZZ cross section as a function of dijet pseudo-rapidity separation	147
7.28	Normalized differential ZZ cross sections as functions of leading and subleading jet transverse momentum	148
7.29	Normalized differential ZZ cross sections as functions of leading and subleading jet pseudorapidity	149
7.30	Normalized differential four-lepton cross section as a function of four-lepton invariant mass with loosened Z mass cuts	150
7.31	VBS signal extraction GBDT output	151
7.32	ZZ invariant mass distribution with example aTGC working points	152
7.33	Asymptotic one- and two-dimensional aTGC limits at 95% confidence level	153
7.34	One-dimensional aTGC limits as a function of the maximum ZZ invariant mass used in the calculation	154
7.35	ZZ invariant mass distribution for dijet events, with example aQGC working points	155

# List of Tables

1.1	Particle content of the standard model . . . . .	5
3.1	LHC beam parameters . . . . .	51
5.1	Four-lepton event yields in data at several points in the analysis flow. . .	100
6.1	Systematic uncertainties on the total yield . . . . .	108
6.2	Fiducial phase space definitions . . . . .	111
7.1	Expected and observed yields for $Z \rightarrow 4\ell$ production. . . . .	122
7.2	Expected and observed yields for Higgs boson production. . . . .	127
7.3	Expected and observed yields for doubly-resonant ZZ production. . . . .	130

## <sup>0</sup> Chapter 1

### <sup>1</sup> The Standard Model

2 The mission of fundamental particle physics is an audacious one. An exercise in  
3 reductionism taken to its logical extreme, the goal of the field is to find the minimal set  
4 of mathematical precepts that underlie all interactions of matter and energy and from  
5 which everything else in the universe is, in principle, an emergent property. Despite  
6 the loftiness of its goals, the program has been extraordinarily successful, yielding  
7 the standard model (SM), a remarkable theory which is elegant in its mathematical  
8 formulation yet expansive and powerful in its predictions, most of which have been  
9 verified in exquisite detail. Calculations done in the framework of the SM have  
10 matched data within the precision of essentially every experiment over roughly four  
11 decades, making it arguably the best-confirmed theory in the history of science. It is  
12 generally believed to be self-consistent; future advances will likely add to it, explain  
13 its free parameters, or find some deeper underlying structure, not contradict it.

14 And yet work remains. There are a few known phenomena that the SM does not  
15 cover, and some of its features seem for now to be surprising coincidences (see Sec-  
16 tion 1.5). One area of particular interest is the physics of the electroweak interaction,  
17 which was the last piece to fall into place. Its final major component, the existence of

18 the Higgs boson, was definitively confirmed only as recently as 2012 and some details  
19 remain hazy or unverified, from an experimental perspective.

20 Chapter 1 gives an overview of the SM with a focus on its electroweak sector,  
21 and describes some of the shortcomings that motivate continued searches for new  
22 physics even now that it is complete. Chapter 1 also describes diboson and multi-  
23 boson processes, interactions involving multiple instances of the particles underlying  
24 electroweak physics, which are valuable tools for understanding how the bosons in-  
25 teract with each other. This thesis presents several studies of the ZZ diboson process,  
26 intended to illuminate the behavior of the neutral part of electroweak interactions.  
27 In particular, the focus of this work is the case in which two Z bosons each decay to  
28 a pair of charged leptons. Such events are rare but experimentally appealing. Two of  
29 the three charged leptons, electrons ( $e$ ) and muons ( $\mu$ ) can be reconstructed with high  
30 precision, and few physics processes aside from ZZ result in four-lepton final states,  
31 so they provide an unmistakable experimental signature that can be easily identified  
32 over small backgrounds. Details of ZZ physics are described in Chapter 2, along with  
33 a review of previous literature.

34 High-energy particle collisions in a laboratory provide a way to investigate ZZ pro-  
35 duction and other fundamental interactions in a controlled setting. CERN’s Large  
36 Hadron Collider (LHC), a proton-proton collider in tunnels running beneath the  
37 Swiss-French border near Geneva, provides collisions at record-breaking energies and  
38 rates, which are used by the Compact Muon Solenoid (CMS) detector to study dibo-  
39 son processes in unprecedented detail. These apparatus are described in Chapter 3.  
40 Accurate simulations of physics and particles’ interactions with the detector are vital  
41 to obtaining valid results; this process is described in Chapter 4. Chapter 5 describes  
42 how physics objects are built from the detector signals, and how those appropriate  
43 for analysis are selected. The strategy for performing the ZZ measurements presented

44 in this thesis is given in Chapter 6. New studies of four-lepton events in a sample of  
45 proton-proton collisions are presented in Chapter 7.

## 46 **1.1 Introduction**

47 The standard model is a set of related theories that together describe matter and its  
48 interactions at a fundamental level. The following sections give a general overview  
49 of the SM and related topics that serve as background material for the four-lepton  
50 processes described in more detail in subsequent chapters. This includes discussions  
51 of the particle content of the SM and the gauge structure that leads to particle in-  
52 teractions, the spontaneous symmetry breaking mechanism that leads to the specific  
53 structure of the electroweak sector of the SM, diboson processes, and the SM’s lim-  
54 itations and how they might be addressed. Some details are also given about the  
55 proton-proton collisions used to probe particle interactions at high energies. More  
56 complete information may be found in a number of texts, including Refs. [1–5]. Ev-  
57 erything that follows uses units such that  $c = \hbar = 1$ , where  $c$  is the speed of light and  
58  $\hbar$  is the reduced Planck’s constant  $\hbar = h/2\pi$ .

## 59 **1.2 Matter and Forces**

60 In the SM, matter is made of fermions (particles with half-integer spin; all SM fun-  
61 damental fermions have spin  $\frac{1}{2}$ ) which interact by exchanging gauge bosons (integer  
62 spin; spin 1 for the SM force carriers). Table 1.1 lists the fundamental particles and  
63 some of their properties. With the exception of the neutral bosons, all particles have  
64 a corresponding antiparticle which is the same except that all its quantum numbers  
65 have opposite sign. The fermions come in two categories, leptons and quarks. All

66 the quarks and half the lepton types carry electric charge and are therefore subject  
 67 to interactions through the electromagnetic force, described by quantum electrodyn-  
 68 namics (QED) [2]. In a QED interaction, two charged particles exchange a photon,  
 69 which carries the momentum transferred from one to the other. The photon is a  
 70 spin-1 gauge boson that is massless and electrically neutral itself, explaining why  
 71 electromagnetic forces are long-range.

72 There are six types of quarks which fall into three “generations:” up and down  
 73 (u and d, first generation); charm and strange (c and s, second generation); and top  
 74 and bottom (t and b, third generation)<sup>1</sup>. Quark masses increase with each successive  
 75 generation. Up-type quarks (u, c, t) have electric charge  $+2/3$  (in units of the positron  
 76 charge  $e$ ) while down-type quarks have  $-1/3$ . Quarks are the building blocks of  
 77 hadrons, including  $q\bar{q}'$  bound states called mesons and  $qq'q''/\bar{q}\bar{q}'\bar{q}''$  bound states called  
 78 baryons, of which protons (uud) and neutrons (udd) are the most familiar. Top  
 79 quarks are too heavy to form bound states; the toponium ( $t\bar{t}$  meson) weak decay  
 80 width is larger than the spacing between its energy levels and its mean lifetime is  
 81 an order of magnitude shorter than its orbital period so no resonance may form [5].  
 82 Hadrons are bound by the strong nuclear force, described by the theory of quantum  
 83 chromodynamics (QCD).

84 The mediator for the strong force is the gluon, which like the photon is a massless  
 85 spin-1 gauge boson. The analog of electric charge is “color”, a notion originally  
 86 introduced [6] as an ad hoc explanation of how identical quarks could exist in the  
 87 symmetric bound state of a hadron despite the Fermi exclusion principle and later  
 88 found to be the charge underlying the strong force [1, 7]. Unlike electric charge,  
 89 there are three types of color charge, typically called red, green, and blue, though  
 90 these names are arbitrary<sup>2</sup>. The analogy with visible color comes primarily from

---

<sup>1</sup>Top and bottom quarks are sometimes called truth and beauty.

<sup>2</sup>Antiquarks carry negative color charges, typically called antired, antigreen and antiblue.

Table 1.1: The particles of the standard model, and some of their properties. All fermions have a corresponding antiparticle with opposite sign for all quantum numbers. Quarks and leptons are grouped by generation. Note that the listed  $T^3$  (the measured component of the weak isospin, described below) applies only to left-handed fermions; right-handed fermions have  $T^3 = 0$  and do not couple to the  $W^\pm$  (right-handed neutrinos, if they exist, do not couple to the  $Z$  either).

Particle	Mass (GeV)	Charge ( $e$ )	$T^3$	Gauge couplings
Scalar boson (spin 0)				
H	125	0		$W^\pm, Z$
Fermion (spin 1/2)				
u	0.023	+2/3	+1/2	$g, \gamma, Z, W^\pm$
d	0.048	-1/3	-1/2	$g, \gamma, Z, W^\pm$
e	$5.11 \times 10^{-4}$	-1	+1/2	$\gamma, Z, W^\pm$
$\nu_e$	$< 2.2 \times 10^{-9}$	0	-1/2	$Z, W^\pm$
c	1.28	+2/3	+1/2	$g, \gamma, Z, W^\pm$
s	0.95	-1/3	-1/2	$g, \gamma, Z, W^\pm$
$\mu$	0.105	-1	+1/2	$\gamma, Z, W^\pm$
$\nu_\mu$	$< 1.7 \times 10^{-4}$	0	-1/2	$Z, W^\pm$
t	172	+2/3	+1/2	$g, \gamma, Z, W^\pm$
b	4.2	-1/3	-1/2	$g, \gamma, Z, W^\pm$
$\tau$	1.77	-1	+1/2	$\gamma, Z, W^\pm$
$\nu_\tau$	$< 0.018$	0	-1/2	$Z, W^\pm$
Vector boson (spin 1)				
g	0	0	0	$g$
$\gamma$	0	0	0	$W^\pm$
Z	91.2	0	0	$W^\pm$
$W^\pm$	80.4	$\pm 1$	$\pm 1$	$\gamma, Z, W^\pm$

91 the heuristic that natural states must be “colorless,” i.e. a hadron may have equal  
92 parts color and corresponding anticolor as in a meson, but it may also be “white,”  
93 containing red, blue, and green in equal measures as in a baryon. This implies that  
94 a color charged object cannot exist on its own, a property known as confinement.

95       Confinement arises from the structure of QCD interactions and gluons themselves.  
96 Among fermions, only quarks interact through the strong force, but gluons also carry  
97 color charge and interact with each other. Because gluons self-interact, have no dis-  
98 tinct antiparticle, and are massless, they can split and radiate infinitely. The resulting  
99 soft gluon interactions around quarks lead to an anti-screening effect that causes the  
100 strength of the strong force to change as a function of the distance between interacting  
101 quarks, with close quarks interacting less strongly as far as a single gluon exchange  
102 is concerned. As quark separation gets larger, the potential energy of strong inter-  
103 actions rises rapidly, until it is energetically favorable for the gluon connecting them  
104 to split into a  $q\bar{q}$  pair that screens them and effectively breaks off the interaction.  
105 A single colored particle will thus cause more colored particles to be produced from  
106 vacuum until only colorless bound states remain, enforcing confinement. This pro-  
107 cess is known as hadronization, and causes single quarks or gluons leaving a hard  
108 scattering interaction to produce “jets” of many hadrons, each carrying a fraction of  
109 the original parton momentum, that enter the detector in a conical shower. This is  
110 why a free quark has never been observed, and is not expected to be found, and why  
111 the strong interaction is short-range even though gluons are massless. It is also why,  
112 for example,  $qq\bar{q}$  bound states are not seen in nature. Conversely, close-range QCD  
113 is relatively feeble, leading to “asymptotic freedom,” the property of partons within  
114 hadrons that they may be considered independent in high-energy collisions, because  
115 their interactions are weak enough that bound state effects may be neglected (see  
116 Section 1.6).

117        Leptons may be electrically charged or neutral, and come in three generations,  
118 each containing one lepton of each type, a charged lepton and a corresponding neu-  
119 trino. In order of charged lepton mass, the generations are the electron and its  
120 neutrino ( $e$  and  $\nu_e$ ), muon and its neutrino ( $\mu$  and  $\nu_\mu$ ), and tau and its neutrino ( $\tau$   
121 and  $\nu_\tau$ ). Taus decay quickly, with a mean lifetime of  $2.9 \times 10^{-13}$  s in their rest frame;  
122 muons also decay, but their lifetime ( $2.2 \mu\text{s}$ ) is long compared to other time scales  
123 involved in particle collider experiments, so they are considered stable particles for  
124 the purposes of this work. Neutrinos are known to have mass [8–10], and the masses  
125 are known to be small but they have not been measured. All leptons and quarks  
126 interact via the weak nuclear force, which is best known for causing the nuclear beta  
127 decay reaction  $n \rightarrow p + e^- + \bar{\nu}_e$ . Neutrinos are notable for coupling to the rest of the  
128 SM only through weak interactions, making them difficult to detect in practice. De-  
129 tectors at particle colliders make no attempt to detect neutrinos, and their presence  
130 is inferred only through the apparent momentum imbalance resulting from the fact  
131 that they are not detected.

132        The weak force operates through two mechanisms, charged-current and neutral-  
133 current interactions. Neutral-current interactions proceed through exchange of a Z  
134 boson, an electrically neutral spin-1 mediator, and are analogous to electromagnetic  
135 interactions except for two important differences. Unlike the  $\gamma$ , the Z has mass—in  
136 fact, one of the largest known masses at 91 GeV [11]—giving it longitudinal polariza-  
137 tion modes [2] and limiting the range of the force because it decays with a halflife on  
138 the order of  $10^{-25}$  s [11]. Also unlike QED, weak interactions do not respect parity  
139 ( $P$ ) symmetry. The Z boson couples more strongly to left-handed fermions (those  
140 with helicity opposite their direction of motion) and right-handed antifermions than  
141 to their opposite-spin counterparts. The degree of asymmetry varies by fermion type;  
142 notably, the Z does not couple at all to right-handed neutrinos. Neutral-current inter-

143 actions are still symmetric under combined charge conjugation (C) and parity (CP)  
 144 transformations, because processes that are odd under P are also odd under C.

145       Charged-current interactions proceed through exchange of an electrically charged  
 146 boson, the  $W^\pm$ , which has a mass around 80 GeV [11]. Leptons couple to  $W^-$  bosons  
 147 in  $\ell^-, \bar{\nu}_\ell$  pairs ( $W^+$  bosons likewise with their antiparticles), causing  $\mu$  and  $\tau$  decays.  
 148 Lepton flavor is conserved in the sense that charged leptons couple to the W only in  
 149 conjunction with the (anti-)neutrino from the same generation, so the total lepton  
 150 number  $N_\ell = n_{\ell^-} - n_{\ell^+} + n_{\nu_\ell} - n_{\bar{\nu}_\ell}$ , where  $n_X$  is the number of X particles in existence,  
 151 is conserved separately for  $\ell \in (\text{e}, \mu, \tau)$ . Flavor conservation does not hold for quarks  
 152 undergoing charged weak interactions. An up-type quark always couples to the W  
 153 in conjunction with a down-type quark, as it must to obey conservation of electric  
 154 and color charge. The pairings are in general described by a unitary  $3 \times 3$  matrix  
 155 known as the Cabibbo–Kobayashi–Maskawa (CKM) matrix which defines the inter-  
 156 generational mixing [12, 13]. Flavor-changing currents allow heavy quarks to decay  
 157 to lighter ones, and are thus responsible for the decay of hadrons that do not contain  
 158 the  $q\bar{q}$  pair necessary for strong or electromagnetic decays.

159       Charged-current interactions also do not respect parity symmetry, and in fact are  
 160 maximally parity violating: the W couples only to left-handed fermions and right-  
 161 handed antifermions. Because neutrinos interact only through the weak force<sup>3</sup>, and  
 162 the Z also couples only to left-handed neutrinos, it is not clear that right-handed  
 163 neutrinos even exist. If they do, they have no way to interact with other matter and  
 164 they are not part of the SM. Unlike neutral-current interactions, charged-current  
 165 interactions violate CP symmetry at a small but measurable rate. CP violation  
 166 was first observed in neutral kaon mixing before the theory of the weak force was  
 167 fully worked out [14]. After flavor-changing charged currents were formalized it was

---

<sup>3</sup>Aside from gravity, presumably, but this interaction is not experimentally accessible and is not covered by the standard model.

168 realized that CP violation could arise from a complex phase in the CKM matrix,  
 169 which arises in models with at least three generations of quarks<sup>4</sup> [13]. CP violation  
 170 was subsequently confirmed by observation in a number of meson decays [15–20].

171 The quantum number analogous to electric charge and color charge for the weak  
 172 interaction is the three-component weak isospin  $T^i$ , which is typically defined such  
 173 that the measured component is  $T^3$ . Left-handed fermions have  $|T| = \frac{1}{2}$ , the  $W^\pm$   
 174 has  $|T| = \pm 1$ , and all other particles have  $|T| = 0$ . Weak isospin is conserved in all  
 175 electromagnetic, strong, and fermion-fermion weak interactions, but is not conserved  
 176 in general because the Higgs boson (see below) carries weak isospin. Electric charge  
 177 is always conserved, and is related to the measured component of the weak isospin  
 178 by the weak hypercharge  $Y$ , which is

$$Y = 2(Q - T^3), \quad (1.1)$$

179 where  $Q$  is the electric charge. This connection between the electromagnetic and weak  
 180 forces, and the parallels between the weak neutral-current interaction and QED, are  
 181 not coincidental. In fact, in the SM, they are unified into a single *electroweak* force.  
 182 The differences we observe between electromagnetic and weak interactions, including  
 183 the masses of the weak gauge bosons, arise from the mechanism of electroweak sym-  
 184 metry breaking, which defines much of the structure of the SM and is described in  
 185 more detail in the next section.

---

<sup>4</sup>At the time, only the first two generations were known, so the observed CP asymmetry was taken as an early indication of the existence of top and bottom quarks.

## 186 1.3 Electroweak Unification and Symmetry

### 187 Breaking, and the Higgs Boson

188 The structures of the fundamental forces arise from symmetries in the underlying  
 189 fields, specifically gauge invariance of the relevant terms in the SM Lagrangian. Much  
 190 of the phenomenology of QCD, for example, arises from the  $SU(3)$  symmetry of  
 191 invariance under local color phase transformations, and the fact that the symmetry  
 192 is non-Abelian (i.e. the transformation operators do not commute). Charges are  
 193 the generators of the relevant symmetry group, the conserved currents of Noether's  
 194 first theorem [21]. A full treatment of the SM's symmetry group structure and its  
 195 connections to the theory's phenomenology is given in a number of books, including  
 196 Refs. [2, 4, 5, 22]. The relevant point here is that the weak force arises from an  
 197  $SU(2)$  symmetry generated by the weak isospin  $T$ , and the electromagnetic force from  
 198 a  $U(1)$  symmetry generated by the electric charge  $Q$ , so a unified electroweak force  
 199 should obey an  $SU(2)_L \times U(1)$  symmetry, where the  $L$  indicates that only left-handed  
 200 fermions transform nontrivially under the  $SU(2)$  symmetry. The resulting unified  
 201 electroweak theory is known as the Glashow–Weinberg–Salam (GWS) model [23–25].

202 An unbroken  $SU(2)_L \times U(1)$  symmetry implies four massless vector gauge fields:  
 203 a triplet  $W_\mu^i (i \in 1, 2, 3)$  which couple to fields with weak isospin (but only for left-  
 204 handed particles), and a singlet  $B_\mu$  which couples to weak hypercharge currents. This  
 205 looks like the weak and electromagnetic forces discussed above, except that the weak  
 206 gauge fields are massless and all three weak bosons are maximally P-violating. The  
 207 gauge bosons can be given mass if the underlying symmetry is somehow broken in the  
 208 theory's vacuum state. Symmetry breaking occurs via the Higgs mechanism<sup>5</sup> [26–28],

---

<sup>5</sup>The Higgs mechanism is also called the Englert–Brout–Higgs–Guralnik–Hagen–Kibble mechanism to acknowledge more of the theorists who developed it, with Anderson and 't Hooft sometimes included as well.

209 which introduces an isospin doublet of complex scalar fields

$$\phi = \begin{pmatrix} \phi^+ \\ \phi^0 \end{pmatrix}, \quad (1.2)$$

210 with a Lagrangian of the form

$$\mathcal{L}_H = (D_\mu \phi)^\dagger (D^\mu \phi) + \mu^2 \phi^\dagger \phi - \lambda^2 (\phi^\dagger \phi)^2 \quad (1.3)$$

211 where  $\mu$  and  $\lambda$  are nonzero real numbers,  $D_\mu$  is the covariant derivative invariant  
212 under  $SU(2)_L \times U(1)_Y$ ,

$$D_\mu = \partial_\mu + igT_i W_\mu^i + i\frac{g'Y}{2}B_\mu, \quad (1.4)$$

213 and  $g$  and  $g'$  are the  $W_\mu^i$  and  $B_\mu$  coupling strengths. Because the potential in Eq. (1.3)  
214 is not minimized at 0, for small excitations around the vacuum expectation value  
215 (VEV)  $v = \frac{\mu}{2\lambda} = 246$  GeV, in appropriately chosen coordinates, the doublet of com-  
216 plex scalar fields is reduced to

$$\phi = \frac{1}{\sqrt{2}} \begin{pmatrix} 0 \\ v + h(x) \end{pmatrix}. \quad (1.5)$$

217 Substituting Eq. (1.5) into Eq. (1.3) introduces mixing terms between the  $W_\mu^i$ ,  
218  $B_\mu$ , and  $h$  fields. The new Lagrangian has mass eigenstates

$$\begin{aligned} W_\mu^\pm &= \frac{1}{\sqrt{2}} (W_\mu^1 \mp W_\mu^2) \\ Z_\mu &= \frac{gW_\mu^3 - g'B_\mu}{\sqrt{g^2 + g'^2}} = W_\mu^3 \cos \theta_W - B_\mu \sin \theta_W \\ A_\mu &= \frac{g'W_\mu^3 + gB_\mu}{\sqrt{g^2 + g'^2}} = W_\mu^3 \cos \theta_W + B_\mu \sin \theta_W \end{aligned} \quad (1.6)$$

219 where  $\theta_W$  is the Weinberg electroweak mixing angle

$$\tan \theta_W = \frac{g'}{g}. \quad (1.7)$$

220 The newly defined fields are the gauge fields for the weak and electromagnetic forces,  
 221 and in this basis, the Lagrangian has terms

$$\mathcal{L}_{m_V} = -\frac{v^2 g^2}{4} W_\mu^+ W^{-\mu} - \frac{v^2(g^2 + g'^2)}{8} Z_\mu Z^\mu, \quad (1.8)$$

222 which imply boson masses

$$\begin{aligned} m_W &= \frac{1}{2} v g \\ m_Z &= \frac{1}{2} v \sqrt{g^2 + g'^2} \\ m_A &= m_\gamma = 0, \end{aligned} \quad (1.9)$$

223 and

$$\cos \theta_W = \frac{m_W}{m_Z}. \quad (1.10)$$

224 The original Higgs doublet in Eq. (1.2) had four degrees of freedom (two complex  
 225 scalars), of which only one remains in the final Higgs field  $H = h - v$ , which is now  
 226 a physical field with a corresponding massive scalar boson. The other three became  
 227 the longitudinal polarization modes of the vector bosons.

228 Electroweak symmetry breaking thus explains the observed structure of the elec-  
 229 tromagnetic and weak forces. Three bosons become massive, while one stays mass-  
 230 less. Because the photon is massless, the theory retains the  $U(1)_{EM}$  gauge symmetry  
 231 observed in electromagnetic interactions and electric charge is conserved, while the  
 232  $SU(2)$  symmetry is broken and its generator  $T^i$  is not. The  $W^\pm$  bosons still couple  
 233 only to left-handed fermions, while the  $Z$  couples right- and left-handed fermions but  
 234 not equally. The nonzero VEV even gives a convenient mechanism for generation of  
 235 fermion masses in Yukawa couplings with Lagrangian terms of the form

$$\mathcal{L}_{m_f} = \sqrt{2} \frac{m_f}{v} (\bar{f}_L f_R + \bar{f}_R f_L). \quad (1.11)$$

236 It also controls off-diagonal terms in the Lagrangian that cause interactions between  
 237 the electroweak bosons, the primary focus of this research.

## 238 1.4 Diboson and Multiboson Physics

239 In addition to the previously discussed boson mass terms introduced into the SM  
 240 Lagrangian by electroweak symmetry breaking, boson interaction terms appear for  
 241 trilinear gauge boson couplings

$$\begin{aligned} \mathcal{L}_{WWV} = & -ig \left[ (W_{\mu\nu}^+ W^{-\mu} - W^{+\mu} W_{\mu\nu}) (A^\nu \sin \theta_W - Z^\nu \cos \theta_W) \right. \\ & \left. + W_\nu^- W_\mu^+ (A^{\mu\nu} \sin \theta_W - Z^{\mu\nu} \cos \theta_W) \right], \end{aligned} \quad (1.12)$$

242 which results in the vertices shown in fig 1.1; quartic gauge couplings

$$\begin{aligned} \mathcal{L}_{WWVV} = & -\frac{g^2}{4} \left\{ \left[ 2W_\mu^+ W^{-\mu} + (A_\mu \sin \theta_W - Z_\mu \cos \theta_W)^2 \right]^2 \right. \\ & - [W_\mu^+ W_\nu^- + W_\nu^+ W_\mu^- \\ & \left. + (A_\mu \sin \theta_W - Z_\mu \cos \theta_W) (A_\nu \sin \theta_W - Z_\nu \cos \theta_W) \right]^2 \left. \right\}, \end{aligned} \quad (1.13)$$

243 (Fig. 1.2); Higgs couplings to the massive vector bosons

$$\mathcal{L}_{HV} = \left( gm_W H + \frac{g^2}{4} H^2 \right) \left( W_\mu^+ W^{-\mu} + \frac{Z_\mu Z^\mu}{2 \cos^2 \theta_W} \right), \quad (1.14)$$

244 (Fig. 1.3); and Higgs self-interactions

$$\mathcal{L}_{HH} = -\frac{gm_H^2}{4m_W} H^3 - \frac{g^2 m_H^2}{32m_W^2} H^4, \quad (1.15)$$

245 (Fig. 1.4).

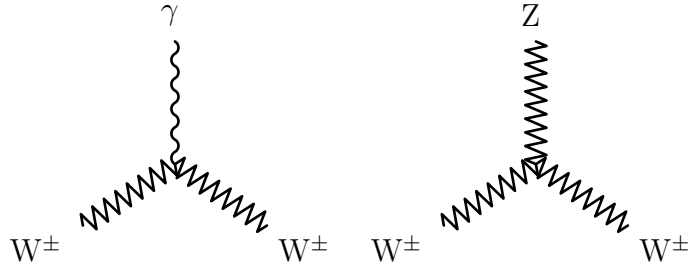


Figure 1.1: Vertex for the trilinear gauge boson couplings allowed at tree level in the SM.

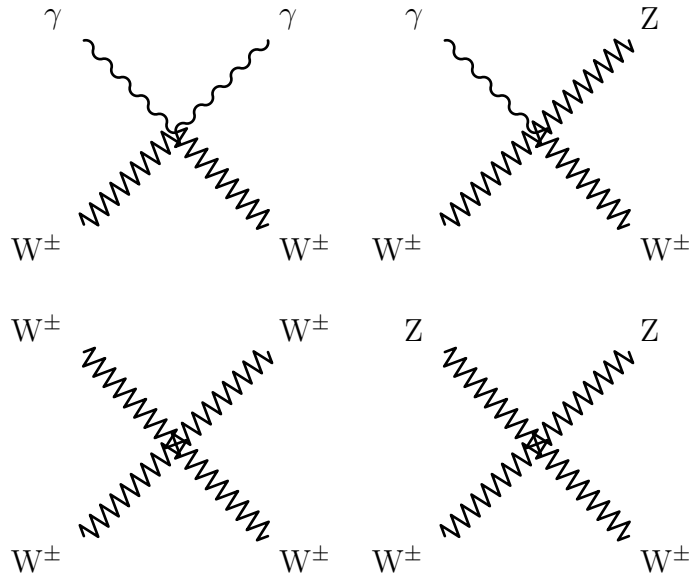


Figure 1.2: Vertices for the quartic gauge boson couplings allowed at tree level in the SM.

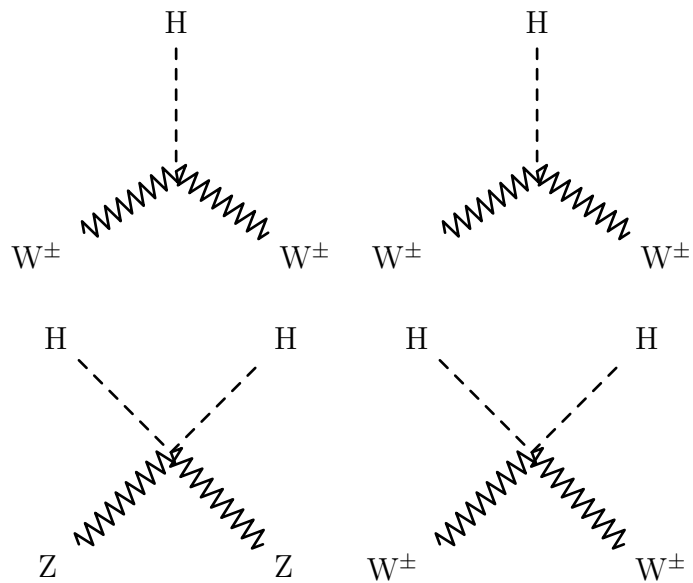


Figure 1.3: Vertices for Higgs boson couplings to gauge bosons allowed at tree level in the SM.

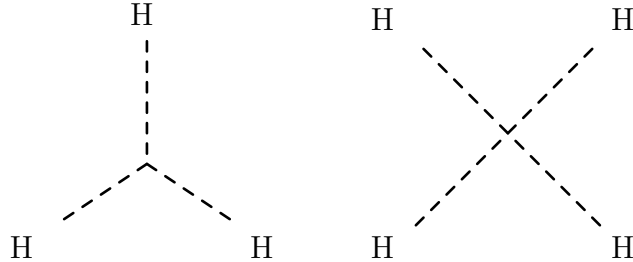


Figure 1.4: Higgs boson trilinear and quartic self-coupling vertices.

246        The structure of the interactions shown in Figs. 1.1–1.4 depends on the details  
 247        of the GWS model and spontaneous symmetry breaking, making multiboson interac-  
 248        tions excellent probes of the SM electroweak and Higgs sectors. One can confirm the  
 249        basic validity of the Higgs mechanism by observation of a Higgs boson, and its inter-  
 250        actions with the massive gauge bosons can be probed in decays to  $ZZ^*$  and  $W^\pm W^\mp$ ,  
 251        which were in fact used in its discovery (see Section 2.2.2.1). The SM makes a num-  
 252        ber of other testable predictions about the behavior of the electroweak bosons, the  
 253        most easily testable of which are the multiboson production cross sections, i.e. the  
 254        rates at which particle collisions result in final states with two or more electroweak  
 255        gauge bosons. The tree-level diagrams for general diboson production in fermion-  
 256        antifermion collisions ( $ff \rightarrow VV$ ) are shown in Fig. 1.5. The cross section for such  
 257        a process will be strongly dependent on the gauge bosons' couplings to fermions, in  
 258        the first diagram in Fig. 1.5, and their couplings to other gauge bosons in the second  
 259        diagram (which does not contribute at all for neutral gauge bosons in the SM). Dibo-  
 260        son production in  $gg$  collisions does not occur at tree level but may proceed through  
 261        a quark loop as in the so-called box diagram of Fig. 1.6.

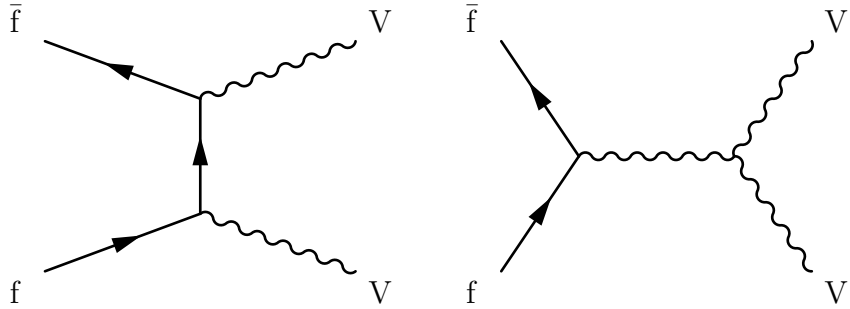


Figure 1.5: Tree-level Feynman diagrams for diboson production in fermion-anti-fermion collisions. The second diagram does not contribute for neutral gauge bosons in the SM.

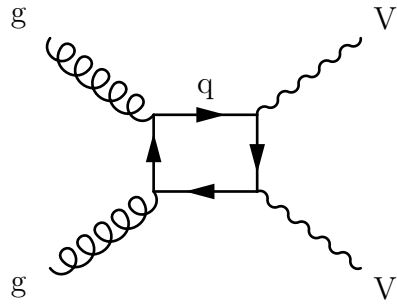


Figure 1.6: Leading order “box” diagram for diboson production through a quark loop in a gluon-gluon fusion event.

### 262 1.4.1 Vector Boson Scattering

263 Quasielastic vector boson scattering (VBS) interactions ( $VV \rightarrow VV$ ) are sensitive  
 264 to a number of features of the SM electroweak sector. If only the vector bosons are  
 265 considered, the scattering amplitude for the process grows quadratically with the  
 266 center-of-mass energy, violating unitarity [29]. Interference from diagrams involving  
 267 the Higgs boson restores unitarity, as shown in Fig. 1.7. The VBS cross section is  
 268 therefore sensitive to both the four-point gauge boson couplings of Fig. 1.2 and the  
 269 structure of the Higgs field, and can be used to distinguish the SM from models  
 270 without a Higgs boson and models with multiple particles that play its role.

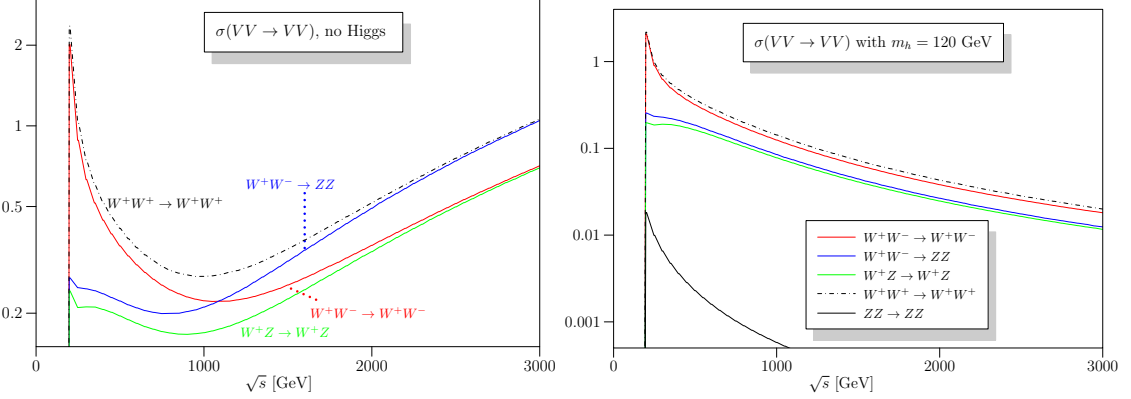


Figure 1.7:  $VV \rightarrow VV$  scattering cross sections as a function of center-of-mass energy for the SM with no Higgs boson (left) and a Higgs boson with  $m_H = 120$  GeV (right), reproduced from Ref. [29]. The model with no Higgs violates unitarity.

## 271 1.5 Limitations and Possible Extensions

272 As noted above, the SM is believed to be fully self-consistent, but it has several notable  
 273 omissions. It makes no mention of gravity, which is too weak to be probed at the  
 274 level of individual particles at energies available in collider experiments. Neutrinos in  
 275 the SM are massless, but they are found experimentally to oscillate between the three  
 276 flavors in flight, which implies that the flavor eigenstates are not mass eigenstates,  
 277 and thus that they have mass. Dark matter, the unidentified substance that makes up  
 278 roughly 80% of the universe’s gravitationally interacting material [11, 30–32], is also  
 279 not described. Some consider the SM to be “ad hoc” in the sense that the fermion  
 280 masses, and a number of other parameters—19 in all—are completely unconstrained,  
 281 and a more aesthetically satisfying theory would make predictions for all of them. A  
 282 nicer theory would also offer thorough explanations for what seem now like remarkable  
 283 coincidences. For example, the so-called hierarchy problem: it is intuitively surprising  
 284 that the strengths of the fundamental forces vary by many orders of magnitude, and  
 285 do so in such a way that large quantum corrections to the effective Higgs potential  
 286 cancel almost exactly, causing the Higgs boson mass to be nonzero but much smaller

287 than the scale of the corrections ( $\mathcal{O}(10^{19} \text{ GeV})$ ) [33–35].

288 A number of theories have been proposed which modify or extend the SM [11,  
 289 32], adding new symmetry groups, unifying the existing ones further, adding new  
 290 particles, etc. A fourth generation of fermions would be a simple extension, but the  
 291 fourth neutrino would have to have a mass more than half the Z boson mass to have  
 292 escaped detection so far, which would be surprising given the small masses of the  
 293 first three [11, 36]. Supersymmetric models, for example, posit a symmetry between  
 294 bosons and fermions, such that each particle would have a “superpartner” with the  
 295 opposite spin statistics which would provide an opposite correction to the effective  
 296 Higgs potential and thus a clean solution to the hierarchy problem [11, 37]. Despite  
 297 extensive searches, no evidence of such models has been found [38].

### 298 1.5.1 Anomalous Gauge Couplings

299 Another simple extension to the SM would be a new force, with mediator gauge bosons  
 300 analogous to the W and Z above the masses accessible at existing colliders. Such a  
 301 force would originate from a previously undiscovered symmetry, which in many models  
 302 could result from a higher symmetry which unifies all the fundamental forces at high  
 303 energy but is broken and effectively reduces to the SM in the low-energy limit [11,  
 304 33, 35, 39]. This, and several other possible extensions to the SM, would appear in  
 305 practice as small deviations from the expected couplings of the gauge bosons. Such  
 306 deviations from standard model interactions are called anomalous gauge couplings  
 307 (aGC), and may involve anomalous trilinear (aTGC) or quartic (aQGC) vertices. Of  
 308 particular interest here are the anomalous neutral couplings, which correspond to  
 309 the vertices shown in Fig. 1.8. These interactions are forbidden in the SM. Their  
 310 existence would increase the cross section for diboson production, and affect the cross  
 311 section for  $ZZ \rightarrow ZZ$  scattering, changing the requirements on the Higgs field needed

312 to preserve unitarity.

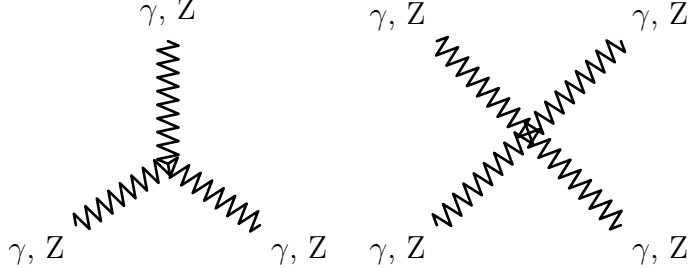


Figure 1.8: Fully-neutral gauge coupling vertices, for aTGCs (left) and aQGCs (right). These are forbidden in the SM.

313 Several theoretical frameworks exist for describing aGCs. For aTGCs, we use the  
 314 effective Lagrangian approach described in Ref. [40–42]. In this parameterization, a  
 315 ZZV coupling (where V may be Z or  $\gamma$ ) has a vertex function corresponding to the  
 316 vertex shown in Fig. 1.9 of the form

$$\Gamma_{\text{V}}^{\alpha,\beta,\delta}(q_1, q_2, P) = i \frac{\hat{s} - m_{\text{V}}^2}{m_Z^2} (f_4^{\text{V}} (P^\alpha g^{\delta\beta} + P^\beta g^{\delta\alpha}) + f_5^{\text{V}} \varepsilon^{\delta\alpha\beta\lambda} (q_1 - q_2)_\lambda), \quad (1.16)$$

317 where  $\hat{s}$  is the center of mass energy squared,  $g^{\mu\nu}$  is the Minkowski metric and  $\varepsilon^{\alpha\beta\gamma\delta}$  is  
 318 the fully antisymmetric tensor with  $\varepsilon^{0123} = 1$ . Neutral aTGCs are then described by  
 319 two parameters  $f_4^{\gamma,Z}$  associated to CP-odd terms and two parameters  $f_5^{\gamma,Z}$  associated  
 320 to CP-even terms.<sup>6</sup> The effective Lagrangians in use here are taken to be low-energy  
 321 approximations invalid at high energy, and are not unitary at high  $\sqrt{\hat{s}}$ . In some  
 322 previous literature (see Section 2.3.1), unitarity is enforced with a generalized dipole  
 323 for factor [42, 43], such that the vertex factor takes an energy dependence,

$$f_i^{\text{V}}(\hat{s}) = \frac{f_{i,0}^{\text{V}}}{(1 + \hat{s}/\Lambda^2)^n}, \quad (1.17)$$

324 where  $\Lambda$  is the energy scale of the new physics process. No such form factor is applied  
 325 in this work, to avoid adding unnecessary model dependence, so  $\Lambda$  is taken to be much  
 326 larger than the energies accessible in the experiment and no form factor is applied.

<sup>6</sup>There are, of course, analogous terms for all anomalous VVV couplings, where V may be any of the electroweak bosons, but only the ZZZ and ZZ $\gamma$  terms are relevant to this work.

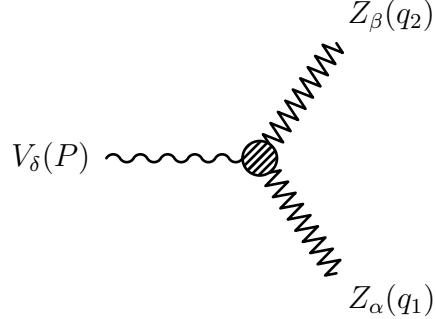


Figure 1.9: An anomalous neutral triple gauge coupling vertex, with momentum labels corresponding to Eq. (1.16).

327 For aQGCs, we adopt an effective field theory approach [44] which parameterizes  
 328 the effects of new physics as a set of field operators [45]. The operators are chosen to  
 329 be dimension-8, because this is the lowest dimension that can yield neutral quartic  
 330 couplings, and the lowest dimension that can produce a theory with aQGCs but no  
 331 aTGCs. Out of the large class of operators which control aQGCs in general, ZZ VBS  
 332 is sensitive to five,

$$\begin{aligned}\mathcal{L}_{T0} &= \frac{f_{T0}}{\Lambda^4} \text{Tr} \left[ \hat{W}_{\mu\nu} \hat{W}^{\mu\nu} \right] \times \text{Tr} \left[ \hat{W}_{\alpha\beta} \hat{W}^{\alpha\beta} \right] \\ \mathcal{L}_{T1} &= \frac{f_{T1}}{\Lambda^4} \text{Tr} \left[ \hat{W}_{\alpha\nu} \hat{W}^{\mu\beta} \right] \times \text{Tr} \left[ \hat{W}_{\mu\beta} \hat{W}^{\alpha\nu} \right] \\ \mathcal{L}_{T2} &= \frac{f_{T2}}{\Lambda^4} \text{Tr} \left[ \hat{W}_{\alpha\mu} \hat{W}^{\mu\beta} \right] \times \text{Tr} \left[ \hat{W}_{\beta\nu} \hat{W}^{\nu\alpha} \right] \\ \mathcal{L}_{T8} &= \frac{f_{T8}}{\Lambda^4} B_{\mu\nu} B^{\mu\nu} B_{\alpha\beta} B^{\alpha\beta} \\ \mathcal{L}_{T9} &= \frac{f_{T9}}{\Lambda^4} B_{\alpha\mu} B^{\mu\beta} B_{\beta\nu} B^{\nu\alpha},\end{aligned}\tag{1.18}$$

333 where

$$\hat{W}_{\mu\nu} = \sum_j W_{\mu\nu}^j \frac{\sigma^j}{2},\tag{1.19}$$

334 and  $\Lambda \gg \sqrt{s}$  is again the scale of the new physics causing the change in the effective  
 335 couplings.

## 336 1.6 Proton-Proton Collisions

337 Our experimental probe of all these interactions is proton-proton collisions. As dis-  
 338 cussed above, protons are bound states of three quarks (uud), known as the valence  
 339 quarks, held together by virtual gluon exchange. The proton constituents, quarks and  
 340 gluons, are collectively called partons. The gluons carry roughly half the total proton  
 341 momentum [2]. Because the number of gluons is not conserved, and they self-interact,  
 342 the gluon structure of the proton is constantly evolving, and gluons produce virtual  
 343  $q\bar{q}$  “sea quark” pairs which annihilate again on time scales of order  $t_{virt} \sim 1/\Delta E$  [3].  
 344 A sufficiently energetic color-charged particle colliding with a proton may therefore  
 345 interact with any kind of quark or with a gluon, and interesting physics in a pp  
 346 collision may be initiated by  $qq$ ,  $q\bar{q}$ ,  $qg$ , or  $gg$  scattering. A particle that scatters  
 347 with a proton of energy  $P$  has a probability of interacting with a parton of a given  
 348 type with momentum  $xP$  given by the parton distribution function (PDF)  $f(x, Q^2)$ ,  
 349 where  $x$  is the fraction of the proton momentum carried by the parton and  $Q$  is the  
 350 momentum transfer of the interaction [3]. Heuristically, the PDF is a function of  $Q$   
 351 because it sets the wavelength of the mediating gauge boson and thus the scale on  
 352 which the interaction can resolve constituent partons. PDFs are nonperturbative and  
 353 have not been calculated from theory, so they are built from fits to experimental data  
 354 from fixed-target and symmetric  $e^\pm p$  deep inelastic scattering (DIS) data, and from  
 355 hadron collider data [46]. The most recent PDFs from the NNPDF collaboration [46]  
 356 are shown in Fig 1.10.

357 As mentioned previously, the rate at which a scattering process occurs is called its  
 358 cross section  $\sigma$ , typically given in barns, a unit of area  $b = 10^{-24} \text{ cm}^2$ . The number  
 359 of collisions is characterized by the luminosity  $\mathcal{L}$  such that the rate of events with

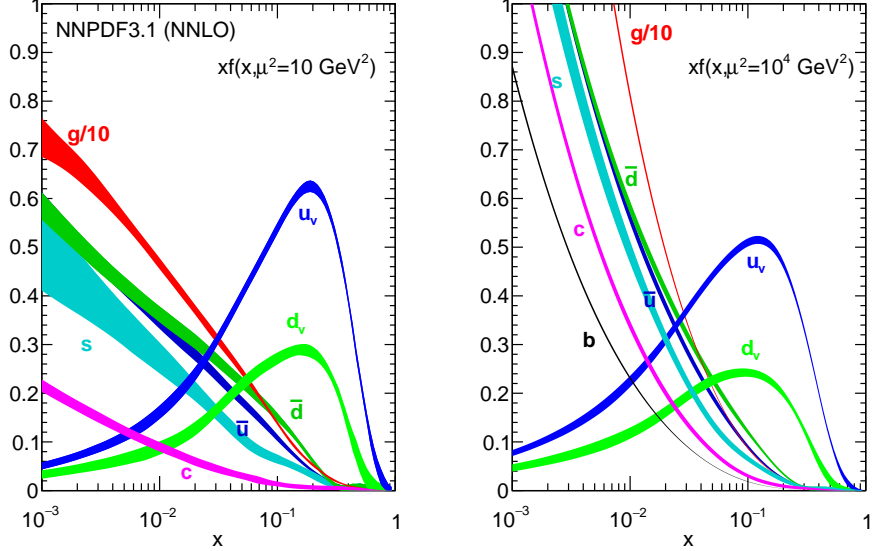


Figure 1.10: Parton distribution functions from NNPDF3.1, reproduced from Ref. [46], which used  $\mu$  for the momentum transfer denoted  $Q$  in the text.

360 final state  $X$  will be given by

$$\frac{dN_X}{dt} = \sigma(pp \rightarrow X) \mathcal{L} \quad (1.20)$$

361 as described in more detail in Section 3.1. If the initial protons each have momen-  
 362 tum  $P$  and collide head on, such that their center-of-mass energy is  $\sqrt{s} = 2P$ , the  
 363 interacting partons will have total energy  $\sqrt{\hat{s}} = \sqrt{2x_1 x_2} P$  where  $x_1$  and  $x_2$  are the  
 364 fraction of its proton's momentum each incoming parton carried. The cross section  
 365 is given by

$$\sigma(pp \rightarrow X) = \sum_{p_1, p_2 \in q, \bar{q}, g} C_{p_1, p_2} \int dx_1 dx_2 f_{p_1}(x_1, Q^2) f_{p_2}(x_2, Q^2) \sigma_{ME}(p_1 + p_2 \rightarrow X), \quad (1.21)$$

366 where  $\sigma_{ME}$  is the matrix element-level cross section for the bare partons to scatter  
 367 to final state  $X$  and  $C_{p_1, p_2}$  is a combinatoric factor based on the number of possible  
 368 color combinations that varies based on the initial state particles  $p_1$  and  $p_2$ . This

369 factorization into perturbative hard process physics and the nonperturbative PDF  
370 greatly simplifies calculations.

## 371 1.7 ZZ Measurements in Context

372 This is the context for the work described in the following chapters: the SM is in-  
373 complete, but it has been tested extensively and no discrepancies have been found  
374 (a partial review of studies that did not exclude the SM can be found in Chapter 2).  
375 Because the electroweak sector was the last to be confirmed experimentally and is  
376 generally best explored at high energies, a number of aspects await detailed confir-  
377 mation and remain a potential area where new physics might be found. This thesis  
378 presents several studies of diboson events with  $\ell^+\ell^-\ell'^+\ell'^-$  ( $\ell, \ell' \in e, \mu$ ) final states  
379 designed to probe the interactions of the neutral electroweak bosons. In particular,  
380 as one can deduce from Eqs. (1.12)–(1.14), ZZ production processes are sensitive to  
381 the details of the couplings between the gauge bosons and can therefore be used to  
382 investigate the GWS model and the Higgs model and spontaneous symmetry break-  
383 ing. Measurements of ZZ production have been made before, but measurements  
384 in a new energy regime and with a very large dataset allow stringent new tests of  
385 the SM and allow the potential observation of previously unseen phenomena within  
386 and beyond it. The results presented here substantially expand our understanding  
387 of ZZ production, with inclusive and differential cross section measurements at the  
388 record-breaking center-of-mass energy of 13 TeV, the most precise measurement of  
389 the  $Z \rightarrow 4\ell$  branching fraction to date, and searches for vector boson scattering and  
390 anomalous neutral gauge couplings.

## **0 Chapter 2**

# **1 ZZ Phenomenology and Previous 2 Results**

3 Four-lepton final states originate primarily from three physics processes: nonresonant  
 4 diboson production, resonant Higgs boson production, and resonant single-Z produc-  
 5 tion. Multi-Z triboson production (WZZ and ZZZ) occurs at negligible rates [47, 48].  
 6 Single-Z triboson production (WWZ) [48, 49] and  $t\bar{t}Z$  production result in final states  
 7 with four prompt leptons, but are considered background (see Section 2.4). The three  
 8 signal processes can be distinguished by kinematics, such as the four-lepton invariant  
 9 mass distribution.

10 The signal processes all involve on- or off-shell Z bosons. The Z was first indirectly  
 11 observed in 1973 when the Gargamelle bubble chamber experiment at CERN recorded  
 12 an elastic muon antineutrino-electron ( $\bar{\nu}_\mu + e^- \rightarrow \bar{\nu}_\mu + e^-$ ) scattering event [50]. Direct  
 13 observation in leptonic decays came roughly a decade later, from the UA1 experiment,  
 14 also at CERN [51]. Clean  $e^+e^-$  collisions at LEP and SLAC, where the center-of-mass  
 15 energy could be adjusted to produce Z bosons copiously, allowed its properties—and a  
 16 number of other parameters of the electroweak theory—to be measured with per-mille

17 precision or better [52]. Of particular importance to this study, its mass is

$$m_Z = 91.1876 \pm 0.0021 \text{ GeV}, \quad (2.1)$$

18 its full width is

$$\Gamma_Z = 2.4952 \pm 0.0023 \text{ GeV}, \quad (2.2)$$

19 its width in leptonic decays is

$$\Gamma_Z(\ell^+ \ell^-) = 83.984 \pm 0.086 \text{ MeV}, \quad (2.3)$$

20 and it decays to a pair of charged leptons 3.3658% of the time for each lepton fla-  
21 vor [11].

## 22 **2.1 Nonresonant ZZ/Z $\gamma^*$ Production and Decay**

23 Leading-order ZZ production is q $\bar{q}$ -initiated and proceeds through *t*-channel quark  
24 exchange, as shown in Fig. 2.1. At next-to-leading order (NLO; several representative  
25 diagrams are shown in Fig. 2.2), production may have a gluon in the initial state  
26 and may have a quark or gluon in the final state which hadronizes and appears  
27 experimentally as a jet [53–55]. Next-to-next-to-leading order (NNLO) adds gluon-  
28 gluon fusion box diagrams (Fig. 2.3), as well as q $\bar{q}$ -initiated production with two  
29 loops, one loop and a final state jet, and two jets [56, 57]. The NLO and NNLO  
30 corrections are generally large, outside the scale uncertainties of the calculations at  
31 previous orders, because diagrams with new initial states contribute only positively  
32 to the cross section. Quark-gluon scattering diagrams introduced at NLO and gluon-  
33 gluon fusion diagrams introduced at NNLO have large amplitudes—the gg  $\rightarrow$  ZZ  
34 process accounts for roughly 60% of the total NNLO correction, for example—due  
35 to the high effective gluon luminosity in multi-TeV proton collisions [56]. Because

36 of the box diagrams' large contribution, “NLO + gg” simulations are often used, in  
 37 which NLO  $q\bar{q}/qg/\bar{q}g \rightarrow ZZ$  and LO  $gg \rightarrow ZZ$  samples are summed even though they  
 38 formally contribute at different orders in  $\alpha_s$ .

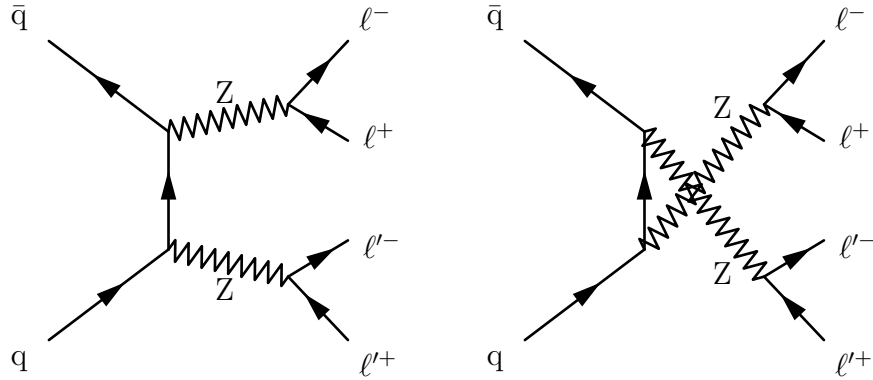


Figure 2.1: Leading order Feynman diagrams for  $ZZ \rightarrow 4\ell$  production in pp collisions.

39 Production of pairs of on-shell Z bosons<sup>1</sup> turns on sharply at the kinematic thresh-  
 40 old  $\sqrt{\hat{s}} = 2m_Z = 182.4$  GeV, and in proton-proton collisions at  $\sqrt{s} = 13$  TeV, peaks  
 41 around  $m_{ZZ} \approx 200$  GeV before falling steeply at higher invariant masses. Continuum  
 42 production occurs below the kinematic threshold when one or both Z bosons are re-  
 43 placed by a  $Z^*/\gamma^*$  admixture, typically in the form of a  $q\bar{q} \rightarrow Z$  event in which one of  
 44 the incoming quarks emits a virtual photon as initial state radiation (ISR). Events of  
 45 interest in this analysis (see Sections 5.4 and 6.3) generally have one on-shell Z, and  
 46 a  $Z^*/\gamma^*$  at a lower mass. Nonresonant  $Z\gamma^*$  production is generally flat as a function  
 47 of invariant mass between roughly 100 GeV and the doubly resonant threshold.

---

<sup>1</sup>Events with two on-shell Z bosons are often called “doubly resonant,” but are a subset of “nonresonant” production in the sense that the ZZ system is not produced by a resonance. Either term may be used to distinguish “continuum” production from “singly resonant” production from  $Z \rightarrow 4\ell$ ,  $H \rightarrow ZZ^*$ , or a potential new particle which decays to ZZ.

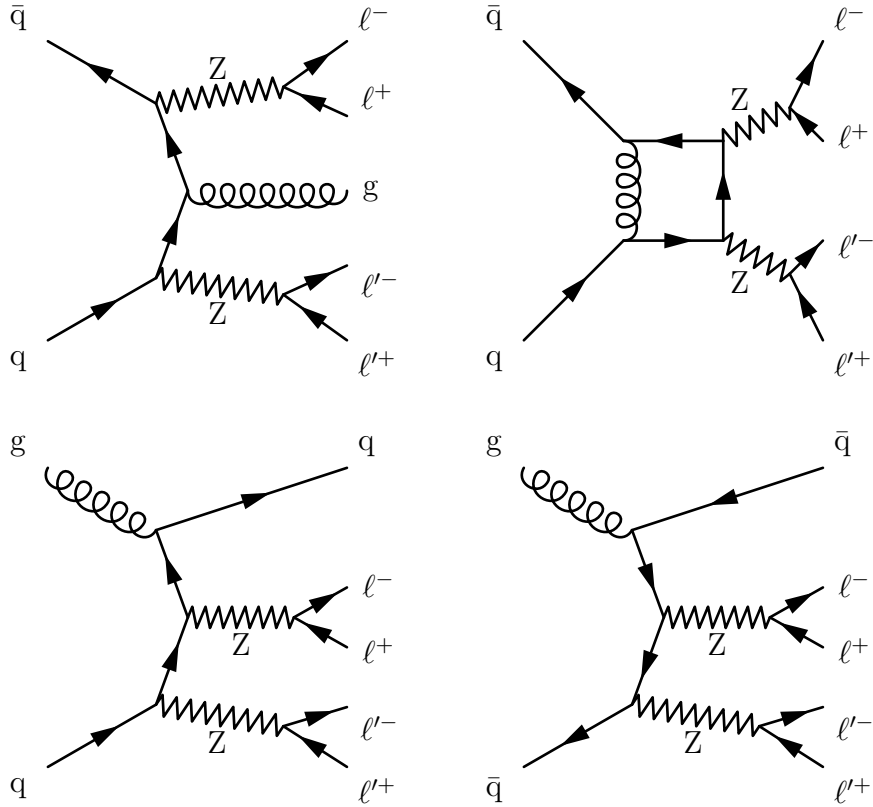


Figure 2.2: Four representative Feynman diagrams that contribute to  $ZZ \rightarrow 4\ell$  production in  $pp$  collisions at NLO. Clockwise from the top right, the diagrams are examples of one-loop diagrams, real antiquark and quark emission, and real gluon emission. The loop diagram (top right) is formally NNLO, but contributes at NLO through interference with NLO  $q\bar{q} \rightarrow ZZ$  diagrams.

### <sup>48</sup> 2.1.1 Vector Boson Scattering

<sup>49</sup> Vector boson scattering proceeds at hadron colliders through the diagrams shown in  
 Fig 2.4, resulting in a  $ZZjj$  final state. This fully electroweak (EWK) production  
 must be distinguished from the background of QCD-initiated  $ZZ + \text{jets}$  events (see  
 Section 2.4). The hallmark of the EWK process is a pair of high energy, high rapidity  
 jets from the quarks, which retain a high boost along the  $z$ -axis even after electroweak  
 boson emission and are thus deflected through a small angle in the lab frame. At the  
 same time, the  $ZZ$  system is produced with low transverse boost compared to QCD-

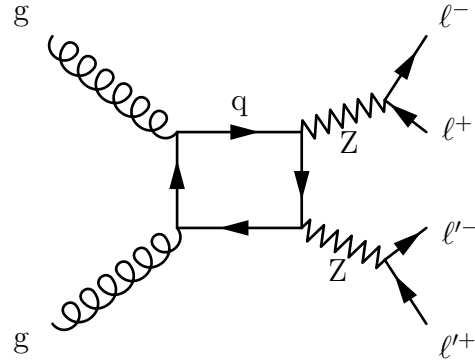


Figure 2.3: A LO box diagram for  $ZZ \rightarrow 4\ell$  production through a quark loop in a gluon-gluon fusion event. This is formally an NNLO diagram for  $ZZ$  production overall, but is often included in NLO calculations because it accounts for a large fraction of the NNLO correction and its contribution to the  $ZZ$  cross section has a similar magnitude to that from the NLO corrections. The  $gg \rightarrow ZZ$  amplitude is so large due to the high effective luminosity of gluons with enough energy to produce a  $Z$  boson pair in proton collisions at high  $Q^2$ ,

56 initiated  $ZZjj$  events, in which the  $ZZ$  system recoils against the jets, and somewhat  
 57 higher invariant mass on average [58]. Because the hard scattering interaction involves  
 58 no color exchange or reconnection [58–60], VBS events are much less likely to have less  
 59 energetic jets between the two high-energy quark jets. Useful variables to discriminate  
 60 between EWK and QCD production therefore include the angle between the jets, the  
 61 jet energies, the dijet invariant mass, the  $ZZ$  invariant mass and rapidity, and the  
 62 number of central jets (see Section 6.5 for a full list and definitions).

### 63 2.1.2 Prior Measurements

64 Doubly resonant  $ZZ$  production was first observed in  $e^+e^-$  collisions at LEP by the  
 65 ALEPH, OPAL, L3, and DELPHI experiments, from 183 GeV, just above the thresh-  
 66 old center-of-mass energy, to the LEP maximum of 209 GeV [61–66]. Because the  $ZZ$   
 67 cross section is very small, these measurements used all possible final states except  
 68 those in which all  $Z$  decay products were neutrinos or taus. This was possible because

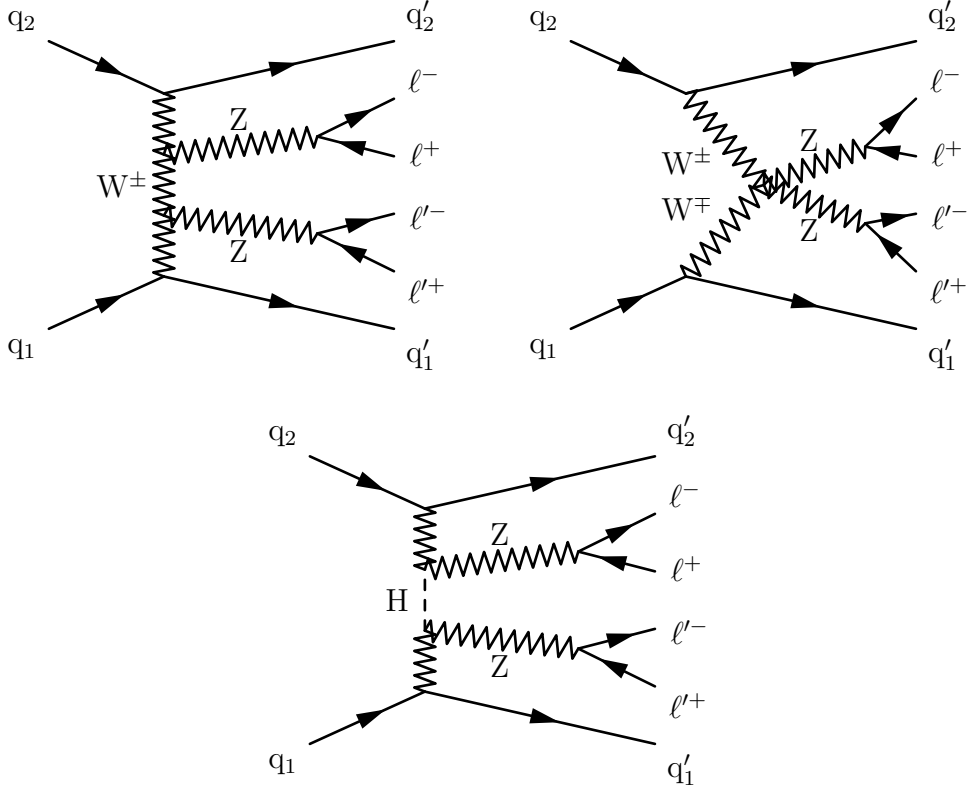


Figure 2.4: The primary ZZ VBS diagrams at hadron colliders. Diagrams also exist with antiquarks and with permutation and crossing of the final state particles. The interaction is only unitary to arbitrarily high energy when all diagrams are considered.

69 jets in  $e^+e^-$  collisions can be reliably matched to a hard scattering process, allowing  
 70 identification of  $Z \rightarrow q\bar{q}$  decays. The measurements agreed with the SM, but were  
 71 dominated by statistical uncertainties. Example measured cross sections from OPAL  
 72 are shown in Fig 2.5 [65].

73 Production in hadron collisions was first observed by the CDF and D0 experi-  
 74 ments, in 1.96 TeV  $p\bar{p}$  events at Tevatron [67–71]. In contrast to the LEP measure-  
 75 ments,  $p\bar{p}$  colliders cause too many extraneous jets for the hadronic channels to be  
 76 seen above the background, so only the  $4\ell$  and  $2\ell 2\nu$  ( $\ell = e, \mu$ ) final states were used.  
 77 These fully leptonic decay modes have small branching fractions on top of the small  
 78 ZZ cross section of around 1.6 pb [53], but the total Tevatron dataset of roughly  $6 \text{ fb}^{-1}$

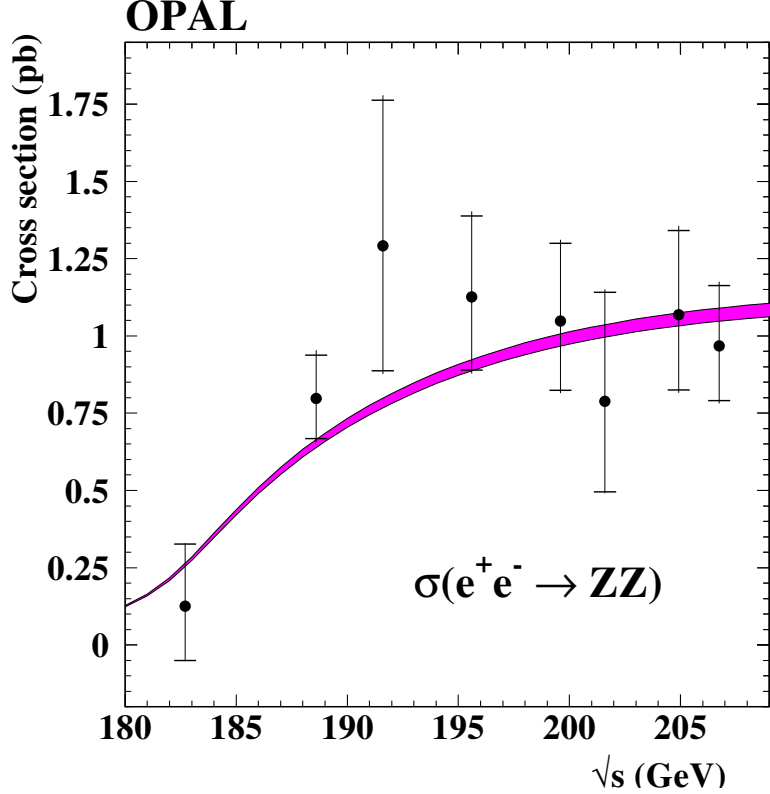


Figure 2.5: Measured  $e^+e^- \rightarrow ZZ$  cross sections from the OPAL experiment, reproduced from Ref. [65]. Points represent the measured values. Vertical bars are the total uncertainty with horizontal bars indicating the statistical uncertainties, which dominate. The band is the SM prediction with a 2% theoretical uncertainty.

79 was large enough for CDF and D0 to find a few dozen events each. Results were again  
 80 fully consistent with the SM but the statistical uncertainties were large, as can be  
 81 seen in the example  $m_{4\ell}$  shown in Fig. 2.6 [70].

82 The first run of the LHC (see Section 3.1) produced large datasets of pp collisions  
 83 at  $\sqrt{s} = 7$  and 8 TeV, producing ZZ events with a higher cross section than at  
 84 Tevatron [56] and with a greater integrated luminosity. The primary measurement  
 85 channels were again the fully leptonic  $4\ell$  and  $2\ell 2\nu$  decays, and the cross sections were  
 86 measured at  $\sqrt{s} = 7$  and 8 TeV by both CMS [72–75] and ATLAS [76–78]. With  
 87 a dataset of roughly  $20\text{ fb}^{-1}$  and signal event counts in the hundreds even for the

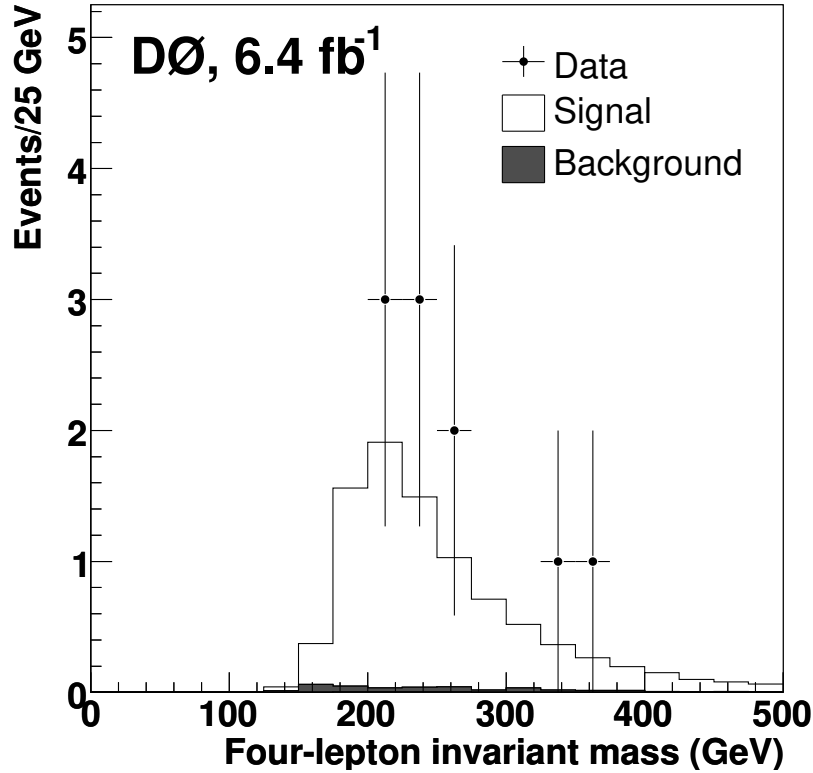


Figure 2.6: Measured  $m_{4\ell}$  distribution from ZZ events collected by D0, reproduced from Ref. [70]. Points represent data with vertical bars showing statistical uncertainties, while the histograms show the SM expectation.

88 low-rate  $4\ell$  channel, the 8 TeV measurements had the statistical power to include  
 89 differential cross sections as functions of kinematic observables for the ZZ system  
 90 and the associated jets. Statistical uncertainties were still larger than the systematic  
 91 uncertainties, but they were at the level of 5–10% for the total cross section, compared  
 92 to 30–50% at Tevatron and 15–150% at LEP depending on the experiment and center-  
 93 of-mass energy<sup>2</sup>. The four-lepton mass spectra from the CMS and ATLAS ZZ cross  
 94 section measurements at 8 TeV are shown in Figs. 2.7 and 2.8, respectively [73, 77]. A  
 95 measurement was also performed on CMS data in the ZZ  $\rightarrow \ell^+\ell^- b\bar{b}$  and ZZ  $\rightarrow \nu\bar{\nu} b\bar{b}$   
 96 channels [79].

---

<sup>2</sup>Most LEP ZZ cross section measurements had statistical uncertainties around 20–40%; see references given in the text for details.

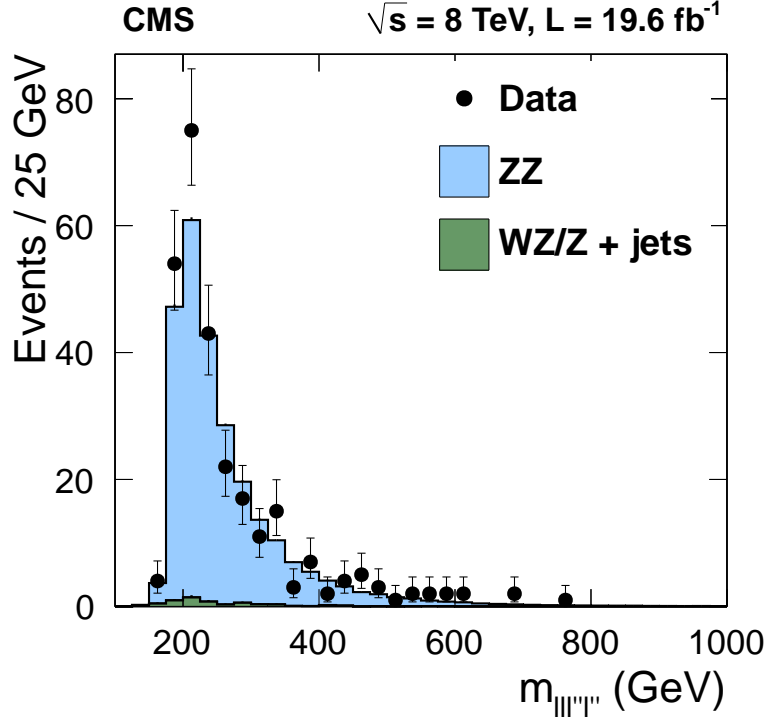


Figure 2.7: Measured  $m_{4\ell}$  distribution from ZZ events collected by CMS at  $\sqrt{s} = 8$  TeV, reproduced from Ref. [77]. Points represent data with vertical bars showing statistical uncertainties, while the histograms show the SM expectation. The grey hatched band represents the total uncertainty on the prediction.

97        CMS found that the total ZZ cross sections, defined as the cross sections of all  
 98        events with two Z bosons in the mass range 60–120 GeV, to be

$$\begin{aligned}\sigma_{ZZ}(7 \text{ TeV}) &= 6.24^{+0.86}_{-0.80} (\text{stat})^{+0.41}_{-0.32} (\text{syst}) \pm 0.14 (\text{lumi}) \text{ pb} \\ \sigma_{ZZ}(8 \text{ TeV}) &= 7.7 \pm 0.5 (\text{stat})^{+0.5}_{-0.4} (\text{syst}) \pm 0.4 (\text{theo}) \pm 0.2 (\text{lumi}) \text{ pb},\end{aligned}\tag{2.4}$$

99        when measured with  $4\ell$  final states [73, 76], and

$$\begin{aligned}\sigma_{ZZ}(7 \text{ TeV}) &= 5.1^{+1.5}_{-1.4} (\text{stat})^{+1.4}_{-1.1} (\text{syst}) \pm 0.1 (\text{lumi}) \text{ pb} \\ \sigma_{ZZ}(8 \text{ TeV}) &= 7.2 \pm 0.8 (\text{stat})^{+1.9}_{-1.5} (\text{syst}) \pm 0.2 (\text{lumi}) \text{ pb}\end{aligned}\tag{2.5}$$

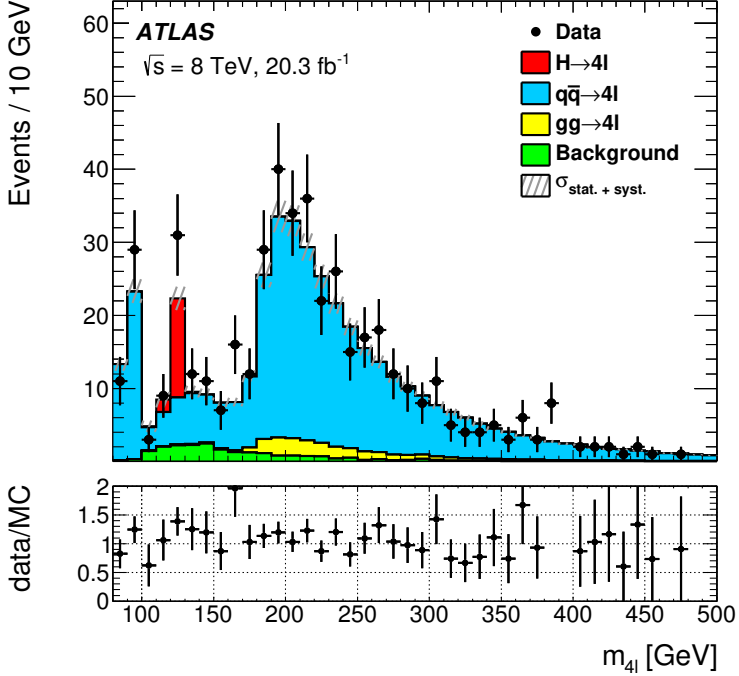


Figure 2.8: Measured  $m_{4l}$  distribution from ZZ events collected by ATLAS at  $\sqrt{s} = 8$  TeV, reproduced from Ref. [70]. Points represent data with vertical bars showing statistical uncertainties, while the histograms show the SM expectation.

100 when measured with  $2\ell 2\nu$  final states [74]. ATLAS found

$$\begin{aligned}\sigma_{ZZ}(7 \text{ TeV}) &= 6.7 \pm 0.7 \text{ (stat)} {}^{+0.4}_{-0.3} \text{ (syst)} \pm 0.3 \text{ (lumi)} \text{ pb} \\ \sigma_{ZZ}(8 \text{ TeV}) &= 7.3 \pm 0.4 \text{ (stat)} \pm 0.3 \text{ (syst)} \pm 0.2 \text{ (lumi)} \text{ pb},\end{aligned}\tag{2.6}$$

101 using  $4\ell$  final states at 7 TeV [76] and a combination of  $4\ell$  and  $2\ell 2\nu$  events at  
 102 8 TeV [78]. ATLAS used a slightly different definition of the Z, considering it to  
 103 have mass in the range 66–116 GeV, which reduces the SM expected cross section  
 104 by 1.6% [80]. Measured cross sections from both experiments are again consistent  
 105 with SM predictions of  $6.7 \pm 0.2$  pb at 7 TeV and  $8.3 \pm 0.2$  pb at 8 TeV, both calcu-  
 106 lated at NNNLO in QCD with MATRIX, with factorization and renormalization scales  
 107  $\mu_F = \mu_R = m_Z$ .

108 Searches for vector boson scattering were first performed at  $\sqrt{s} = 8$  TeV. The first

process examined was the low-background same-sign WW process  $\text{pp} \rightarrow W^\pm W^\pm jj$  studied at ATLAS, where evidence for electroweak production was observed at the level of a  $3.6\sigma$  standard deviation excess over the null hypothesis [81], and at CMS, where a  $2.0\sigma$  excess was found [82]. Subsequent searches for electroweak  $Z\gamma jj$  production found a  $3.0\sigma$  excess above the null hypothesis at CMS [83] and no significant excess at ATLAS [84]. A CMS measurement of  $W\gamma jj$  production found a  $2.7\sigma$  excess above the null hypothesis consistent with electroweak production [85]. Searches for photon-photon VBS were performed as searches for exclusive and quasi-exclusive  $\gamma\gamma \rightarrow W^+W^-$  production  $\text{pp} \rightarrow p^{(*)}W^+W^-p^{(*)}$ , in which the protons do not collide but instead both radiate photons, which scatter. CMS found evidence at the level of  $3.4\sigma$  above the null hypothesis [86], and ATLAS saw a  $3.0\sigma$  excess [87]. Roughly contemporaneously with this work, electroweak same-sign WW production was observed at CMS in 13 TeV collisions, with a significance of  $5.5\sigma$  [88]. No searches for Electroweak ZZ production had been performed prior to the analysis described in the following chapters.

## 124 **2.2 Resonant ZZ<sup>\*</sup>/γ<sup>\*</sup>γ<sup>\*</sup> Production**

125 Resonant production appears as a sharp peak in the four-lepton invariant mass distribution over the broad spectrum from nonresonant production. There are two known 126 four-lepton resonances: single-Z decays to four leptons around 91 GeV, and Higgs 127 decays to ZZ<sup>\*</sup> around 125 GeV. Another resonance, caused by a new particle, could 128 still be discovered at high mass, or at low mass but with a very small cross section.

### 130 2.2.1 Z Boson Decays to Four Leptons

131 A single Z boson may decay to a four-lepton final state when a lepton from a normal  
 132  $Z \rightarrow \ell^+ \ell^-$  decay radiates a virtual photon, as shown in Fig 2.9. In a window around  
 133 the Z mass of  $80 < m_{4\ell} < 100$  GeV,  $t$ - and  $u$ -channel production (the diagrams of  
 134 Fig 2.1 with  $\gamma^*$  for both bosons) contribute at the few-percent level (4% at  $\sqrt{s} =$   
 135 13 TeV). Four-fermion decays were studied in detail at LEP [89]. This included  
 136 four-lepton decays, but used all  $\ell^+ \ell^- f\bar{f}$  ( $\ell = e, \mu, \tau$ ) final states, where  $f$  could be any  
 137 fermion except the neutrinos.  $Z \rightarrow 4\ell$  decays were also observed at 7 and 8 TeV at  
 138 CMS, where the branching fraction was found to be  $\mathcal{B}(Z \rightarrow 4\ell) = 4.2^{+0.9}_{-0.8}$  (stat)  $\pm$   
 139  $0.2$  (syst)  $\times 10^{-6}$  [90], and at ATLAS, where it was found to be  $3.20 \pm 0.25$  (stat)  $\pm$   
 140  $0.13$  (syst)  $\times 10^{-6}$  in a slightly different phase space [91]. After correcting for phase  
 141 space differences, the measurements are compatible with each other and with the SM.

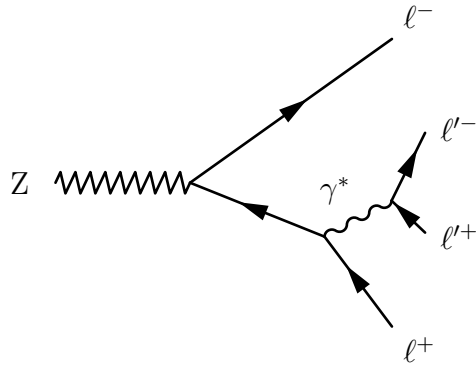


Figure 2.9: Tree-level Feynman diagram for  $Z \rightarrow 4\ell$  production. Either initial lepton may radiate the  $\gamma^*$ .

### 142 2.2.2 Higgs Boson Production

143 The primary Higgs production mechanism in multi-TeV hadron collisions is gluon-  
 144 gluon fusion through a quark loop, because of the gluon's high effective luminosity and  
 145 the top quark's strong Yukawa coupling. Other mechanisms, in decreasing order by

146 cross section, include vector boson fusion (VBF), vector boson associated production  
 147 (VH or “Higgsstrahlung”), and top-antitop associated production ( $t\bar{t}H$ ). Tree-level  
 148 Feynman diagrams for all four are shown in Fig. 2.10. The SM cross sections for  
 149 the various production mechanisms, and the Higgs branching fractions, are shown as  
 150 functions of  $m_H$  near the measured mass of 125 GeV in Fig. 2.11. Gluon-gluon fusion  
 151 has roughly an order of magnitude higher rate than the others. The VBF process  
 152 contributes to the unitarization of vector boson scattering along with the diagrams  
 153 in Fig. 2.4. Decays to four leptons are heavily suppressed by the fact that, since  
 154  $m_H < 2m_Z$ , energy conservation requires at least one of the Z bosons to be far off  
 155 its mass shell. Decays to four charged leptons are further suppressed by the small  
 156  $Z \rightarrow \ell^+\ell^-$  branching fraction. However, the distinctive signature of four high-energy  
 157 charged leptons in a single event is easy to detect with high efficiency and background  
 158 rejection, and the momentum of electrons and muons can in general be measured with  
 159 high precision, allowing the Higgs resonance to be easily seen as a sharp peak over  
 160 a small, relatively flat background.  $H \rightarrow 4\ell$  became the most attractive channel for  
 161 Higgs discovery and measurement of its properties in spite of its low rate.

### 162 **2.2.2.1 Prior Measurements**

163 Higgs boson searches at LEP were for Z-associated production, which has the highest  
 164 cross section in  $e^+e^-$  collisions. The maximum LEP center-of-mass energy, 209 GeV,  
 165 was just under the ZH threshold around 216 GeV. The LEP combined 95% confidence  
 166 level (CL) lower limit on  $m_H$  was 114.4 GeV [93], and a combination of LEP data and  
 167 electroweak precision measurements set an upper limit of 193 GeV [94]. Searches at  
 168 the CDF and D0 experiments at the Tevatron were combined to find a  $3.0\sigma$  local  
 169 excess ( $2.8\sigma$  global) consistent with  $m_H = 125$  GeV [95], with the  $H \rightarrow b\bar{b}$  search  
 170 alone finding a local excess of  $3.3\sigma$  ( $3.1\sigma$  local) [96]. Results from all the Tevatron

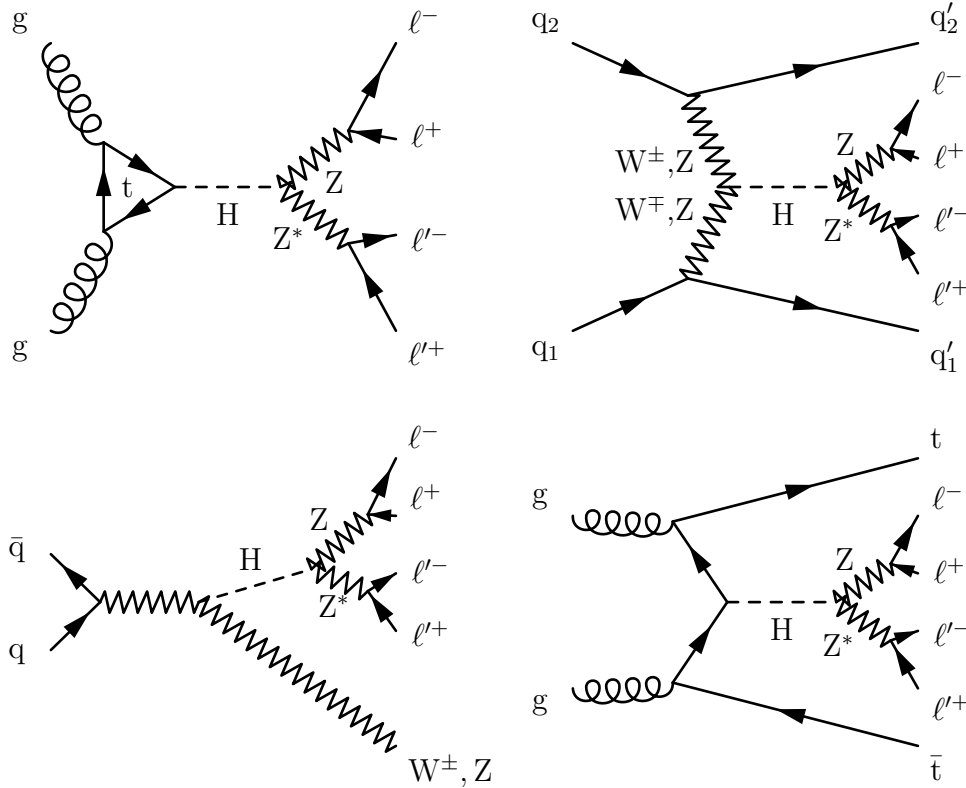


Figure 2.10: Tree-level Higgs production diagrams for gluon-gluon fusion (top left), VBF (top right), VH (bottom left), and  $t\bar{t}H$ , decaying to four leptons.

and LEP measurements and electroweak precision measurements were combined to place an upper mass limit of 158 GeV at 95% CL [97]. The Higgs was finally discovered simultaneously by the CMS and ATLAS collaborations with a combination of 7 and 8 TeV data [98, 99]. The four-lepton channel was, as anticipated, one of the most important [98, 100]. Its properties were subsequently investigated in detail at both experiments. The Higgs mass was found to be

$$m_H = 125.09 \pm 0.21 \text{ (stat)} \pm 0.11 \text{ (syst)} \text{ GeV} \quad (2.7)$$

based on a combination of data from the two experiments [101], and SM predictions of its properties have been confirmed by a number of measurements [102].

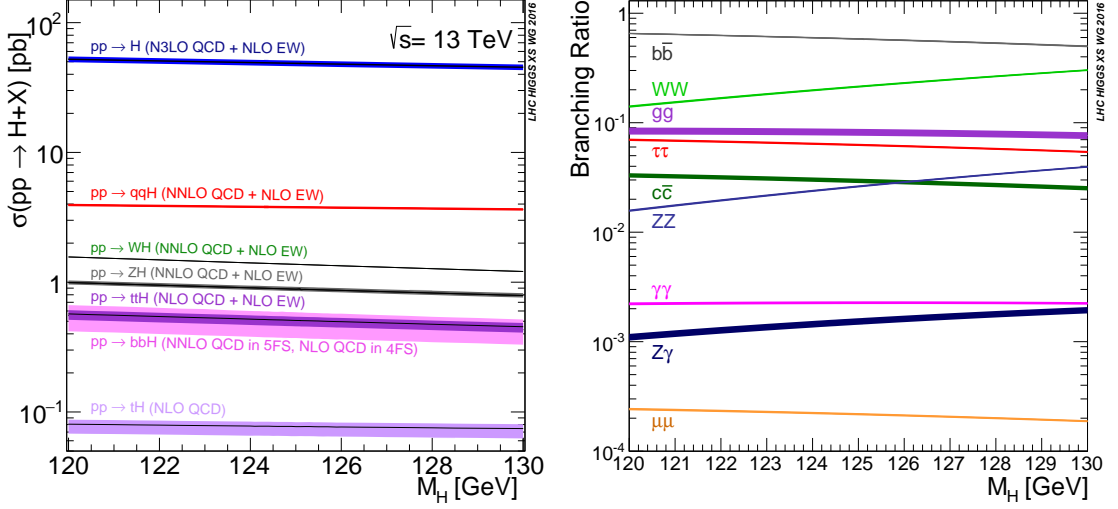


Figure 2.11: The SM cross sections for each Higgs boson production mode (left) and the Higgs branching fraction to several important final states (right), as a function of Higgs mass near the measured mass of 125 GeV. Both plots are reproduced from Ref. [92].

## 179 2.3 Anomalous Gauge Couplings

180 The most visible characteristic of anomalous couplings is an enhanced cross section  
 181 at center-of-mass energies of order 1 TeV [42]. The increase in cross section at high  
 182  $m_{4\ell}$  implies higher transverse momentum for the outgoing Z bosons and leptons, as  
 183 shown for two example aTGC models in Fig. 2.12. Searches for high-mass ZZ events  
 184 are attractive because SM continuum production cross sections are extremely small  
 185 above a few hundred GeV and all other sources of prompt or nonprompt four-lepton  
 186 events are negligible, so even a handful of events would be an unambiguous sign of  
 187 new physics. The search for nonzero aTGCs is performed using inclusive ZZ events,  
 188 because the aTGC parameters should not have a large effect on jet distributions. The  
 189 aQGC search is performed in ZZjj events because it would specifically enhance the  
 190 VBS cross section at high mass.

191 The neutral aTGC parameters  $f_4^V$  and  $f_5^V$  are expected to have almost identi-

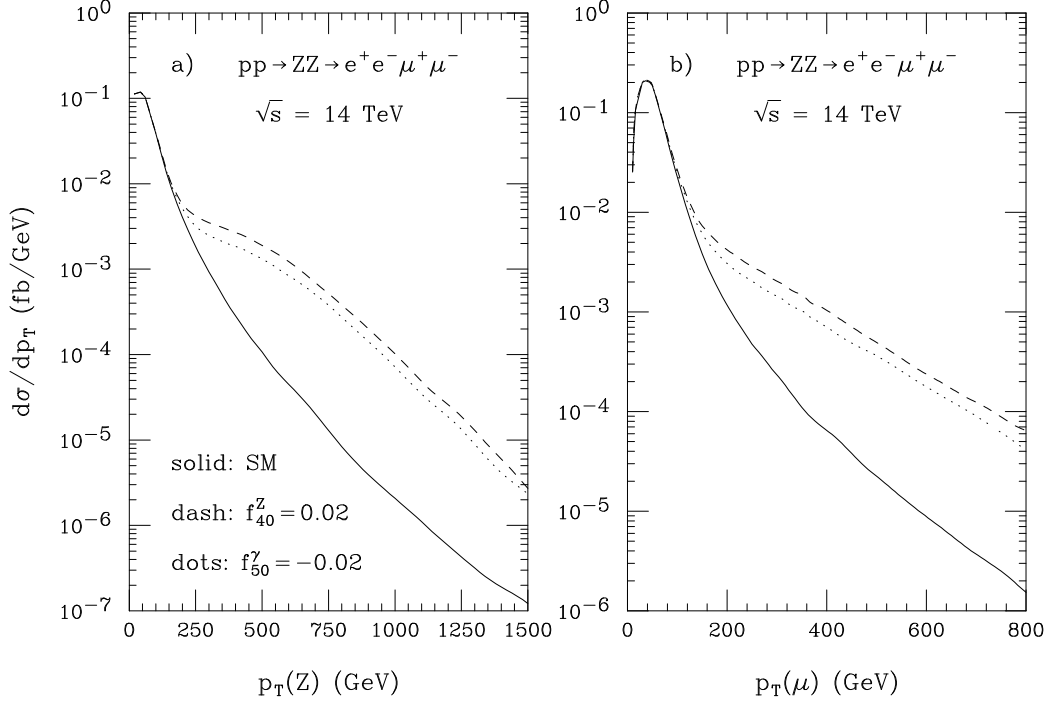


Figure 2.12: Cross section enhancements at high  $Z$  and  $\mu$  momenta caused by example nonzero aTGCs. Reproduced from Ref. [42].

192 cal effects at high energy, so the search variables cannot be used to determine the  
 193 relative strengths of the possible anomalous couplings [42]. However, because the  
 194 terms governed by  $f_4^V$  have opposite behavior to the terms governed by  $f_5^Z$  under  
 195 parity transformations, they affect the helicity amplitudes of the  $Z$  bosons and al-  
 196 ter the angular distributions of the final-state leptons. Figure 2.13 shows the cross  
 197 section as a function of total angular distance and the azimuthal angular difference  
 198 between muons from the same  $Z$  decay for several example nonzero aTGCs and for  
 199 the SM. These distributions could be used to distinguish between the possible aTGC  
 200 parameters and determine the sign of the CP-conserving  $f_5^V$  terms.

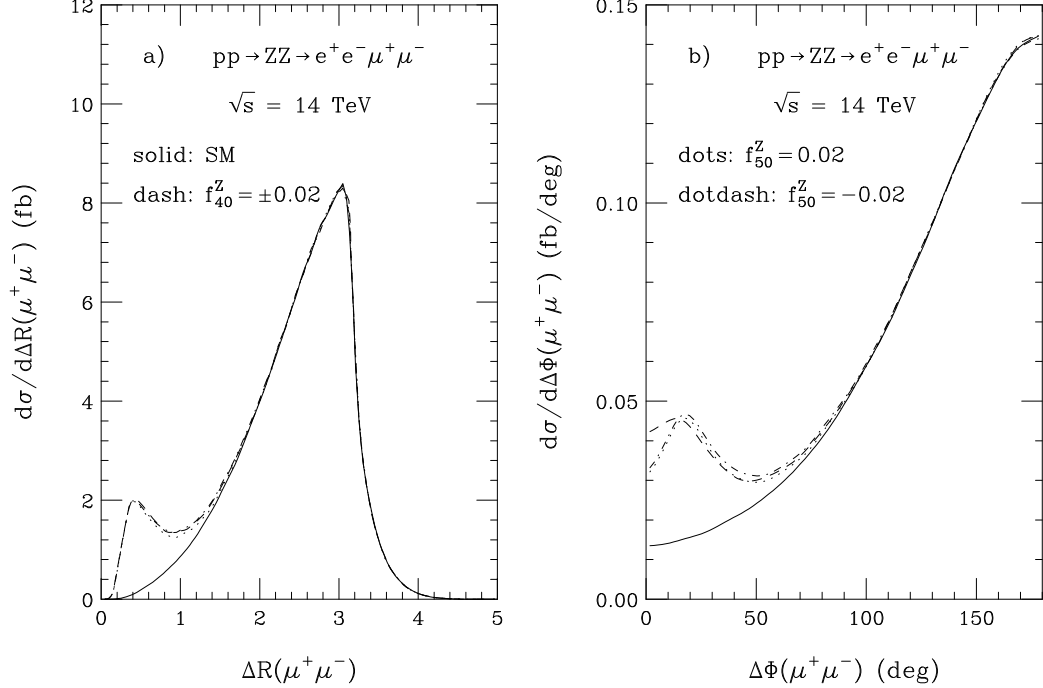


Figure 2.13: Total angular distance and azimuthal angular difference between muons from the same Z decay caused by several example nonzero aTGCs. Reproduced from Ref. [42].

### 2.3.1 Previous Limits

The first neutral aTGC searches were performed at LEP using ZZ and  $Z\gamma$  events [65, 66, 103, 104]. Depending on the experiment and parameter, 95% CL limits were generally  $\mathcal{O}(\pm 1)$ , and the statistical combination set limits around 0.2–0.4 [94]. The first searches in hadron collisions were performed at Tevatron by CDF collaboration, which set symmetric 95% CL limits in the range  $\pm 0.10$ –0.13 for all parameters [105], and the D0 collaboration, which set symmetric limits around  $\pm 0.20$ –0.31 for all parameters [106]. Both Tevatron experiments used a unitarity-preserving cut-off of  $\Lambda = 1.2$  TeV. CMS and ATLAS set 95% CL limits at 7 TeV at  $\mathcal{O}(\pm 0.1)$  [72, 76, 107], and  $\mathcal{O}(\pm 0.005)$  at 8 TeV [73, 108]. ATLAS presented limits from 7 TeV data with and without a unitarizing form factor; their 8 TeV results, and all CMS results,

212 did not use one. Prior to this work, the most stringent limits on all four neutral  
 213 aTGC parameters were set by CMS with a combination of 7 and 8 TeV data [74],

$$\begin{aligned} -0.0022 < f_4^Z < 0.0026, \quad -0.0023 < f_5^Z < 0.0023, \\ -0.0029 < f_4^\gamma < 0.0026, \quad -0.0026 < f_5^\gamma < 0.0027. \end{aligned} \quad (2.8)$$

214 The two-dimensional aTGC limits set by CMS with the 8 TeV dataset are shown in  
 215 Fig. 2.14 [73].

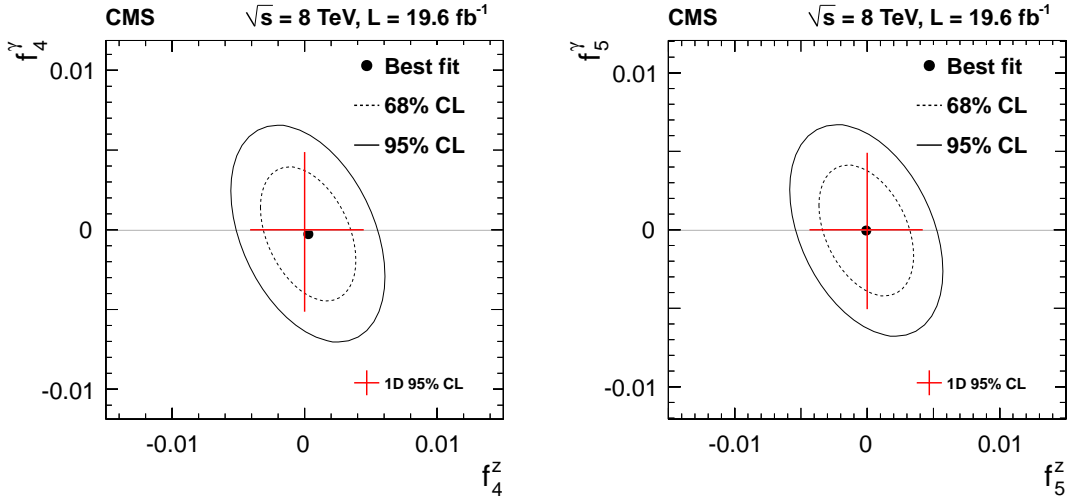


Figure 2.14: Two-dimensional 95% CL aTGC limits set by CMS, reproduced from Ref. [73].

216 No prior aQGC searches were performed using ZZ processes, but both LHC ex-  
 217 periments set limits on the ZZ-sensitive effective field theory operators using other  
 218 channels. The most stringent limits on  $f_{T0}$  were from  $\sqrt{s} = 8$  TeV  $Z\gamma qq$  events at  
 219 ATLAS [84], found to be

$$-3.4 < f_{T0}/\Lambda^4 < 2.9 \text{ TeV}^{-4} \quad (2.9)$$

220 at 95% CL, with similar results produced by CMS [83]. The most stringent limits on  
 221  $f_{T1}$  and  $f_{T2}$  were set by CMS at 8 TeV using same-sign WWqq events [82], and were

222 found to be

$$-2.1 < f_{T1}/\Lambda^4 < 2.4 \text{ TeV}^{-4} \quad (2.10)$$

223 and

$$-5.9 < f_{T2}/\Lambda^4 < 7.1 \text{ TeV}^{-4}. \quad (2.11)$$

224 CMS and ATLAS produced nearly identical limits on  $f_{T8}$  and  $f_{T9}$  in the same  $Z\gamma qq$   
225 searches that set limits on  $f_{T0}$ ,

$$-1.8 < f_{T8}/\Lambda^4 < 1.8 \text{ TeV}^{-4} \quad (2.12)$$

226 and

$$-3.9 < f_{T9}/\Lambda^4 < 3.9 \text{ TeV}^{-4}. \quad (2.13)$$

## 227 2.4 Background Processes

228 Spurious events are categorized as irreducible backgrounds, i.e. those that are ex-  
229 pected to have four prompt leptons, and reducible backgrounds, which have two  
230 or three prompt leptons and another object that is misidentified as a prompt lep-  
231 ton. The only nontrivial irreducible backgrounds to inclusive  $ZZ/Z\gamma^*$  production are  
232 WWZ triboson events in which all three bosons decay leptonically, and  $t\bar{t}Z$  events  
233 in which both top quarks and the Z all decay leptonically as shown at tree level in  
234 Fig. 2.15. The most prominent reducible backgrounds are  $WZ \rightarrow 3\ell\nu$  events in which  
235 a jet fragment is misidentified as a prompt lepton,  $Z + \text{jets}$  events in which two jet  
236 fragments are misidentified, and leptonic  $t\bar{t}$  events with two misidentified fragments  
237 from the secondary b-jets. For the VBS search, the background is real  $ZZ$  events  
238 which have two jets, but the jets originate from QCD interactions instead of the fully  
239 electroweak processes of Fig. 2.4. An example non-VBS  $ZZ + 2\text{jets}$  diagram is also  
240 shown in Fig. 2.15.

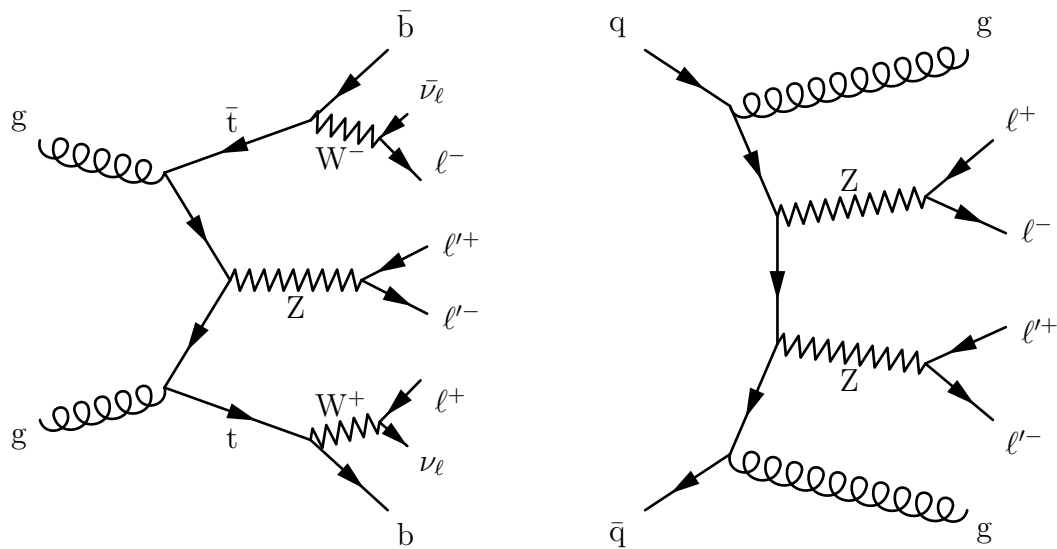


Figure 2.15: An example tree-level  $t\bar{t}Z$  diagram (left), which is an irreducible background for inclusive  $ZZ/Z\gamma^*$  production, and an example non-electroweak  $ZZjj$  diagram (right).

## **0 Chapter 3**

# **1 The CMS Experiment and the 2 CERN LHC**

3 Production of controlled high-energy particle collisions, and detection of particles  
4 created in those collisions, are monumental technical challenges. The apparatus used  
5 to obtain the results presented in this thesis are the result of decades of work by  
6 thousands of scientists and engineers, making use of many techniques developed in  
7 the course of building and operating previous experiments. The LHC [109, 110]  
8 accelerates pairs of charged hadron (proton or lead ion) beams and collides them  
9 to provide a source of high energy particle interactions for several fully independent  
10 detectors, including CMS [111], which collected the data used in the studies presented  
11 here. Detailed descriptions of the LHC and CMS follow.

### **12 3.1 The CERN Large Hadron Collider**

13 The LHC, the most powerful particle accelerator and collider ever built, is a 26.7 km  
14 circumference ring of superconducting magnets running through tunnels roughly

15 100 m below the suburbs and countryside near Geneva, Switzerland. It first produced  
 16 collisions suitable for collecting physics data in 2010 before generating large datasets  
 17 with beam energies of 3.5 TeV in 2011 and 4 TeV in 2012. Following a shutdown  
 18 for upgrades and repairs, it operated in 2015 and 2016 to deliver beam energies of  
 19 6.5 TeV. Beams collide head-on so that the center-of-mass frame of the proton-proton  
 20 system is the rest frame of the detectors, giving proton-proton center-of-mass ener-  
 21 gies of 7, 8, and 13 TeV respectively for collisions in 2010–2011, 2012, and 2015–2016.  
 22 Each successive energy was the highest ever achieved in controlled hadron-hadron  
 23 collisions, giving unprecedented access to extremely high-energy processes at every  
 24 step.

25 In addition to increasing collision energies, the LHC increased its rate of collisions  
 26 with each new machine configuration. The average event rate  $dN/dt$  for a process  
 27 with production cross section  $\sigma$  is determined by the instantaneous luminosity  $\mathcal{L}$  of  
 28 the collider,

$$\frac{dN}{dt} = \mathcal{L}\sigma \quad (3.1)$$

29 so a high instantaneous luminosity enables the observation of rare processes like Higgs  
 30 boson production. The LHC’s unprecedented luminosities have allowed collection of  
 31 the largest physics datasets in history.

32 The desire for high luminosities drove the decision to collide protons with other  
 33 protons instead of with antiprotons as was done at Tevatron, LHC’s predecessor at  
 34 Fermilab in Batavia, IL. Antiprotons simply cannot be produced in sufficient quan-  
 35 tities for a collider on this scale. Tevatron was designed to study many processes  
 36 that are  $q\bar{q}$ -initiated, so it is useful to have valence antiquarks available in the col-  
 37 lisions. The LHC was designed with Higgs boson production in mind, and the two  
 38 most important Higgs production modes are proton/antiproton agnostic. Even for  
 39  $q\bar{q}$ -initiated processes, valence antiquarks are less critical at the LHC because, for the

40 same center of mass energy, the effective  $q\bar{q}$  luminosity is higher for proton-proton  
41 collisions at LHC energies than at Tevatron energies (1.98 TeV center-of-mass energy)  
42 as discussed in Section 1.6.

43 In addition to protons, the LHC can accelerate beams of lead nuclei to 2.51 TeV  
44 per nucleon, also the highest ever achieved. All studies presented in this thesis were  
45 performed on proton-proton collision data, rendering the details of so-called “heavy  
46 ion” beams beyond the scope of this document.

47 Beams are maintained and manipulated with magnets, most of them made of  
48 superconducting niobium-titanium (NbTi) windings cooled to 1.9 K by superfluid  
49 helium. Dipole magnets with fields up to 8.33 T bend the beam around the ring,  
50 interspersed with quadrupoles for focusing. More quadrupoles and higher-moment  
51 magnets keep the beams focused, squeeze them for collisions, and apply a number  
52 of corrections. Superconducting radio frequency (RF) cavities operating at 400 MHz  
53 accelerate the beam, maintain it at its final energy, and maintain bunch shape and  
54 spacing.

### 55 3.1.1 Accelerator Chain, Layout, and Detectors

56 The LHC was built in tunnels originally constructed for the Large Electron-Positron  
57 Collider (LEP), an  $e^+e^-$  collider that operated from 1989 to 2000. Using existing cav-  
58 erns, tunnels, and infrastructure was a substantial cost-saving measure, but imposed  
59 several important constraints on the LHC’s design. In LEP, the electron and positron  
60 beams could be accelerated in opposite directions by the same magnets, because they  
61 are oppositely charged. Conversely, proton beams require opposite magnetic fields for  
62 the two beams. Because the tunnels were not wide enough to accommodate two com-  
63 pletely separate beam lines, most of the magnets in the LHC use a twin-bore design,  
64 shown schematically in Fig. 3.1, in which the pipes and windings for the two beams

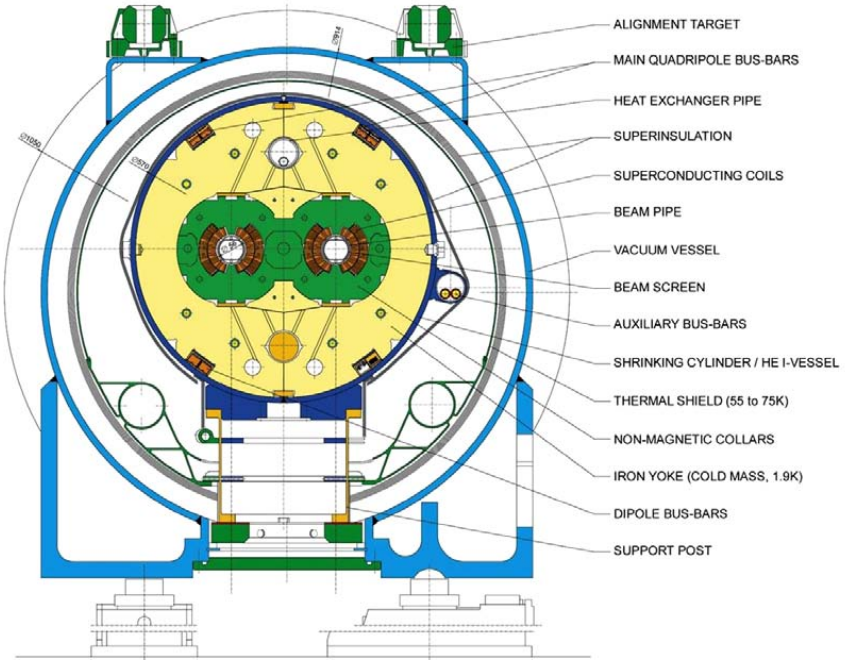


Figure 3.1: Schematic cross section of an LHC dipole and its attendant electrical and cryogenic infrastructure, reproduced from Ref. [109].

65 share a common cryogenic system. The electromagnetic, mechanical, and cryogenic  
66 coupling of the two beamlines represents a significant engineering challenge [109, 110].

67 Because no single accelerator has the dynamic range necessary to take a stationary  
68 proton to TeV-scale energies, a chain of smaller accelerators repurposed from previous  
69 experiments feeds moderate-energy protons into LHC. Protons are obtained by ion-  
70 izing hydrogen atoms, then accelerated to 50 MeV by the Linac 2 linear accelerator  
71 and injected into the Proton Synchrotron Booster (PSB), the first of several circu-  
72 lar accelerators. The PSB feeds 1.4 GeV protons into the Proton Synchrotron (PS),  
73 which in turn injects them into the Super Proton Synchrotron (SPS) at 26 GeV. The  
74 protons are then accelerated to 450 GeV in the SPS before being injected into LHC.

75 A diagram of the entire accelerator chain is shown in Fig. 3.2.

76 The LHC ring is divided into eight sectors, each of which features a 528 m straight  
77 section connected to the adjacent sections by 2.45 km arcs. The straight section length

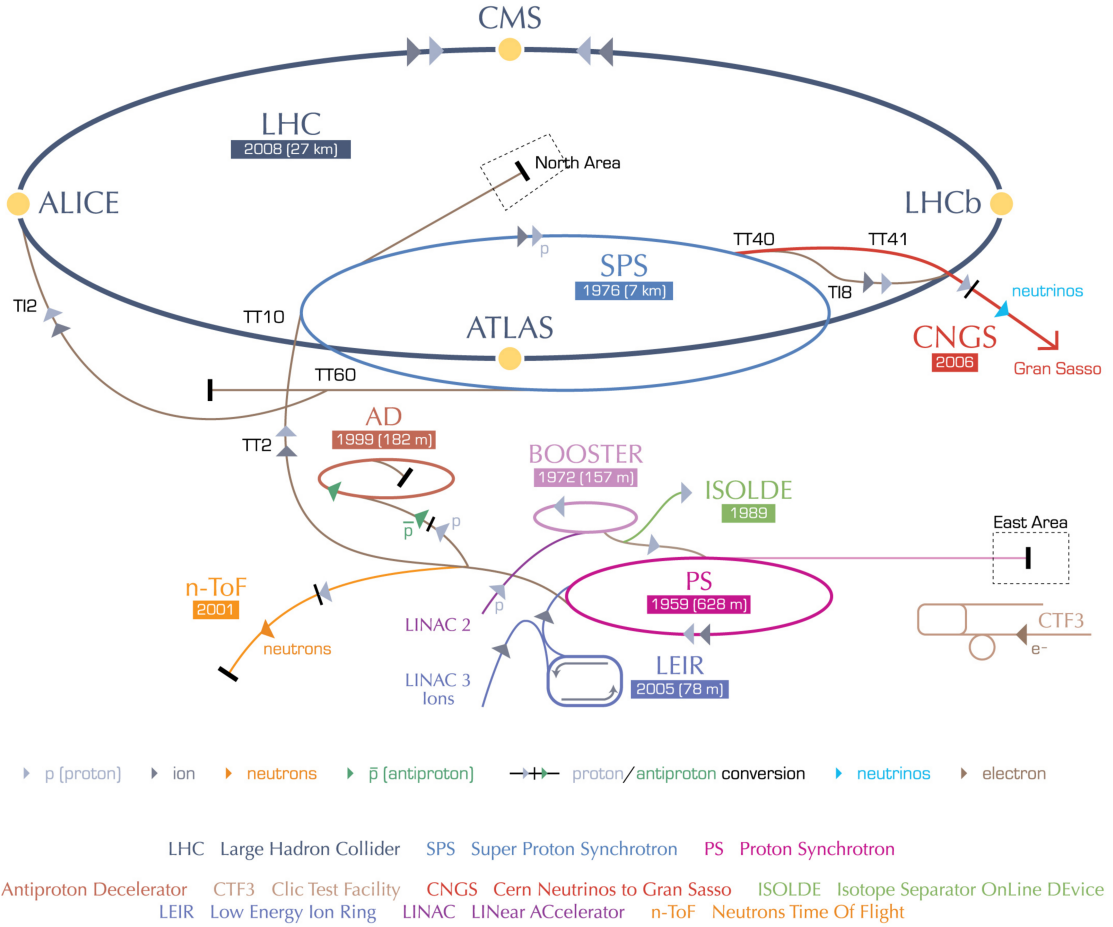


Figure 3.2: A schematic of the LHC accelerator chain and peripheral experiments, reproduced from Ref. [112].

78 was set by the need for RF cavities to accelerate LEP beams to counteract synchrotron  
 79 radiation, which is a primary factor limiting electron and positron beam energy. This  
 80 is not ideal for proton beams; protons' much higher mass means they radiate less and  
 81 need fewer RF cavities. The straight sections feature access points numbered with  
 82 Point 1 at the main CERN site in Meyrin, Switzerland, and the rest numbered 2–8,  
 83 increasing in the clockwise direction when viewed from above. Points 1, 2, 5, and 8  
 84 have beam crossing points and host detectors to study the resulting proton-proton  
 85 collisions. Points 3 and 7 feature collimators to reduce momentum and betatron  
 86 nonuniformities in the beams. The RF cavities are at Point 4 and the beams are

87 dumped after use or in the event of a magnet quench at Point 6. Beams are disbursed  
 88 and deflected into an 8 m long water-cooled graphite absorber by fast kicker magnets  
 89 which activate in a 3  $\mu$ s-long bunch-free region of the beam known as the abort gap.

90 The CMS detector is at Point 5 in Cessy, France, the furthest point on the ring  
 91 from the Meyrin site and Point 1, which houses ATLAS [113], a similar but fully  
 92 independent general-purpose particle detector. CMS and ATLAS use complemen-  
 93 tary detector technology so that any measurement or discovery by one can be made  
 94 concurrently or verified by the other. The other two experimental insertions feature  
 95 specialized detectors studying collisions at lower-luminosity beam interaction points.  
 96 The LHCb detector [114], at Point 8, studies hadronic physics with an emphasis on  
 97 b-hadrons, and ALICE [115] studies heavy ion collisions at Point 2. Three smaller  
 98 experiments share interaction points with the larger detectors, with TOTEM [116]  
 99 studying proton structure and the total proton-proton interaction cross section next  
 100 to CMS; LHCf [117] studying the  $\pi^0$  energy spectrum and multiplicity near ATLAS;  
 101 and MoEDAL [118] searching for magnetic monopoles or other heavy, stable, ionizing  
 102 particles at Point 8 with LHCb.

### 103 3.1.2 Operating Parameters

104 With the beam energy set by the radius of the ring and the strength of available  
 105 magnets, the number of interesting physics events produced in LHC collisions depends  
 106 only on the integrated luminosity

$$\mathcal{L}_{int} = \int \mathcal{L} dt, \quad (3.2)$$

107 where  $\mathcal{L}$  is the instantaneous luminosity defined in Eq. (3.1) and the integral runs  
 108 over the time the machine spends in collisions mode. LHC's availability for colli-  
 109 sions depends on the electrical and mechanical stability of the accelerators and their

110 support systems, including the cryogenics and the vacuum in the beam pipe. The  
 111 instantaneous luminosity while running depends only on the beam parameters. For  
 112 symmetric beams which each have  $n_b$  colliding gaussian bunches of intensity (i.e. num-  
 113 ber of protons in the bunch)  $N_b$ , orbiting the ring with frequency  $f_{rev}$  and relativistic  
 114 factor  $\gamma = E_p/m_p$ , the instantaneous luminosity is give by

$$\mathcal{L} = f_{rev} \frac{n_b N_b^2 \gamma}{4\pi \beta^* \epsilon_N} R, \quad (3.3)$$

115 where  $\beta^*$  is the amplitude of the beams' betatron oscillations around the nominal  
 116 ring path at the interaction point, the normalized emittance  $\epsilon_N$  is a measure of the  
 117 beams' spread in both position and momentum space, and  $R$  is a geometrical factor  
 118 accounting for the beam crossing angle,

$$R = \sqrt{1 + \left( \frac{\theta_c \sigma_z}{2\sigma^*} \right)^2}. \quad (3.4)$$

119 Here  $\theta_c$  is the beams' crossing angle, and  $\sigma_z$  and  $\sigma^*$  are respectively the longitudinal  
 120 and transverse RMS widths of the bunches in the lab frame.

### 121 3.1.2.1 Design

122 The machine parameters in the LHC design specification can be seen in the first col-  
 123 umn of Table 3.1. Machine parameters during data taking have in general been quite  
 124 different, due to both technological advances and technical challenges. In particular,  
 125 beam energy and number of colliding bunches are both lower than designed due to  
 126 commissioning issues with the magnets and their safety systems [119], but increases in  
 127 the number of collisions per bunch crossing (“pileup”) have more than compensated,  
 128 leading to a peak instantaneous luminosity in 2016 that was more than 50% higher  
 129 than designed. Operating parameters have changed frequently during data taking  
 130 and upgrades are always ongoing.

Table 3.1: LHC beam parameters as designed and in practice. As stated in the text,  $n_b$  is the number of colliding bunches,  $N_b$  is the number of protons in each bunch,  $\beta^*$  is the betatron amplitude at the interaction point,  $\epsilon_N$  is the normalized emittance, and  $\mathcal{L}_{(int)}$  is the instantaneous (integrated) luminosity.

Year	Design		Run I		Run II	
		2010	2011	2012	2015	2016
Energy per beam (TeV)	7	3.5	3.5	4	6.5	6.5
Bunch spacing (ns)	25	150	50	50	25	25
$n_b$	2808	348	1331	1368	2232	2208
$N_b (10^{11})$	1.15	1.2	1.5	1.7	1.15	1.25
$\beta^*$ (m)	0.55	3.5	1.0	0.6	0.8	0.4
$\epsilon_N$ (mm mrad)	3.75	2.2	2.3	2.5	3.5	3.0
Peak pileup		4	17	37	22	49
Peak $\mathcal{L} (10^{34} \text{cm}^{-2}\text{s}^{-1})$	1	0.02	0.35	0.77	0.52	1.53
$\mathcal{L}_{int} (\text{fb}^{-1})$		0.04	6.1	23.3	4.2	41.1

### 131 3.1.2.2 Run I

132 The LHC came online in 2010 with a beam energy of 3.5 TeV, which was increased  
 133 to 4 TeV in 2012. Bunches were spaced 50 ns apart instead of 25 ns to allow full  
 134 exploitation of excellent injection chain performance [120]. Beams exiting the SPS  
 135 had bunch intensity as much as 50% higher than anticipated in the original LHC  
 136 design and beam emittance as low as 67% of nominal. This allowed the LHC to  
 137 achieve 77% of its design instantaneous luminosity in 2012 despite having roughly  
 138 half as many bunches in each beam.

139 Machine availability was overall good considering the complexity and relative  
 140 newness of the LHC, with about 36% of scheduled time spent in stable beams. In all,  
 141 LHC delivered  $6.1 \text{ fb}^{-1}$  to CMS and ATLAS in 2011 and  $23.3 \text{ fb}^{-1}$  in 2012, enough to  
 142 allow discovery of the Higgs boson. The integrated luminosity for each year of LHC  
 143 operation is shown as a function of calendar month and day in Fig. 3.3.

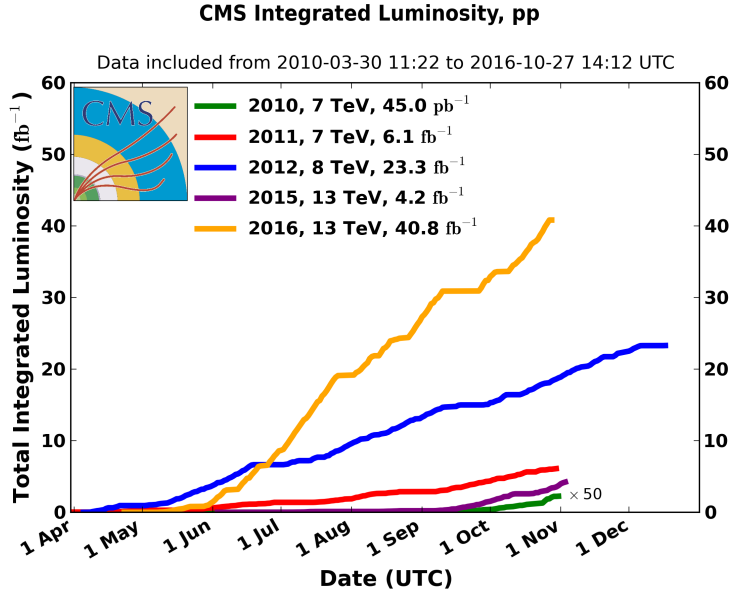


Figure 3.3: The integrated luminosity delivered to CMS in each year of LHC operation, shown as a function of the date within the year.

### 144 3.1.2.3 Run II

145 The LHC shut down for 2013 and 2014 to allow a number of repairs and upgrades,  
 146 including measurements, repairs and upgrades on the electrical connections and cryo-  
 147 genic safety systems. Beam energies were increased to 6.5 TeV, close to the nominal  
 148 7 TeV. The bunch spacing was decreased to 25 ns while maintaining low emittance  
 149 and high bunch intensity with the implementation of the beam compression merging  
 150 and splitting (BCMS) scheme in which bunches are merged in the PS before they  
 151 are split for injection into SPS, allowing higher bunch intensity [121]. This was offset  
 152 by vacuum problems in the SPS beam dump, which limited the total number of col-  
 153 liding bunches to around 2200 [122]. Improvements in collimators and beam optics  
 154 reduced  $\beta^*$  to 40 cm in 2016, lower than the design  $\beta^*$  of 55 cm. Overall instantaneous  
 155 luminosities were substantially higher than originally designed.

156 Machine availability in Run II was excellent, with over 60% of planned time spent  
 157 in stable beams [122]. The world's first 13 TeV collisions in 2015 were the subject of

158 a number of measurements and searches, though the  $4.2 \text{ fb}^{-1}$  integrated luminosity  
159 delivered to Points 1 and 5 in 2015 was less than planned due to several mechanical is-  
160 sues. The integrated luminosity achieved in 2016,  $41.1 \text{ fb}^{-1}$ , was far above the roughly  
161  $25 \text{ fb}^{-1}$  expected and more than all previous runs combined, allowing measurements  
162 and searches of unprecedented sensitivity and reach, including those presented in this  
163 Thesis.

## 164 **3.2 The Compact Muon Solenoid Detector**

165 The CMS detector [111] is a general-purpose particle detector located in a cavern  
166 roughly 100 m below the surface at LHC Point 5. Though designed to do a wide  
167 range of physics analyses, CMS was designed specifically with Higgs boson discovery  
168 in mind. Primary design goals include

- 169     • High-efficiency reconstruction of charged particles with precise measurement of  
170         their trajectories and momenta
- 171     • Good electromagnetic energy resolution, including diphoton and dielectron mass  
172         resolution
- 173     • Hermetic calorimetry for good missing transverse energy and dijet mass resolu-  
174         tion
- 175     • Good muon identification, momentum resolution (including dimuon mass reso-  
176         lution), and charge determination over a broad range of energies

177 To this end, CMS features a silicon tracker, a scintillating crystal electromagnetic  
178 calorimeter (ECAL), and a hermetic hadronic calorimeter (HCAL) inside a  $3.8 \text{ T}$   
179 solenoid magnet surrounded by ionized gas muon tracking devices, all of which can

180 be seen as part of the whole detector in Fig. 3.4. Decisions on which events to read  
 181 out are made on-line by a two-level trigger system. Descriptions of these systems  
 182 follow.

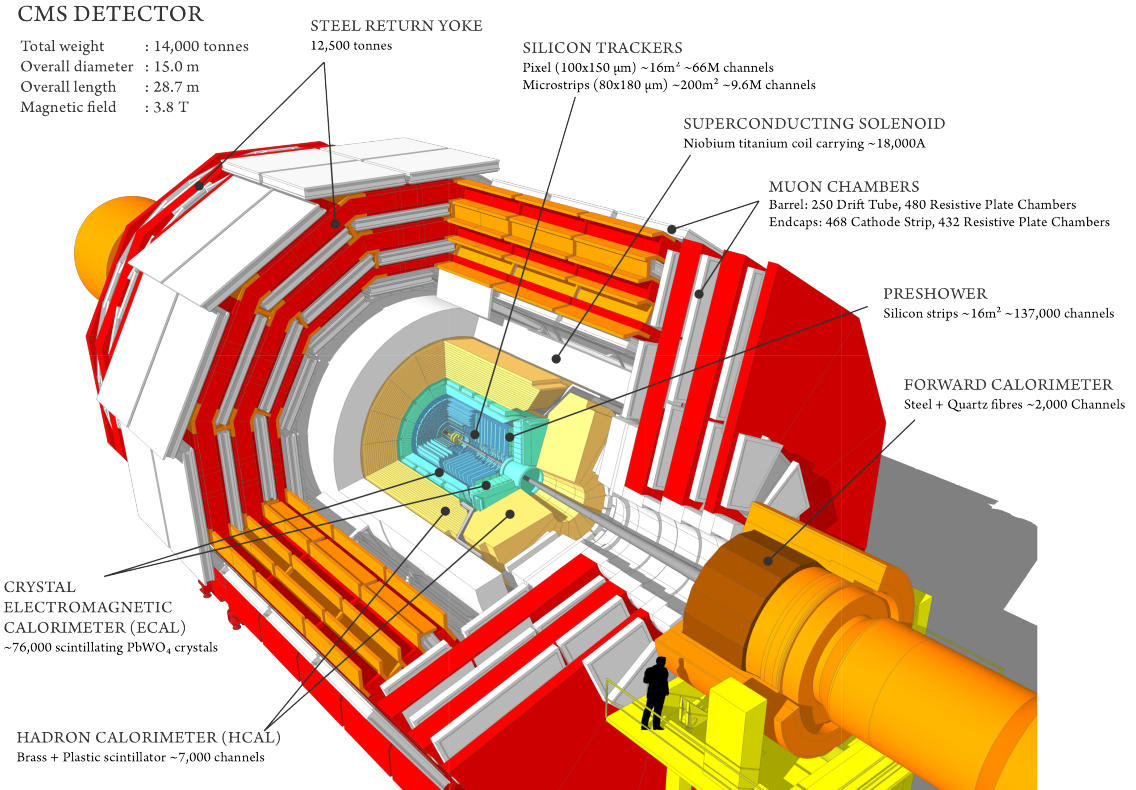


Figure 3.4: Cutout schematic of CMS with all major subdetectors, the beamline, the magnet, and the return yoke visible. Reproduced from Ref. [123].

### 183 3.2.1 Terminology and Geometry

184 The CMS detector systems are arranged in cylindrical layers with the interaction  
 185 point at the center, serving as the origin for the coordinate system. The coordinate  
 186 system is defined with the positive-*x* direction pointing toward the center of the  
 187 ring, positive-*y* pointing vertically up, and positive-*z* pointing parallel to the beam  
 188 in the counterclockwise direction when the LHC ring is viewed from above. Particle

189 momenta are typically expressed in quasicylindrical coordinates  $(p_T, \eta, \phi)$ . Here  $p_T$  is  
 190 the magnitude of the particle's momentum transverse to the beam

$$p_T \equiv \sqrt{p_x^2 + p_y^2}, \quad (3.5)$$

191 and  $\phi$  is the azimuthal angle, i.e. the angle from the  $x$ -axis to the particle's trajectory  
 192 in the  $x$ - $y$  plane. The pseudorapidity  $\eta$  is defined as

$$\eta \equiv -\ln \left[ \tan \left( \frac{\theta}{2} \right) \right] \quad (3.6)$$

193 where  $\theta$  is the polar angle measured from the  $z$ -axis. The relativistic rapidity

$$y \equiv \frac{1}{2} \ln \left( \frac{E + p_z}{E - p_z} \right), \quad (3.7)$$

194 converges to the pseudorapidity in the limit of massless particles. Pseudorapidity  
 195 is preferred to rapidity because it is purely geometrical, with no dependence on the  
 196 particle energy. Both are preferred over  $\theta$  because rapidity differences are invariant  
 197 under longitudinal boosts, and because hadron flux at colliders is roughly constant as  
 198 a function of rapidity. The transverse energy  $E_T$  is the the magnitude of the particle's  
 199 four-momentum transverse to the beam, equal to  $p_T$  in the limit of massless particles.  
 200 Spatial coordinates are expressed as  $(r, \eta, \phi)$ , where  $r$  is the distance from the beam  
 201 in the  $x$ - $y$  plane.

### 202 3.2.2 Magnet and Inner Tracking System

203 A particle of charge  $q$  moving through a uniform magnetic field of strength  $B$  that  
 204 points in the  $z$  direction will travel in a helix of radius  $R$ , given by

$$R = \frac{p_T}{|q|B}, \quad (3.8)$$

205 with the chirality of the helix determined by the sign of  $q$ . Thus one can determine the  
 206 transverse momentum of the particle by measuring its path through the magnetic field

207 and finding the radius of curvature. In practice, all but the lowest-energy particles  
 208 leave too short an arc in the detector for direct measurement of the radius, so the  
 209 sagitta of the arc is used instead, given by

$$s = \frac{qBL^2}{8p_T} \quad (3.9)$$

210 where  $L$  is the length of the chord spanning the arc (typically equal to the radius of  
 211 the tracking system). The transverse momentum resolution varies as

$$\frac{\delta p_T}{p_T} \propto \frac{p_T}{BL^2}, \quad (3.10)$$

212 so a strong field and a large tracking volume are vital to keeping measurements precise  
 213 even at high energies.

214 To this end, CMS contains the world's largest superconducting magnet<sup>1</sup>, a solenoid  
 215 13 m long and 6 m in diameter, which generates a nearly-uniform 3.8 T field in the  
 216 centralmost part of the detector [124]. To measure the paths of charged particles in  
 217 the field, the volume closest to the interaction point contains layers of silicon sensors  
 218 that detect hits from charged particles with high efficiency and excellent position  
 219 resolution, between 4.4 cm and 1.1 m from the beam for 2.7 m on either side of the  
 220 interaction point. This system, called the inner tracker and shown schematically  
 221 in Fig. 3.5, consists of an inner pixel detector surrounded by a larger silicon strip  
 222 detector. Both consist of concentric cylinders of sensors covering the barrel of the  
 223 detector capped by discs covering the high- $\eta$  region, up to  $|\eta| < 2.5$ . With a total of  
 224 roughly 200 m<sup>2</sup> of silicon, the inner tracker is the largest silicon tracker in the world.  
 225 Tracks may be reconstructed with hits in as many as 14 layers. The downside of  
 226 this is that the tracker and its mechanical support structure represent a substantial  
 227 amount of material for electrons and photons to interact with before they reach the

---

<sup>1</sup>Largest in the sense of having the largest stored energy when at constant full field. The largest by size is the ATLAS barrel toroid.

228 calorimeters, with total material budget between 0.4 radiation lengths ( $\eta = 0$ ) and 1.8  
 229 radiation lengths ( $|\eta| \approx 1.4$ ), as shown in Fig. 3.6. The tracker-only  $p_T$  uncertainty  
 230 is around 1.2% at 200 GeV and 15% at 1 TeV. Tracker readout is too slow for it to  
 231 be used in the L1 trigger (see Section 3.2.6.1), the first set of trigger decisions must  
 232 be made using only information from the calorimeters and outer muon system.

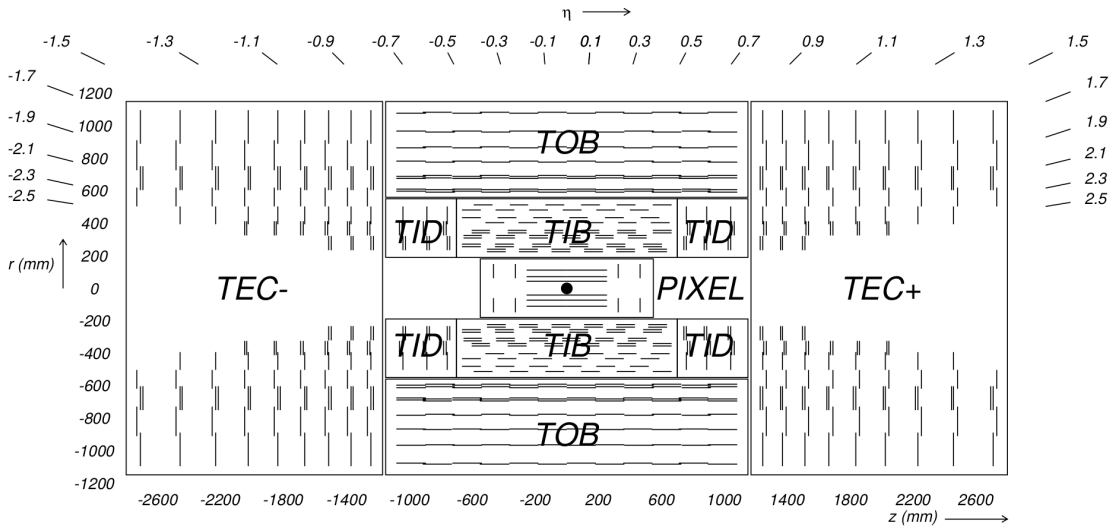


Figure 3.5: Diagram of the inner tracker layout, reproduced from Ref. [111].

233 As the system closest to the interaction point, the inner tracker is subject to  
 234 extremely high radiation doses, equivalent to 840 kGy for the innermost pixel layer  
 235 over an integrated luminosity of  $500 \text{ fb}^{-1}$ , so radiation tolerance is a major design  
 236 constraint for both the sensors and readout electronics [125]. Leakage currents in  
 237 the sensors, which degrade sensor performance, increase linearly with radiation fluence  
 238 and exponentially with temperature. Because leakage currents cause self-heating in  
 239 the silicon, they can create a dangerous positive thermal feedback loop if the sensors  
 240 are not cooled below  $-10^\circ \text{C}$  during operation. Reverse annealing, a process by which  
 241 radiation-induced defects in the silicon can cause further damage months after the  
 242 radiation dose is received, can be mitigated by keeping the sensors below  $0^\circ \text{C}$  at  
 243 all times except for brief maintenance periods [111]. Therefore, to improve tracker

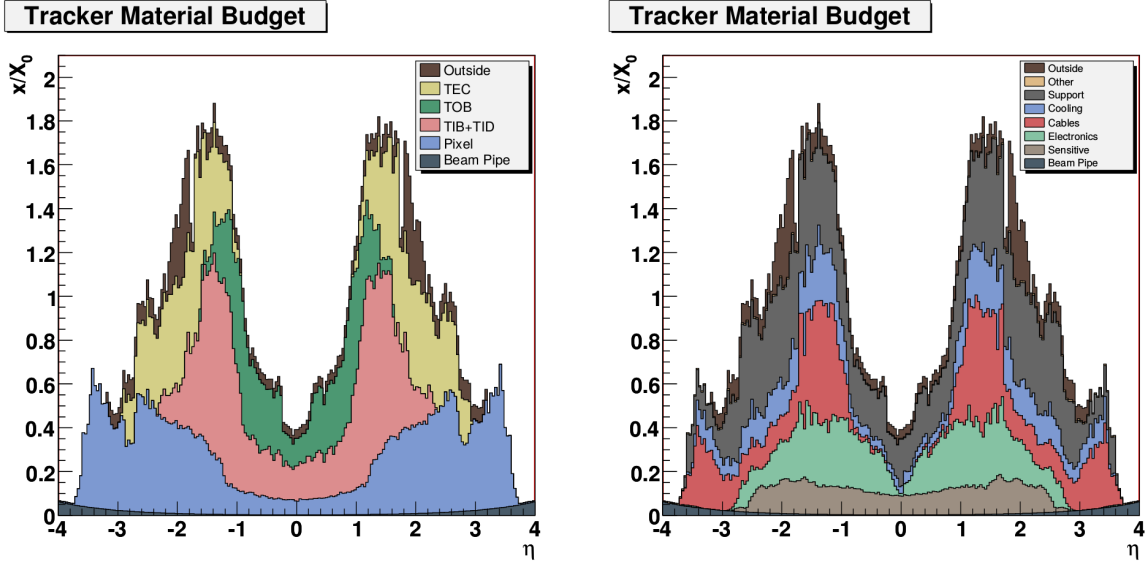


Figure 3.6: Total tracker material budget in units of electromagnetic radiation lengths, as a function of pseudorapidity. At (left) the total is divided by detector subsystem, at (right) by the function of the material. Reproduced from Ref. [111].

244 performance and increase the detectors' lifetimes, a gas cooling system is used to  
 245 keep the strip tracker around  $-15^{\circ}\text{C}$  and the pixel detector around  $-20^{\circ}\text{C}$  during  
 246 operation.

### 247 3.2.2.1 Pixel Detector

248 The pixel detector [125], consisting of three layers in the barrel and two in the endcap,  
 249 is responsible for accurate reconstruction of primary proton-proton interaction ver-  
 250 tices and secondary vertices from decays of b-hadrons or other long-lived particles, as  
 251 well as providing "seed" tracks that may be used in strip tracker reconstruction. As  
 252 the system closest to the interaction point, the pixel system experiences the highest  
 253 charged-particle flux and therefore must have extremely fine granularity to differen-  
 254 tiate between nearby particles. The 66 million pixels in the system have a cell size of  
 255  $100 \times 150 \mu\text{m}^2$ . Interpolation of the analog signals from the individual pixels allows  
 256 a final spatial resolution of  $15 \mu\text{m}$  in each direction. The outermost barrel layer is

257 10.2 cm from the beam, and the second endcap disk is 46.5 cm from the interaction  
 258 point. The sensor modules are arranged such that at least three sensors cover the  
 259 solid angle within the pixel detector's acceptance.

260 **3.2.2.2 Strip Tracker**

261 Outside the pixels is the silicon strip tracker [125], extending out to 1.1 m in the  $r$   
 262 direction and  $\pm 2.8$  m in the  $z$  direction. The tracker is divided into inner and outer  
 263 subdetectors, each of which has both barrel cylinders and endcap discs. In total,  
 264 there are ten layers in the barrel and nine in each of the endcaps. The inner tracker  
 265 uses 320  $\mu\text{m}$ -thick sensors with a typical strip cell size of 10 cm  $\times$  80  $\mu\text{m}$ , leading to  
 266 hit resolutions of 23–35  $\mu\text{m}$ . The outer tracker uses 500  $\mu\text{m}$ -thick sensors with typical  
 267 strip sizes up to 25 cm  $\times$  180  $\mu\text{m}$ , leading to hit resolutions of 35–53  $\mu\text{m}$ .

268 **3.2.3 Electromagnetic Calorimeter**

269 Outside of the tracker is the electromagnetic calorimeter (ECAL), which is designed  
 270 to absorb and measure the energy of electrons and photons. ECAL is made of 68,524  
 271 radiation tolerant lead tungstate ( $\text{PbWO}_4$ ) crystals arranged in a cylindrical barrel  
 272 (EB) covering  $|\eta| < 1.444$  and two endcap discs (EE) covering  $1.566 < |\eta| < 3.0$ .  
 273 The geometry of the ECAL barrel and endcap can be seen in Fig. 3.7; the small  
 274 gap between the barrel and endcap is necessary to accommodate cabling and support  
 275 structures for the tracker.  $\text{PbWO}_4$  crystals scintillate blue-green light and are op-  
 276 tically transparent, so the resulting light can be read out by avalanche photodiodes  
 277 (APDs) in the barrel and vacuum phototriodes (VPTs) in the endcap. ECAL's gran-  
 278 ularity is set by  $\text{PbWO}_4$ 's small Molière radius of 2.2 cm, which is also the size of the  
 279 square front faces of the barrel crystals, which flare out to 2.6 cm at the back, giving

them a truncated pyramid shape covering a roughly  $0.0174 \times 0.174$  area of  $\eta\phi$  space.  
 The endcap crystals go from 2.86 cm squares at the front to 3.0 cm at the back.

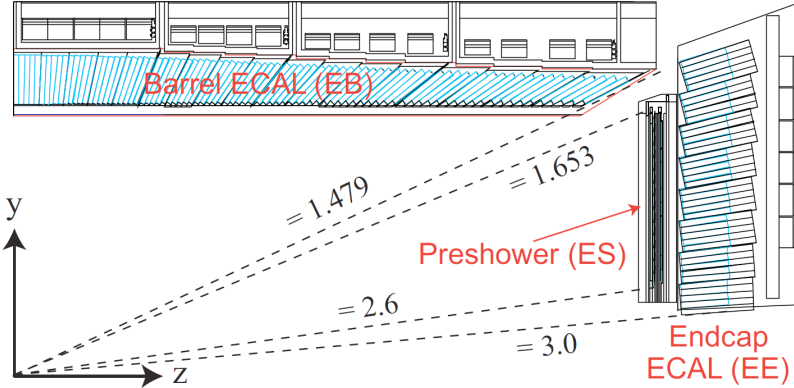


Figure 3.7: Diagram of ECAL geometry, reproduced from Ref. [126].

One of the primary design innovations of CMS—the eponymous compactness—was to place the calorimetry inside the magnet so that tracks can be unambiguously associated with energy deposits in the calorimeters without interference from scattering in the magnet coils. This is possible in part thanks to the high density ( $8.28 \text{ g/cm}^3$ ) and short radiation length (0.89 cm) of  $\text{PbWO}_4$ , which allow ECAL crystals to be only 23 cm long in the barrel and 22 cm long in the endcap while still spanning 25.8 and 24.7 radiation lengths, respectively. This is enough to ensure that few electrons or photons escape ECAL with any appreciable remaining energy.

The total scintillation light yield is relatively low, averaging just 4.5 photons per MeV deposited. This is partially compensated by the fact that virtually all of ECAL is active material and no energy is lost to uninstrumented absorbers, but Poisson fluctuations in the yield are still the largest contribution to ECAL energy resolution for most electron and photon energies. This statistical uncertainty is represented by the first term in the full resolution equation,

$$\left(\frac{\delta E}{E}\right)^2 = \left(\frac{2.8\%}{\sqrt{E/\text{GeV}}}\right)^2 + \left(\frac{0.12}{E/\text{GeV}}\right)^2 + (0.30\%)^2. \quad (3.11)$$

296 The second term comes from electronic noise and noise from pileup, and the last term  
 297 represents intrinsic differences between crystals. The upside to PbWO<sub>4</sub>'s scintillation  
 298 is that it is fast: roughly 80% of the light is emitted in the 25 ns between bunch  
 299 crossings, so energy measurements require integration over only a few bunch crossings.

### 300 3.2.4 Hadronic Calorimeter

301 Between ECAL and the magnet is the hadronic calorimeter (HCAL), responsible for  
 302 measuring the energy of hadronic jets. HCAL is a sampling calorimeter, meaning  
 303 that the hadrons pass through dense, uninstrumented material and the products of  
 304 the resulting interactions deposit energy in scintillators which are used to measure the  
 305 total energy of the original incoming particles. The HCAL barrel (HB,  $|\eta| < 1.305$ )  
 306 and endcap (HE,  $1.305 < |\eta| < 3.0$ ) are made of layers of brass absorber interleaved  
 307 with plastic scintillating tiles. The energy resolution in HB and HE is given by

$$\left(\frac{\delta E}{E}\right)^2 = \left(\frac{90\%}{\sqrt{E/\text{GeV}}}\right)^2 + (4.5\%)^2. \quad (3.12)$$

308 The first term is from the stochastic evolution of hadronic showers in the absorber,  
 309 the second is from calibration uncertainties.

310 The geometry of HB, HE, and HO is shown in Fig. 3.8. The thickness of HB and  
 311 HE is constrained by the size of the magnet, varying from 5.4 nuclear interaction  
 312 lengths in the central barrel to more than 10 in the endcaps. Because HB is not thick  
 313 enough to absorb all hadrons in the barrel, there is an extra outer HCAL component  
 314 (HO) outside of the magnet, consisting of two more layers of scintillator on either  
 315 side of a 20 cm-thick iron “tail catcher” covering  $|\eta| < 1.3$ . With HO and the 1.1  
 316 interaction lengths in ECAL considered, no part of the calorimeter system spans  
 317 fewer than 11.8 interaction lengths except in the gaps between barrel and endcap,  
 318 minimizing the flux of hadronic “punchthrough” interacting with the muon system.

319 The total material budget in front of the layers of the muons systems is shown in  
 320 Fig. 3.9.

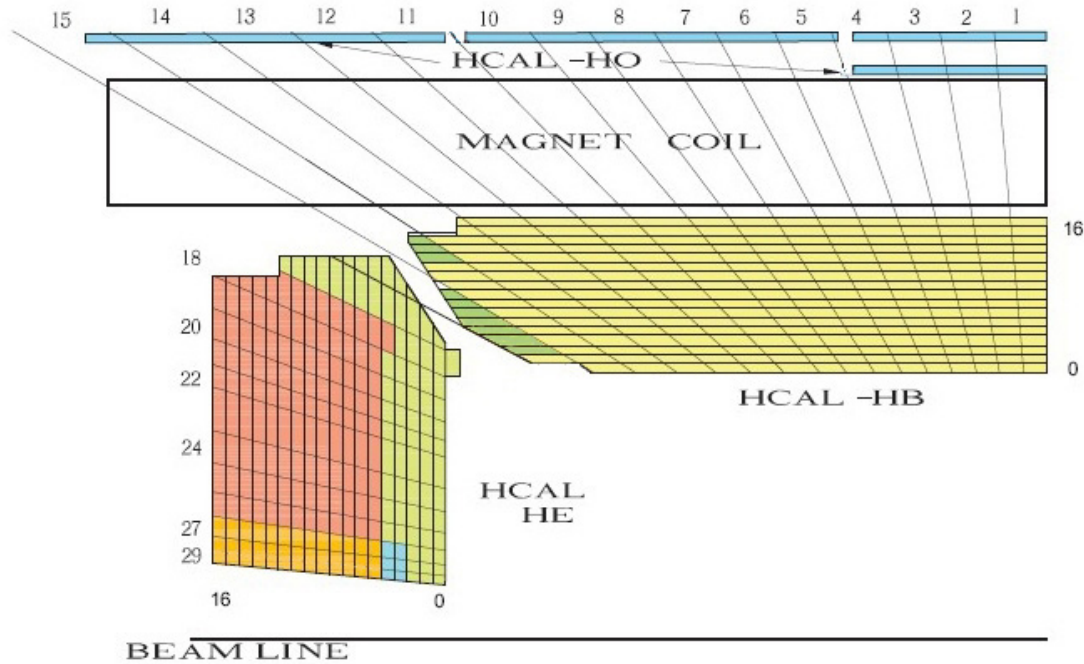


Figure 3.8: Diagram of HCAL geometry, reproduced from Ref. [111].

321 Closer to the beam line on each side, the forward hadronic calorimeter (HF,  $3.0 <$   
 322  $|\eta| < 5.2$ ) is made of iron and quartz fibers instead of brass and plastic scintillator to  
 323 maximize radiation hardness. It acts as a Cherenkov detector with the quartz fibers  
 324 as the active detection element. Half the fibers extend the entire depth of HF, while  
 325 the other half start after the hadrons have traversed 22 cm of iron, allowing some  
 326 differentiation between electromagnetic and hadronic energy. The energy resolution  
 327 in HF is given by

$$\left(\frac{\delta E}{E}\right)^2 = \left(\frac{172\%}{\sqrt{E/\text{GeV}}}\right)^2 + (9\%)^2, \quad (3.13)$$

328 where the terms have the same physical interpretation as those in Eq. (3.12). HF  
 329 improves CMS's missing energy resolution by roughly a factor of three.

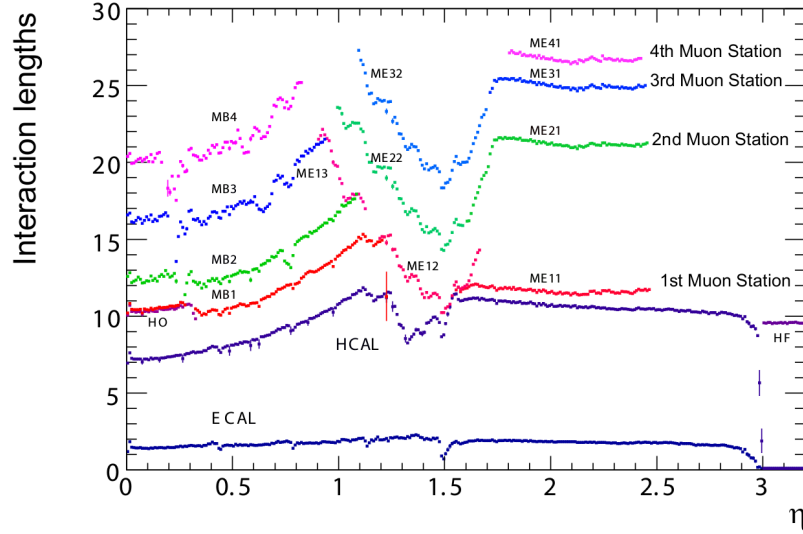


Figure 3.9: Total material budget in units of nuclear interaction lengths, as a function of pseudorapidity, reproduced from Ref. [111].

### 3.2.5 Muon Spectrometer

Many of the most interesting physics processes at the LHC involve high energy muons, so muon identification, triggering, and momentum measurement are important design goals. Muons leave very little energy in the calorimeters, so ECAL and HCAL cannot be used for triggering and identification as they are for electrons, photons and hadrons, or to improve momentum measurements of high- $p_T$  muons whose tracks are too straight to allow good measurements of their curvature. Instead, these functions are provided for muons by three gas-based systems surrounding the rest of the detector [127, 128]. In all three, ionizing gas chambers provide hits which form a track. The magnetic field for this is provided by the return yoke, a set of steel plates interleaved with the muon chambers which confine the solenoid's magnetic return field. The yoke plates weigh a total of 10,000 t and are fully saturated by the solenoid.

Unlike the inner tracker, the muon systems can be read out fast enough to provide triggering. Because muons above 3 GeV generally traverse the muon system while most other measurable particles are stopped in the calorimeters, magnets, or return

345 yoke, the muon system provides high efficiency, low-background muon identification.  
 346 The muon system's momentum measurements are not competitive with the inner  
 347 tracker's at low  $p_T$ , but a combined fit of the inner track and the muon system  
 348 ("standalone") track improves muon  $p_T$  resolution above roughly 200 GeV. The  
 349 geometry of all three muon systems and the return yoke can be seen in Fig. 3.10.

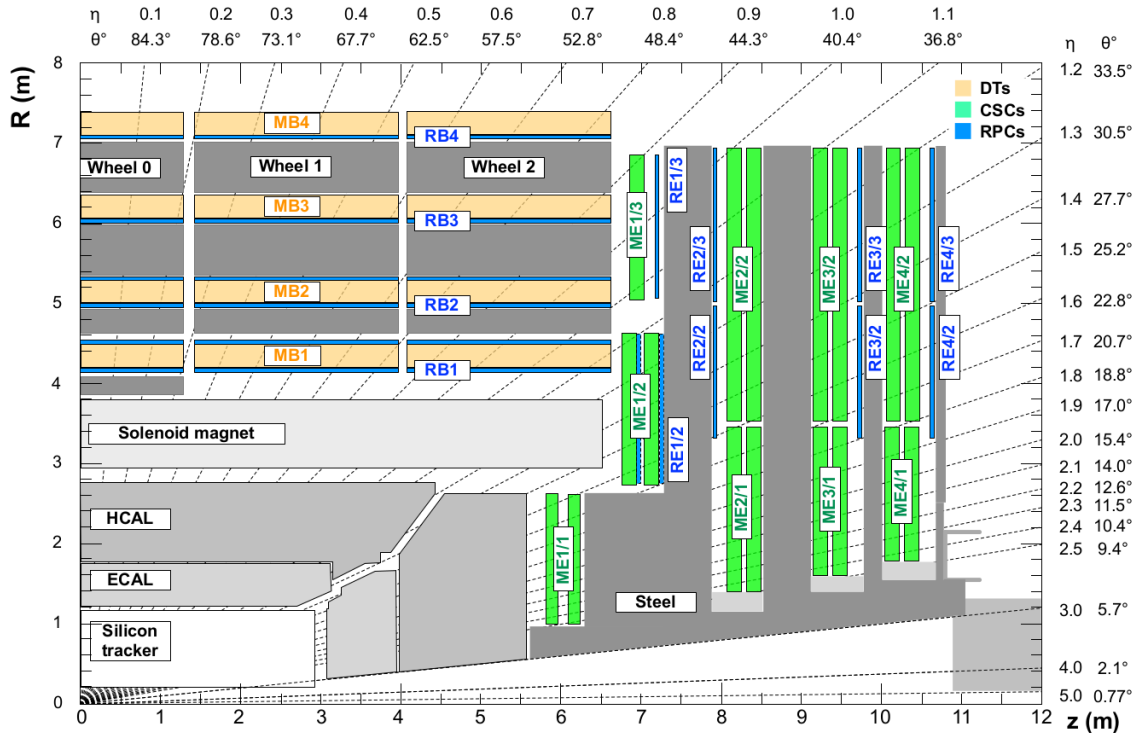


Figure 3.10: Diagram of muon system and return yoke geometry, reproduced from Ref. [128]. The magnet, calorimeters, and inner tracker are also visible.

### 350 3.2.5.1 Drift Tubes

351 In the barrel ( $|\eta| < 1.2$ ), drift tube (DT) chambers are arranged in four "stations"  
 352 separated by the steel layers of the yoke. Stations are made of two or three superlayers  
 353 (SLs) of four layers of rectangular drift cells. Adjacent layers are staggered latterally  
 354 by half a drift cell width to avoid gaps. Each station has two SLs with wires running  
 355 parallel to the beam to measure muon tracks in the  $r\phi$  plane, separated by an

356 aluminum honeycomb lattice to provide mechanical rigidity and act as a spacer. The  
 357 inner three stations contain an extra SL on the outer side of the spacer with wires  
 358 perpendicular to the beam line, to measure muon position along the  $z$ -axis.

359        Each drift cell contains a roughly 2.4 m-long wire in gas (85% Ar, 15% CO<sub>2</sub>). The  
 360 electric field in the cell is provided by aluminum tape glued to the top and bottom  
 361 of the cell and held at +1.8 kV relative to the grounded aluminum plates above and  
 362 below. Aluminum tape cathodes on the side of the cell are held at -1.2 kV, while the  
 363 wires act as +3.6 kV anodes. The width of each cell perpendicular to muon motion,  
 364 42 mm, was chosen for a maximum drift time of 380 ns, sufficient to obviate the need  
 365 for double-hit readout logic in this low-occupancy region of the detector. The height  
 366 of 13 mm set by mechanical and space constraints. Track timing resolution in each  
 367 SL is a few nanoseconds when all cells are allowed to read out all deposited charge.  
 368 The  $r$ - $\phi$  position resolution available for online use in the trigger is about 1.5 mm in  
 369 each SL; offline, for a single wire it is roughly 250  $\mu$ m, leading to an overall offline  
 370 resolution of 100  $\mu$ m at each station.

### 371 3.2.5.2 Cathode Strip Chambers

372 Muons with  $1.2 < |\eta| < 2.4$  are detected by the cathode strip chambers (CSCs).<sup>2</sup>  
 373 The CSC system's trapezoidal chambers are arranged on discs interleaved with the  
 374 endcap yoke in four layers. Chambers close to the beamline each cover 20° sections  
 375 in  $\phi$  while outer chambers cover 10° sections, with overlap to avoid gaps.

376        A CSC chamber is made of seven panels sandwiched together to make six gaps  
 377 filled with a gas mixture (40% Ar, 50% CO<sub>2</sub>, 10% CF<sub>4</sub>). Six of the plates have cathode  
 378 strips milled into one side, varying in pitch from 8.4 mm at the narrow end of the  
 379 trapezoid to 16 mm at the wide end, with 0.5 mm gaps between strips. Three panels

---

<sup>2</sup>Where the CSCs and DTs overlap ( $0.9 < |\eta| < 1.2$ ), tracks are formed from hits in both.

380 are wrapped with anode wires, alternating with the other panels so that every gas  
 381 gap has a plane of wires. Wires are spaced 3.2 mm apart and run azimuthally around  
 382 the detector, except for the innermost chamber closest to the interaction point, which  
 383 are inside the magnet and must have their wires tilted 29° so that charge collected  
 384 by the wires moves parallel to them despite the Lorentz forces from the solenoid.

385 A typical muon will deposit charge in 3–4 cathode strips and a similar number of  
 386 anode wires per gas gap, allowing hit position to be interpolated using all these sig-  
 387 nals as well as timing information. The single-plane spatial resolution can be as good  
 388 as 80  $\mu\text{m}$  but depends strongly on where in the width of the strip the muon hits. The  
 389 strips in alternating planes are therefore offset by half their width. Measurements  
 390 from all six gas gaps in a chamber are combined into a segment with position reso-  
 391 lution in the 30–80  $\mu\text{m}$  range, which depends on the chamber but not where in the  
 392 chamber the muon hit.

393 Anodes and cathodes are held 3.6 kV from each other, leading to a drift time of  
 394 roughly 300 ns. Single anode planes have an RMS timing resolution of around 11 ns,  
 395 insufficient for assigning a hit unambiguously to an individual bunch crossing, as  
 396 required for triggering. However, information from all six anode planes in a chamber  
 397 can be combined to yield a segment timing resolution around 5 ns. Segments are  
 398 therefore the unit of information sent to the trigger. Segment position resolution at  
 399 trigger level is 1–2 mm.

#### 400 3.2.5.3 Resistive Plate Chambers

401 To provide a redundant set of muon momentum measurements, as well as precise  
 402 timing of muon hits, CMS has six layers of resistive plate chambers (RPCs) in the  
 403 barrel and four in the endcap up to  $|\eta| < 1.6$ . RPC chambers consist of two thin  
 404 layers of intert gas (95.2%  $\text{C}_2\text{H}_2\text{F}_4$ , 4.5%  $\text{C}_4\text{H}_{10}$ , 0.3%  $\text{SF}_6$ ) each between a pair of

405 Bakelite electrodes held at 9.3 kV. The two “gas gaps” are placed on either side of  
406 a plane of copper strips. When a passing muon ionizes the gas, the high voltage  
407 causes a fast electron avalanche read out by the strips. The narrow gap allows the  
408 RPCs to have single-hit timing resolution around 1 ns, but the spatial resolution is  
409 limited to about 1 cm by the size of the readout strips. The DTs and CSCs both  
410 have better momentum resolution than the RPCs, but RPCs are a simple, robust  
411 auxiliary system and the timing resolution can be used in conjunction with the other  
412 systems to improve overall muon measurements. The gaps between RPC chambers  
413 do not align with the gaps in the other outer muon systems, increasing the muon  
414 spectrometer’s geometrical acceptance.

### 415 **3.2.6 Data Acquisition and Trigger**

416 With a bunch crossing rate of 40 MHz and over 40 collisions possible in each crossing,  
417 the collision rate can exceed 1.6 GHz. Event sizes on disk of 1–2 MB mean that the  
418 raw data generation rate of CMS could potentially be several PB/s, substantially  
419 more than can be read out, stored or analyzed with current technology. However,  
420 most events consist only of low-energy, well-understood QCD interactions, so the  
421 data rate can be drastically reduced by reading out and storing only events likely to  
422 have interesting physics content. CMS reduces the event rate with a two-level trigger  
423 system.

424 The level-1 (L1) trigger uses custom hardware operating on trigger primitives  
425 (TPs) containing lower-granularity detector information to reduce the event rate to  
426 100 kHz or less. The inner tracker’s readout is too slow for use in the trigger, so only  
427 the calorimeters and muon systems generate TPs. Events accepted at level-1 are fully  
428 read out, digitized, and sent to the high level trigger (HLT), where they are partially  
429 reconstructed in software and filtered further, reducing the final rate of stored events

430 to roughly 1 kHz.

431 **3.2.6.1 Level-1 Trigger**

432 LHC beams collide at too high a rate for trigger decisions to be made in software,  
 433 so the L1 trigger is instead implemented in custom hardware, with processing done  
 434 using field-programmable gate arrays (FPGAs) as much as possible for flexibility, and  
 435 application-specific integrated circuits (ASICs) where required. Hardware limitations  
 436 of other CMS subsystems—in particular, the inner tracker’s readout speed and buffer  
 437 capacity—impose strict constraints on the system. The rate of events passing at  
 438 level-1 cannot exceed 100 kHz and the system’s overall latency cannot exceed roughly  
 439 4.2  $\mu$ s from the proton-proton interaction to data storage at level-1. These goals are  
 440 achieved while maintaining high efficiency for interesting physics events by using low-  
 441 granularity detector information, to reduce the bandwidth needed within the trigger  
 442 system. Information flows through several processing steps, with the data throughput  
 443 reduced at each step. Calorimeter and muon information are processed in parallel  
 444 and combined only in the final step. Optical links between systems provide high-  
 445 bandwidth data transfer and allow flexibility in the overall trigger architecture. The  
 446 calorimeter trigger was upgraded with respect to the Run I configuration in 2015,  
 447 and the whole trigger system was overhauled in 2016 [129]. Both configurations will  
 448 be described here.

449       Calorimeter information is compressed into TPs for use in the trigger by trigger  
 450 primitive generators (TPGs). Each TP represents a “tower” consisting of a  $5 \times 5$   
 451 cluster of barrel or endcap ECAL crystals and the HCAL tower behind them, or a  
 452 section of the HF. The TP contains an 8-bit transverse energy sum and a quality bit  
 453 for each calorimeter, and six bits of error checking and bookkeeping information. In  
 454 2015, TPs were sent to the Regional Calorimeter Trigger (RCT) [130], which processed

455 18 portions of the detector (segmented in  $\phi$  with  $+\eta$  and  $-\eta$  treated separately) in  
 456 parallel in separate crates of electronics, using several ASICs and one FPGA in each  
 457 crate for processing [131]. Each RCT crate summed the TPs with  $|\eta| < 3.0$  into  
 458  $4 \times 4$  tower regions, and found isolated and non-isolated  $2 \times 1$  tower  $e/\gamma$  and  $\tau$   
 459 candidates. These objects were sent to Stage 1 Layer 2, which selected the best  $e/\gamma$   
 460 and  $\tau$  candidates from the entire detector, clustered regions into  $3 \times 3$  region jet  
 461 candidates, and computed global quantities like missing transverse energy and the  
 462 scalar sum of transverse momentum for all particles in the event. Pileup subtraction  
 463 was performed with a lookup table (LUT) based on the number of regions in the  
 464 detector with no energy.

465 In 2016, the whole calorimeter trigger was replaced with a new two-tiered system.  
 466 Stage 2 Layer 1 (“CaloL1”) consists of 18 FPGA-based Calorimeter Trigger Proces-  
 467 sor 7 (CTP7) cards [132], which calibrate and reformat the TPs before forwarding  
 468 them to Stage 2 Layer 2 (“CaloL2”) [131], an FPGA-based time-multiplexed system  
 469 which finds  $e/\gamma$ ,  $\tau$ , and jet candidates and computes global quantities for whole events  
 470 in parallel using tower-level information.

471 In 2015, the DTs and CSCs fed track segments into track finders (DTTF [133] and  
 472 CSCTF [134]) which used pattern recognition algorithms to reconstruct tracks and  
 473 measure their  $p_T$ , sharing information between the track finders to avoid inefficiency  
 474 in the overlap region. The RPCs made their own tracks. Since the 2016 upgrade,  
 475 track finding has been done by geometrical region of the detector rather than detector  
 476 subsystem alone, with separate track finders for the barrel (BMTF,  $|\eta| < 0.85$ ) using  
 477 DT and RPC information [135], the endcap (EMTF,  $1.25 < |\eta| < 2.4$ ) using CSC and  
 478 RPC information [129], and the overlap region (OMTF,  $0.85 < |\eta| < 1.25$ ) using all  
 479 three muon systems [136]. The track finders feed into the Global Muon Trigger (GMT,  
 480 upgraded to  $\mu$ GMT in 2016) [137, 138], which merges and sorts tracks, analyzes their

481 quality and selects the best ones.

482 The calorimeter and muon trigger systems, which have up to this point worked  
 483 entirely in parallel, both send their selected candidates and global quantities to the  
 484 Global Trigger (GT, upgraded to  $\mu$ GT) [139, 140]. The Global Trigger contains the  
 485 trigger menu, the configurable set of algorithms used to determine whether an event  
 486 is accepted or not. These algorithms can use combinations of the objects from the  
 487 calorimeter and muon trigger systems, including imposing topological requirements,  
 488 e.g. requiring a large  $\Delta\eta$  between muons in a pair. The final decision is a logical OR  
 489 of all triggers in the menu, but each trigger may be prescaled, i.e. only included in  
 490 the final decision a fraction of the time in order to reduce its rate. When an event is  
 491 accepted, a level 1 accept (L1A) signal is sent to all CMS subsystems instructing them  
 492 to read out information collected in the accepted event, which is stored in buffers until  
 493 it can be read out or safely discarded. A diagram of the whole 2016 L1 trigger system  
 494 and its information flow is shown in Fig. 3.11.

#### 495 3.2.6.2 High-Level Trigger

496 After an accepted event is read out and digitized, it must undergo another level  
 497 of screening before being stored. The High Level Trigger (HLT) uses full detector  
 498 information reconstructed with versions of the normal CMS reconstruction algorithms  
 499 specially optimized for speed, running on a large farm of commercial computers [141].  
 500 Much of HLT’s power comes from having tracker information, allowing more precise  
 501 momentum measurements, isolation calculations and identification algorithms than  
 502 are available at L1. For example, the pixels can be used to reconstruct vertices and  
 503 tag b-quark jets, and requirements can be placed on the invariant mass of a lepton  
 504 pair. However, track reconstructions is slow, so it is typically only done as one of the  
 505 last steps in the filtering process, allowing the event to be rejected based on more

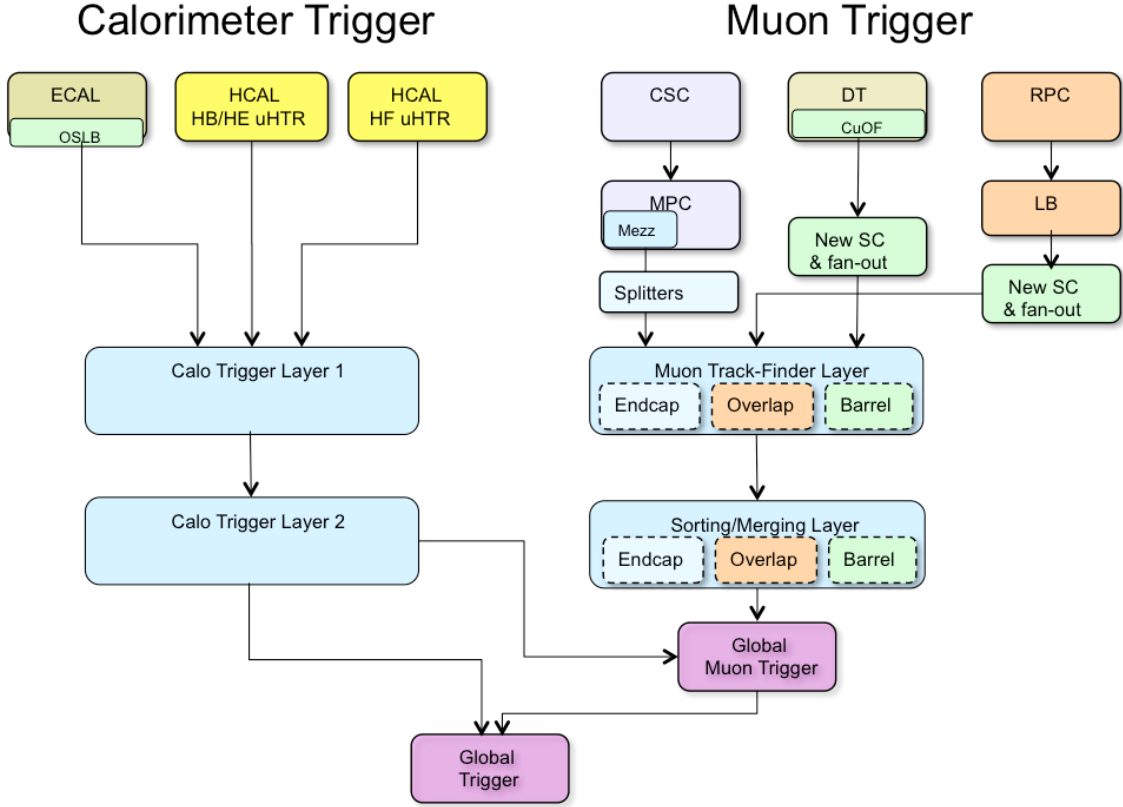


Figure 3.11: Data flow diagram for the CMS L1 trigger after the 2016 overhaul, reproduced from Ref. [129].

506 easily reconstructed objects like tracks in the muon system. Other optimizations  
 507 include only reconstructing tracks near objects passed in by the L1 Global Trigger.  
 508 The final result is that the rate of events saved for later analysis is around 1 kHz.

### 509 3.2.7 Luminosity Determination

510 A precise measurement of the luminosity delivered by the LHC is critical to precisely  
 511 measuring any cross section. The instantaneous luminosity for  $n_b$  colliding bunch  
 512 pairs with intensity  $N_b$  and orbit frequency  $f_{rev}$  is given by

$$\mathcal{L} = \frac{n_b N_b^2 f_{rev}}{A_{\text{eff}}} \quad (3.14)$$

513 where  $A_{\text{eff}}$  is the effective area of the beam-beam overlap. If beam  $i$  has a gaussian  
 514 density profile in the  $u$  direction of width  $\sigma_{i,u}$ , and the beam densities are uncorrelated  
 515 in each direction, then

$$A_{\text{eff}} = 2\pi \sqrt{\sigma_{1,x}^2 + \sigma_{2,x}^2} \sqrt{\sigma_{1,y}^2 + \sigma_{2,y}^2}. \quad (3.15)$$

516 The beam widths  $\sigma_{i,u}$ , the only unknowns in Eq. (3.14), are purely geometrical and  
 517 can be found with the Van de Meer (VdM) scan method [142, 143]. In a VdM scan,  
 518 for which LHC has a special run mode, one beam is held fixed while the position  
 519 of the other is scanned in the  $x$ - $y$  plane, and detector activity is measured as a  
 520 function of beam displacement. Because the width of the interaction rate distribution  
 521 is independent of its overall normalization, the detector activity metric may be any  
 522 quantity linearly proportional to the interaction rate.

523 Over the course of an LHC run,  $n_b$ ,  $N_b$ , and  $A_{\text{eff}}$  are all subject to change, and  
 524 in fact the VdM scans are performed regularly, so in practice the procedure outlined  
 525 above provides a calibration and overall scale for luminosity measurements during  
 526 physics collisions. For a given detector metric labeled  $Q$  with rate  $R^Q$  that peaked  
 527 at  $R_0^Q$  with no beam displacement, the VdM scan yields a visible cross section, the  
 528 constant of proportionality between the rate and the instantaneous luminosity,

$$\sigma_{\text{vis}}^Q \equiv \frac{R^Q}{\mathcal{L}} = \frac{A_{\text{eff}} R_0^Q}{f_{\text{rev}}}. \quad (3.16)$$

529 CMS has several such metrics; the primary one used for measuring integrated lumi-  
 530 nosity is the number of pixel hit clusters [144, 145]. The instantaneous luminosity is  
 531 given by

$$\mathcal{L} = \frac{\langle N_c \rangle f_{\text{rev}}}{\sigma_{\text{vis}}^{\text{PCC}}} = \frac{\langle N_c \rangle f_{\text{rev}}}{A_{\text{eff}} \langle N_c \rangle_0} \quad (3.17)$$

532 where  $\langle N_c \rangle = R^{\text{PCC}} / f_{\text{rev}}$  is the average number of pixel hit clusters at each bunch  
 533 crossing and  $\langle N_c \rangle_0$  is its peak value during the VdM scan.

534 A number of complications must be accounted for or included in systematic un-  
535 certainty estimates. Beam-beam interation effects, correlations between the proton  
536 density distributions in the  $x$  and  $y$  directions, drifts in the beam orbit, and nor-  
537 malization uncertainties on the bunch intensity and absolute distance scale from the  
538 beam spot must all be handled with care. The result is a total integrated luminosity  
539 uncertainty of 2.3% in 2015 [144] and 2.5% in 2016 [145].

## <sup>0</sup> Chapter 4

### <sup>1</sup> Simulation

<sup>2</sup> Comparing data collected by CMS to theoretical predictions is a complex task. The  
<sup>3</sup> theories described in Chapter 1 are understood in great detail, but using this knowl-  
<sup>4</sup> edge to calculate observables is a nontrivial enterprise. Once calculated, observables  
<sup>5</sup> must be compared to data from a detector with finite resolution and subject to a  
<sup>6</sup> number of experimental effects that do not exist in the rarefied world of quantum  
<sup>7</sup> field theory. The general strategy is to employ numerical simulations of individual  
<sup>8</sup> collision events that involve a physics process of interest, and apply accurate simu-  
<sup>9</sup> lations of the detector’s response to these events to obtain samples that are directly  
<sup>10</sup> comparable to data. The success of all steps in this process at a high-luminosity  
<sup>11</sup> hadron collider is one of the triumphs of the LHC era, with many observables in  
<sup>12</sup> interesting processes simulated accurately to the level of a few percent.

#### <sup>13</sup> 4.1 Monte Carlo Event Generation

<sup>14</sup> Even in trivial cases, it would be impossible to integrate over the phase space of hard  
<sup>15</sup> scattering outcomes determined from theory, convolved with matter interactions, de-

16 tector effects, and other experimental factors, to calculate observables analytically.  
 17 Particle interactions are well-understood on a microscopic scale, but it is extremely  
 18 difficult to extrapolate from this first-principles understanding to a description of  
 19 the macroscopic behavior of an ensemble of particles as needed to make predictions  
 20 about fundamentally stochastic processes. Observable spectra are therefore modeled  
 21 with the Monte Carlo (MC) method [11, 146], a numerical integration technique so  
 22 named because, like a casino, it relies heavily on random numbers<sup>1</sup>. The scatter-  
 23 ing amplitudes for a process are calculated from theory at a chosen perturbative  
 24 order [148], and for each simulated event a configuration of final state particles is  
 25 selected at random from this phase space. The final state particles are propagated  
 26 through decays, radiation, hadronization, and interaction with other matter—such as  
 27 the detector—based on well-understood physics principles, and the outcome of any  
 28 stochastic process is chosen at random from a realistic set or distribution of possi-  
 29 bilities. In the limit of a large number of simulated events, the distributions from  
 30 the simulated detector will converge to be directly comparable to aggregated data.  
 31 Individual steps in this process are detailed in the following sections.

### 32 **4.1.1 Matrix Element and Hard Process Generation**

33 Event generator programs start by calculating the scattering amplitudes for a pro-  
 34 cess at a chosen order in perturbation theory. For example, the generator MAD-  
 35 GRAPH5\_aMC@NLO [149] generates all the relevant Feynman diagrams up to NLO  
 36 and calculates the matrix elements for them. Others, like POWHEG [150–152], SHER-  
 37 PA [153] and MCFM [53, 54, 154], are not fully general but have a broad range of  
 38 physics processes implemented at NLO; SHERPA and MCFM can do some calculations

---

<sup>1</sup>Pseudorandom numbers are actually used, but there is no difference in practice as long as a good pseudorandom number generator (PRNG) is chosen and seeded properly. The Mersenne Twister algorithm [147] is the modern standard among general-purpose PRNGs in physics and elsewhere.

39 at NNLO [155]. Events are generated across the entire allowed phase space, either  
 40 uniformly or with the specific distribution dictated by one of several “importance  
 41 sampling” techniques [11, 156] which ensure appropriate statistical coverage in re-  
 42 gions where the distribution has a large slope or value. Each event is assigned a  
 43 weight  $w \in (0, 1)$  based on the scattering amplitude in that region of phase space and  
 44 the probability of having an appropriate initial state based on the PDFs discussed in  
 45 Section 1.6. The sample is then “unweighted” to a subset that is directly comparable  
 46 to data by removing events with a probability proportional to  $1 - w$ .

#### 47 4.1.2 Parton Shower, Hadronization, and Underlying Event

48 Processes generated beyond leading order may have extra radiation, as in the real  
 49 emission diagrams of Fig. 2.2. In the case of calculations at higher orders in QCD, the  
 50 emissions are quarks and gluons which fragment, hadronize, decay, etc. This process  
 51 is handled by a parton shower (PS) MC program such as PYTHIA8 [59] (used for most  
 52 simulations used in this analysis), HERWIG [157, 158], or SHERPA [153]. In PYTHIA8,  
 53 parton showering is simulated with the Lund string model [11, 159–161], which treats  
 54 gluons as strings connecting color charged particles whose tension increases as the  
 55 quarks move apart. When a string stretches too far, it breaks, producing a quark  
 56 pair at the new string ends.

57 Parton shower programs also handle radiation of soft gluons from color charged  
 58 particles and photons from electrically charged particles [162]. The emitter may be  
 59 an incoming parton (initial state radiation, ISR), a virtual particle exchanged during  
 60 the interaction, or an outgoing particle (final state radiation, FSR). The distinction  
 61 between “soft” radiation that should be handled by the PSMC and “hard” emission  
 62 present in the matrix element is not well defined, so it is important to avoid double-  
 63 counting regions of phase space at the boundary between the processes. This is done

64 with jet matching [11, 149]. At tree level, matching may be achieved by enforcing  
 65 a jet energy cutoff: partons from the matrix element must have energy  $E > E_{\text{cut}}$ ,  
 66 and the PSMC is responsible for any softer radiation. At NLO, loop diagrams carry  
 67 divergences that must be canceled by divergences of opposite sign in the infrared  
 68 radiation regime, which the cutoff would prevent, so a more sophisticated scheme must  
 69 be used which weights some events negatively to handle destructive interference [149]  
 70 or modifies the shower development algorithm [150, 151].

71 When combining showered samples that have different jet multiplicities at the  
 72 hard process level, the task becomes even more difficult because the phase space of  
 73 events with  $n$  jets in the matrix element that gain another from the PS overlaps with  
 74 the phase space of events with  $n + 1$  jets at matrix element level. This problem can  
 75 be solved with one of several jet merging algorithms [149, 163–165]. The MLM [166]  
 76 and CKKW [167] algorithms implement merging for tree-level diagrams of different  
 77 jet multiplicities by cutting (MLM) or weighting (CKKW) events based on the prob-  
 78 ability that such an event would originate from the matrix element or PS. The FxFx  
 79 algorithm implements merging when one-loop diagrams are included [168], and there-  
 80 fore plays the same role in NLO calculations that the MLM and CKKW algorithms  
 81 play in LO calculations.

82 PSMC programs provide several more features that are vital in obtaining a faith-  
 83 ful reproduction of data, especially in events with only soft hadronic activity. The  
 84 radiation described above affects the  $p_T$  of the hard scatter system, so PSMCs must  
 85 “retroactively” adjust the kinematics generated by the matrix element MC. The  
 86 underlying event and further QCD interactions that happen below the regime that  
 87 can be calculated perturbatively are modeled phenomenologically [11, 59]. This in-  
 88 cludes soft color exchange between fragments of the colliding hadrons that sends  
 89 proton remnants into the detector in the form of extra soft hadrons [169]. There

90 is also a possibility that multiple pairs of partons will undergo hard interactions in  
 91 the same proton-proton collision, essentially combining two quasi-independent hard  
 92 scatters [162, 170].

### 93 4.1.3 Pileup Simulation

94 The high per-bunch luminosity of the LHC causes multiple proton-proton collisions to  
 95 occur in each bunch crossing. The extra interactions are called pileup. To account for  
 96 this effect, CMS simulations include extra minimum-bias collision events overlaid on  
 97 top of the primary collision [171, 172]. This includes simulated pileup interactions that  
 98 are time evolved to reproduce the effects of “out-of-time” pileup from previous bunch  
 99 crossings, because detector electronics generally have relaxation times longer than  
 100 a single bunch crossing time so signals overlap. Because MC samples are produced  
 101 before the pileup profile can be measured in data, simulated events are reweighted  
 102 based on the number of pileup interactions such that the distribution of the number  
 103 of reconstructed vertices becomes similar to that in data.

### 104 4.1.4 Samples Used in this Analysis

105 The  $q\bar{q} \rightarrow ZZ$ ,  $qg \rightarrow ZZ$ ,  $gg \rightarrow H \rightarrow ZZ^*$ , and  $q\bar{q} \rightarrow Z \rightarrow 4\ell$  samples are produced  
 106 at NLO with POWHEG 2.0 [55, 150–152, 173] and scaled to the NNLO total cross  
 107 section with  $K$  factors of 1.7 for the Higgs sample and 1.1 for the others [56]. The non-  
 108 Higgs POWHEG samples include  $ZZ$ ,  $Z/\gamma^*$ , and  $\gamma^*\gamma^*$  production with a generator-level  
 109 constraint of  $m_{\ell\ell} > 4$  GeV for all opposite-charge lepton pairs, to limit the generated  
 110 phase space to only regions of interest and far from infrared divergences. For the  
 111 inclusive cross sections and differential cross sections in fully leptonic observables,  
 112 this POWHEG sample is considered the primary theory prediction. For the differential

113 cross sections in jet-related variables, `MADGRAPH5_aMC@NLO` 2.3.3 [149] is used for  
 114 the nominal sample, because it has an extra jet at matrix-element level, merged with  
 115 the PS jets using the FxFx scheme. Box diagram  $gg \rightarrow ZZ$  samples are generated  
 116 with `MCFM` 7.0 at LO [174]; these are scaled to NLO with a  $K$  factor of 1.7 [57].

117 Background  $WZ$  events are produced with `POWHEG` with the same settings as the  
 118  $ZZ$  sample while  $t\bar{t}Z$  and  $WWZ$  samples are generated at LO with `MADGRAPH5-`  
 119 `_aMC@NLO`. Electroweak and non-VBS  $ZZjj$  samples are produced with `MADGRAPH-`  
 120 `5_aMC@NLO` for the VBS and aQGC searches and with `PHANTOM` 1.2.8 for the cross  
 121 section measurements [175]. Samples with nonzero aTGCs are generated at LO with  
 122 `SHERPA` 2.1.1 [153] and scaled such that the total yield from the SM `SHERPA` sample  
 123 is the same as the yield from the `POWHEG`  $ZZ$  sample. Signal samples for the aQGC  
 124 search are made with `MADGRAPH5_aMC@NLO`.

125 All samples use the `NNPDF3.0` PDF sets [176]. Parton showering, hadronization,  
 126 and underlying event simulation are done with `PYTHIA8` using the CUETP8M1  
 127 tune [177] for all samples except the aTGC samples, for which `SHERPA` performs  
 128 these tasks.

## 129 4.2 Detector Simulation

130 To incorporate experimental effects into MC samples, the detector and the final state  
 131 particles' interactions with it are simulated with the highest possible level of de-  
 132 tail [171, 172]. The detector geometry and material, including both instrumented  
 133 and non-instrumented components, are modeled with the `GEANT4` package [178],  
 134 which describes microscopic particle interactions with matter over a wide range of  
 135 energies and propagates the effects of these interactions to their macroscopic conse-  
 136 quences. Stochastic effects are again implemented with Monte Carlo methods that

137 select outcomes at random from realistic distributions of possibilities. The GEANT4  
138 simulation includes a detailed model of the magnetic field, so particle trajectories are  
139 calculated correctly, and the generation of secondary particles like  $e^+e^-$  pairs from  
140 photons interacting with tracker material. Charge deposition in silicon, scintillation  
141 in clear crystals, hadronic showers from nuclear interactions, and ionization, are all  
142 included, among many other processes. Detector signals are derived from microscopic  
143 interactions, and GEANT4 simulates signals in the analog front end detector electron-  
144 ics and has signal digitization capabilities which ensure that the signals coming out of  
145 the simulated detector are exactly those that would be produced by the real detector  
146 in the same situation.

147 The simulated signals are fed into the same reconstruction software as is used  
148 for data (see Chapter 5). The same analysis strategy may then be used for MC  
149 samples and data, and comparing the results is meaningful. Though every effort is  
150 made to model the detector accurately, no simulation can incorporate all real effects  
151 with perfect fidelity. Monte Carlo samples must be produced before data are actually  
152 collected, so the final detector alignment cannot be known exactly, and conditions and  
153 calibrations may change mid-run if—for example—a subdetector channel goes dead or  
154 LHC beam conditions change. Residual corrections for these small effects are applied  
155 to final physics objects in the final steps of the analysis to make distributions of  
156 interest, such as dilepton mass around the Z resonance or the overall jet  $p_T$  spectrum,  
157 match in aggregate. The overall level of agreement between data and simulation may  
158 be seen in Fig. 4.1, which shows the invariant mass of  $e^+e^-$  events around the Z  
159 resonance for simulated samples and data, and their ratio.

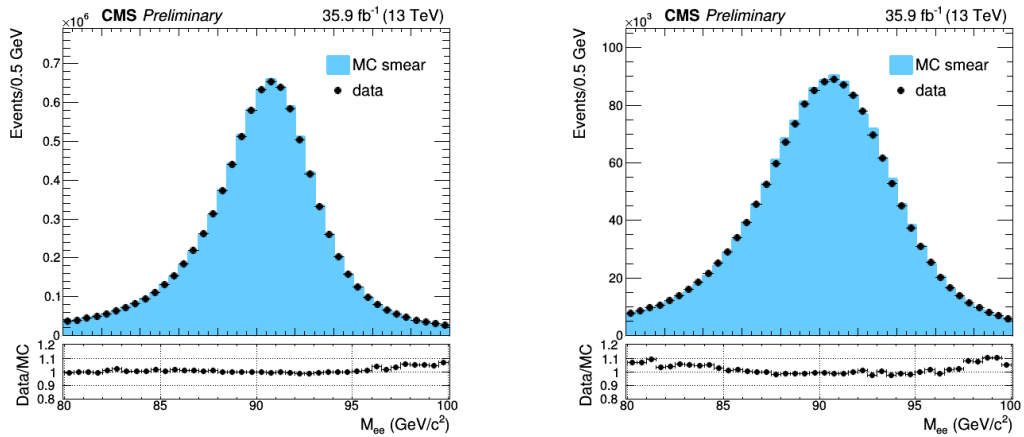


Figure 4.1: The invariant mass of  $e^+e^-$  events with both electrons in the barrel (left) and both electrons in the endcaps (right) in the whole 2016 dataset after all corrections are applied. The lower plots show the ratio of data and simulation to show the level of agreement achieved.

## **0 Chapter 5**

# **1 Object Reconstruction and 2 Selection**

3 The raw detector information stored on disk after an event passes trigger selections  
4 is not yet suitable for physics analysis. Hits in the tracker and muon systems, and  
5 energy deposits in the calorimeters, require significant processing to build physics  
6 objects that are interpretable in terms of the physics of the hard scatter. Patterns in  
7 the tracker and muon system hits are found and used to construct charged particle  
8 and muon tracks, and energy deposits in the calorimeters are grouped into clusters.  
9 Final state particles that interact with CMS are reconstructed from the tracks and  
10 calorimeter clusters, final state particles are clustered into jets, charged particles are  
11 clustered by track origin to find proton-proton collision vertices, and visible particle  
12 momenta are summed to find the transverse momentum imbalance from undetectable  
13 particles (in the SM, neutrinos). The resulting physics objects undergo selection to  
14 determine which represent real particles of interest for the analysis. Selected particles  
15 are used to reconstruct the hard interaction from the collision—in the analyses pre-  
16 sented here, leptons are paired to form  $Z/\gamma^*$  boson candidates which may be paired

17 to form Higgs or Z boson candidates or nonresonant ZZ candidates, and jets are  
18 used to construct hadronic observables and to distinguish electroweak and QCD ZZ  
19 production.

20 **5.1 Track Reconstruction and Vertex  
21 Identification**

22 Tracks are reconstructed in the inner tracker by iterative application of a combina-  
23 torial Kalman filter algorithm [179–182]. At each iteration, tracks found in the pixel  
24 detector are used as “seeds”, track segments which serve as the initial trajectories on  
25 which strip tracker hits from the same particle are expected. The pixel seed supplies  
26 the initial parameters for the combinatorial Kalman filter. At each tracker layer, the  
27 algorithm predicts where the particle will hit the next layer based on the track’s cur-  
28 rent parameters, taking into account the effects of particle interaction with tracker  
29 material. The extrapolated trajectory is used to find compatible hits in the next layer  
30 with a  $\chi^2$  test, and if possible the most compatible hit is added to the track and its  
31 parameters are updated accordingly. If no hits are compatible, a “ghost” hit which  
32 does not contribute to the track parameters may be added to account for the possibil-  
33 ity of a missing hit in the corresponding layer. This procedure is repeated recursively  
34 at each tracker layer, from the innermost layer past the seed to the outermost layer  
35 of the silicon strip tracker. If two tracks found in an iteration share too many hits,  
36 they are assumed to be from the same particle and the one with fewer hits is rejected,  
37 using the total  $\chi^2$  of all hits as a tiebreaker. The first iterations of the track finding  
38 algorithm searches for high- $p_T$  tracks from primary proton-proton interactions, which  
39 are easier to find because they are close to straight and originate from the beam line.  
40 When a track is found, its constituent hits are removed from consideration in future

41 iterations, reducing the computational complexity of finding the more difficult tracks  
 42 from lower- $p_T$  particles and products of b hadron decays which happen away from  
 43 the beam line.

44 Because the Kalman filter obtains the final track parameters only at the out-  
 45 ermost tracker layer, each track is refit and smoothed with further Kalman filters,  
 46 improving track quality and reducing fake rate. Spurious tracks are rejected from the  
 47 final collection with requirements on the number of layers hit, the  $\chi^2$  of the fit, and  
 48 compatibility with a primary vertex.LHC The efficiency for reconstructing tracks of  
 49 all prompt charged particles with  $p_T > 900$  MeV is around 94% in the barrel and  
 50 85% in the endcap; for isolated muons, it is virtually 100% in the whole tracker  
 51 acceptance [182].

52 Electrons lose substantially more energy to interactions with the tracker material  
 53 than other charged particles, often breaking the assumption of Gaussian energy loss  
 54 inherent to the Kalman filter. To mitigate the impact of the resulting poor track  
 55 fits, tracks with many missing hits or a poor  $\chi^2$  are refit using a Gaussian sum filter  
 56 (GSF) [183]. Any Kalman filter or GSF tracks with trajectories that intersect ECAL  
 57 energy clusters (see below) are considered electron track candidates and refit with a  
 58 second, more complicated GSF. This GSF track collection is used as inputs to the  
 59 PF electron reconstruction described below.

60 Proton-proton interaction vertices are found by clustering tracks by minimizing  
 61 the figure of merit

$$\chi^2 = \sum_i \sum_j p_{ij} \frac{(z_j^t - z_i^V)^2}{\sigma_j^2}, \quad (5.1)$$

62 where  $z_i^V$  is the  $z$  position of vertex  $i$ ,  $z_j^t$  is the  $z$  position of track  $j$  at its closest  
 63 point to the beamline, and  $\sigma_j^2$  is its uncertainty. The track-vertex association matrix  
 64  $p_{ij}$  maps tracks to their associated vertices, i.e.  $p_{ij} = 1$  if vertex  $i$  and track  $j$  are  
 65 associated,  $p_{ij} = 0$  if they are not. Rather than minimize Eq. (5.1) directly with an

66 unknown number of vertices, the CMS clustering algorithm [182, 184] uses a tech-  
 67 nique known as deterministic annealing [185], which treats the system as a statistical  
 68 ensemble of associations between the tracks and an unknown number of vertices. The  
 69 association matrix  $p_{ij}$  is then the probability that vertex  $i$  and track  $j$  are associated.  
 70 If every possible set of assignments, for every possible number and arrangement of  
 71 vertices, is considered equally probable, this is analogous to a thermodynamic system  
 72 at high temperature, with  $\chi^2$  playing the role of energy. The system is simulated at  
 73 high “temperature” and the analog of free energy is minimized to determine  $p_{ij}$ . The  
 74 temperature is then lowered in steps, with track-vertex associations deterministic in  
 75 the limit of zero temperature.

76 Among the interaction vertices in an event, the one whose associated charged  
 77 particles have the highest sum of  $p_T^2$  is labeled the primary vertex (PV). A PV must  
 78 be less than 24 cm from the nominal beam spot in the  $z$  direction and less than  
 79 2 cm from it in the  $x$ - $y$  plane. Many commonly-used analysis observables are strongly  
 80 dependent on the number of secondary proton-proton interaction vertices in the event,  
 81 colloquially called the pileup. The pileup distributions used in Monte Carlo samples  
 82 are not the same as the distribution in data, biasing sensitive quantities. Monte  
 83 Carlo events are therefore reweighted based on the number of simulated pileup vertices  
 84 such that the overall  $N_{vtx}$  (number of proton-proton interaction vertices) distributions  
 85 match.

## 86 5.2 Particle Flow Reconstruction

87 The simplest conceivable algorithm would reconstruct each type of particle mostly  
 88 with information from single subsystems: muons with the outer muon system, elec-  
 89 trons and photons with ECAL (using HCAL to differentiate them from hadrons), jets

90 with the calorimeters aided by inner tracker information to handle b jet vertexing, etc.  
 91 This approach is sufficient for many analyses and sophisticated versions of the general  
 92 principle have performed admirably at a number of experiments, but it is suboptimal.  
 93 It fails to exploit the full detector information for many objects—for example, not  
 94 using the inner tracker’s precise measurements of low-energy charged hadrons in jets  
 95 made by clustering calorimeter deposits—and misses significant correlations between  
 96 detector systems. The CMS collaboration takes a different approach, using a particle  
 97 flow (PF) algorithm combining subdetector signals for optimal particle reconstruction  
 98 and identification [186–188].

99 Several features of CMS facilitate PF reconstruction, as described in Section 3.2.  
 100 The most important is that the calorimeters are inside the magnet and close to the  
 101 tracker, so charged particles are much less likely to interact with material between  
 102 them. The inner tracker’s precise position measurement and ECAL’s fine segmen-  
 103 tation thus allow tracks to be associated to calorimeter clusters even for individual  
 104 charged hadrons of modest energy.

### 105 5.2.1 PF Candidates

106 The inputs to the PF algorithm are inner tracker tracks, muon system tracks, and  
 107 clusters of energy deposits in the calorimeters, all of which are calibrated beforehand.  
 108 Calorimeter clusters are built independently for each subsystem, with ECAL and  
 109 HCAL barrel and endcaps considered separately. Topological clusters are built by  
 110 combining adjacent cells with energy deposits over a threshold, using cells that are  
 111 local energy maxima as seeds. Within the topological clusters, the final calorime-  
 112 ter clusters are built by fitting the energy deposits with the sum of several two-  
 113 dimensional Gaussians, one Gaussian for each seed in the topological cluster.

114 The first step of the PF algorithm is to link tracks and clusters across subdetec-

115 tors. Tracks are linked to calorimeter clusters by extrapolating from the track to the  
 116 calorimeter cells the particle would be expected to hit. To account for bremsstrahlung  
 117 photons from electron interactions with tracker material, GSF tracks are linked with  
 118 ECAL clusters compatible ( $\Delta\eta < 0.05$ ) with a tangent to the track where it hit the  
 119 tracker. Overlapping ECAL and HCAL clusters are linked outside the inner tracker  
 120 acceptance. Inner tracks are linked to muon system tracks if their hits can be propa-  
 121 gated onto a common surface and merged into a single track within the resolution of  
 122 the muon system (see Section 3.3 of Ref. [188]). The groups of linked objects, called  
 123 “PF blocks”, usually originate from one or a few particles and are the basic unit of  
 124 PF reconstruction.

### 125 5.2.1.1 Muons

126 Muon candidates in CMS [189] come in three flavors: “standalone”, “tracker”, and  
 127 “global” muons. Standalone muons use only the track from the muon spectrometer  
 128 (the “standalone track”), built with a fit to track segments made of clusters of hits in  
 129 the DTs, CSCs, and RPCs. Tracker muons use only the inner track, identified as a  
 130 muon because the track is compatible with one or more track segments in the muon  
 131 system within 3 cm transverse to the track direction, or four standard deviations  
 132 of the track’s angular position uncertainty. Global muons use a combined “global  
 133 track” made by fitting the hits in an inner track and a compatible standalone track  
 134 to a common muon trajectory through the whole detector. By construction, global  
 135 muons have corresponding standalone and tracker muons. Tracker muons are merged  
 136 into their corresponding global muons, which use the inner track momentum for  
 137 muons with  $p_T < 200$  GeV and the momentum of the track with the best normalized  
 138  $\chi^2$  otherwise. When a muon candidate is reconstructed, its constituent tracks are  
 139 removed from the PF block and are therefore not used in further reconstruction.

140 **5.2.1.2 Electrons and Prompt Photons**

141 Electron reconstruction uses GSF tracks linked with ECAL clusters [183, 190]. The  
 142 cluster associated with a track and the bremsstrahlung candidate clusters on tangents  
 143 to the track are collectively called the “supercluster”. Prompt photons are recon-  
 144 structed from superclusters without associated tracks except displaced track pairs  
 145 consistent with photon-initiated electron-positron pair production in the tracker ma-  
 146 terial [191]. In both cases, the HCAL energy near the supercluster cannot be more  
 147 than 10% of the supercluster energy. Non-isolated photons, i.e. those with substan-  
 148 tial nearby tracks or calorimeter deposits or a high ratio of HCAL energy to ECAL  
 149 energy, are assumed to be from  $\pi^0$  decays and are described with neutral hadrons in  
 150 the next section. Tracks and clusters used to reconstruct electrons and photons are  
 151 removed from the PF block and are not used in hadron reconstruction.

152 **5.2.1.3 Charged and Neutral Hadrons**

153 With muon, electron, and prompt photon constituents removed, remaining detector  
 154 signals are taken to be from charged and neutral hadrons (including non-prompt  
 155 photons) [186, 188]. Clusters in ECAL without associated tracks are taken to be  
 156 photons from  $\pi^0$  decays, because neutral hadrons deposit very little energy in ECAL.  
 157 Trackless clusters in HCAL are taken to be neutral hadrons. Both are removed from  
 158 the PF blocks, so all that remain are linked clusters and tracks. Paired tracks and  
 159 clusters with compatible energies are taken to be charged hadrons. If the track  $p_T$   
 160 is much less than the calorimeter-measured  $p_T$ , the pair is labeled as overlapping  
 161 charged and neutral hadrons.

162 **5.2.2 Jets**

163 Effective clustering of hadrons, non-prompt photons, and non-prompt leptons into jets  
 164 is critically important for many physics analyses, including the ZZ + jets differential  
 165 cross section measurements and the ZZ VBS search (see Sections 6.5 and 5.4.3).  
 166 Clustering must be efficient, to ensure the tagging jets in VBS events are found,  
 167 but the clustering algorithm should not tag spurious jets, as the number of jets in  
 168 an event is sensitive to higher-order QCD corrections and therefore an interesting  
 169 quantity to compare to theoretical predictions. Similarly, the algorithm should not  
 170 erroneously cluster particles from the same initial parton into multiple jets or merge  
 171 jets from multiple original partons, because the kinematics of the original quarks and  
 172 gluons are also of theoretical interest and the detector-level jet kinematics should  
 173 accurately reflect them. A clustering algorithm is said to be “infrared safe” if the  
 174 presence of low-energy hadrons from soft gluon radiation does not change the number  
 175 of jets or have a qualitatively significant effect on jet shapes and kinematics. This  
 176 fits with the intuition that a single 1 GeV pion should have essentially no effect in  
 177 an event with multiple jets with energies on the order of hundreds of GeV [192].  
 178 An algorithm is said to be “collinear safe” if the jets are not changed substantially  
 179 by splitting one hadron into two nearly collinear hadrons with the same total four-  
 180 momentum. This also fits with physical intuition in that jets deposit energy over  
 181 an area significantly larger than the spatial resolution of the detector, so increasing  
 182 the detector granularity enough to resolve two very close particles (without changing  
 183 their total four-momentum) should have little or no effect on the jet.

184 Infrared and collinear (IRC) safety are critically important for comparing data  
 185 to theoretical predictions [193]. Collinear splittings and soft gluon radiation during  
 186 jet fragmentation should not affect the dynamics of the TeV-scale hard scattering  
 187 processes we wish to probe, but they are nonperturbative and difficult to model

188 (see Section 4.1.2), and experimental analysis can only probe the underlying hard  
 189 interaction if it is insensitive to this kind of mismodeling. Experimental detectors'  
 190 finite resolution and inability to measure arbitrarily soft particles enforces some level  
 191 of IRC safety on any algorithm, but the results of an analysis methods that uses  
 192 an IRC unsafe clustering will depend on the complex, detector-dependent details  
 193 of this partial IRC regularization. In any case, the most meaningful comparisons  
 194 between data and theory should use the same definition of a jet in the experimental  
 195 analysis and the perturbative calculation, and perturbative calculations require IRC  
 196 safe observables to preserve unitarity.

197 These considerations, and the desire for conical jets with a well-defined area in  
 198 the  $\eta$ - $\phi$  plane, lead most CMS analyses (including this one) to use jets clustered with  
 199 the anti- $k_T$  algorithm [194, 195]. The anti- $k_T$  algorithm defines the distance between  
 200 two particles  $i$  and  $j$  as

$$d_{ij} = \min(p_{Ti}^{-2}, p_{Tj}^{-2}) \frac{\Delta_{ij}}{R}, \quad (5.2)$$

201 where  $\Delta_{ij}$  is the distance in the rapidity-polar angle plane,

$$\Delta_{ij}^2 \equiv (y_i - y_j)^2 + (\phi_i - \phi_j)^2, \quad (5.3)$$

202 and  $R$  is a parameter setting the size of the resulting jets. The algorithm proceeds  
 203 iteratively. At each iteration, if the smallest  $d_{ij}$  between any pair of particles in the  
 204 event is smaller than the smallest  $p_T^{-2}$  of any single particle, the particles in the pair  
 205 are merged into a single particle with their total four-momentum. If the minimum  
 206 single-particle  $p_T^{-2}$  is smaller than the minimum  $d_{ij}$ , the single particle is labeled a  
 207 jet and removed from further consideration. Iteration proceeds until all particles are  
 208 part of a jet. In this analysis, the size parameter used is  $R = 0.4$ .

209 Charged hadrons whose tracks originate in pileup interactions are not included in  
 210 jet clustering [196]. The contribution of neutral hadrons from pileup is estimated with

211 a jet area technique [197–199] in which the energy density of neutral hadrons from  
 212 pileup is calculated event-by-event and multiplied by the area of the jet to estimate  
 213 the neutral pileup contribution, which is subtracted from the jet energy. Jets in  
 214 Monte Carlo samples have their energy shifted and stochastically smeared such that  
 215 the overall energy scale and resolution match that of jets in data [197, 200].

### 216 5.2.3 Missing Transverse Energy

217 Neutrinos—or, hypothetically, WIMP dark matter or other new particles that do not  
 218 decay or interact directly with the detector—escape and cannot be directly measured.  
 219 Because the beams have no momentum in the  $x$ - $y$  plane, the transverse momentum  
 220 of the visible particles must balance the transverse momentum of the invisible ones.  
 221 The missing transverse momentum is thus

$$\vec{p}_T^{\text{miss}} = - \sum_{\text{visible}} \vec{p}_T, \quad (5.4)$$

222 where the sum runs over the transverse momenta of all PF candidates in the event.  
 223 The missing transverse energy,  $E_T^{\text{miss}}$ , is its magnitude. The  $E_T^{\text{miss}}$  is calibrated by  
 224 propagating the jet energy scale corrections to the  $E_T^{\text{miss}}$  calculation [201–203]. All  
 225 PF candidates are included in the sum in Eq. (5.4), including those originating from  
 226 pileup interactions, because these soft collisions are very unlikely to produce neutrili-  
 227 nos, so including them biases the measurement less than trying to determine which  
 228 neutral particles should be considered pileup and which should not.

## 229 5.3 Object Identification and Selection

230 The reconstruction algorithms described above are general purpose in the sense that  
 231 they can be used in nearly any analysis, but do not address the specific needs of

any, so further selections are essentially always required to optimize object efficiency and purity for studying a specific physics process. The leptons used in this analysis are required to pass identification requirements on top of those imposed during PF reconstruction, and are required to be isolated from other particles in the event, to reject fake objects from jet fragmentation. Four-lepton processes have low reducible backgrounds, so the selections presented here are generally loose, optimized for high efficiency compared to most CMS analyses.

### 5.3.1 Electrons

Electrons are required to have  $p_T > 7 \text{ GeV}$  and to be in the tracker acceptance,  $|\eta| < 2.5$ . They must be compatible with the PV, with minimum track-PV distance  $d_z < 1 \text{ cm}$  in the  $z$  direction and  $d_{xy} < 5 \text{ mm}$  in the plane transverse to the beam. Each electron's 3-dimensional impact parameter (IP)  $d_{3\text{D}}$  must satisfy a requirement on its significance,

$$\text{SIP}_{3\text{D}} \equiv \frac{d_{3\text{D}}}{\sigma_{d_{3\text{D}}}}, \quad (5.5)$$

where  $\sigma_{d_{3\text{D}}}$  is the uncertainty on the IP. The  $\text{SIP}_{3\text{D}}$  requirement is  $\text{SIP}_{3\text{D}} < 10$  for the ZZ and  $Z \rightarrow 4\ell$  cross section measurements and the aTGC search, and  $\text{SIP}_{3\text{D}} < 4$  for the Higgs boson measurement and the VBS and aQGC searches. Distributions of  $\text{SIP}_{3\text{D}}$  are shown for electrons and muons in Fig. 5.1. To remove fake electrons arising from muon tracks being associated to photons or other incidental ECAL energy clusters, electrons within  $\Delta R < 0.05$  of a muon are vetoed.

To further reduce photon and jet fragment backgrounds while maintaining high prompt electron efficiency, a further selection is applied using a multivariate discriminator made with a boosted decision tree (BDT) [204, 205]. The BDT uses 21 input variables, which fall into three broad categories:

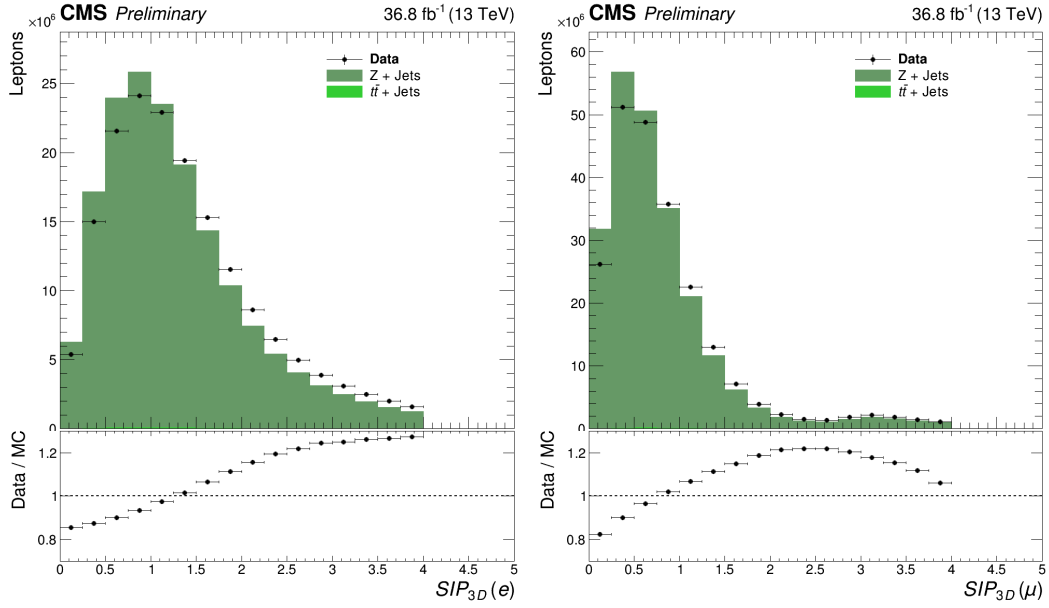


Figure 5.1: Vertex compatibility in the form of the  $SIP_{3D}$  distribution for electrons (left) and muons (right) in a single-Z sample. The distribution extends only to 4 because these events were used for Higgs boson measurements.

- 255     • Track-related observables like the number of hits and normalized  $\chi^2$  of the
- 256        Kalman and GSF tracks and the energy lost to bremsstrahlung according to
- 257        the GSF fit. These are intended to discriminate between electrons and charged
- 258        hadrons.
- 259     • Calorimetric information including a number of supercluster shape observables
- 260        and the amount of HCAL energy near the supercluster, to discriminate electrons
- 261        from electromagnetically rich jets.
- 262     • Track-cluster observables comparing the positions and momenta of the particles
- 263        seen in the tracker and by ECAL.
- 264        The BDT training and working point selection are done separately for electron can-
- 265        didates with  $p_T$  above and below 10 GeV and in three bins of  $|\eta|$  (0–0.8, 0.8–1.479,

and 1.479–2.5). The working points are chosen to correspond to 98% efficiency for single signal electrons in each bin.

To ensure that electron candidates are not part of a jet, they are required to be isolated from other particles in the event. The relative isolation is defined as

$$R_{\text{Iso}} = \left( \sum_{\text{charged}} p_{\text{T}} + \max \left[ 0, \sum_{\text{neutral}} p_{\text{T}} + \sum_{\text{photons}} p_{\text{T}} - p_{\text{T}}^{\text{PU}}(\ell) \right] \right) / p_{\text{T}}^{\ell} \quad (5.6)$$

where the sums run over the  $p_{\text{T}}$  of PF hadrons and photons in a cone of  $\Delta R < 0.3$  around the electron trajectory. To mitigate the contribution of pileup to the isolation calculations, charged hadrons are included only if they originate from the event’s PV. The estimated neutral contribution to isolation from pileup,  $p_{\text{T}}^{\text{PU}}(\ell)$ , is defined for electrons as

$$p_{\text{T}}^{\text{PU}}(\ell) \equiv \rho \times A_{\text{eff}}, \quad (5.7)$$

where the average transverse-momentum flow density  $\rho$  is calculated in each event using the jet area method described above. The effective area  $A_{\text{eff}}$  is the geometric area of the isolation cone times an  $\eta$ -dependent correction factor that accounts for the residual dependence of the isolation on pileup. Electrons are considered isolated if their relative isolations satisfy  $R_{\text{iso}} < 0.35$ . Relative isolation distributions are shown for electrons and muons in Fig. 5.2.

Efficiencies for GSF track reconstruction, electron reconstruction and identification, and electron isolation criteria, are found with a “tag-and-probe” method [206]. In this technique, events are selected which contain at least one high- $p_{\text{T}}$  “tag” electron passing strict ID and isolation requirements, and a “probe” track with the opposite sign that combines with the electron to have an invariant mass close to the Z boson mass. The resulting sample is enriched with  $Z \rightarrow e^+e^-$  events, so the track is likely to correspond to a real prompt electron. Unlike all background processes,  $Z \rightarrow e^+e^-$  production forms a distinct resonance peak in the  $m_{\ell\ell}$  distribution, so shape fits can

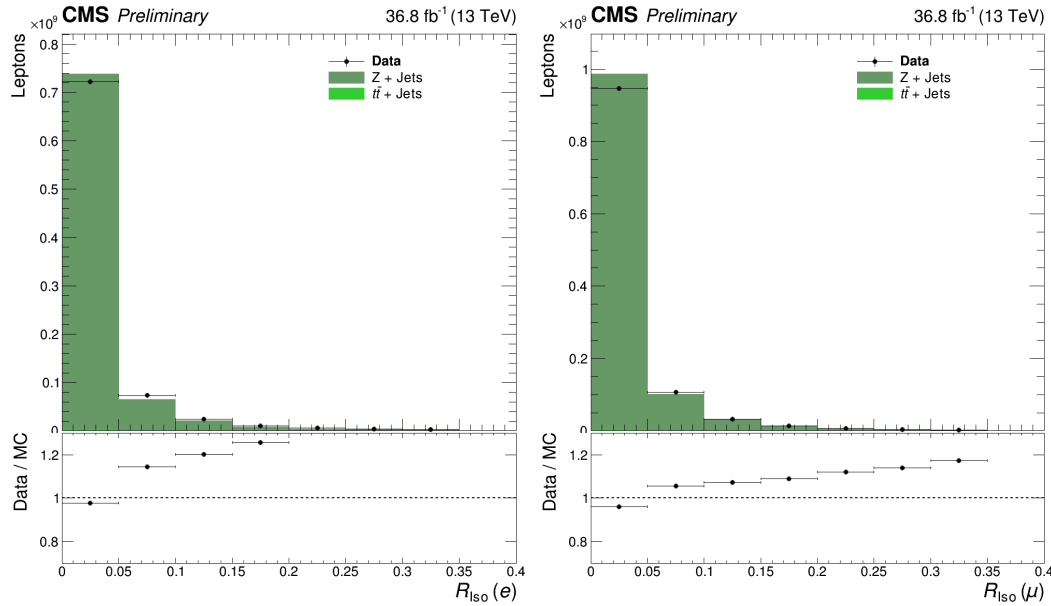


Figure 5.2: Relative isolation for electrons (left) and muons (right) in single-Z events.

be used to find the overall purity of the sample, and thus the number of prompt electrons among the probes. The selection efficiency is then the number of passing probes divided by the total number of prompt probes. This procedure is performed in bins of  $p_T$  and  $\eta$  for data and Monte Carlo events, and residual differences in efficiency in Monte Carlo samples are corrected to match data by weighting events by the ratio of data and Monte Carlo efficiency for each electron candidate. Overall electron efficiency varies between roughly 85% in the inner endcap ( $|\eta| > 2.0$ ) to around 95% in the central barrel ( $|\eta| < 0.8$ ).

### 5.3.2 Muons

Muon selection is similar to electron selection, but simpler because muon backgrounds are much smaller. Candidate muons are required to be tracker or global muons with  $p_T > 5 \text{ GeV}$  within the muon system acceptance ( $|\eta| < 2.4$ ). They are subject to the same PV compatibility criteria as electrons,  $d_z < 1 \text{ cm}$ ,  $d_{xy} < 5 \text{ mm}$ , and  $\text{SIP}_{3D} < 10$

302 or 4 depending on the analysis. Muon candidates are further subject to the so-called  
 303 “PF ID” criteria, which require them to be isolated from calorimeter deposits or to  
 304 have high-quality tracks with good fits [188].

305 Isolation is defined as in Eq. (5.6), the same as for electrons except for the defini-  
 306 tion of the neutral pileup contribution, which for muons is based on using the known  
 307 charged pileup density to estimate the neutral pileup based on the average charge  
 308 composition of pileup jets,

$$p_T^{\text{PU}}(\mu) \equiv 0.5 \sum_{\text{charged}} p_T^{\text{PU}}, \quad (5.8)$$

309 where the sum runs over the charged particles from all pileup vertices. As for elec-  
 310 trons, the radius of the isolation cone is 0.3 in the  $\eta$ - $\phi$  plane and the selection criterion  
 311 is  $R_{\text{iso}} < 0.35$ . Muon efficiencies are measured and corrected with the same tag-and-  
 312 probe technique as used for electrons, and found to be around 97%.

### 313 5.3.3 Final State Photon Radiation

314 Final-state radiation (FSR) photons emitted by muons are not included in the PF  
 315 momentum reconstruction, and some photons emitted by electrons may be missed,  
 316 degrading Z boson reconstruction. Photons are considered FSR candidates if they  
 317 have  $p_T > 2 \text{ GeV}$ ,  $|\eta| < 2.4$ , relative isolation  $R_{\text{iso}} < 1.8$  as defined in Eq. (5.6) (with  
 318 no neutral pileup correction), and  $\Delta R(\ell, \gamma) < 0.5$  with respect to the nearest lepton.  
 319 To avoid double counting, photons in electron superclusters are not considered. Be-  
 320 cause FSR has a higher energy spectrum than photons from pileup and is expected  
 321 to be quasi-collinear with the emitting leptons, a photon is accepted as FSR and  
 322 included in the ZZ final state if  $\Delta R(\ell, \gamma) / E_{T\gamma}^2 < 0.012$ . The performance of this  
 323 algorithm is tuned and evaluated with comparisons to generator-level information in  
 324 MC samples, and is found to have efficiency around 60% for a purity around 80%.

325 FSR photons are omitted from the isolation determination for emitting leptons. In  
 326 the rest of this thesis, the momentum of any FSR photons found is included in  $Z/\gamma^*$   
 327 and ZZ four-momenta unless otherwise stated.

### 328 5.3.4 Jets

329 Jets are considered for analysis if they have  $p_T > 30 \text{ GeV}$  and  $|\eta| < 4.7$ . Loose criteria  
 330 are applied to reject spurious jets by requiring they contain multiple particles, and  
 331 the particles be a mix of charged and neutral consistent with hadronic jets. Jets are  
 332 removed from consideration in the event if a lepton or FSR photon is in its cone  
 333 ( $\Delta R < 0.4$  with respect to the jet's total momentum vector).

### 334 5.3.5 Misidentified Objects

335 The reducible background estimation method described in Section 6.1 requires the use  
 336 of “loose” lepton candidates which are similar to candidates passing the full selection  
 337 but much more likely to be jet fragments or other non-prompt objects. Loose lepton  
 338 candidates pass the  $p_T$  and  $\eta$  cuts and vertex compatibility criteria, but the other  
 339 identification criteria are reduced. The electron BDT discriminator is not applied to  
 340 loose electrons. Loose muons must still be tracker or global muons, but the PF ID is  
 341 not applied. Isolation requirements are not applied to loose candidates. Depending  
 342 on their use, loose candidates may have no further requirements applied, or may be  
 343 required to fail the tight ID and/or isolation requirements, as detailed in Section 6.1,  
 344 where the fake rates for electrons and muons are shown in Fig. 6.1. Aside from the  
 345 ID and isolation criteria, loose leptons are treated the same as their tight cousins,  
 346 with FSR recovery performed with the same algorithm. Jets near loose leptons are  
 347 only removed if the loose lepton is taken to be one of the four in the ZZ candidate in

348 the final event interpretation.

## 349 5.4 ZZ Candidate and Event Selection

350 Online event selections used single, double, and triple lepton triggers. The double  
 351 lepton triggers were the primary paths, with single and triple lepton triggers correct-  
 352 ing for residual inefficiencies to bring the overall trigger efficiency above 99%. Exact  
 353 HLT parameters changed over the course of datataking as instantaneous luminosities  
 354 changed and trigger rates rose, so many thresholds are shown here as ranges.

- 355 • Single muon  $p_T$  thresholds were between 20 and 24 GeV for isolated muons.  
 356 Nonisolated single muons were required to have  $p_T > 50$  GeV or  $p_T > 45$  GeV  
 357 and  $|\eta| < 2.1$ . Single electron  $p_T$  thresholds were 25 or 27 GeV depending on  
 358 ID criteria applied.
- 359 • Leading lepton  $p_T$  thresholds in double lepton paths were 17 or 23 GeV. Trailing  
 360 lepton thresholds were 12 GeV and 8 GeV for electrons and muons, respectively.  
 361 Isolation requirements and requirements on the  $z$ -axis distance between lepton  
 362 track origins were added part way through datataking.
- 363 • The  $p_T$  requirements in triple lepton paths varied between 5 and 16 GeV, with  
 364 no isolation or vertex requirements.

365 An event is considered for the analysis if any of these triggers fires.

366 Several distinct analyses fall under the four-lepton umbrella, each with different  
 367 requirements and therefore different selection criteria. The sets of selections will be  
 368 listed here with brief descriptions of their uses, and detailed in full below.

- 369     • The *full spectrum selection* picks a phase space that encompasses all four-lepton  
 370       events, and all other selection sets yield strict subsets of the full spectrum phase  
 371       space.
- 372     • The *singly resonant ( $Z \rightarrow 4\ell$ ) selection* picks events with four-lepton mass  
 373       around the  $Z$  boson resonance.
- 374     • The *Higgs selection* is that used for the Higgs boson discovery and properties  
 375       measurements. It is similar to the full spectrum selection but with slightly  
 376       tighter requirements on the second  $Z/\gamma^*$  candidate, because  $Z \rightarrow 4\ell$  events are  
 377       of less interest and some backgrounds may be reduced by excluding events with  
 378       an on-shell  $Z$  boson and a low mass lepton pair that could be a decay of an  $\Upsilon$   
 379       or similar meson.
- 380     • The *on-shell or doubly resonant selection* requires both  $Z$  candidates to be  
 381       compatible with a resonant  $Z$  boson. It is used for the ZZ and ZZ + jets cross  
 382       section measurements and the aTGC search.
- 383     • The *dijet (ZZjj) selection* uses the on-shell selection for the four-lepton system,  
 384       and additionally requires at least two jets. It is used for the VBS and aQGC  
 385       searches.

### 386 5.4.1 $Z/\gamma^*$ Candidate Selection

387 A  $Z/\gamma^*$  candidate is built from a pair of opposite-sign, same-flavor leptons with  
 388 invariant mass between 4 and 120 GeV. The  $Z/\gamma^*$  candidate with mass closest to the  
 389 nominal  $Z$  boson mass is labeled  $Z_1$ , the other is labeled  $Z_2$ . Mass requirements on  
 390 the  $Z/\gamma^*$  candidates are among the primary differences between the various analysis  
 391 selections. The full spectrum,  $Z \rightarrow 4\ell$ , and Higgs selections require  $m_{Z_1} > 40$  GeV.

392 The Higgs selection additionally requires  $m_{Z_2} > 12 \text{ GeV}$ . The on-shell and dijet  
 393 selections require both  $Z_1$  and  $Z_2$  to have  $m_{Z_i} > 60 \text{ GeV}$ . The mass range thus  
 394 allowed,  $60 < m_{Z_{1,2}} < 120 \text{ GeV}$ , serves as the definition of an on-shell Z boson for  
 395 purposes of this analysis.

Table 5.1: The number of events in data reconstructed as having two pairs of opposite-sign, same-flavor leptons, at several points in the analysis flow. Best candidate selection is done only with the full spectrum selection, and an event may have candidates in multiple channels, so channel yields do not sum to the total yield in early steps.

Selection	4e	2e2 $\mu$	4 $\mu$	Total
Trigger	580633	645640	399212	1598705
Lepton ID	2195	6760	11614	20563
Lepton Isolation	597	1189	1548	3334
Full Spectrum	440	1111	838	2389
$Z \rightarrow 4\ell$	78	206	225	509
$H \rightarrow 4\ell$	19	41	34	94
$ZZ \rightarrow 4\ell$	220	543	335	1098

### 396 5.4.2 ZZ Candidate Selection

397 Four-lepton candidates are built from pairs of  $Z/\gamma^*$  candidates. Among the four lep-  
 398 tons in the candidate, all opposite-sign pairs must have invariant mass  $m_{\ell^+\ell'^-} > 4 \text{ GeV}$   
 399 regardless of flavor, to remove events in which decay products of a light, leptonically  
 400 decaying particle like a  $J/\psi$  are erroneously paired with the two leptons from a real Z  
 401 boson to form two false  $Z/\gamma^*$  candidates by chance when paired incorrectly. The re-  
 402 quirement on all pairs does not include FSR photons, because the mesons that would  
 403 cause such a problem are generally found in jets which include photons from  $\pi^0$  decays,  
 404 whcih are likely to be misidentified as FSR. All lepton pairs must have  $\Delta R > 0.02$   
 405 to avoid “ghost” leptons with shared tracks. The leading and lepton among the four

406 must have  $p_T > 20 \text{ GeV}$ , and the subleading lepton must have  $p_T > 10 \text{ GeV}$  if it is  
 407 an electron or  $p_T > 12 \text{ GeV}$  if it is an electron. The  $Z \rightarrow 4\ell$  selection requires the  
 408 candidate to have  $80 < m_{4\ell} < 100 \text{ GeV}$ , consistent with resonant single-Z production.

409 All allowed pairings of leptons into  $Z/\gamma^*$  candidates are examined separately, so  
 410 an event with two electrons and two positrons, for example, will yield two possible  
 411 ZZ candidates, with the only difference being how the electrons are paired into  $Z_1$   
 412 and  $Z_2$ . In the case that multiple interpretations of the same event pass the full  
 413 selection, the one with  $Z_1$  closest to the nominal Z mass is chosen. In the rare case of  
 414 further ambiguity, which may arise in events with five or more leptons,  $Z_2$  is chosen  
 415 to maximize the scalar  $p_T$  sum of the four leptons. This best candidate selection is  
 416 done after the full selection is applied, and the other analysis selections are applied to  
 417 the disambiguated events in the full spectrum phase space. Like the mass cut on all  
 418 opposite-sign lepton pairs, this prevents events with one on-shell Z and one lower-mass  
 419  $\gamma^*$  from passing the on-shell Z mass cuts with an erroneous lepton pairing.

420 The number of events found in data after several analysis steps is shown in Table x.  
 421 Specifically, the numbers in Table x include events with four objects reconstructed as  
 422 two opposite-sign, same-flavor lepton pairs. Early in the analysis flow, most of these  
 423 objects are fakes later removed by lepton ID and isolation requirements. The total  
 424 signal efficiency of all selections is estimated by finding the fraction of events in the  
 425 POWHEG and MCFM ZZ samples which pass both the fiducial cuts at generator level  
 426 and the full analysis selection after detector simulation and reconstruction. For the  
 427 doubly on-shell selection ( $60 < m_{\ell\ell} < 120 \text{ GeV}$ ), the efficiency is 54% for 4e events,  
 428 65% for 2e2 $\mu$  events, and 78% for 4 $\mu$  events. For  $Z \rightarrow 4\ell$  events, the efficiencies for  
 429 the 4e, 2e2 $\mu$ , and 4 $\mu$  channels are, respectively, 24%, 36%, and 73%.

### 430 5.4.3 Dijet and VBS Signal Selection

431 The dijet selection, used for the VBS and aQGC searches, requires the event to contain  
432 two or more jets. The two highest- $p_T$  jets are called the “tagging jets.” The tagging  
433 dijet system must have  $m_{jj} > 100$  GeV. This criterion is not intended to preferentially  
434 select the EWK signal, which is concentrated at much higher dijet masses, but rather  
435 to provide a minimal selection for the sample on which to perform the multivariate  
436 VBS analysis described in Section 6.5 and the shape-based aQGC analysis described  
437 in Section 6.6. No further selections are applied, and the VBS signal efficiency is  
438 therefore close to 100%.

## <sup>0</sup> Chapter 6

### <sup>1</sup> Analysis Strategy

2 Four-lepton signal processes are generally well modeled, and backgrounds are small,  
3 so most analyses can use simple “cut and count” comparisons between data and  
4 Monte Carlo samples’ yields after applying the selections described in Chapter 5. The  
5 comparisons include the contribution from reducible backgrounds, which is estimated  
6 with a data-driven technique. Inclusive and differential cross sections are extracted  
7 from the observed yields with maximum likelihood estimation techniques. The search  
8 for vector boson scattering extracts the signal yield with a multivariate discriminator,  
9 and the searches for anomalous couplings use a profile likelihood method to extract  
10 limits from the bin-by-bin yields in the  $m_{4\ell}$  distribution. These techniques are all  
11 described in this chapter, as are the relevant systematic uncertainties, which are  
12 taken into account by varying the input parameters to the yields and observing the  
13 resulting changes in yield and spectrum shape.

## <sup>14</sup> 6.1 Background Estimation

15 Reducible backgrounds for four-lepton events typically have two or three prompt  
 16 leptons and two or one other objects—typically jet fragments, sometimes photons—  
 17 which are misidentified as prompt leptons. The largest source of background contam-  
 18 ination is from events in which a Z boson is produced in association with a photon  
 19 and a jet, a leptonically-decaying W boson and a jet, or two jets. There is also a  
 20 contribution from  $t\bar{t}$  events in which both top quarks decay to a lepton, a neutrino,  
 21 and a b quark jet. For simplicity, the two sets of processes are not treated separately  
 22 in what follows, and are collectively labeled “Z + X” events<sup>1</sup>.

23 The contributions of the reducible backgrounds to the selected four-lepton sig-  
 24 nal samples are evaluated using the tight-to-loose “fake rates” method, described in  
 25 Ref. [207]. In this procedure, the likelihood of a nonprompt (“fake”) object to be  
 26 misidentified as a prompt lepton is estimated and applied to control regions enriched  
 27 with Z + X events to estimate their contribution to the signal region. The lepton  
 28 misidentification rate  $f_\ell(p_T^\ell, \eta^\ell)$  is measured from a sample of Z +  $\ell_{\text{fake}}$  events, where  
 29 the Z boson candidate is selected as in the signal region but with  $|m_{\ell\ell} - m_Z| < 10 \text{ GeV}$ ,  
 30 and the  $\ell_{\text{fake}}$  object is a lepton candidate that passes relaxed ID requirements as de-  
 31 fined in Section 5.3.5, with no isolation or tight ID requirements applied.

32 The misidentification rate is defined as the fraction of  $\ell_{\text{fake}}$  candidates which pass  
 33 full lepton identification and isolation critera, in bins of  $p_T$  and  $\eta$ . One should note  
 34 that the misidentification rate cannot be interpreted as a probability in the usual  
 35 sense, and if fact there is no simple physical interpretation of it. Events with three  
 36 prompt leptons can contaminate this control region and bias the misidentification  
 37 rate, because the non-Z lepton is falsely assumed fake. To mitigate this bias, the

---

<sup>1</sup>This is a bit of a misnomer, as “Z + X” does not accurately describe  $t\bar{t}$  events, but the terminology is retained here for consistency with the CMS papers on these analyses.

38 WZ  $\rightarrow 3\ell\nu$  yields in the numerator and denominator in each bin are estimated from  
 39 a simulated sample and subtracted before the ratio of yields is taken. Figure 6.1  
 40 shows the misidentification rates for electrons and muons separately as a function of  
 41  $p_T$  and  $\eta$ .

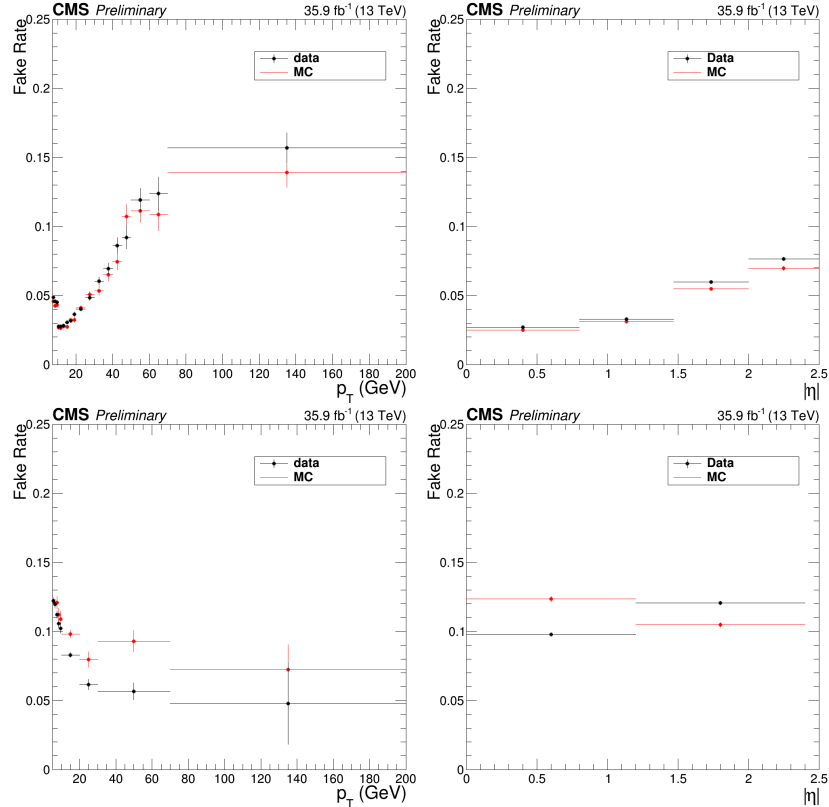


Figure 6.1: Fake rate for electrons (top) and muons (bottom) as a function of  $p_T$  (left) and  $\eta$  (right).

42 To estimate the total reducible background yield, the misidentification rates are  
 43 applied to two Z + X enriched control samples, each containing a Z boson candidate  
 44 passing all signal region requirements plus two more lepton candidates which pass the  
 45 relaxed identification criteria and would make a second Z boson candidate according  
 46 to Section 5.4.1 except that one or both fail the full identification or isolation criteria.  
 47 The sample with one failing lepton, called the “3P1F” sample for “3 prompt 1 fake,”

48 covers the contribution from WZ events, while the sample with both leptons in the  
 49 second Z boson failing (“2P2F”) covers Z + jets, Z $\gamma$  + jets, and t $\bar{t}$  events. The fake  
 50 object transfer factor

$$F_\ell(p_T^\ell, \eta^\ell) = \frac{f_\ell(p_T^\ell, \eta^\ell)}{1 - f_\ell(p_T^\ell, \eta^\ell)} \quad (6.1)$$

51 is the ratio of nonprompt objects passing the relaxed and full selection criteria, and  
 52 thus serves as a per-lepton extrapolation factor between control sample yields and  
 53 signal sample yields.

54 The total reducible background yield is thus

$$N_{\text{bkg}} = \sum_{\ell \in \text{3P1F}} F_\ell(p_T^\ell, \eta^\ell) - \sum_{\ell_1, \ell_2 \in \text{2P2F}} F_{\ell_1}(p_T^{\ell_1}, \eta^{\ell_1}) F_{\ell_2}(p_T^{\ell_2}, \eta^{\ell_2}). \quad (6.2)$$

55 The minus sign prevents double-counting of Z+2jets events in which one jet fragment  
 56 is misidentified. The failing lepton candidates in the 3P1F and 2P2F control samples  
 57 are assumed to truly be jet fragments or other nonprompt objects, but selection  
 58 inefficiencies may cause prompt leptons to fail and contaminate the control regions  
 59 with signal events. The yield of such signal events in the background control regions is  
 60 estimated by applying the same fake factors to failing events in the ZZ signal Monte  
 61 Carlo samples, and subtracted from the result of Eq. (6.2).

62 There are also irreducible background contributions from t $\bar{t}$ Z and WWZ events,  
 63 which can have four prompt leptons. Expected yields for these processes are taken  
 64 from simulation.

## 65 6.2 Systematic Uncertainties

66 Systematic uncertainties for trigger efficiency are taken to be the difference between  
 67 trigger efficiencies in data and in simulated signal events, found to be around 2%  
 68 of the final event yield. Because leptons in Z  $\rightarrow$  4 $\ell$  events generally have lower  $p_T$ ,

69 the uncertainty increases to 4% for  $Z \rightarrow 4e$  events. In both data and simulated  
 70 events, trigger efficiencies are found with a tag-and-probe technique [206], performed  
 71 on four-lepton events.

72 The lepton identification and isolation efficiencies in simulation are corrected with  
 73 scaling factors derived with the tag-and-probe method, performed on  $Z \rightarrow \ell^+ \ell^-$  events  
 74 in data and a single-Z Monte Carlo sample. To find the uncertainties associated with  
 75 these corrections, the total yield is recomputed with the scaling factors varied up and  
 76 down by one standard deviation of the uncertainties from the tag-and-probe method,  
 77 treating all bins as correlated. The resulting changes in the  $ZZ \rightarrow 4\ell$  yield, taken to  
 78 be the one sigma variations resulting from lepton efficiency uncertainties, are found  
 79 to be 6% in the  $4e$  final state, 3% in the  $2e2\mu$  final state, and 2% in the  $4\mu$  final state.  
 80 Leptons in  $Z \rightarrow 4\ell$  events tend to have lower  $p_T$ , and the tag-and-probe samples  
 81 for leptons with  $p_T$  below about 15 GeV are smaller and more contaminated with  
 82 nonprompt objects, so the uncertainties are larger; they are found to be 10%, 6%,  
 83 and 7% for the  $4e$ ,  $2e\mu$ , and  $4\mu$  final states, respectively.

84 The uncertainty on the integrated luminosity of the data sample is 2.5% [145].

85 The uncertainty on lepton fake rates is 40%, which includes both statistical un-  
 86 certainty and systematic uncertainties associated with the loosened lepton selections  
 87 defined in Section 5.3.5 and the differences in the underlying physics processes be-  
 88 tween events in the  $Z + \ell_{\text{fake}}$ , 3P1F, and 2P2F control samples [73]. Statistical uncer-  
 89 tainties arising from the limited size of the  $Z + X$  control samples are also included  
 90 as a systematic uncertainty on the background yield. The total uncertainty on the  
 91 background yield varies by channel but is below 1% of the expected total yield.

92 Uncertainties due to the effect of QCD scale on the  $ZZ \rightarrow 4\ell$  acceptance are  
 93 evaluated with POWHEG and MCFM, by varying the QCD scales up and down by a  
 94 factor of two with respect to the default  $\mu_R = \mu_F = m_{ZZ}$ . Parametric uncertainties

95 ( $\text{PDF} + \alpha_s$ ) are evaluated according to the PDF4LHC prescription in the acceptance  
 96 calculation [208], and with NNPDF3.0 in the cross section calculations. An additional  
 97 theoretical uncertainty arises from scaling the  $q\bar{q} \rightarrow ZZ$  and  $gg \rightarrow ZZ$  simulated  
 98 samples to their NNLO and NLO predicted cross sections, respectively, with the  
 99  $K$  factors described in Section 4.1.4. The corresponding change in the acceptance,  
 100 1.1%, is added to the previous theoretical errors in quadrature.

101 Systematic uncertainties on expected signal yield are summarized in Table 6.1. To  
 102 obtain uncertainties in the inclusive fiducial and total cross sections, each uncertainty  
 103 source is treated as a nuisance parameter in the fits described in Section 6.3.1. For  
 104 differential cross section and other shape uncertainties, the calculation is fully redone  
 105 for each uncertainty source, with the inputs shifted by one standard deviation in each  
 106 direction. Variations across bins are taken to be fully correlated for each uncertainty  
 107 source. Lepton and jet momentum scale and resolution uncertainties are taken to be  
 108 trivial for the overall yield, but they are considered among the shape uncertainties.

Table 6.1: The contributions of each source of signal systematic uncertainty in the total yields. The integrated luminosity uncertainty and the PDF and scale uncertainties are considered separately. All other uncertainties are added in quadrature into a single systematic uncertainty. Uncertainties that vary by decay channel are listed as a range.

Uncertainty	$Z \rightarrow 4\ell$	$ZZ \rightarrow 4\ell$
Lepton efficiency	6–10%	2–6%
Trigger efficiency	2–4%	2%
MC statistics	1–2%	0.5%
Background	0.6–1.3%	0.5–1%
Pileup	1–2%	1%
PDF	1%	1%
QCD Scales	1%	1%
Integrated luminosity	2.5%	2.5%

### 109 6.3 Fiducial and Total Cross Section Calculation

110 Inclusive cross section measurements can be treated as simple binned counting exper-  
 111 iments, where the bins are the three decay channels ( $4e$ ,  $2e2\mu$ , and  $4\mu$ ). If  $\nu$  events are  
 112 expected in a given bin, the probability of observing  $n$  events is given by the Poisson  
 113 distribution,

$$f(n; \nu) = e^{-\nu} \frac{\nu^n}{n!}. \quad (6.3)$$

114 In a particle physics analysis like this one,  $\nu$  takes the form

$$\nu = \nu_s(\vec{\theta}_s) + \nu_b(\vec{\theta}_b) = \mu(\vec{\theta}_s) \mathcal{L}_{int} \sigma_{SM} \epsilon + \nu_b(\vec{\theta}_b) \quad (6.4)$$

115 where  $\nu_s$  and  $\nu_b$  are respectively the expected signal and background yields,  $\sigma_{SM}$  is  
 116 the standard model expectation for the cross section of the signal process and  $\epsilon$  is our  
 117 efficiency for detecting and identifying its events. The signal and background nuisance  
 118 parameter vectors  $\vec{\theta}_s$  and  $\vec{\theta}_b$  represent hidden quantities that we do not measure  
 119 directly but which affect our yields, i.e. systematic effects. The signal strength  $\mu$   
 120 compares our expectation to what we actually measure:

$$\mu = \frac{\sigma_{meas}}{\sigma_{SM}}. \quad (6.5)$$

121 Of the variables in Eqs. (6.3) and (6.4),  $\sigma_{SM}$  is known from theoretical calculations,  
 122 and  $\epsilon$  is determined from simulation. The CMS detector is designed to measure  $n$   
 123 and  $\mathcal{L}_{int}$ ,  $\nu_b$  is estimated from data or simulation, and inferring  $\sigma_{meas}$  is a matter of  
 124 finding the most likely value of the signal strength  $\mu$  given the observed data. Then  
 125 the measured cross section is simply

$$\sigma_{meas} = \mu \sigma_{SM}. \quad (6.6)$$

126 One interesting feature of this method is that  $\sigma_{SM}$  is used in the calculation of  $\mu$   
 127 (Eq. (6.4)) and in the final cross section (Eq. (6.6)) in such a way that it cancels out,

128 and in fact anything proportional to the true cross section may be used. In practice,  
 129 this means that the order at which  $\sigma_{SM}$  is calculated does not matter to the extent  
 130 that higher order corrections to the kinematics of the events do not affect  $\epsilon$ .

131 Typically,  $\sigma_{meas}$  in Eq. (6.6) is the fiducial cross section, the cross section for the  
 132 process in a phase space similar to (typically, slightly larger than) the phase space  
 133 in which the experimental analysis can in principle detect events. In the four-lepton  
 134 case, the fiducial phase space is a space of  $2\ell 2\ell'$  ( $\ell, \ell' \in e, \mu$ ) events defined by criteria  
 135 on lepton kinematics, dilepton invariant masses, and four-lepton mass. Table 6.2  
 136 shows the fiducial definitions for both the  $Z \rightarrow 4\ell$  and  $ZZ \rightarrow 4\ell$  cross section mea-  
 137 surements. Lepton kinematic requirements and an invariant mass requirement on  
 138 all opposite-sign, same-flavor lepton pairs in the event are common to both mea-  
 139 surements; requirements on the invariant masses of  $Z/\gamma^*$  boson candidates and the  
 140 four-lepton system are different.

141 The total  $ZZ$  cross section is defined subject to no constraints except the require-  
 142 ment that  $m_{Z_1}$  and  $m_{Z_2}$  be between 60 and 120 GeV, which serves as the definition  
 143 of a  $Z$  boson. The fiducial cross section is related to the total cross section by the  
 144 branching fraction  $\mathcal{B}$  to the final state in question—here, two factors of the  $Z/\gamma^*$   
 145 branching ratio to electron and muon pairs—and an acceptance factor  $\mathcal{A}$  which is the  
 146 fraction of events falling in the fiducial phase space,

$$\sigma_{fid} = \mathcal{A}\sigma_{tot} (\mathcal{B}(Z \rightarrow 2\ell))^2. \quad (6.7)$$

147 The acceptance factor  $\mathcal{A}$  is determined entirely from theory, and is well known [11], so  
 148 it is straightforward to calculate the total cross section once the fiducial cross section  
 149 is known. Calculating both fiducial and total cross sections is interesting because  
 150 it effectively factorizes experimental and theoretical uncertainties. The experimental  
 151 uncertainties are contained entirely in the uncertainties on  $\epsilon$ ,  $\mathcal{L}_{int}$ , and  $\nu_b$  in Eq. (6.4),

which have little or no dependence on theory, while the theoretical uncertainties are contained entirely in the uncertainty on  $\mathcal{A}$ , which is determined with no experimental input. Thus the uncertainty on  $\sigma_{fid}$  is entirely experimental, and the theoretical uncertainties enter only in the uncertainty on  $\sigma_{tot}$ .

Table 6.2: Fiducial phase space definitions for the  $Z \rightarrow 4\ell$  and  $ZZ \rightarrow 4\ell$  cross section measurements. The common requirements apply to both. The  $m_{\ell^+\ell^-}$  criterion is applied to all opposite-sign same-flavor lepton pairs in the event.

Measurement	Fiducial requirements
Common	$p_T^{\ell_1} > 20 \text{ GeV}$ , $p_T^{\ell_2} > 10 \text{ GeV}$ , $p_T^{\ell_{3,4}} > 5 \text{ GeV}$ , $ \eta^\ell  < 2.5$ , $m_{\ell^+\ell^-} > 4 \text{ GeV}$
$Z \rightarrow 4\ell$	$m_{Z_1} > 40 \text{ GeV}$ , $80 < m_{4\ell} < 100 \text{ GeV}$
$ZZ \rightarrow 4\ell$	$60 < m_{Z_1}, m_{Z_2} < 120 \text{ GeV}$

### 6.3.1 Signal Strength Extraction

The signal strength is found by the method of maximum likelihood [11, 209]. The likelihood function is the product of the probability distributions across all bins,

$$L(\vec{\theta}_s, \vec{\theta}_b) = \prod_{bins} f(n; \nu(\vec{\theta}_s, \vec{\theta}_b)). \quad (6.8)$$

The most likely value of  $\nu$  is the one that maximizes  $L$ . In practice,  $\log L$  is typically maximized instead because it is easier to work with,

$$\frac{\partial^2 \log L}{\partial \vec{\theta}_s \partial \vec{\theta}_b} = 0. \quad (6.9)$$

This maximization is performed simultaneously for all bins, yielding a single signal strength across all channels. Systematic uncertainties enter as log-normal constraints imposed on the fit, encoded in  $\vec{\theta}_s$  and  $\vec{\theta}_b$ . The fit is performed numerically.

<sup>164</sup> **6.3.2  $Z \rightarrow 4\ell$  Branching Fraction**

<sup>165</sup> The total  $Z$  cross section can be calculated from the  $Z \rightarrow 4\ell$  fiducial cross section  
<sup>166</sup> with Eq. (6.7), but it is better measured in the  $2\ell$  channel, where the larger branching  
<sup>167</sup> fraction yields samples several orders of magnitude larger than the  $Z \rightarrow 4\ell$  sample  
<sup>168</sup> used here. It is therefore more interesting to use  $\sigma_{fid}(Z \rightarrow 4\ell)$  for a measurement of the  
<sup>169</sup> four-lepton branching fraction  $\mathcal{B}(Z \rightarrow 4\ell)$ . After applying the acceptance correction  
<sup>170</sup> to obtain  $\sigma_{tot}(Z \rightarrow 4\ell) = \sigma_{fid}(Z \rightarrow 4\ell) / \mathcal{A}$ , the four-lepton branching fraction is given  
<sup>171</sup> by

$$\mathcal{B}(Z \rightarrow 4\ell) = \frac{\sigma_{tot}(Z \rightarrow 4\ell)}{\mathcal{C}_{80-100}^{60-120} \sigma(Z \rightarrow 2\ell)} \mathcal{B}(Z \rightarrow 2\ell), \quad (6.10)$$

<sup>172</sup> where  $\sigma(Z \rightarrow 2\ell)$  is the dileptonic  $Z$  cross section in the 60–120 GeV mass range and  
<sup>173</sup>  $\mathcal{C}_{80-100}^{60-120}$  corrects for the fact that  $\sigma(Z \rightarrow 4\ell)$  is found in a mass range of 80–100 GeV.

<sup>174</sup> **6.4 Differential Cross Sections**

<sup>175</sup> Measurement of a differential fiducial cross section is also a problem of finding the  
<sup>176</sup> most likely true distribution given observed yields in multiple bins, estimated back-  
<sup>177</sup> ground yields, and detector effects understood through simulation. Unlike the inclu-  
<sup>178</sup> sive cross section, however, finite detector resolution leads to “smearing” effects that  
<sup>179</sup> cause events to migrate across bins, in addition to the same inefficiencies. The mean  
<sup>180</sup> detector-level distribution  $\vec{\delta}$  is related to the true distribution  $\vec{\theta}$  by a response matrix  
<sup>181</sup>  $\mathbf{R}$ :

$$\vec{\delta} = \mathbf{R}\vec{\theta}. \quad (6.11)$$

<sup>182</sup> The observed distribution in data  $\vec{d}$  is sampled from the Poisson distribution with  
<sup>183</sup> mean  $\vec{\delta}$  independently in each bin. CMS simulation software is sufficiently sophis-  
<sup>184</sup> ticated to give a good estimate of  $R$ , reproducing the real detector’s resolution and  
<sup>185</sup> smearing effects at the level of a few per cent or better for all distributions of interest.

186 If  $\mathbf{R}$  is square and invertible, the maximum likelihood estimate (MLE) of the true  
 187 distribution,  $\hat{\vec{\theta}}$ , is given by

$$\hat{\vec{\theta}} = \mathbf{R}^{-1} \vec{d}. \quad (6.12)$$

188 Even when  $\mathbf{R}$  is invertible, however, it is frequently ill-conditioned, giving  $\hat{\vec{\theta}}$  unphysical  
 189 features like large bin-by-bin fluctuations or even negative bins as a consequence of the  
 190 stochastic nature of  $\vec{d}$ . It is therefore necessary to use a more sophisticated procedure  
 191 to ensure the differential cross section distributions obey physics-inspired constraints.  
 192 The variables used for differential cross sections in this analysis are in general well-  
 193 measured, so bin-to-bin fluctuations are small and the response matrices are nearly  
 194 diagonal, but some bins have low occupancy which can still cause pathologies.

### 195 6.4.1 Unfolding

196 The technique used here is an iterative frequentist method developed in high energy  
 197 physics by D'Agostini [210] and independently in other fields [211–214], as imple-  
 198 mented in ROOUNFOLD [215]. At iteration  $k$ , bin  $j$  of the predicted true distribution  
 199 is set based on its expected contribution to all other bins, weighted by the observed  
 200 data yield in each:

$$\begin{aligned} \theta_j^{(k+1)} &= \sum_i \mathbf{R}_{ij} \theta_j^{(k)} \frac{d_i}{\delta_i} \\ &= \sum_i \mathbf{R}_{ij} \theta_j^{(k)} \frac{d_i}{\sum_m \mathbf{R}_{im} \theta_m^{(k)}}. \end{aligned} \quad (6.13)$$

201 After several iterations,  $\vec{\theta}^{(k)}$  depends only weakly on the ansatz  $\vec{\theta}^{(0)}$ .

202 The sequence will converge to the MLE for any non-pathological choice of  $\vec{\theta}^{(0)}$  [216]  
 203 but again the MLE often displays unphysical behavior. If  $\vec{\theta}^{(0)}$  is strictly positive,  $\vec{\theta}^{(k)}$   
 204 will be strictly positive for all  $k$ , and in this case  $\hat{\vec{\theta}}$  (as defined in Eq. (6.12)) will be  
 205 the asymptotic unfolded distribution as long as it is also strictly positive. Choosing a

smooth function for  $\vec{\theta}^{(0)}$  will generally lead to smooth  $\vec{\theta}^{(k)}$  for small  $k$ ; typical choices include a flat initial distribution and the truth-level distribution used to construct  $\mathbf{R}$  (used in this analysis). What constitutes “small”  $k$  depends on the condition of  $\mathbf{R}$ , but for most physics distributions of interest, including all those used in this analysis, nonphysical fluctuations do not arise until after  $\vec{\theta}^{(k)}$  is close to convergence. Full regularization is therefore imposed by ceasing iteration early. For all distributions shown here, stopping after four iterations was found to obtain a result close to the asymptotic distribution without artificially increasing the bin-to-bin variance.

### 6.4.2 Uncertainties

The largest uncertainties in the unfolded distributions arise from the unfolding procedure itself, which can inflate statistical uncertainties present in the detector-level distributions. The correlation matrix which gives the full uncertainty—considered the statistical uncertainty of the unfolded distribution—does not have a closed form due to the nonlinearity of the method. The covariance matrix is therefore estimated by propagating the statistical error of the inputs at each iteration of the method, as laid out in Ref. [210] and improved in Ref. [215]. This procedure does not account for the bias introduced by regularization, but this is expected to be negligible relative to other systematic uncertainties for the well-modeled processes studied here.

Most systematic uncertainties are propagated through unfolding by recomputing the response matrix with the training sample shifted or reweighted to reflect a  $1\sigma$  shift in the quantity in question. The uncertainty related to that quantity is taken to be the resulting shape difference in the final unfolded distribution. Systematic uncertainties are negligible compared to statistical uncertainties in most bins, as seen in Fig. 6.2, which shows the sources of shape uncertainties on the normalized differential cross section as a function of four-lepton invariant mass.

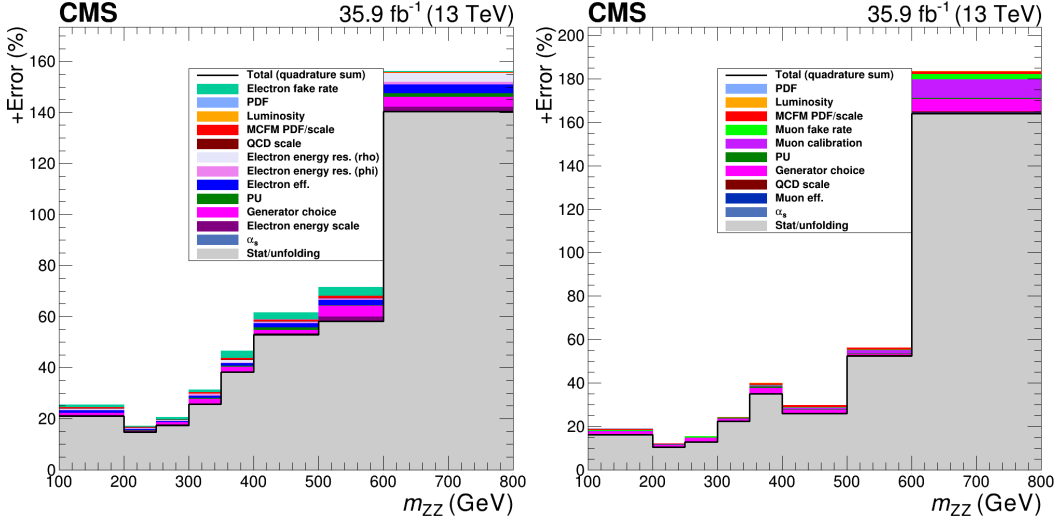


Figure 6.2: Sources of positive shape uncertainties for the normalized differential cross section as a function of four-lepton mass, for 4e events (left) and 4μ events (right). The grey histogram represents statistical errors, propagated through the unfolding procedure, and the histograms stacked on top of it represent various sources of systematic uncertainty. The thick black line represents the sum of all the uncertainties in quadrature. The systematic uncertainties are generally negligible compared to the statistical uncertainty.

## 231 6.5 VBS Signal Extraction

232 The VBS signal search considers events passing the selections described in Sec-  
 233 tion 5.4.3. The electroweak yield is insufficient to have sensitivity at 35.9 fb<sup>-1</sup>, even  
 234 with further cut optimization, so a gradient-boosted decision tree (GBDT), imple-  
 235 mented with the SCIKIT-LEARN package [217], is used to extract the signal. Hyper-  
 236 parameters of the GBDT are optimized with a grid search. Each Monte Carlo sample  
 237 used in the VBS search (see Section 4.1.4) is split into a “training” subsample, used to  
 238 train the GBDT, and a “test” subsample used to evaluate its performance and make  
 239 templates for use in the statistical analysis. The GBDT performance is nearly the  
 240 same for the test and training samples, a sign that the algorithm is not overtrained.

241 A number of observables have been proposed to discriminate VBS events from

background [58], of which  $m_{jj}$  and  $\Delta\eta_{jj}$  are the most powerful. Other commonly-used variables include  $m_{4\ell}$ ,  $\eta^{j_1} \times \eta^{j_2}$ ,  $\Delta\phi_{Z_1 Z_2}$ , and the so-called Zeppenfeld variables, defined as

$$\eta_P^* = \eta_P - \frac{\eta_{j_1} - \eta_{j_2}}{2}, \quad (6.14)$$

where  $P$  may stand for  $Z_1$ ,  $Z_2$ , or  $j_3$ , the highest- $p_T$  untagged jet in the event. In addition to these “traditional” quantities, several other groups of observables have been examined, including production angles, decay angles, measures of total hadronic activity in the event, properties of individual leptons and jets and of the  $ZZjj$  system, and a discriminator designed to distinguish jets originating from quarks and gluons [218]. The hadronic activity and quark-gluon tagging variables have some discriminating power, but they differ significantly depending on the Monte Carlo generator used and were therefore considered too poorly-modeled to use. New GBDTs were trained, each with the traditional observables and one other group of observables, and the groups that improved the GBDT discrimination power significantly were retained. This procedure yielded 17 observables, including the hard process relative transverse momentum, defined as the ratio of the  $p_T$  of the  $ZZjj$  system to the scalar sum of the  $p_T$  of each object,

$$p_T^{rel.\ hard} = \frac{p_T^{ZZjj}}{\sum_{Z_1, Z_2, j_1, j_2} p_T}, \quad (6.15)$$

and the dijet relative transverse momentum,

$$p_T^{rel.\ jj} = \frac{p_T^{jj}}{\sum_{j_1, j_2} p_T}. \quad (6.16)$$

The list of observables was further optimized by retraining the GBDT once with each variable dropped and eliminating the one with the least discriminating power. This pruning was repeated until seven observables remained, namely  $m_{jj}$ ,  $\Delta\eta_{jj}$ ,  $m_{4\ell}$ ,  $\eta_{Z_1}^*$ ,  $\eta_{Z_2}^*$ ,  $p_T^{rel.\ hard}$ , and  $p_T^{rel.\ jj}$ . The resulting GBDT performs only marginally worse ( $0.2\sigma$  less expected significance on the VBS signal) than a version with all observables

264 included, and is faster and easier to train, simpler, and less susceptible to biases and  
 265 systematic uncertainties from mismodeling.

266 The signal and background yields are extracted from the GBDT output spectrum  
 267 with a binned maximum likelihood fit to templates from the test Monte Carlo samples.  
 268 To obtain templates with better fit convergence properties, the GBDT output is  
 269 mapped to the range  $[0, 1]$  with the logistic transformation

$$x \rightarrow \frac{1}{1 - e^{-x}}. \quad (6.17)$$

270 This provides better separation between signal and background and allows uniform  
 271 binning in the templates.

## 272 6.6 Anomalous Gauge Coupling Searches

273 The new physics represented by aGCs would generally manifest as an increase in  
 274 events with high invariant mass, so it is natural to use the shape of the  $m_{4\ell}$  distribution  
 275 for the search. For the aTGC search, the doubly on-shell ZZ selection is used, while  
 276 the aQGC search is performed with the ZZjj selection described in Section 5.4.3.

277 Monte Carlo samples with nonzero aTGCs are generated at grids of points in the  
 278  $f_4^Z$ - $f_4^\gamma$  and  $f_5^Z$ - $f_5^\gamma$  planes. In each bin of the  $m_{4\ell}$  distribution, the yields at the various  
 279 working points are fit to a function of the form

$$y(f^Z, f^\gamma) = x_0 + x_1 f^Z + x_2 f^\gamma + x_3 f^Z f^\gamma + x_4 (f^Z)^2 + x_5 (f^\gamma)^2 \quad (6.18)$$

280 where  $y(f^Z, f^\gamma)$  is the yield in the bin,  $f^V$  can be  $f_4^Z$  and  $f_4^\gamma$  or  $f_5^Z$  and  $f_5^\gamma$ , and  $x_i$   
 281 are the parameters to be fit.

282 A similar procedure is performed for the aQGC search. Rather than simulating a  
 283 full sample for each working point, which is computationally expensive, events from  
 284 MADGRAPH5\_AMC produced at LO are used to obtain samples for nonzero values

285 of  $f_{T0}/\Lambda^4$ ,  $f_{T1}/\Lambda^4$ ,  $f_{T2}/\Lambda^4$ ,  $f_{T8}/\Lambda^4$ , and  $f_{T9}/\Lambda^4$  by matrix element reweighting [149].

286 The yields in each  $m_{4\ell}$  bin are fit to parabolas as a function of the five aQGC parameters separately.

288 A binned profile likelihood method [11] is used to derive the limits. Systematic  
 289 uncertainties are taken into account by varying the number of signal and background  
 290 events within their uncertainties. Exclusion limits are found by comparing the p-  
 291 values of the signal hypothesis and the background only hypothesis

$$CL_s = \frac{p_{s+b}}{1 - p_b} \quad (6.19)$$

292 to set thresholds. Further details on the method can be found in Ref. [219]. The  
 293 software for setting limits, implemented with RooStats, has been validated and  
 294 used extensively by the CMS and ATLAS collaborations [220].

## <sup>0</sup> Chapter 7

## <sup>1</sup> Results

2 A number of measurements and analyses fall under the umbrella of four-lepton  
3 physics, and results presented in this thesis were originally made public in several  
4 journal articles and Physics Analysis Summary documents released by the CMS col-  
5 laboration. The first CMS measurement of the ZZ inclusive cross section at 13 TeV  
6 used roughly half the 2015 dataset ( $1.34 \text{ fb}^{-1}$ ) and was made public in Ref. [221] in  
7 December 2015 as one of the first measurements done on 13 TeV collision data. That  
8 analysis was expanded to use the whole  $2.6 \text{ fb}^{-1}$  collected in 2015, and to include  
9 the  $Z \rightarrow 4\ell$  branching fraction measurement, as reported in Ref. [222], submitted in  
10 July 2016 and published the following December. With the full 2016 dataset, the ZZ  
11 cross section and  $Z \rightarrow 4\ell$  branching ratio were measured again to greater precision in  
12 Ref. [80], which also included differential cross section measurements and aTGC lim-  
13 its, made public in March 2017. A new paper including these measurements [OUR  
14 PAPER] also includes a combination of the 2015 and 2016 inclusive cross section  
15 measurements. Differential cross sections with respect to jet-related observables, and  
16 searches for EWK ZZ production and aTGCs, were reported in May 2017 in Ref. [223],  
17 with a paper on only the VBS and aQGC searches following [224]. The Higgs boson

18 was studied in the four-lepton final state in Refs. [225–227]. In the following, results  
 19 for each topic are only shown for 2016 data, which significantly exceed the accuracy  
 20 of the results from 2015 data.

## 21 **7.1 Four-Lepton Yields and Inclusive Cross 22 Sections**

### 23 **7.1.1 Full Spectrum**

24 The full four-lepton invariant mass spectrum is shown in Fig. 7.1. The single-Z  
 25 resonance can be seen below 100 GeV, the Higgs resonance is visible—though it is  
 26 not sharply resolved with this binning—in the  $Z/\gamma^*$  region below  $2m_Z$ , where doubly  
 27 resonant ZZ continuum production begins. The dilepton invariant mass spectrum is  
 28 shown for both  $Z/\gamma^*$  candidates in Fig. 7.2 and for the  $Z/\gamma^*$  candidate closest to the  
 29 nominal Z boson mass ( $Z_1$ ) in Fig. 7.3. Figure 7.4 shows  $m_{Z_2}$  plotted against  $m_{Z_1}$   
 30 for data events representative of all four-lepton production. Clusters of events with  
 31 zero ( $Z \rightarrow 4\ell$  and nonresonant  $\gamma^*\gamma^*$  production), one ( $H \rightarrow ZZ^*$  and nonresonant  $Z\gamma^*$   
 32 production), and two (nonresonant ZZ production) on-shell Z bosons can be clearly  
 33 seen.

### 34 **7.1.2 $Z \rightarrow 4\ell$ Resonance**

35 Expected and observed yields for events satisfying the  $Z \rightarrow 4\ell$  selection criteria  
 36 ( $80 < m_{4\ell} < 100$  GeV) are shown in Table 7.1. The invariant mass distribution of  
 37 these events is shown in Fig. 7.5. Figure 7.6 shows  $m_{Z_2}$  plotted against  $m_{Z_1}$  for  
 38 all data events consistent with  $Z \rightarrow 4\ell$  production. Predictions from Monte Carlo

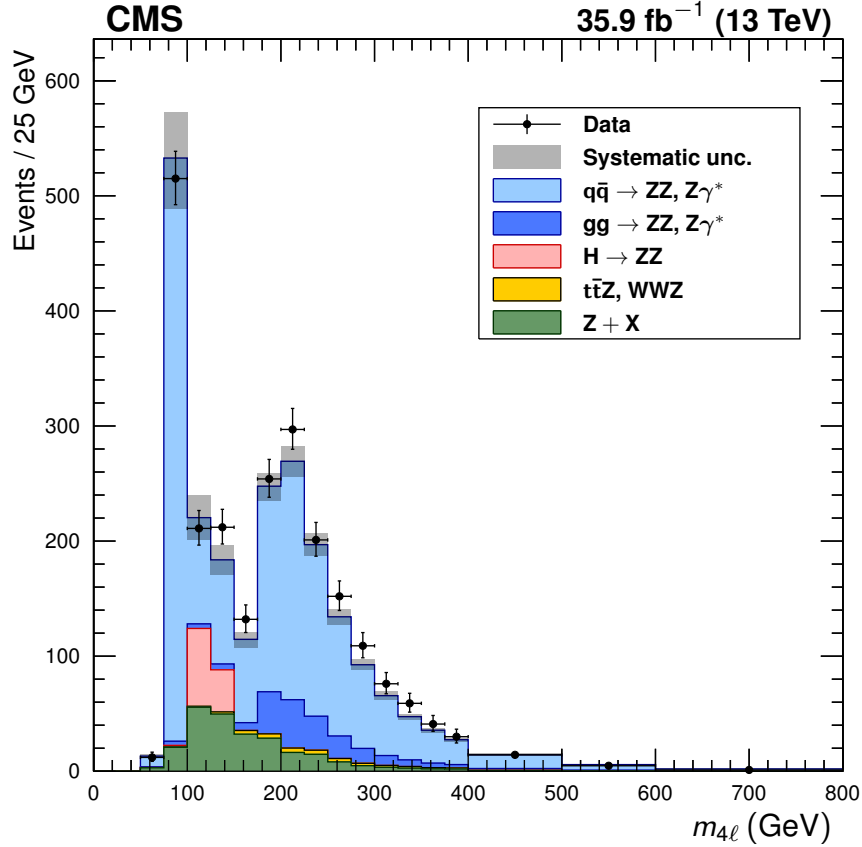


Figure 7.1: Distribution of the four-lepton invariant mass  $m_{4\ell}$  of all events in the full spectrum selection. Points represent data, with statistical uncertainty bars. The stack of filled histograms represents the SM signal prediction and background estimate, with a grey band showing the sum in quadrature of the statistical and systematic uncertainties on the total expected yield.

39 samples generally agree well with the data, allowing us to measure the  $Z \rightarrow 4\ell$  cross  
 40 section and branching fraction.

41 The signal strength in the  $Z \rightarrow 4\ell$  selection is

$$\mu = 0.980^{+0.046}_{-0.044} (\text{stat})^{+0.065}_{-0.059} (\text{syst}) \pm 0.025 (\text{lumi}), \quad (7.1)$$

42 yielding a fiducial cross section

$$\sigma_{\text{fid}} (\text{pp} \rightarrow Z \rightarrow 4\ell) = 31.2^{+1.5}_{-1.4} (\text{stat})^{+2.1}_{-1.9} (\text{syst}) \pm 0.8 (\text{lumi}) \text{ fb}. \quad (7.2)$$

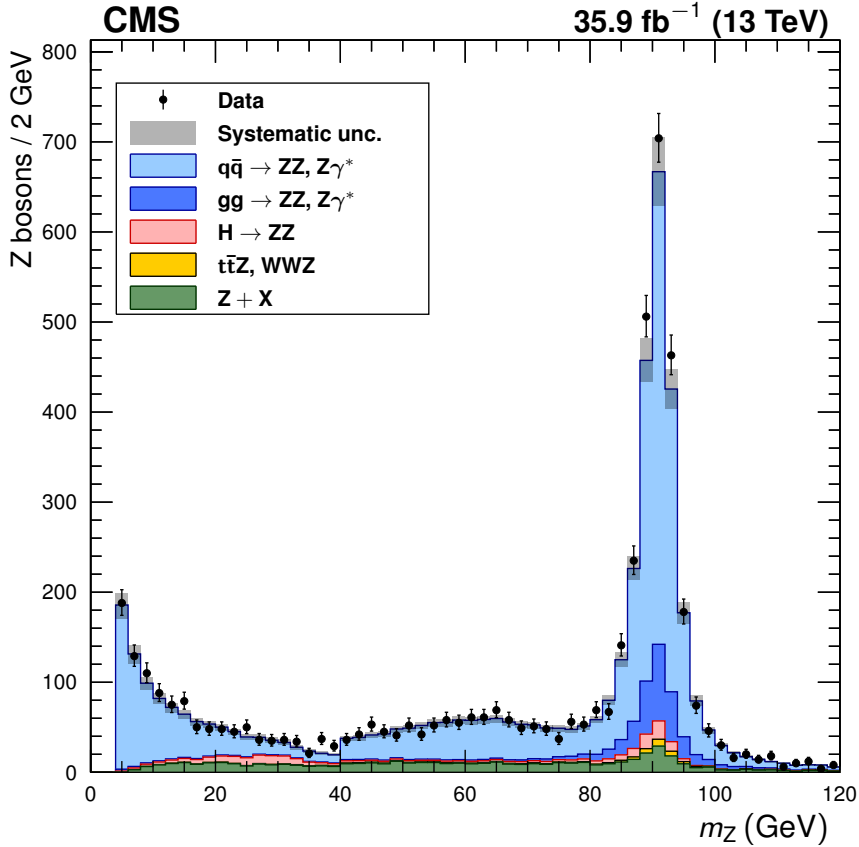


Figure 7.2: Distribution of the dilepton invariant mass of  $Z/\gamma^*$  candidates in all events in the full spectrum selection, regardless of whether the lepton pair is labeled  $Z_1$  or  $Z_2$ . Points represent data, with statistical uncertainty bars. The stack of filled histograms represents the SM signal prediction and background estimate, with a grey band showing the sum in quadrature of the statistical and systematic uncertainties on the total expected yield.

Table 7.1: Observed and expected yields of  $Z \rightarrow 4\ell$  events, including expected background yields, shown for each final state and summed to the total. Uncertainties are statistical, then systematic, not including the integrated luminosity uncertainty.

Final state	Expected $N_{4\ell}$	Background	Total expected	Observed
$4\mu$	$224 \pm 1 \pm 16$	$7 \pm 1 \pm 2$	$231 \pm 2 \pm 17$	225
$2e2\mu$	$207 \pm 1 \pm 14$	$9 \pm 1 \pm 2$	$216 \pm 2 \pm 14$	206
4e	$68 \pm 1 \pm 8$	$4 \pm 1 \pm 2$	$72 \pm 1 \pm 8$	78
Total	$499 \pm 2 \pm 32$	$19 \pm 2 \pm 5$	$518 \pm 3 \pm 33$	509

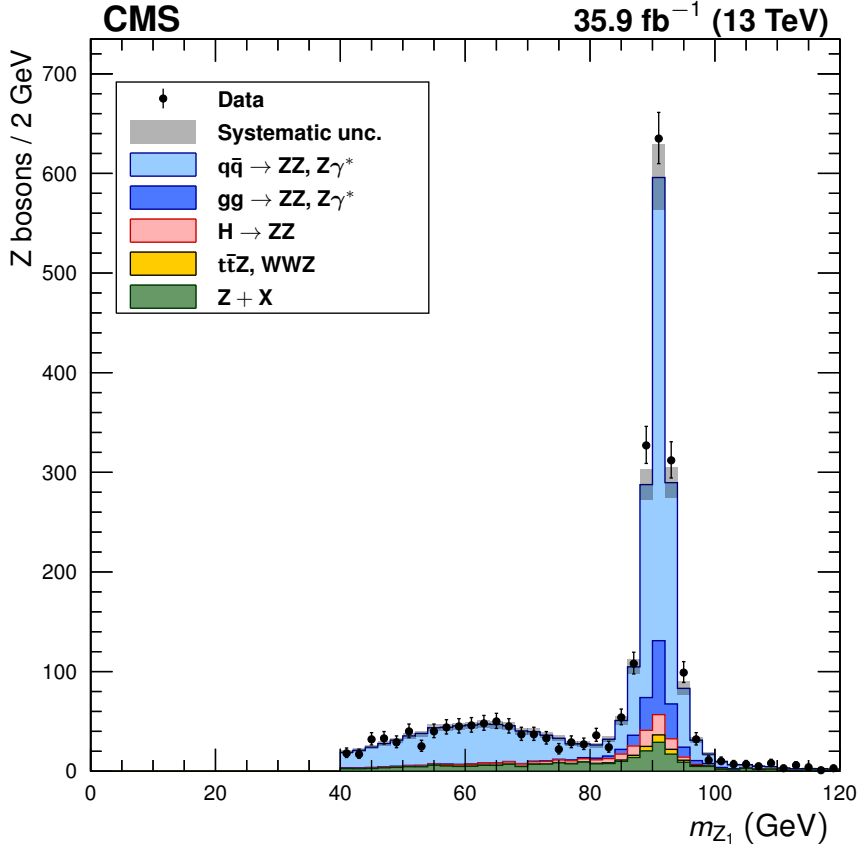


Figure 7.3: Distribution of the dilepton invariant mass of  $Z_1$ , the  $Z/\gamma^*$  candidate in each event closest to the nominal  $m_Z$ , in the full spectrum selection. Points represent data, with statistical uncertainty bars. The stack of filled histograms represents the SM signal prediction and background estimate, with a grey band showing the sum in quadrature of the statistical and systematic uncertainties on the total expected yield.

43 This is scaled by an acceptance correction factor  $\mathcal{A} = 0.125 \pm 0.002$ , estimated with  
 44 POWHEG v2.0, to the total  $Z \rightarrow 4\ell$  cross section times branching ratio,

$$\sigma(\text{pp} \rightarrow Z) \times \mathcal{B}(Z \rightarrow 4\ell) = 249 \pm 8 \text{ (stat)}^{+9}_{-8} \text{ (syst)} \pm 4 \text{ (theo)} \pm 6 \text{ (lumi)} \text{ fb.} \quad (7.3)$$

45 Equation (6.10) is used to calculate the branching fraction. The  $Z$  cross section  
 46 times dilepton branching ratio is calculated with FEWZ v2.0 [228] at NNLO in QCD  
 47 to be  $\sigma(Z \rightarrow 2\ell) = 1870^{+50}_{-40}$  pb. The  $Z$  mass window correction factor is calculated  
 48 with POWHEG and found to be  $\mathcal{C}_{80-100}^{60-120} = 0.926 \pm 0.001$ . Its uncertainty includes

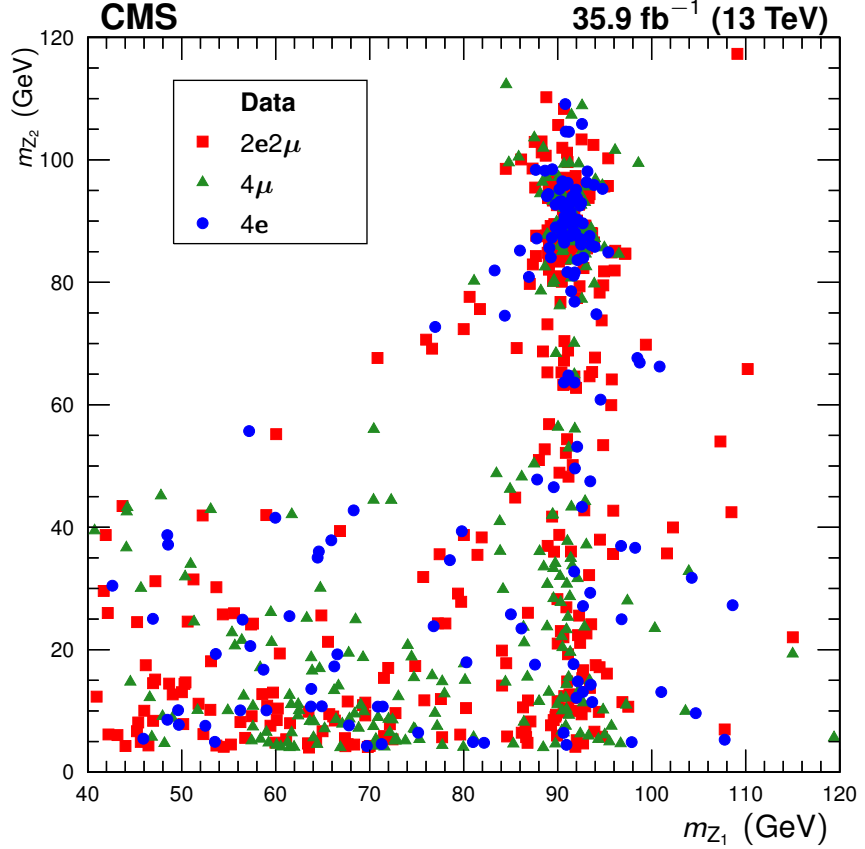


Figure 7.4: The reconstructed  $m_{Z_2}$  plotted against the reconstructed  $m_{Z_1}$  for data events in the full spectrum selection, with distinctive markers for each final state. For readability, only every fourth event is drawn. Clusters of events from different production modes are visible, as discussed in the text.

49 scale and PDF variations [208]. The nominal Z to dilepton branching fraction is  
 50  $\mathcal{B}(Z \rightarrow 2\ell) = 0.03366$  [11]. The four-lepton branching fraction is measured to be

$$\mathcal{B}(Z \rightarrow 4\ell) = 4.8 \pm 0.2 \text{ (stat)} \pm 0.2 \text{ (syst)} \pm 0.1 \text{ (theo)} \pm 0.1 \text{ (lumi)} \times 10^{-6}. \quad (7.4)$$

51 This value is consistent with the theoretical value of  $4.6 \times 10^{-6}$ , calculated with  
 52 MADGRAPH5\_aMC@NLO v2.3.3, and with previous measurements from CMS and  
 53 ATLAS [90, 91, 222], which had uncertainties 2–4 times larger.

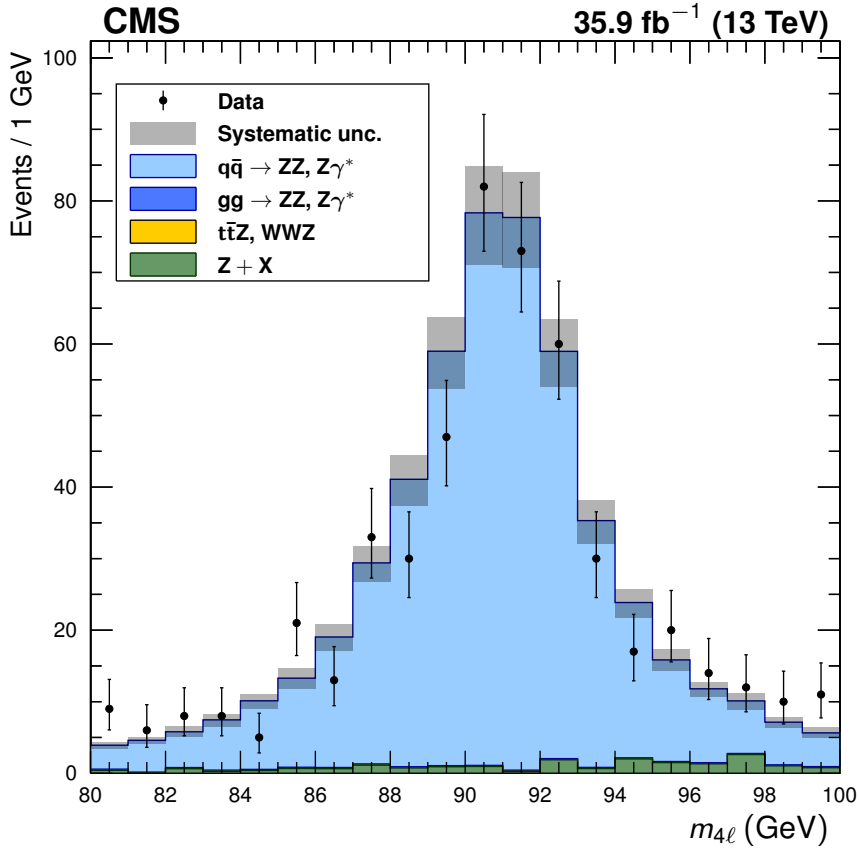


Figure 7.5: Distribution of the four-lepton invariant mass  $m_{4\ell}$  of all events in the mass range  $80 < m_{4\ell} < 100$  GeV, the  $Z \rightarrow 4\ell$  selection. Points represent data, with statistical uncertainty bars. The stack of filled histograms represents the SM signal prediction and background estimate, with a grey band showing the sum in quadrature of the statistical and systematic uncertainties on the total expected yield.

### 54 7.1.3 Higgs Resonance

55 Figure 7.7 shows the four-lepton invariant mass around the Higgs resonance, which  
 56 can be clearly seen above the SM continuum background, for events passing the Higgs  
 57 selection ( $m_{Z_2} > 12$  GeV,  $SIP_{3D} < 4$  for all leptons). Table 7.2 shows the observed  
 58 and expected yields in the mass range  $118 < m_{4\ell} < 130$  GeV. Here, SM continuum  
 59 production—considered signal in all other parts of this analysis—is considered back-  
 60 ground. Figures 7.8–7.10 show the  $Z_1$  mass, the  $Z_2$  mass, and the scatter plot of

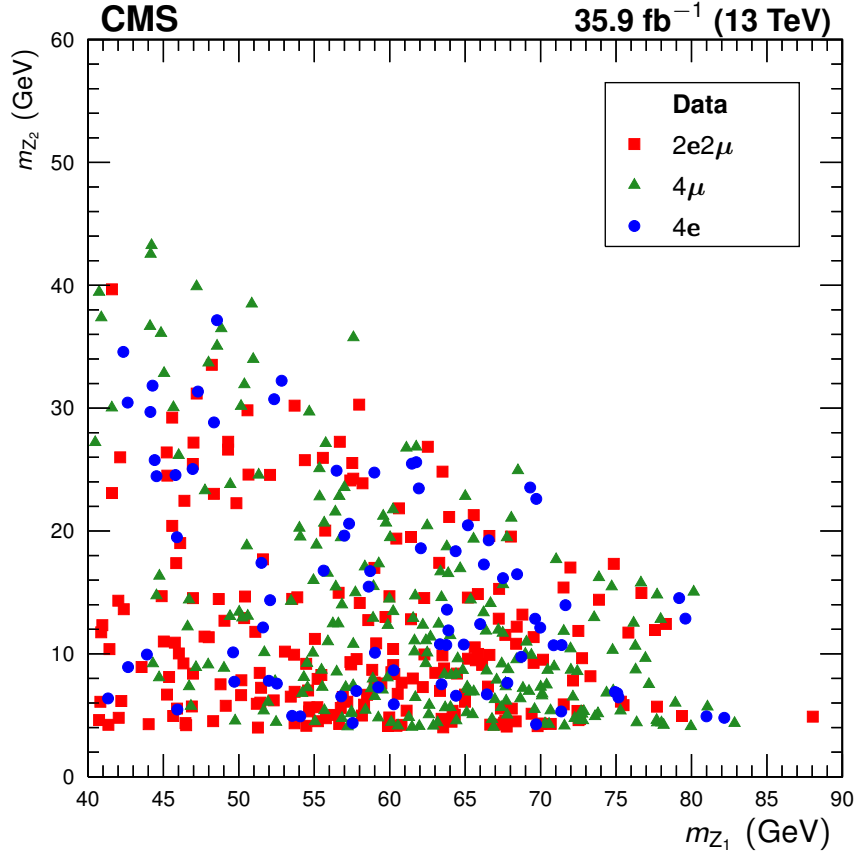


Figure 7.6: The reconstructed  $m_{Z_2}$  plotted against the reconstructed  $m_{Z_1}$  for all data events with  $80 < m_{4\ell} < 100$  GeV, with distinctive markers for each final state.

61  $m_{Z_2}$  against  $m_{Z_1}$ , for events in the same four-lepton mass region around the Higgs  
 62 resonance. Agreement between predictions and data is again good, allowing measure-  
 63 ments of Higgs boson properties, couplings, and production rates. These are beyond  
 64 the scope of this thesis, but were reported in Ref. [227].

#### 65 7.1.4 ZZ Production

66 Expected and observed yields for on-shell ZZ events are shown in Table 7.3. The corre-  
 67 sponding four-lepton and Z boson candidate invariant masses are shown in Figs. 7.11  
 68 and 7.12, respectively. Figure 7.13 shows the distribution of the number of jets ( $N_{\text{jets}}$ )

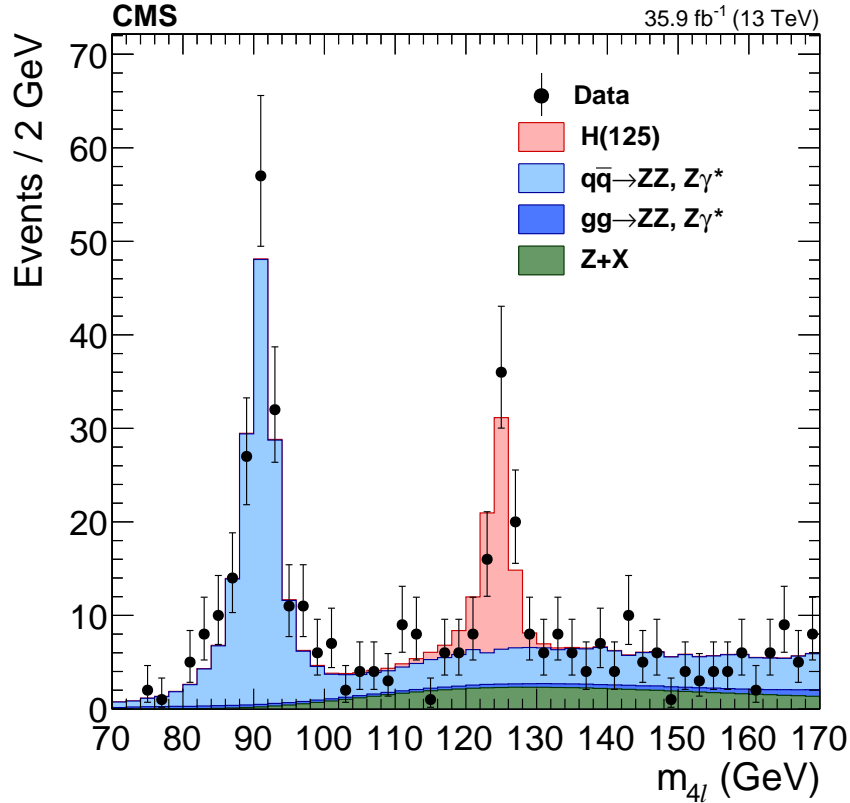


Figure 7.7: Distribution of the four-lepton invariant mass  $m_{4\ell}$  for events in the Higgs selection. Points represent data, with statistical uncertainty bars. The stack of filled histograms represents the signal and SM background predictions and the reducible background estimate.

Table 7.2: Observed and expected yields of  $H \rightarrow ZZ^* \rightarrow 4\ell$  events, including expected background yields, for events passing the Higgs selection in the mass range  $118 < m_{4\ell} < 130 \text{ GeV}$ , shown for each final state and summed to the total. Uncertainties are statistical and systematic combined.

Final state	Expected $N_H$	SM continuum background	$Z + X$	Total expected	Observed
$4\mu$	$21.6 \pm 1.9$	$9.4^{+0.6}_{-0.7}$	$4.7^{+2.0}_{-1.8}$	$35.8 \pm 2.9$	34
$2e2\mu$	$26.5 \pm 2.3$	$11.0^{+0.7}_{-0.8}$	$6.9^{+3.1}_{-2.9}$	$44.4^{+3.7}_{-3.6}$	41
4e	$10.2 \pm 1.1$	$3.6 \pm 0.3$	$1.9^{+0.8}_{-1.0}$	$15.8 \pm 1.6$	19
Total	$58.3 \pm 5.0$	$24.1^{+1.5}_{-1.6}$	$13.5^{+3.7}_{-3.5}$	$96.0 \pm 6.7$	94

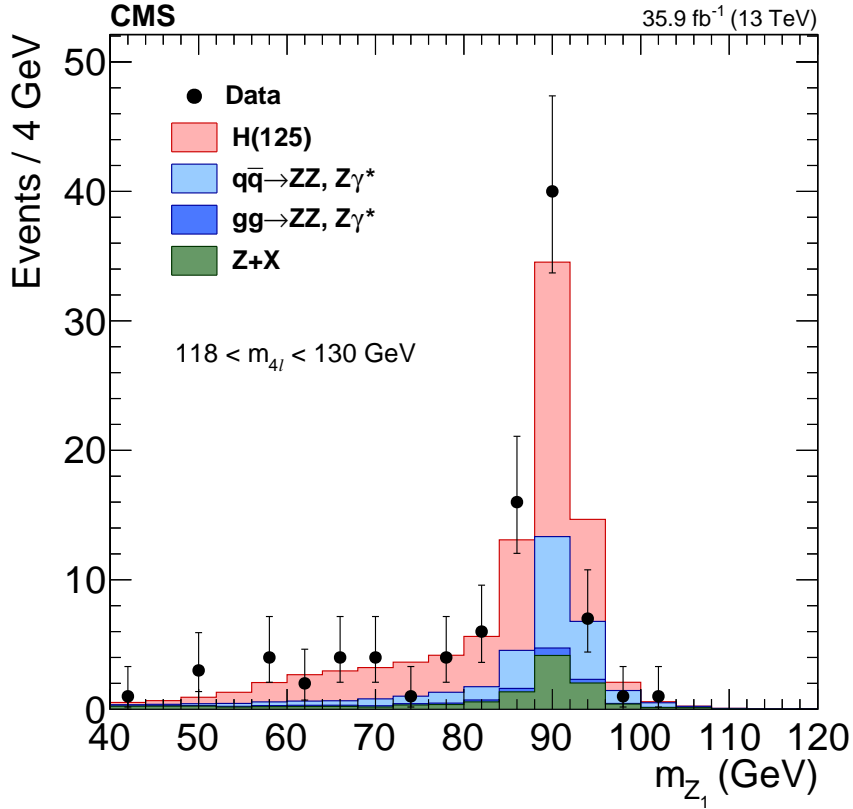


Figure 7.8: Distribution of the dilepton invariant mass of  $Z_1$ , the dilepton candidate in each event closest to the nominal  $m_Z$ , in events in the Higgs selection with  $118 < m_{4\ell} < 130 \text{ GeV}$ . Points represent data, with statistical uncertainty bars. The stack of filled histograms represents the signal and SM background predictions and the reducible background estimate.

in these events. The leading and subleading jet  $p_T$  are shown separately in Fig. 7.14, and the leading and subleading jet  $|\eta|$  are shown separately in Fig. 7.15, for all events with at least one (leading) or two (subleading) jets. Figures 7.16 and 7.17 show the  $m_{jj}$  and  $|\Delta\eta_{jj}|$  distributions for tagging jet pairs in the dijet selection. Again, agreement is good overall, indicating that the observables shown are well modeled up to the precision achievable with current data. These are the first such distributions published at  $\sqrt{s} = 13 \text{ TeV}$ , and statistical uncertainties are smaller than those published at any energy, allowing theorists to make more detailed comparisons to their models

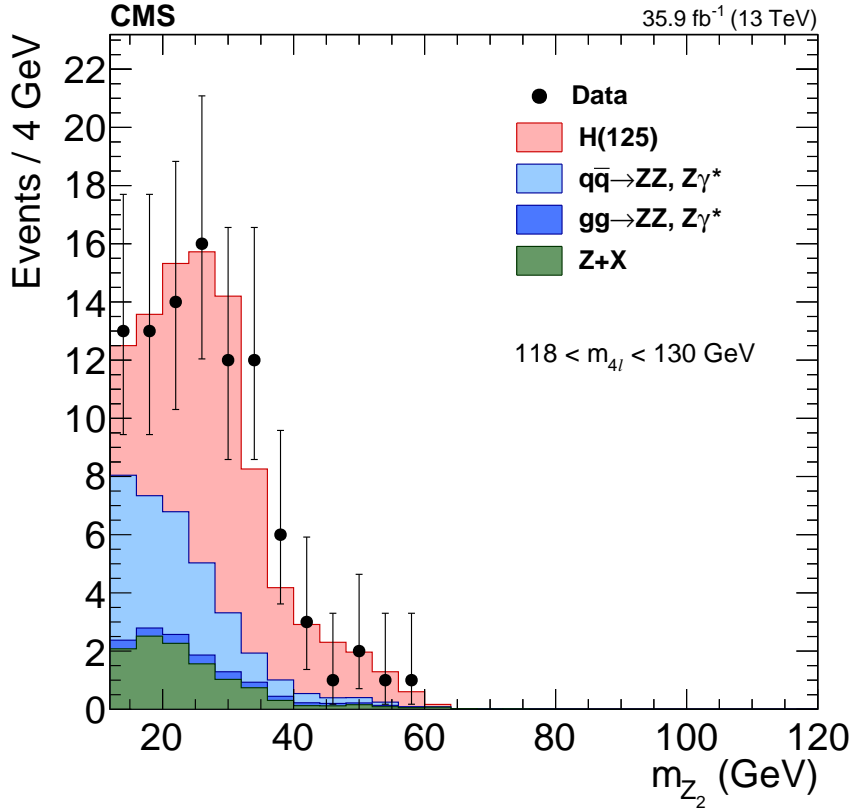


Figure 7.9: Distribution of the dilepton invariant mass of  $Z_2$ , the dilepton candidate in each event farther from the nominal  $m_Z$ , in events in the Higgs selection with  $118 < m_{4\ell} < 130 \text{ GeV}$ . Points represent data, with statistical uncertainty bars. The stack of filled histograms represents the signal and SM background predictions and the reducible background estimate.

77 and, in the case of the jet-related distributions, to QCD and shower modeling.

78 The yields shown in Table 7.3 and the systematic uncertainties of Table 6.1 are  
 79 used as inputs to the maximum likelihood method described in Section 6.3.1 to obtain  
 80 the on-shell ZZ signal strength across all four-lepton final states,

$$\mu = 1.040^{+0.033}_{-0.032} (\text{stat})^{+0.037}_{-0.035} (\text{syst}) \pm 0.026 (\text{lumi}), \quad (7.5)$$

81 which gives a fiducial cross section

$$\sigma_{\text{fid}}(\text{pp} \rightarrow \text{ZZ} \rightarrow 4\ell) = 40.9 \pm 1.3 (\text{stat}) \pm 1.4 (\text{syst}) \pm 1.0 (\text{lumi}) \text{ fb}, \quad (7.6)$$

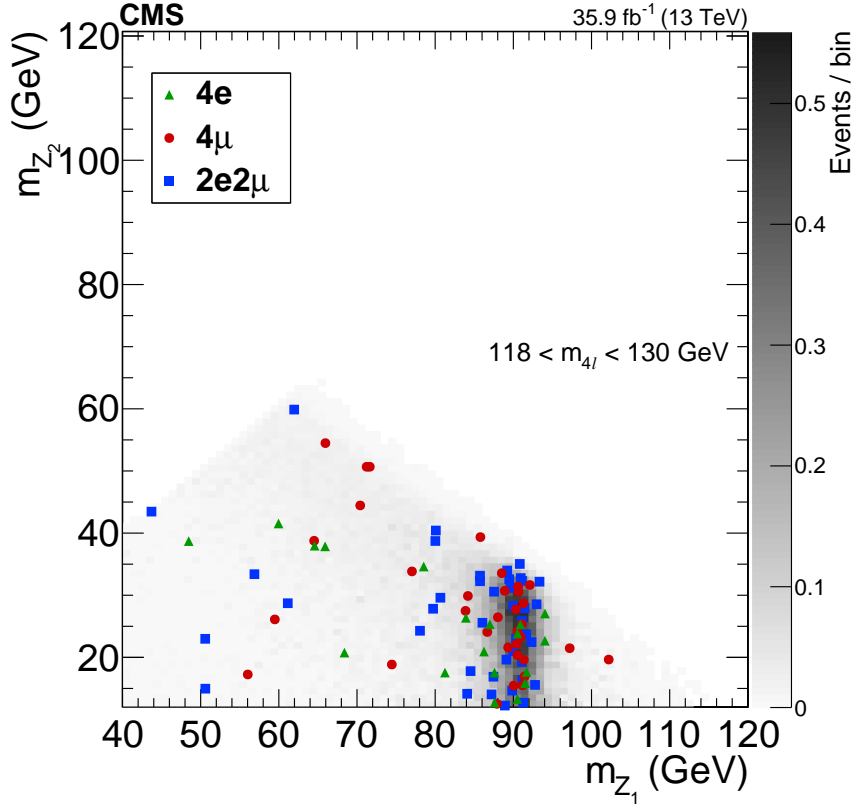


Figure 7.10: The reconstructed  $m_{Z_2}$  mass plotted against the reconstructed  $m_{Z_1}$  for data events in the Higgs selection with  $118 < m_{4\ell} < 130$  GeV, with distinctive markers for each final state. The shading represents the expected number of events in the bin.

Table 7.3: Observed and expected yields of ZZ events, including expected background yields, in the on-shell selection, shown for each final state and summed to the total. Uncertainties are statistical, then systematic, not including the integrated luminosity uncertainty.

Final state	Expected $N_{ZZ}$	Background	Total expected	Observed
$4\mu$	$301 \pm 2 \pm 9$	$10 \pm 1 \pm 2$	$311 \pm 2 \pm 9$	335
$2e2\mu$	$503 \pm 2 \pm 19$	$31 \pm 2 \pm 4$	$534 \pm 3 \pm 20$	543
4e	$205 \pm 1 \pm 12$	$20 \pm 2 \pm 2$	$225 \pm 2 \pm 13$	220
Total	$1009 \pm 3 \pm 36$	$60 \pm 3 \pm 8$	$1070 \pm 4 \pm 37$	1098

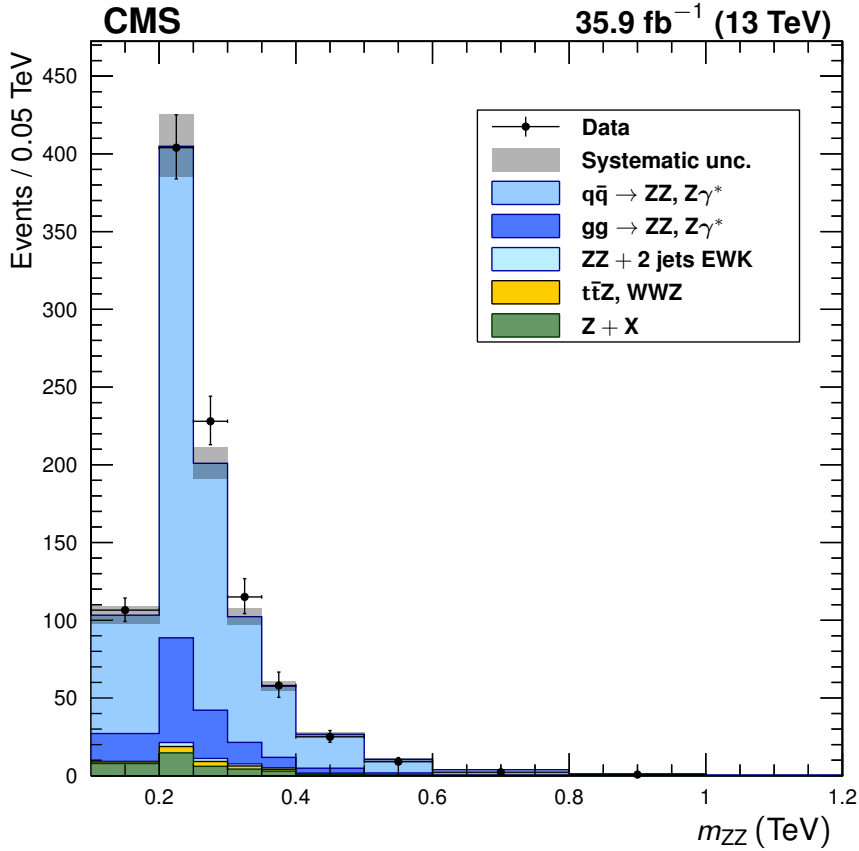


Figure 7.11: Distribution of the four-lepton invariant mass  $m_{ZZ}$  of all events in the on-shell selection. Points represent data, with statistical uncertainty bars. The stack of filled histograms represents the SM signal prediction and background estimate, with a grey band showing the sum in quadrature of the statistical and systematic uncertainties on the total expected yield.

82 in the  $ZZ \rightarrow 4\ell$  fiducial phase space of Table 6.2. The corresponding total cross  
 83 section is

$$\sigma(pp \rightarrow ZZ) = 17.5^{+0.6}_{-0.5} (\text{stat}) \pm 0.6 (\text{syst}) \pm 0.4 (\text{theo}) \pm 0.4 (\text{lumi}) \text{ pb.} \quad (7.7)$$

84 This measurement, on 2016 data, agrees with the result of the 2015 measure-  
 85 ment [222],

$$\sigma(pp \rightarrow ZZ) = 14.6^{+1.9}_{-1.8} (\text{stat})^{+0.3}_{-0.5} (\text{syst}) \pm 0.2 (\text{theo}) \pm 0.4 (\text{lumi}) \text{ pb.} \quad (7.8)$$

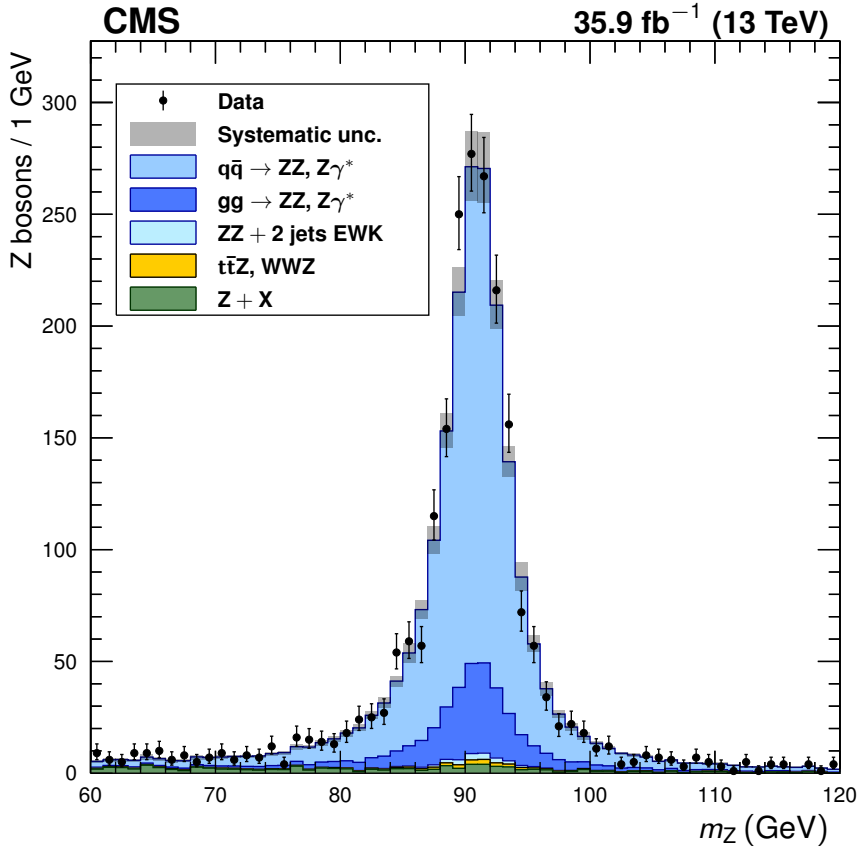


Figure 7.12: Distribution of the dilepton invariant mass of Z candidates in all events in the on-shell selection, regardless of whether the lepton pair is labeled  $Z_1$  or  $Z_2$ . Points represent data, with statistical uncertainty bars. The stack of filled histograms represents the SM signal prediction and background estimate, with a grey band showing the sum in quadrature of the statistical and systematic uncertainties on the total expected yield.

86 One may combine the measurements by doing a six-bin simultaneous fit with the bins  
 87 representing the same final state in 2015 and 2016 considered separately. The degree  
 88 of correlation between the systematic uncertainties in the 2015 and 2016 runs is not  
 89 known, but the 2015 contribution is small enough that the systematic uncertainties  
 90 are dominated by those in the 2016 dataset, and the degree of correlation will have  
 91 only a small effect on the measurement. We therefore do the fit twice, once treating  
 92 the experimental uncertainties as fully correlated between the datasets, and again

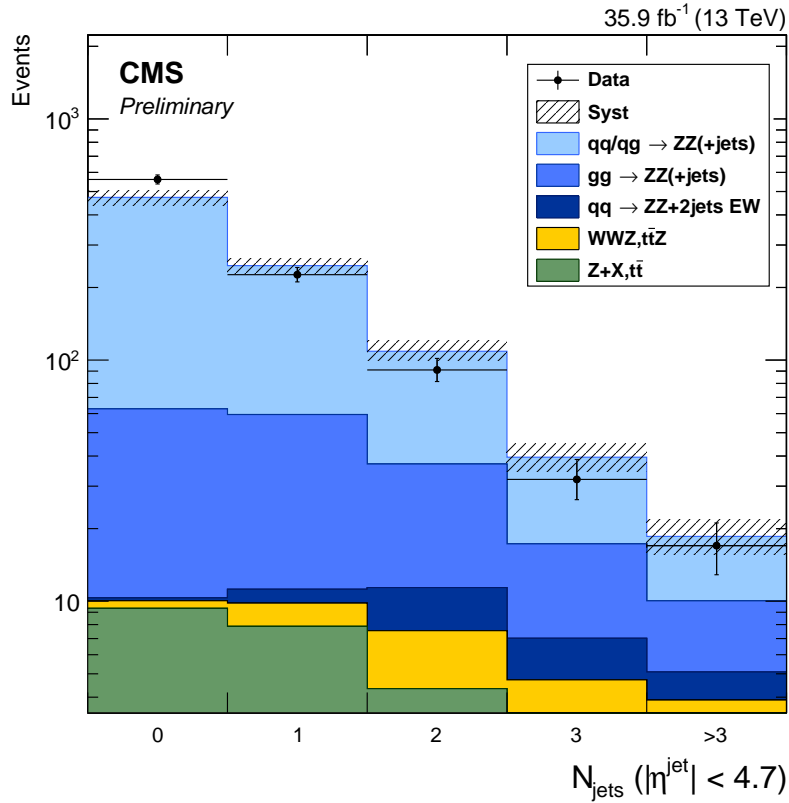


Figure 7.13: Distribution of jet multiplicity in ZZ events. Points represent data, with statistical uncertainty bars. The stack of filled histograms represents the SM signal prediction and background estimate, with a hatched band showing the sum in quadrature of the statistical and systematic uncertainties on the total expected yield.

93 treating them as fully uncorrelated. The small difference in the central value obtained  
 94 is added linearly to the systematic error of the result. After the full combination, the  
 95 “2015 + 2016” total cross section is found to be

$$\sigma(pp \rightarrow ZZ) = 17.2 \pm 0.5 \text{ (stat)} \pm 0.7 \text{ (syst)} \pm 0.4 \text{ (theo)} \pm 0.4 \text{ (lumi)} \text{ pb.} \quad (7.9)$$

96 These results can be compared to the MATRIX v1.0.0\_beta4 prediction of  $16.2^{+0.6}_{-0.4}$  pb,  
 97 computed at NNLO in QCD, or the MCFM v7.0 prediction of  $15.0^{+0.7}_{-0.6} \pm 0.2$  pb, cal-  
 98 culated at NLO in QCD with LO gg → ZZ diagrams included. Both predictions use  
 99 the NNPDF3.0 PDF sets and fixed scales  $\mu_F = \mu_R = m_Z$ .

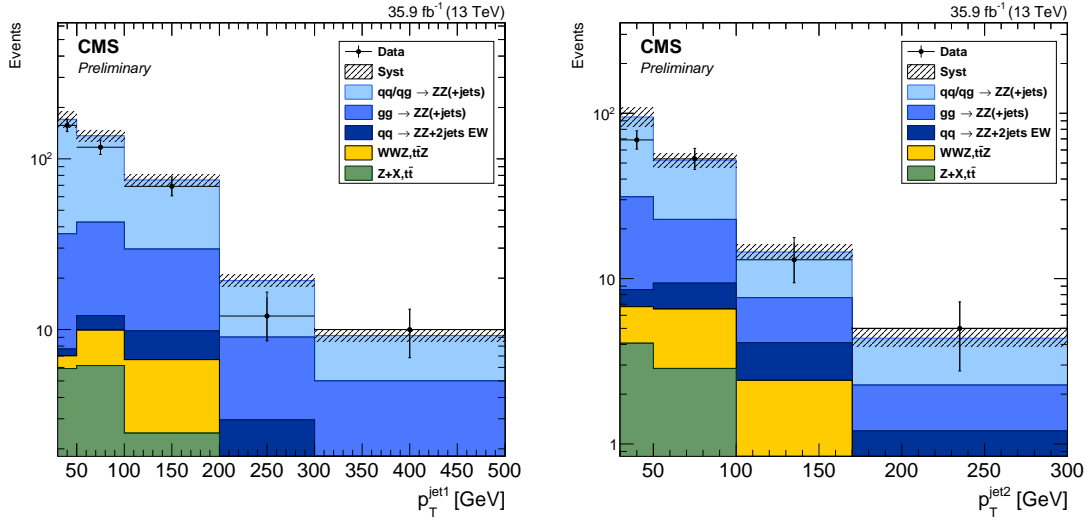


Figure 7.14: Distribution of leading (left) and subleading (right) jet  $p_T$  for all ZZ events with at least one jet and at least two jets, respectively. Points represent data, with statistical uncertainty bars. The stack of filled histograms represents the SM signal prediction and background estimate, with a hatched band showing the sum in quadrature of the statistical and systematic uncertainties on the total expected yield.

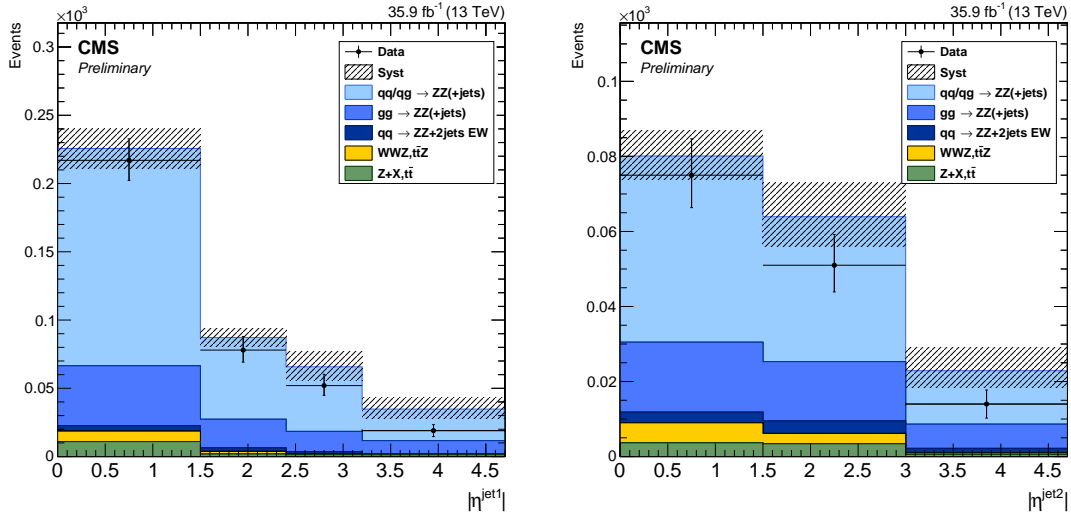


Figure 7.15: Distribution of leading (left) and subleading (right) jet  $|\eta|$  for all ZZ events with at least one jet and at least two jets, respectively. Points represent data, with statistical uncertainty bars. The stack of filled histograms represents the SM signal prediction and background estimate, with a hatched band showing the sum in quadrature of the statistical and systematic uncertainties on the total expected yield.

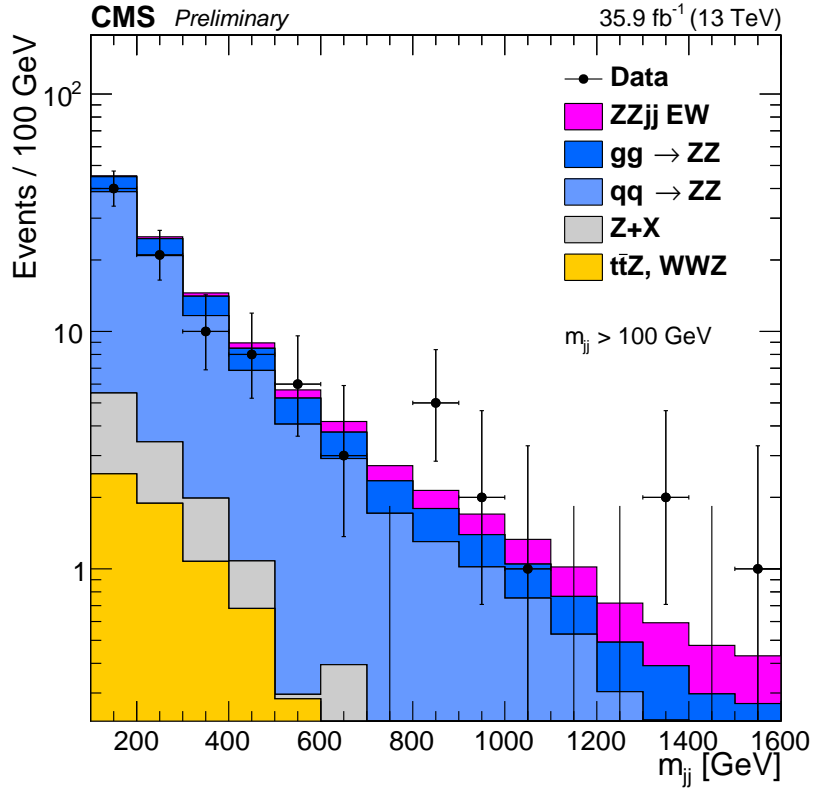


Figure 7.16: Dijet invariant mass  $m_{jj}$  of the tag jets in ZZ events passing the dijet selection ( $m_{jj} > 100$  GeV). Points represent data, with statistical uncertainty bars. The stack of filled histograms represents the SM signal prediction, including EWK production, and background estimate.

100        The total cross section is shown as a function of  $\sqrt{s}$  in Fig. 7.18. Measurements from CMS [72–74, 222] and ATLAS [76, 77, 108] are compared to NLO predictions made with MCFM (with contributions from leading order gluon-gluon fusion diagrams), and NNLO predictions made with MATRIX. Results from both experiments agree with the predictions, verifying this aspect of the SM to within the measurements’ uncertainties.

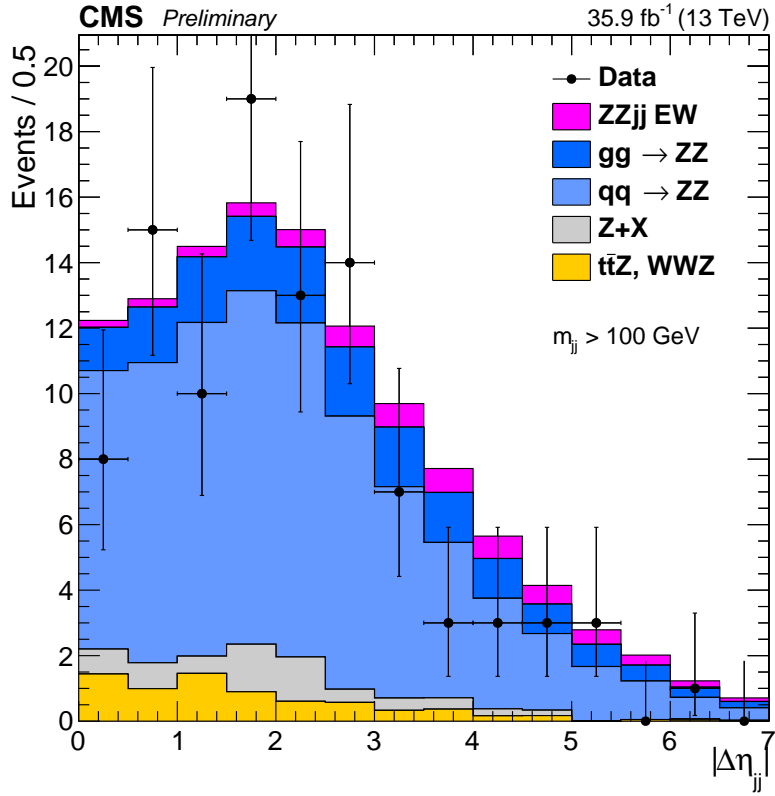


Figure 7.17: Pseudorapidity separation  $|\Delta\eta_{jj}|$  of tag jets in ZZ events passing the dijet selection ( $m_{jj} > 100 \text{ GeV}$ ). Points represent data, with statistical uncertainty bars. The stack of filled histograms represents the SM signal prediction, including EWK production, and background estimate.

## <sup>106</sup> 7.2 Differential Cross Sections

<sup>107</sup> Detector-level distributions are unfolded to calculate differential cross sections as de-  
<sup>108</sup> scribed in Section 6.4. Figures 7.19–7.30 show measured differential cross sections  
<sup>109</sup> and corresponding theory predictions, as functions of different observables. All dis-  
<sup>110</sup> tributions are normalized to the inclusive fiducial cross section, such that the integral  
<sup>111</sup> of each is unity, including overflow bins (not shown). The observables in Figs. 7.19–  
<sup>112</sup> 7.24 consider only the four-lepton system. For the calculation of these distributions,  
<sup>113</sup> as well as the differential cross section as a function of  $N_{\text{jets}}$  (Fig. 7.25), all events

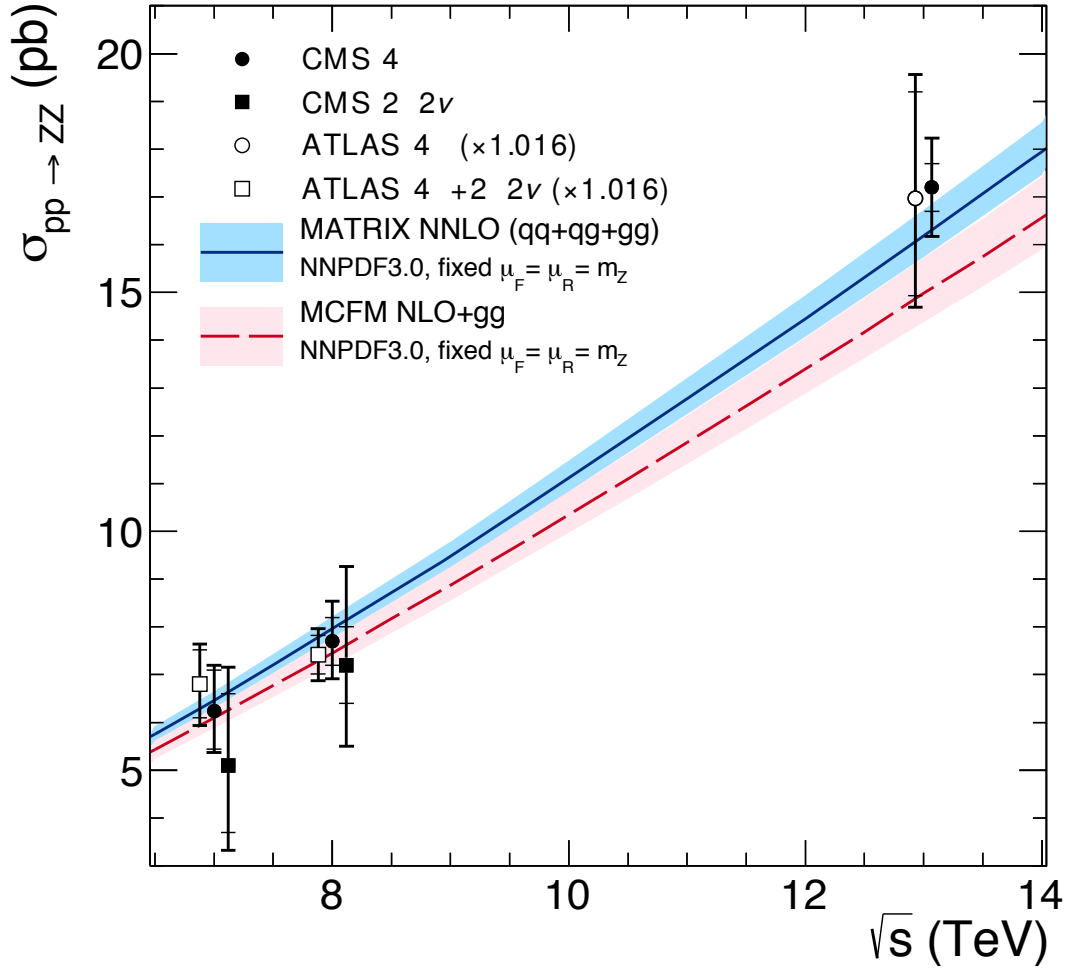


Figure 7.18: The total ZZ cross section is shown as a function of  $\sqrt{s}$ . Measurements from CMS and ATLAS are both shown, with the ATLAS numbers adjusted upward by 1.6% to account for differences in Z mass window choice. Points at the same center-of-mass energy are shifted slightly in the horizontal direction for clarity. Experimental measurements are compared to predictions from MCFM at NLO in QCD with additional contributions from LO gluon-gluon fusion diagrams, and MATRIX at NNLO in QCD. Both sets of predictions use the NNPDF3.0 PDF sets and fixed scales  $\mu_F = \mu_R = m_Z$ .

114 passing the on-shell selection of Table 6.2 are used. Figures 7.26 and 7.27 show  $m_{jj}$   
 115 and  $|\Delta\eta_{jj}|$  for all ZZ events with at least two jets, while Figs 7.28 and 7.29 show  $p_T$   
 116 and  $\eta$ , respectively, for the leading jet in events with  $N_{jets} \geq 1$  on the left and the  
 117 subleading jet in events with  $N_{jets} \geq 2$  on the right. In Fig. 7.30, the phase space is  
 118 expanded to the full spectrum selection of Table 6.2 at both detector and true level,  
 119 to show the four-lepton differential cross section through all production modes as a  
 120 function of  $m_{4\ell}$ . Measured cross sections overall agree with the theoretical predictions  
 121 within their uncertainties, which are dominated by statistical uncertainties in all bins.

### 122 **7.3 Vector Boson Scattering**

123 Figure 7.31 shows the output of the GBDT discussed in Section 6.5 for events in  
 124 the dijet selection. The search procedure finds a modest excess of events compatible  
 125 with VBS ZZjj signal, at the level of 2.7 standard deviations over the null hypothesis  
 126 of the SM without VBS ZZ production. The expected significance is 1.6 standard  
 127 deviations. This corresponds to a VBS fiducial cross section of

$$\sigma_{fid}(pp \rightarrow ZZjj(EWK) \rightarrow 4\ell jj) = 0.40^{+0.21}_{-0.16} (\text{stat})^{+0.13}_{-0.09} (\text{syst}) \text{ fb}, \quad (7.10)$$

128 which is consistent with the SM prediction of  $0.29^{+0.02}_{-0.03}$  fb.

### 129 **7.4 Anomalous Coupling Limits**

130 The ZZ invariant mass is shown in Fig. 7.32 for all events in the on-shell selection,  
 131 with two example distributions shown for potential scenarios with nonzero aTGCs,  
 132 one of which sets  $f_5^\gamma = 0.0019$  and  $f_5^Z = 0.0015$ , and the other  $f_4^\gamma = 0.0019$  and  
 133  $f_4^Z = 0.0015$ . The limit setting procedure described in Section 6.6 is applied to  
 134 each aTGC parameter, with all other couplings fixed to their SM values, to yield

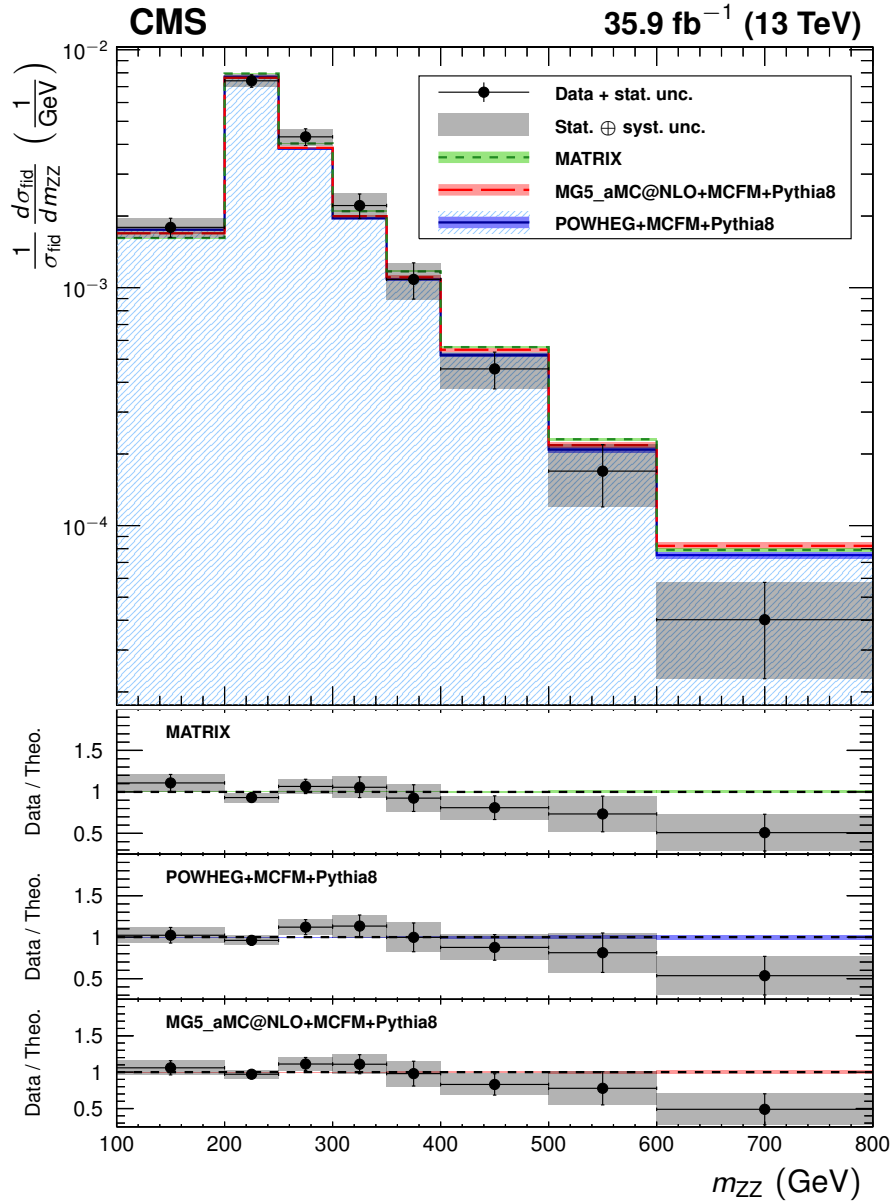


Figure 7.19: The ZZ differential cross section as a function of  $m_{ZZ}$ , normalized to the inclusive fiducial cross section. Points represent the unfolded data, with vertical bars showing the statistical uncertainty and a grey band showing the sum in quadrature of the statistical and systematic uncertainties. Blue, red, and green histograms represent the POWHEG+MCFM, MADGRAPH5\_aMC@NLO+MCFM, and MATRIX predictions, respectively, with bands around each which represent their combined statistical, scale, and PDF uncertainties. The lower sections of the plot represents the ratio of the measured cross section to each of the predictions.

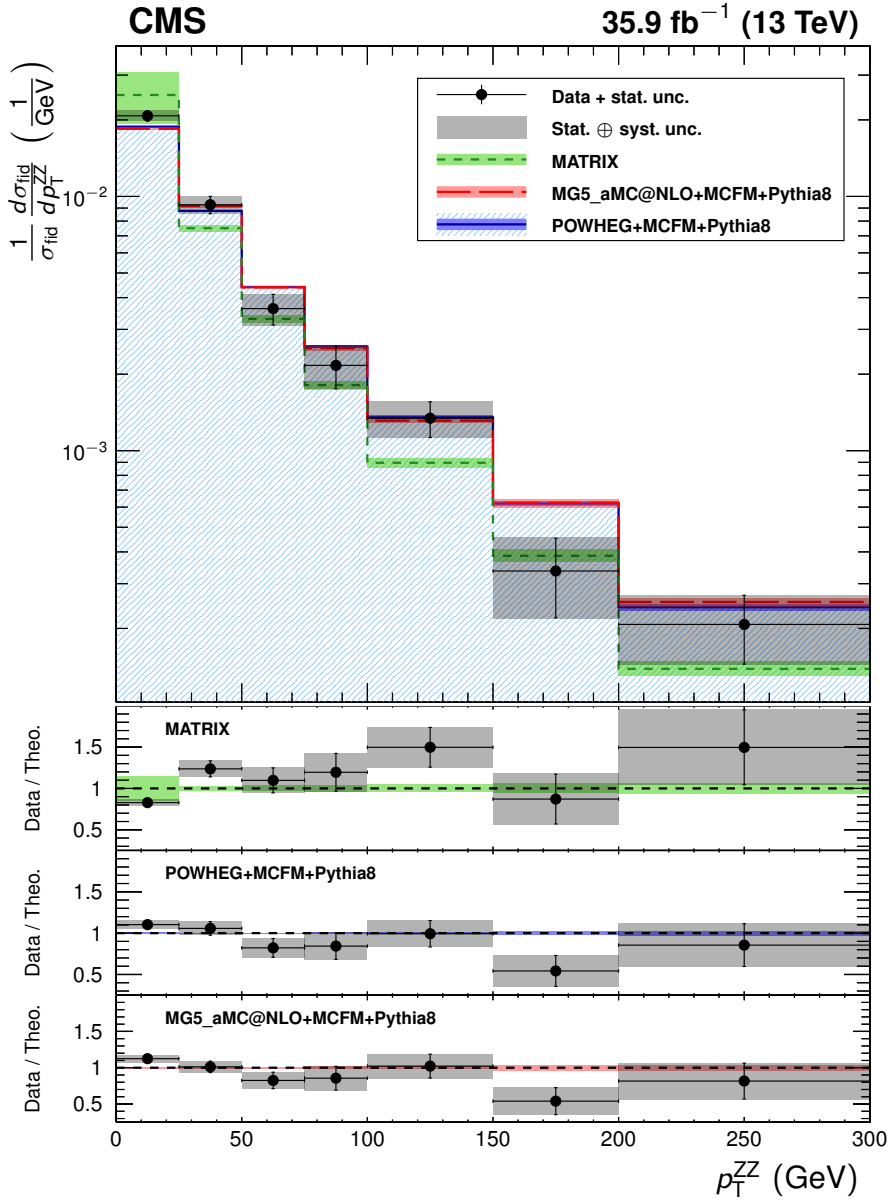


Figure 7.20: The ZZ differential cross section as a function of the four-lepton  $p_T$ , normalized to the inclusive fiducial cross section. Points represent the unfolded data, with vertical bars showing the statistical uncertainty and a grey band showing the sum in quadrature of the statistical and systematic uncertainties. Blue, red, and green histograms represent the POWHEG+MCFM, MADGRAPH5\_aMC@NLO+MCFM, and MATRIX predictions, respectively, with bands around each which represent their combined statistical, scale, and PDF uncertainties. The lower sections of the plot represents the ratio of the measured cross section to each of the predictions.

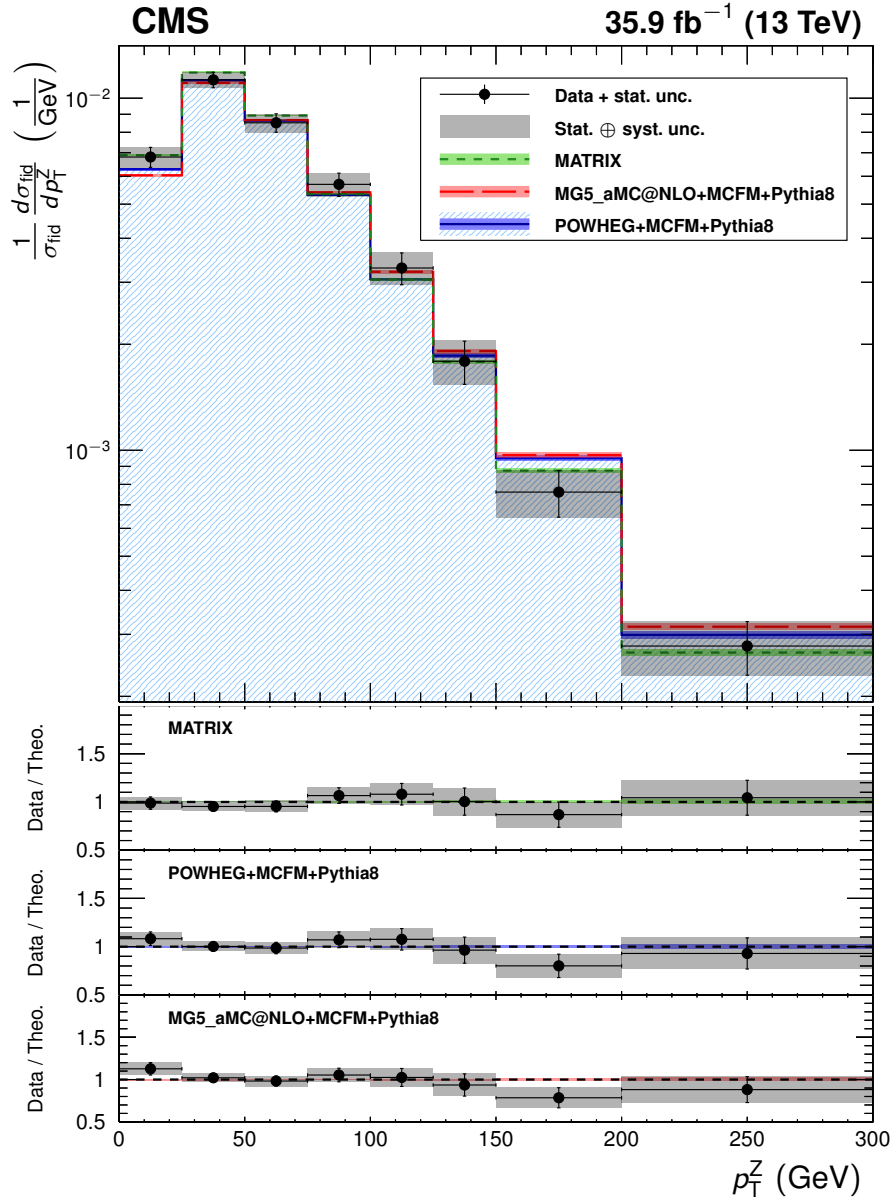


Figure 7.21: The ZZ differential cross section as a function of the  $p_T$  of both Z boson candidates, regardless of which one is  $Z_1$  and which is  $Z_2$ , normalized to the inclusive fiducial cross section. Points represent the unfolded data, with vertical bars showing the statistical uncertainty and a grey band showing the sum in quadrature of the statistical and systematic uncertainties. Blue, red, and green histograms represent the POWHEG+MCFM, MADGRAPH5\_aMC@NLO+MCFM, and MATRIX predictions, respectively, with bands around each which represent their combined statistical, scale, and PDF uncertainties. The lower sections of the plot represents the ratio of the measured cross section to each of the predictions.

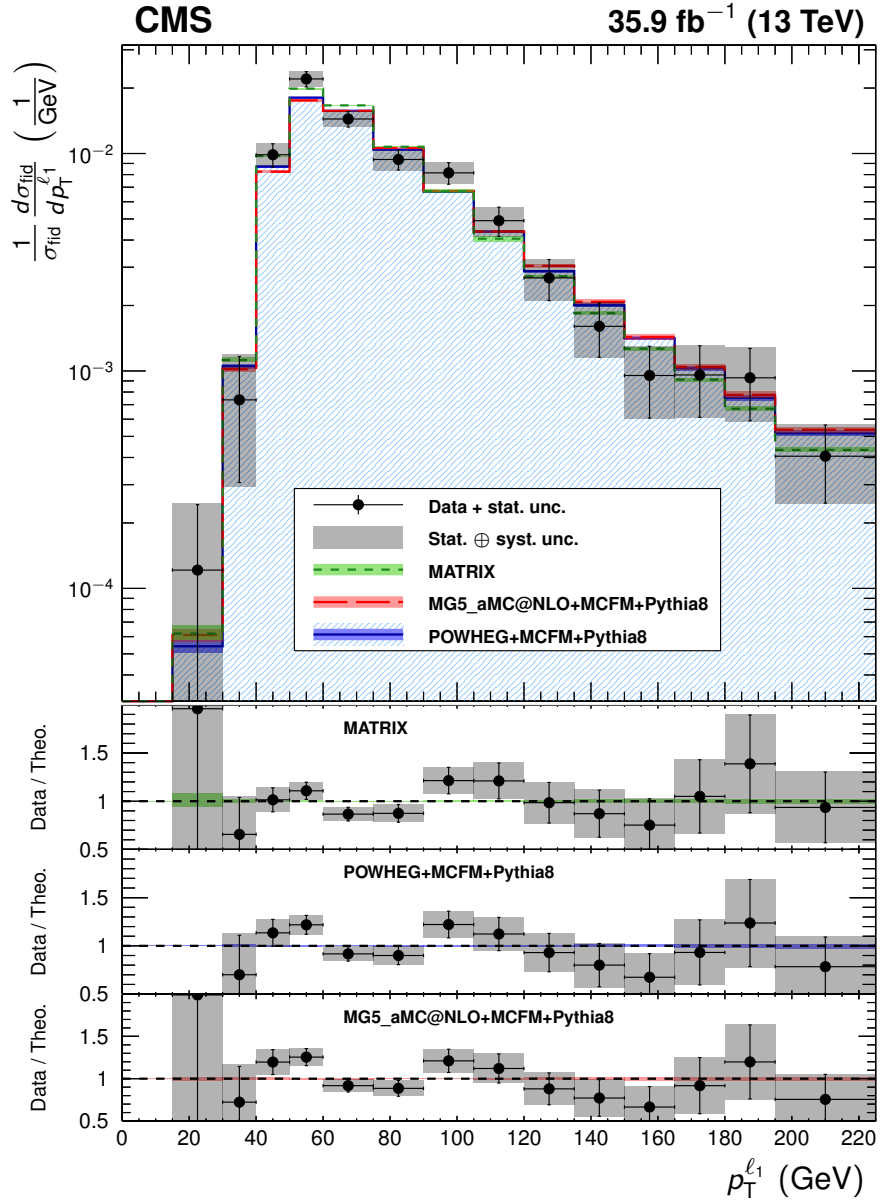


Figure 7.22: The ZZ differential cross section as a function of leading lepton  $p_T$ , normalized to the inclusive fiducial cross section. Points represent the unfolded data, with vertical bars showing the statistical uncertainty and a grey band showing the sum in quadrature of the statistical and systematic uncertainties. Blue, red, and green histograms represent the POWHEG+MCFM, MADGRAPH5\_aMC@NLO+MCFM, and MATRIX predictions, respectively, with bands around each which represent their combined statistical, scale, and PDF uncertainties. The lower sections of the plot represents the ratio of the measured cross section to each of the predictions.

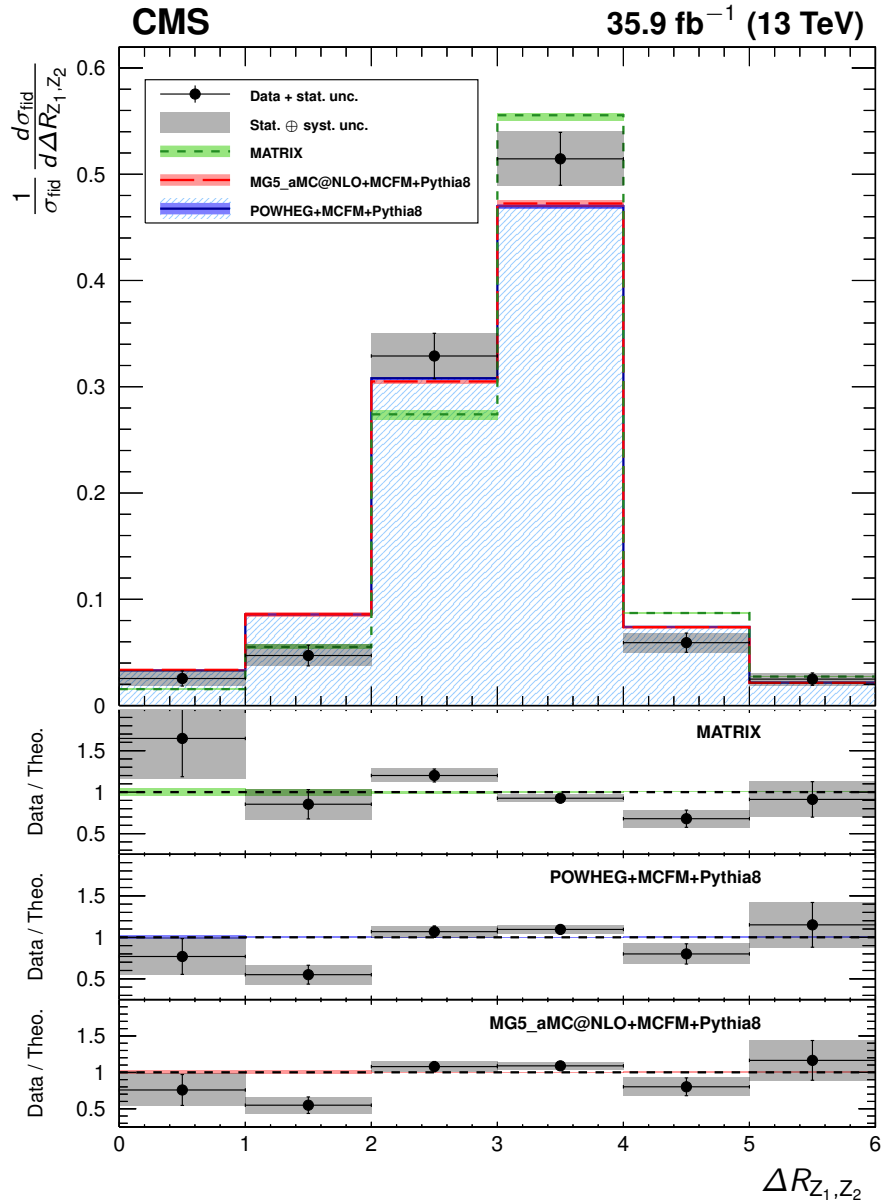


Figure 7.23: The ZZ differential cross section as a function of  $\Delta R$  between the two Z bosons, normalized to the inclusive fiducial cross section. Points represent the unfolded data, with vertical bars showing the statistical uncertainty and a grey band showing the sum in quadrature of the statistical and systematic uncertainties. Blue, red, and green histograms represent the POWHEG+MCFM, MADGRAPH-5\_amc@NLO+MCFM, and MATRIX predictions, respectively, with bands around each which represent their combined statistical, scale, and PDF uncertainties. The lower sections of the plot represents the ratio of the measured cross section to each of the predictions.

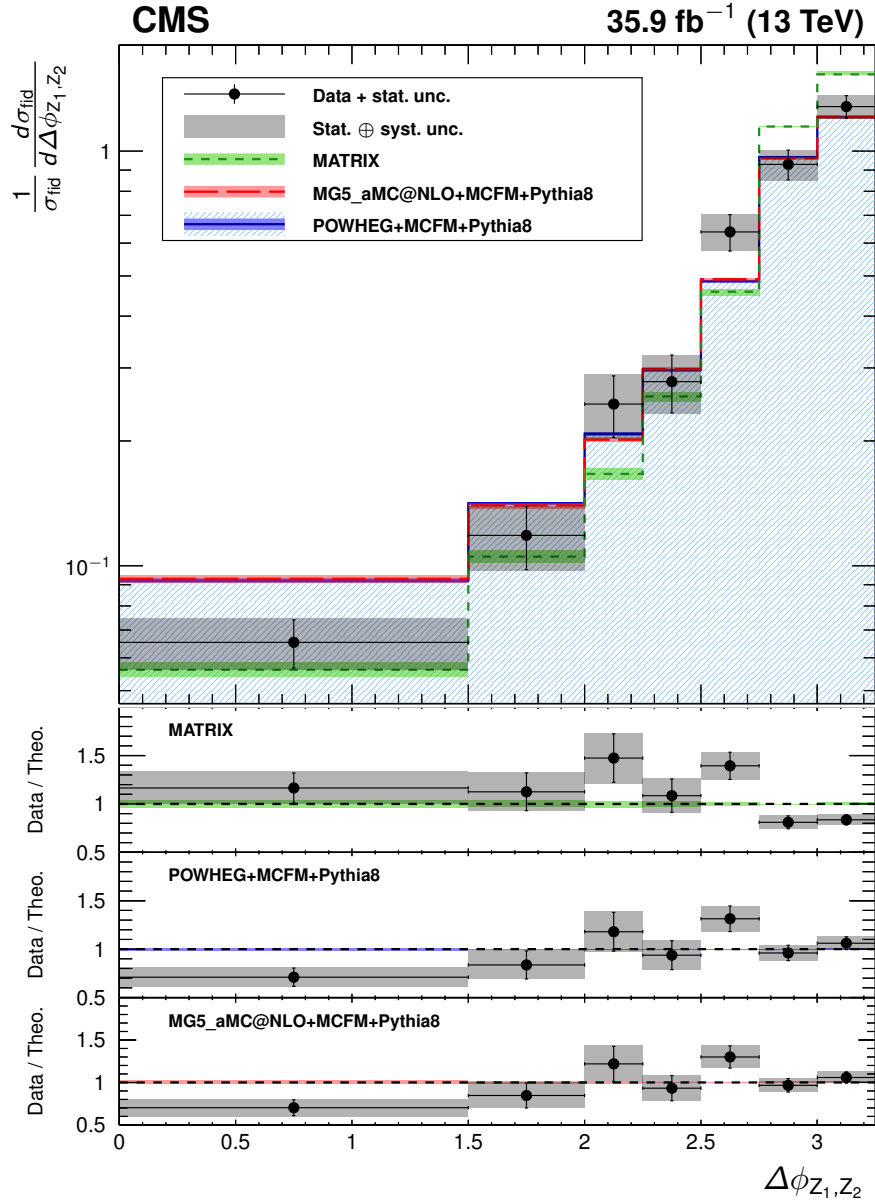


Figure 7.24: The ZZ differential cross section as a function of  $\Delta\phi$  between the two Z bosons, normalized to the inclusive fiducial cross section. Points represent the unfolded data, with vertical bars showing the statistical uncertainty and a grey band showing the sum in quadrature of the statistical and systematic uncertainties. Blue, red, and green histograms represent the POWHEG+MCFM, MADGRAPH-5\_aMC@NLO+MCFM, and MATRIX predictions, respectively, with bands around each which represent their combined statistical, scale, and PDF uncertainties. The lower sections of the plot represents the ratio of the measured cross section to each of the predictions.

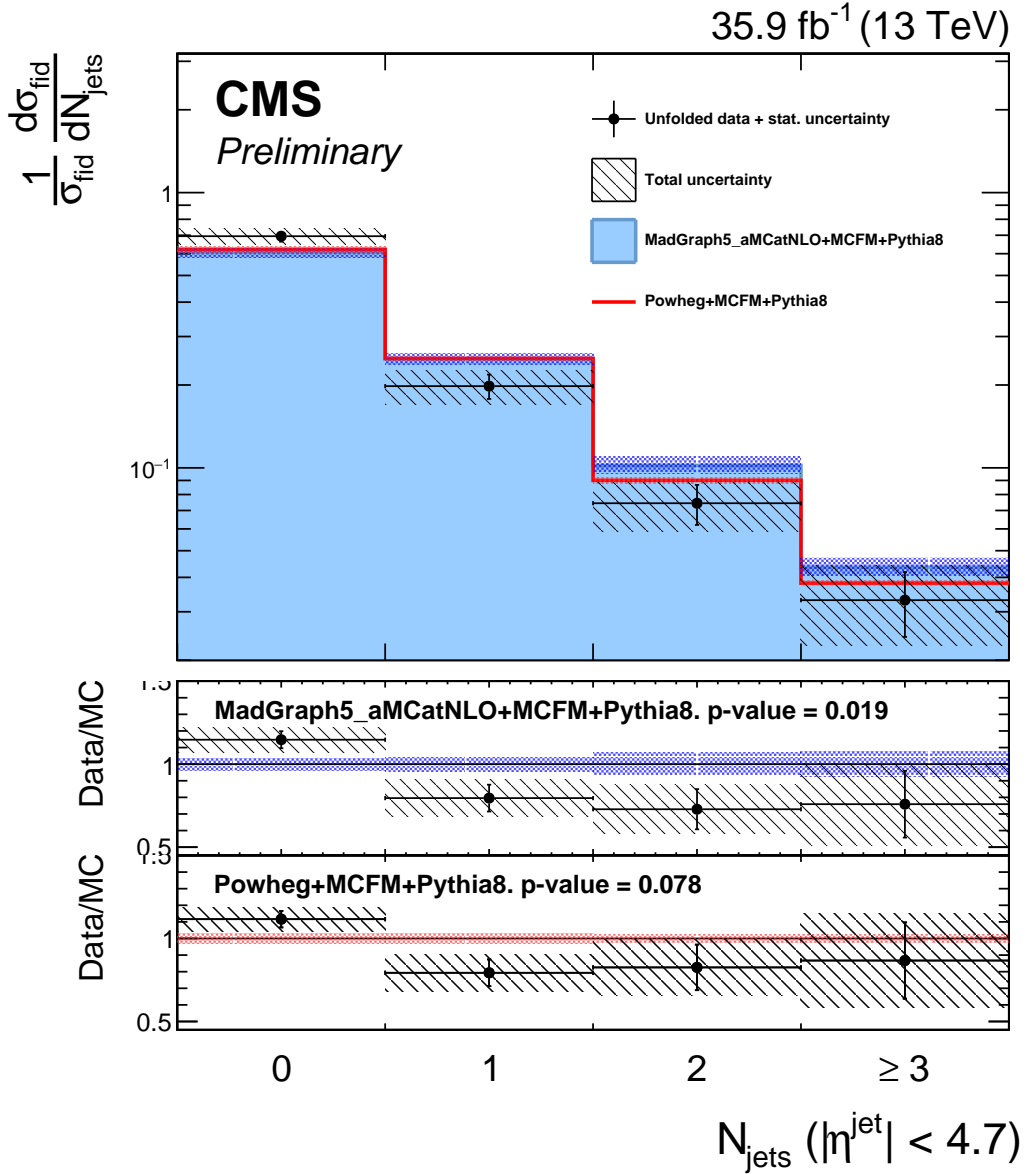


Figure 7.25: The ZZ differential cross section as a function of the jet multiplicity  $N_{\text{jets}}$ , normalized to the inclusive fiducial cross section. Points represent the unfolded data, with vertical bars showing the statistical uncertainty and a hatched band showing the sum in quadrature of the statistical and systematic uncertainties. Red and blue histograms represent the POWHEG+MCFM and MADGRAPH5\_aMC@NLO+MCFM predictions, respectively, with bands around each which represent their combined statistical, scale, and PDF uncertainties. The lower sections of the plot represents the ratio of the measured cross section to each of the predictions.

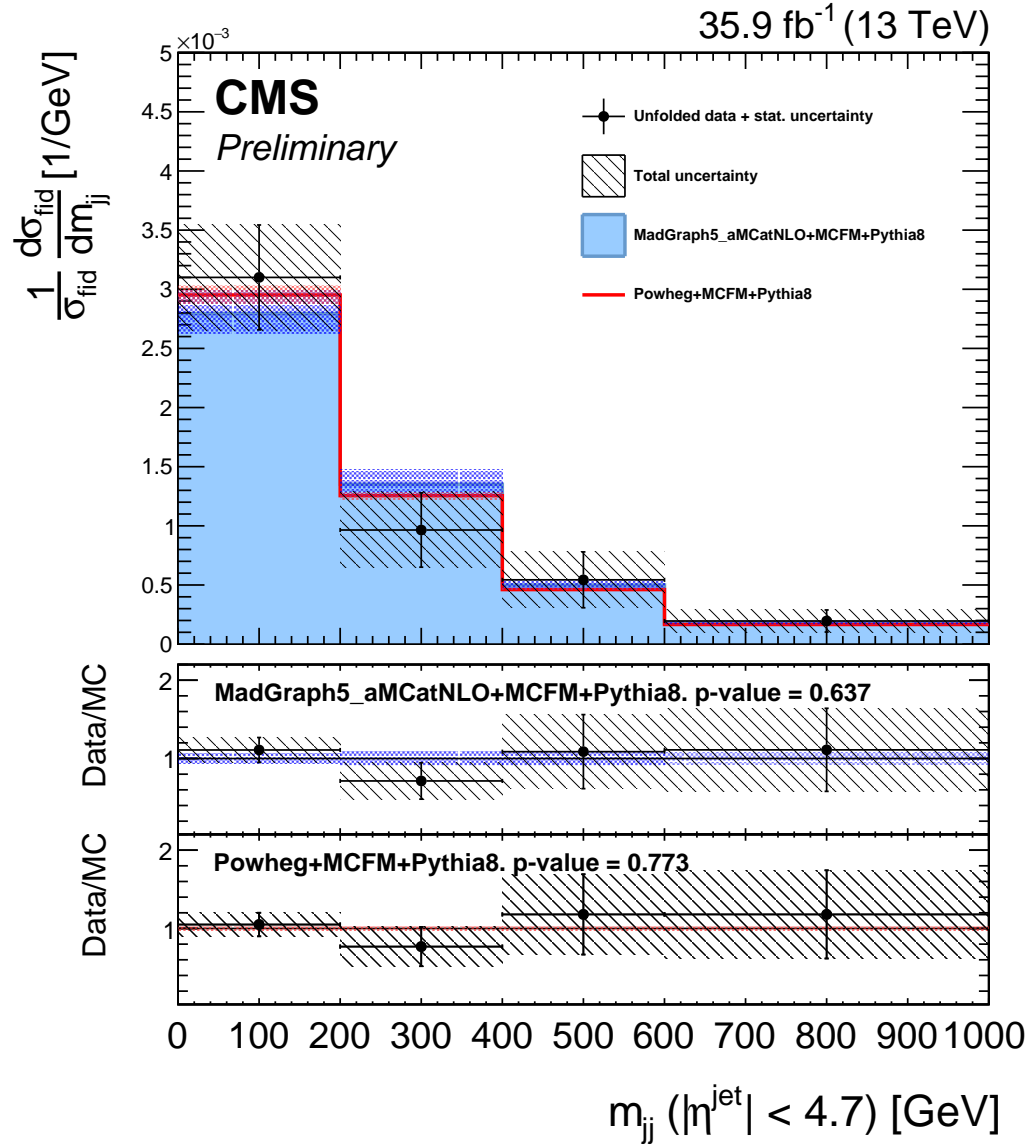


Figure 7.26: The ZZ differential cross section as a function of the invariant mass of the two highest- $p_T$  jets  $m_{jj}$ , including all ZZ events with at least two jets, normalized to the inclusive fiducial cross section. Points represent the unfolded data, with vertical bars showing the statistical uncertainty and a hatched band showing the sum in quadrature of the statistical and systematic uncertainties. Red and blue histograms represent the POWHEG+MCFM and MADGRAPH5\_aMC@NLO+MCFM predictions, respectively, with bands around each which represent their combined statistical, scale, and PDF uncertainties. The lower sections of the plot represents the ratio of the measured cross section to each of the predictions.

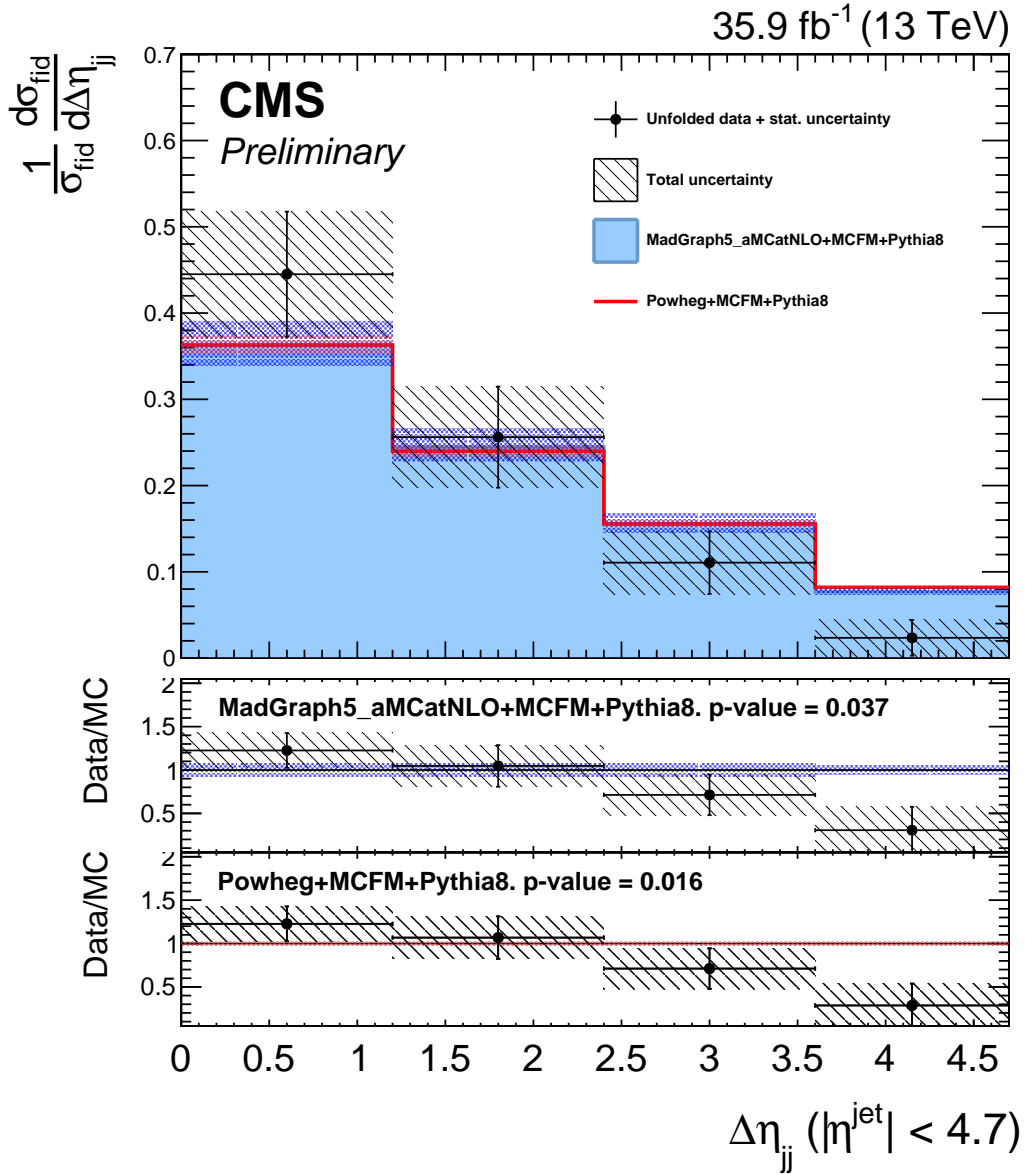


Figure 7.27: The ZZ differential cross section as a function of the absolute pseudo-rapidity separation of the two highest- $p_T$  jets  $|\Delta\eta_{jj}|$ , including all ZZ events with at least two jets, normalized to the inclusive fiducial cross section. Points represent the unfolded data, with vertical bars showing the statistical uncertainty and a hatched band showing the sum in quadrature of the statistical and systematic uncertainties. Red and blue histograms represent the POWHEG+MCFM and MADGRAPH5\_aMC@NLO+MCFM predictions, respectively, with bands around each which represent their combined statistical, scale, and PDF uncertainties. The lower sections of the plot represents the ratio of the measured cross section to each of the predictions.

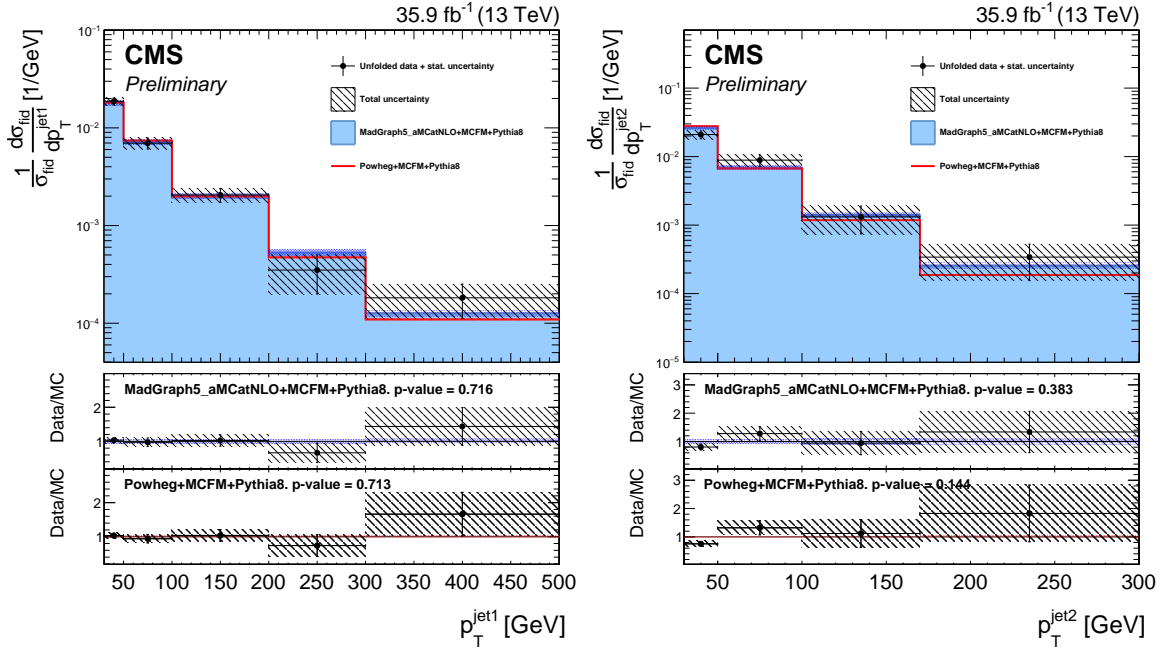


Figure 7.28: The ZZ differential cross section as a function of the leading (left) and subleading (right) jet  $p_T$ , in ZZ events with at least one jet and at least two jets respectively, normalized to the inclusive fiducial cross section. Points represent the unfolded data, with vertical bars showing the statistical uncertainty and a hatched band showing the sum in quadrature of the statistical and systematic uncertainties. Red and blue histograms represent the POWHEG+MCFM and MADGRAPH5\_aMC@NLO+MCFM predictions, respectively, with bands around each which represent their combined statistical, scale, and PDF uncertainties. The lower sections of the plots represent the ratio of the measured cross section to each of the predictions.

135 one-dimensional 95% CL limits,

$$\begin{aligned} -0.0012 < f_4^Z < 0.0010, \quad -0.0010 < f_5^Z < 0.0013, \\ -0.0012 < f_4^\gamma < 0.0013, \quad -0.0012 < f_5^\gamma < 0.0013. \end{aligned} \tag{7.11}$$

136 These results improve the previous CMS limits, which were the most stringent set  
 137 previously, by factors of 2–3 [74] and are the most stringent limits to date on the  
 138 parameters in question. Recent preliminary limits from ATLAS using 13 TeV data  
 139 are 50–80% looser [229]. Two-dimensional limits are set in the  $f_4^\gamma$ - $f_4^Z$  and  $f_5^\gamma$ - $f_5^Z$   
 140 planes, holding all other parameters to the SM values in each calculation. One- and

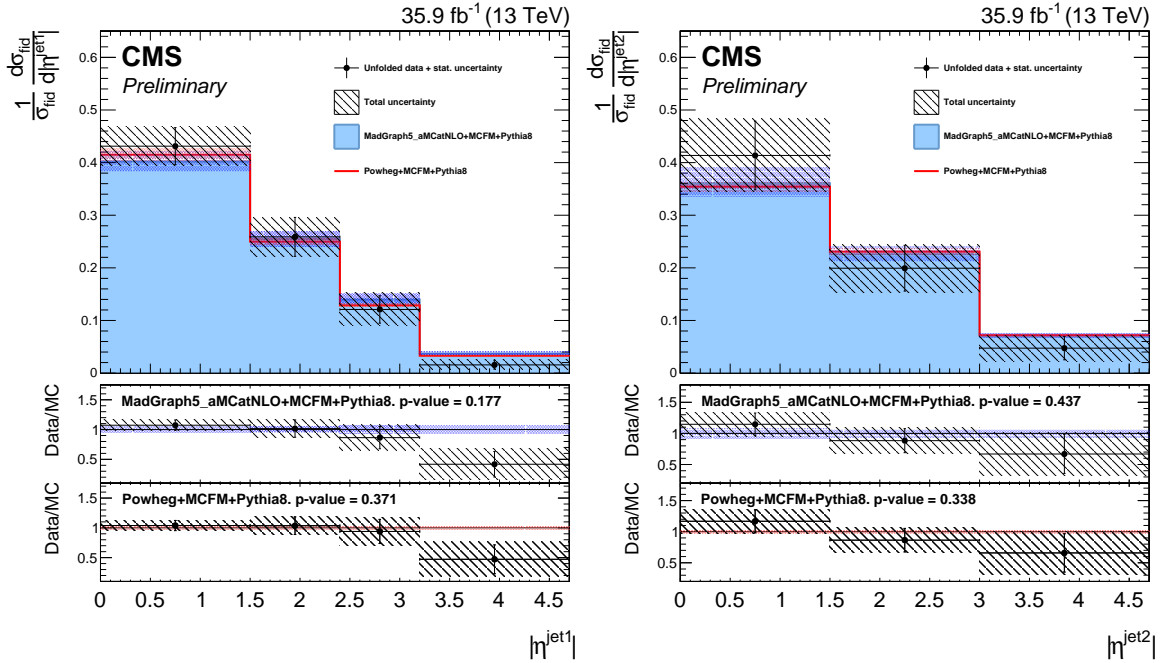


Figure 7.29: The ZZ differential cross section as a function of the leading (left) and subleading (right) jet  $\eta$ , in ZZ events with at least one jet and at least two jets respectively, normalized to the inclusive fiducial cross section. Points represent the unfolded data, with vertical bars showing the statistical uncertainty and a hatched band showing the sum in quadrature of the statistical and systematic uncertainties. Red and blue histograms represent the POWHEG+MCFM and MADGRAPH5\_aMC@NLO+MCFM predictions, respectively, with bands around each which represent their combined statistical, scale, and PDF uncertainties. The lower sections of the plots represent the ratio of the measured cross section to each of the predictions.

141 two-dimensional 95% CL limits are shown in Fig. 7.33.

142 No unitarizing form factor (c.f. Section 1.5.1) is applied when calculating the  
 143 limits of Eq. (7.11). One way to enforce unitarity without a form factor would be  
 144 to restrict the maximum ZZ invariant mass used, and set the limits considering only  
 145 events with  $m_{ZZ}$  below some cutoff. The limits would then depend on the cutoff  
 146 chosen, converging to the nonunitary limits when the cutoff is larger than the energies  
 147 accessible in the experiment. The limit computations are repeated with multiple  
 148 cutoff values, and the resulting expected and observed limits are shown in Fig. 7.34

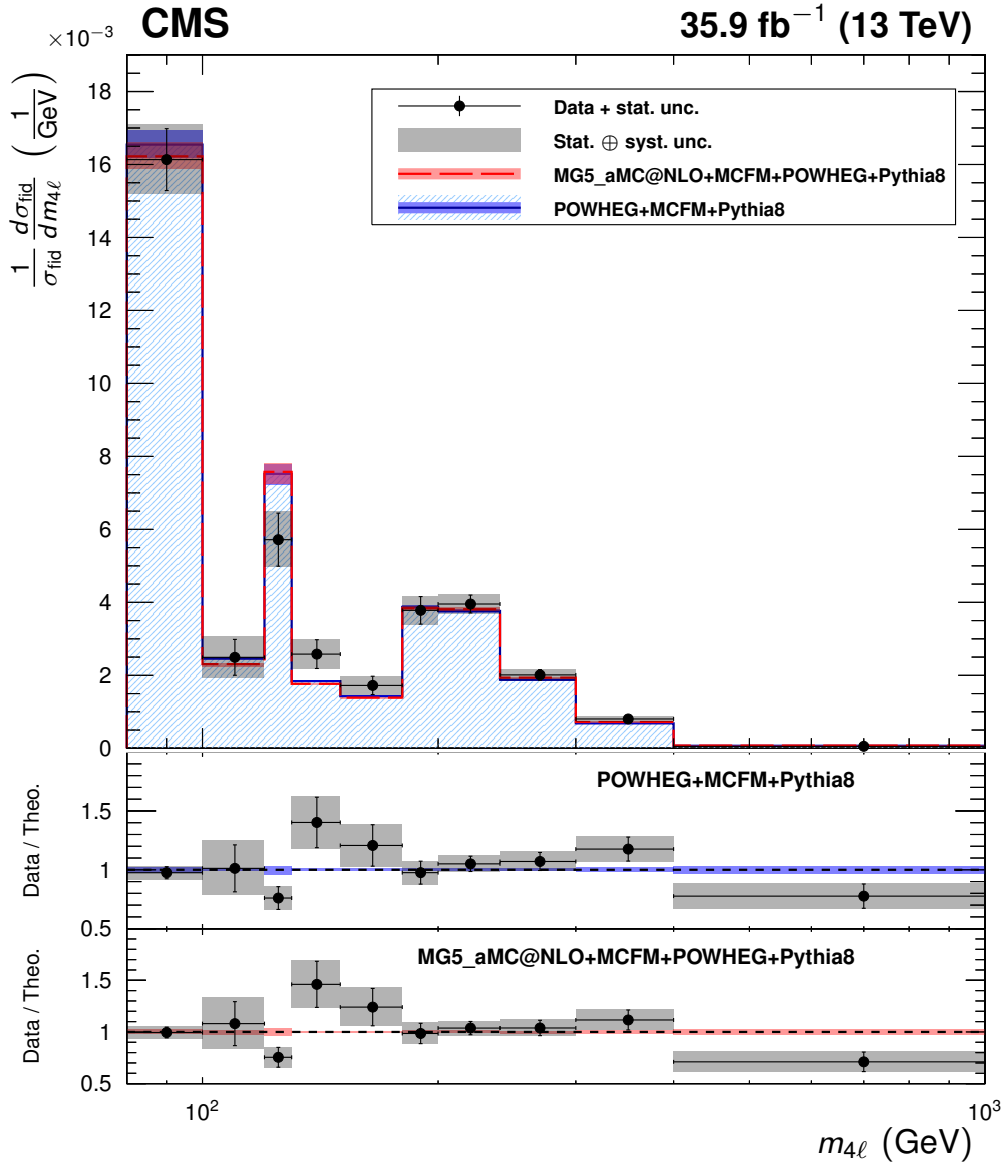


Figure 7.30: The four-lepton differential cross section as a function of  $m_{4\ell}$  under the full spectrum selections, normalized to the inclusive fiducial cross section. Points represent the unfolded data, with vertical bars showing the statistical uncertainty and a grey band showing the sum in quadrature of the statistical and systematic uncertainties. Blue and red histograms represent the POWHEG+MCFM and MADGRAPH5\_aMC@NLO+MCFM predictions, respectively, with bands around each which represent their combined statistical, scale, and PDF uncertainties. The lower sections of the plot represents the ratio of the measured cross section to each of the predictions.

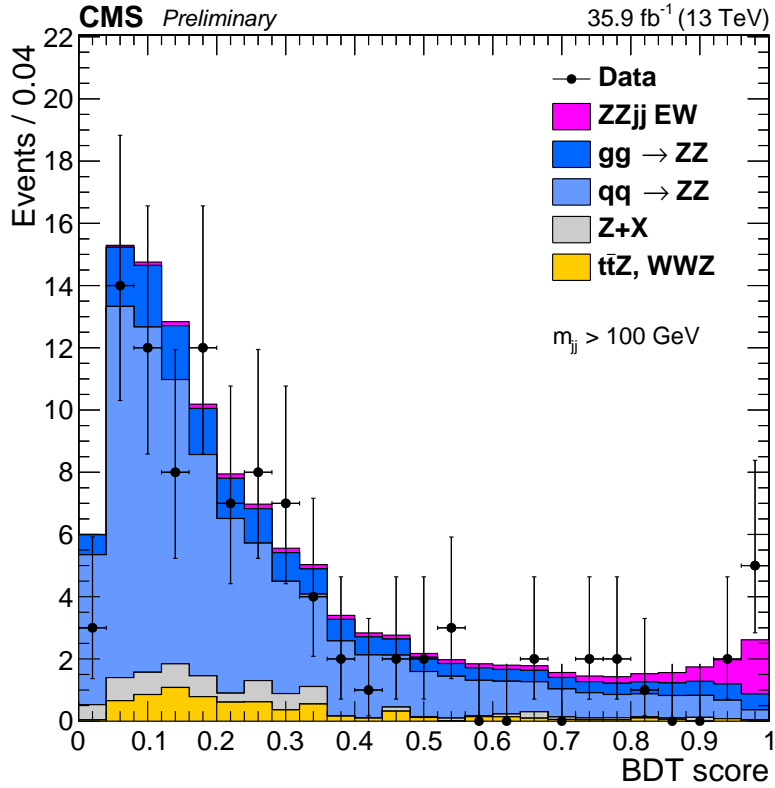


Figure 7.31: Output distribution of the VBS signal extraction GBDT, for events in the dijet selection. Points represent data, with statistical uncertainty bars. The stack of filled histograms represents the SM signal prediction and background estimate.

149 as a function of the maximum  $m_{ZZ}$  used.

150 The aQGC search proceeds the same way, but using events in the dijet selection.

151 The observable used for limit setting is again  $m_{ZZ}$ , which is shown for these events

152 in Fig. 7.35 along with two example distributions for scenarios with nonzero aQGCs,

153 one with  $f_{T8}/\Lambda^4 = 1\text{TeV}^{-4}$ , the other with  $f_{T9}/\Lambda^4 = 2\text{TeV}^{-4}$ . In the aQGC search, a

154 unitarity bound is imposed, chosen with VBFNLO [230] to be the value of  $m_{ZZ}$  at which

155 the scattering amplitude would violate unitarity if the aQGC parameter in question

156 were set to its 95% CL limit value. While limits are set for each parameter, all other

157 parameters and their unitarity bounds are set to zero. The observed 95% CL limits

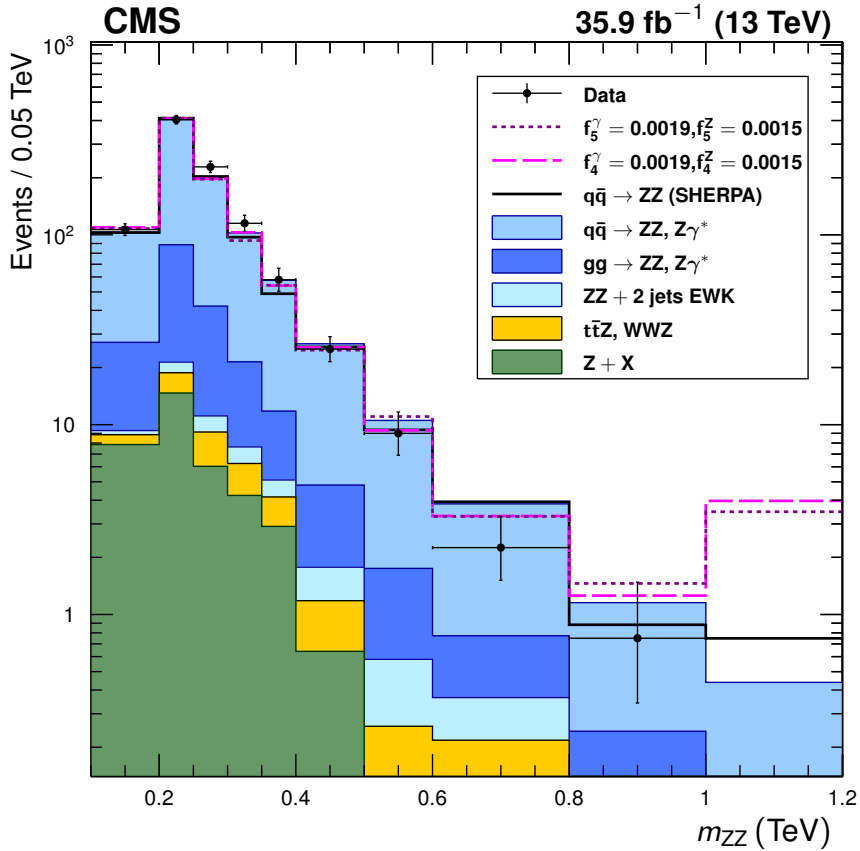


Figure 7.32: Distribution of ZZ invariant mass for all events in the on-shell selection. Points represent data, with statistical uncertainty bars. The stack of filled histograms represents the SM signal prediction and background estimate. The unfilled histograms represent two example SHERPA predictions for nonzero aTGC hypotheses (dashed) and the SHERPA SM prediction (solid), included to illustrate the shape differences between the SHERPA and POWHEG+MCFM SM predictions. The SHERPA distributions are normalized such that the SM prediction's total yield matches that of the other generators. The last bin includes the overflow contributions from events at masses above 1.2 TeV.

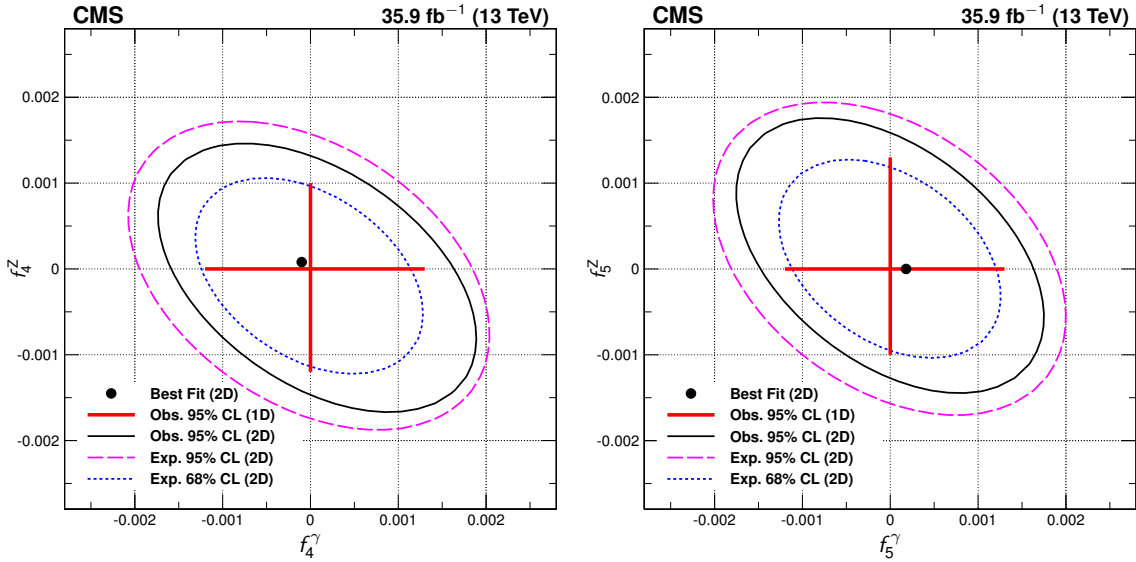


Figure 7.33: Two-dimensional observed 95% CL limits (solid contour) and expected 68 and 95% CL limits (dashed contours) in the  $f_4^\gamma$ - $f_4^Z$  (left) and  $f_5^\gamma$ - $f_5^Z$  (right) planes. The regions outside the contours are excluded at the corresponding confidence level. The dot is the point of maximum likelihood in the two-dimensional fits. Solid, straight lines at the center show the observed one-dimensional 95% CL limits for  $f_{4,5}^\gamma$  (horizontal) and  $f_{4,5}^Z$  (vertical). No form factor is used.

158 on the coefficients of the effective field theory operators covering ZZjj production  
159 are

$$\begin{aligned}
 -0.46 &< f_{T0}/\Lambda^4 &< 0.44 \text{ TeV}^{-4}, \\
 -0.61 &< f_{T1}/\Lambda^4 &< 0.61 \text{ TeV}^{-4}, \\
 -1.2 &< f_{T2}/\Lambda^4 &< 1.2 \text{ TeV}^{-4}, \\
 -0.84 &< f_{T8}/\Lambda^4 &< 0.84 \text{ TeV}^{-4}, \\
 -1.8 &< f_{T9}/\Lambda^4 &< 1.8 \text{ TeV}^{-4}.
 \end{aligned} \tag{7.12}$$

160 These are the most stringent constraints to date on all five parameters, improving on  
161 the previous best by factors of 2–8 (see Section 2.3.1). This is the first time any of  
162 them have been measured in the ZZjj channel.

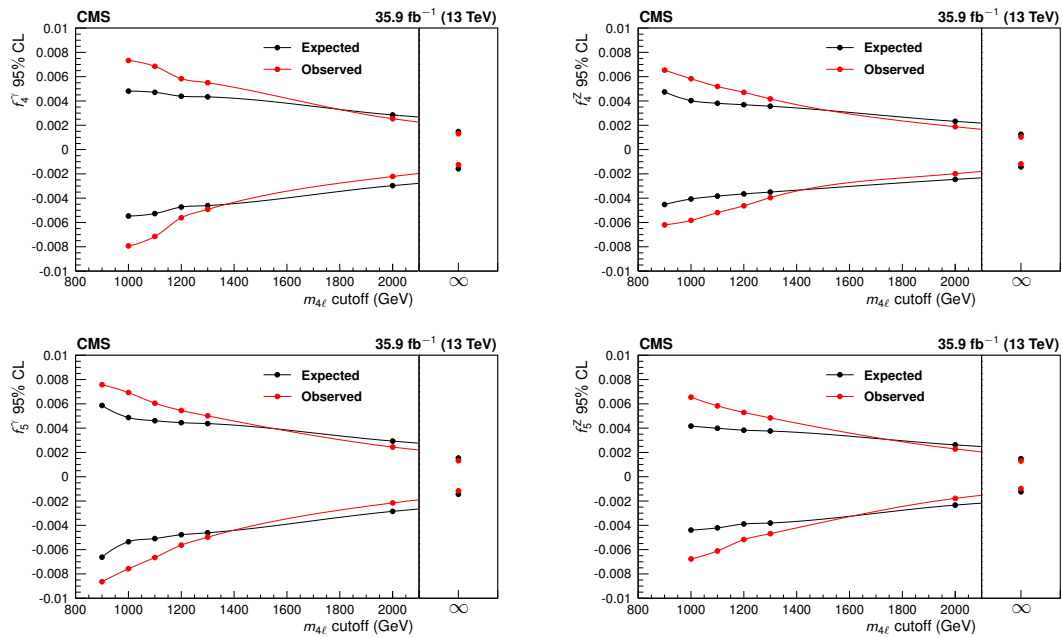


Figure 7.34: Expected and observed one-dimensional limits on the four aTGC parameters, as functions of the  $m_{ZZ}$  cutoff used to enforce unitarity. No form factor is used.

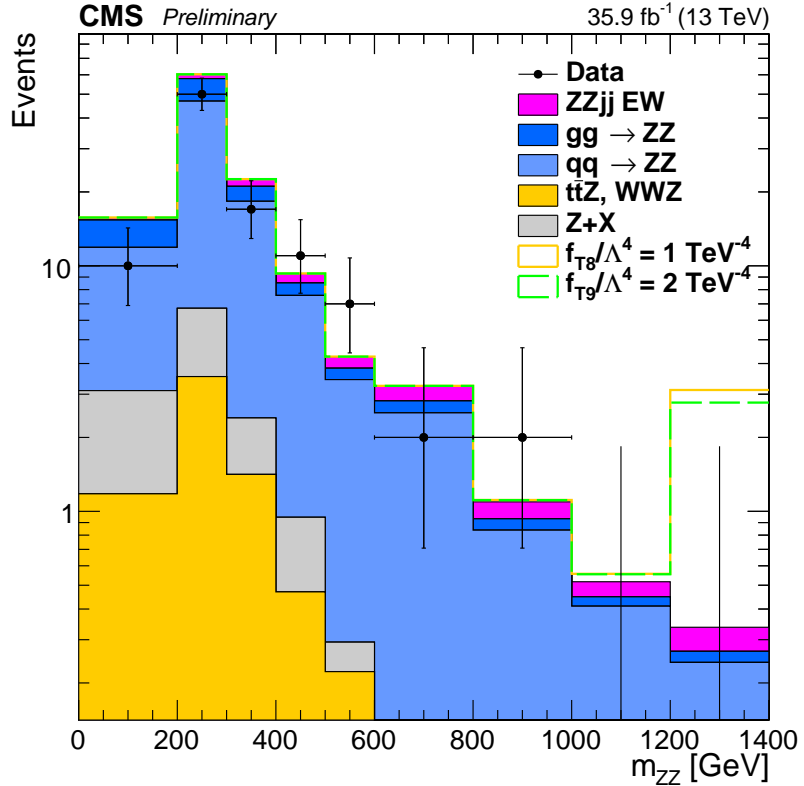


Figure 7.35: Distribution of ZZ invariant mass for events in the dijet selection. Points represent data, with statistical uncertainty bars. The stack of filled histograms represents the SM signal prediction and background estimate. The unfilled histograms represent two example MADGRAPH5\_aMC@NLO distributions for nonzero aQGC hypotheses. The last bin includes the overflow contributions from events at masses above 1.4 TeV.

## **0 Chapter 8**

# **1 Conclusions**

## **2 8.1 Summary**

3 Diboson studies in high-energy particle collisions are important probes of the elec-  
4 troweak sector of the standard model. In particular, measurements of resonant and  
5 nonresonant four-lepton production shed light on the couplings between the neutral  
6 gauge bosons and on the details of electroweak symmetry breaking. Decays to four  
7 charged leptons (electrons or muons) are rare, but they can be easily identified and  
8 fully reconstructed, and they represent a clean channel with low backgrounds. The  
9 LHC at CERN has generated proton-proton collisions with a center-of-mass energy of  
10 13 TeV at record-breaking luminosities, providing an unprecedented opportunity to  
11 study such processes. The CMS detector is well designed for these measurements and  
12 collected a high-quality dataset corresponding to an integrated luminosity of  $35.9 \text{ fb}^{-1}$   
13 in 2016. Several studies of four-lepton production were performed with this dataset  
14 and reported here.

15 Because the four-lepton channel is so clean, event selections are loose and effi-  
16 ciencies are high. Most backgrounds are estimated from data. The full four-lepton

17 spectrum includes resonant single-Z decays ( $pp \rightarrow Z \rightarrow 4\ell$ ), resonant Higgs boson  
 18 decays ( $pp \rightarrow H \rightarrow 4\ell$ ), continuum production of a single Z boson and a nonres-  
 19 onant lepton pair ( $pp \rightarrow Z\gamma^* \rightarrow 4\ell$ ), and continuum production of two on-shell  
 20 ( $60 < m_{\ell\ell} < 120$  GeV) Z bosons ( $pp \rightarrow ZZ \rightarrow 4\ell$ ).

21 Both inclusive and differential ZZ cross sections were measured. Inclusive cross  
 22 sections were measured with a signal strength found by a maximum likelihood fit.  
 23 The measured fiducial ZZ cross section, subject to the requirements of Table 6.2, is

$$\sigma_{\text{fid}}(pp \rightarrow ZZ \rightarrow 4\ell) = 40.9 \pm 1.3 \text{ (stat)} \pm 1.4 \text{ (syst)} \pm 1.0 \text{ (lumi)} \text{ fb.} \quad (8.1)$$

24 The total ZZ cross section, subject only to the constraint that both Z bosons be on-  
 25 shell, was extrapolated with an acceptance correction and combined with the smaller  
 26 ( $2.9 \text{ fb}^{-1}$ ) dataset collected in 2015. Its measured value is

$$\sigma(pp \rightarrow ZZ) = 17.2 \pm 0.5 \text{ (stat)} \pm 0.7 \text{ (syst)} \pm 0.4 \text{ (theo)} \pm 0.4 \text{ (lumi)} \text{ pb.} \quad (8.2)$$

27 The  $Z \rightarrow 4\ell$  branching fraction was measured for events with  $80 < m_{4\ell} < 100$  GeV  
 28 and a requirement of  $m_{\ell\ell} > 4$  GeV for all opposite-sign, same-flavor lepton pairs, and  
 29 found to be

$$\mathcal{B}(Z \rightarrow 4\ell) = 4.8 \pm 0.2 \text{ (stat)} \pm 0.2 \text{ (syst)} \pm 0.1 \text{ (theo)} \pm 0.1 \text{ (lumi)} \times 10^{-6}. \quad (8.3)$$

30 Differential cross sections were measured as functions of a number of observables  
 31 including fully leptonic kinematic variables and quantities related to the production  
 32 of associated jets. All results are in agreement with SM predictions.

33 A search was performed for fully electroweak ZZjj production using a gradient-  
 34 boosted decision tree. An excess consistent with VBS was found at the level of 2.7  
 35 standard deviations above the null hypothesis ( $1.6\sigma$  expected). This corresponds to  
 36 a measured electroweak fiducial cross section of

$$\sigma_{\text{fid}}(pp \rightarrow ZZ\text{jj(EWK)} \rightarrow 4\ell\text{jj}) = 0.40^{+0.21}_{-0.16} \text{ (stat)}^{+0.13}_{-0.09} \text{ (syst)} \text{ fb,} \quad (8.4)$$

37 consistent with SM predictions.

38 Searches were performed for anomalous triple and quartic gauge couplings. The  
 39 aTGC search, considered in an effective lagrangian framework, used the invariant  
 40 mass of inclusive ZZ events to set the most stringent 95% CL limits to date on ZZZ  
 41 and ZZ $\gamma$  couplings,

$$\begin{aligned} -0.0012 < f_4^Z < 0.0010, \quad -0.0010 < f_5^Z < 0.0013, \\ -0.0012 < f_4^\gamma < 0.0013, \quad -0.0012 < f_5^\gamma < 0.0013. \end{aligned} \quad (8.5)$$

42 Two-dimensional limits were also set. The aQGC search, performed in an effective  
 43 field theory parameterization with ZZjj events, set the most stringent 95% CL limits  
 44 to date on several dimension-8 operators which govern quartic gauge couplings,

$$\begin{aligned} -0.46 &< f_{T0}/\Lambda^4 &< 0.44 \text{ TeV}^{-4}, \\ -0.61 &< f_{T1}/\Lambda^4 &< 0.61 \text{ TeV}^{-4}, \\ -1.2 &< f_{T2}/\Lambda^4 &< 1.2 \text{ TeV}^{-4}, \\ -0.84 &< f_{T8}/\Lambda^4 &< 0.84 \text{ TeV}^{-4}, \\ -1.8 &< f_{T9}/\Lambda^4 &< 1.8 \text{ TeV}^{-4}. \end{aligned} \quad (8.6)$$

## 45 8.2 Outlook

46 Diboson measurements have great potential to shed further light on the SM or find  
 47 deviations from it. In the long term, cross section measurements at higher center-of-  
 48 mass energies are of great interest because new physics should be most obvious at high  
 49  $\sqrt{s}$ . With no new colliders expected in the near future<sup>1</sup>, progress will first come in the  
 50 form of precision measurements of processes that are in principle accessible now. The  
 51 statistical uncertainties of the measured inclusive cross sections are now comparable

---

<sup>1</sup>The LHC may operate at  $\sqrt{s} = 14$  TeV in the near future, which would be useful but only marginally more likely to reveal new physics, in line with the marginal increase in energy.

52 to or smaller than the systematic uncertainties, and systematics should dominate after  
53 the inclusion of data collected in 2017, even if new techniques are developed which  
54 reduce lepton efficiency and trigger uncertainties somewhat. Systematic uncertainty  
55 reductions that may be developed in the near future have the potential to bring total  
56 experimental uncertainties down to a similar level to the theoretical uncertainties.

57 Differential cross sections and searches, however, will be statistically limited for  
58 some time and will benefit greatly from additional luminosity at  $\sqrt{s} = 13$  TeV. Sta-  
59 tistical uncertainties dominate in almost all bins in the differential cross sections.  
60 Assuming no deviations from the SM, data collected in 2017 will likely be enough to  
61 allow  $3\sigma$  evidence for VBS, when added to the 2016 data presented here. New data  
62 will likewise reduce the electroweak ZZ production cross section uncertainty substan-  
63 tially as the process' anticipated discovery draws near. The statistical power for the  
64 aGC searches comes largely from the highest-mass bins, where very few events have  
65 been observed—only three above 800 GeV and none above 1 TeV, even in the inclusive  
66 selection. Further data collection will improve these limits substantially and place  
67 stringent restrictions on BSM neutral gauge boson couplings—or discover them.

# 68 Bibliography

- 69 [1] D. J. Griffiths, *Introduction to elementary particles; 2nd rev. version*, ser.  
70 Physics textbook. New York, NY: Wiley, 2008.
- 71 [2] F. Halzen and A. Martin, *Quarks & Leptons: An introductory course in*  
72 *modern particle physics*. New York, USA: John Wiley & Sons, 1984.
- 73 [3] V. Barger and R. Phillips, *Collider Physics*, ser. Frontiers in physics. Avalon  
74 Publishing, 1997, ISBN: 9780201149456.
- 75 [4] M. E. Peskin and D. V. Schroeder, *An Introduction to quantum field theory*.  
76 Reading, USA: Addison-Wesley, 1995, ISBN: 9780201503975, 0201503972.
- 77 [5] J. F. Donoghue, E. Golowich, and B. R. Holstein, *Dynamics of the Standard*  
78 *Model*, ser. Cambridge monographs on particle physics, nuclear physics, and  
79 cosmology. Cambridge: Cambridge Univ. Press, 1992.
- 80 [6] O. W. Greenberg, “Spin and unitary-spin independence in a paraquark  
81 model of baryons and mesons,” *Phys. Rev. Lett.*, vol. 13, p. 598, 20 1964.  
82 DOI: 10.1103/PhysRevLett.13.598. <https://link.aps.org/doi/10.1103/PhysRevLett.13.598>.
- 84 [7] S. L. Glashow, “Quarks with color and flavor,” *Scientific American*, vol. 233,  
85 p. 38, 1975. <http://www.jstor.org/stable/24949915>.
- 86 [8] Super-Kamiokande Collaboration, “Evidence for oscillation of atmospheric  
87 neutrinos,” *Phys. Rev. Lett.*, vol. 81, pp. 1562–1567, 1998. DOI: 10.1103/  
88 PhysRevLett.81.1562. arXiv: [hep-ex/9807003](https://arxiv.org/abs/hep-ex/9807003) [hep-ex].
- 89 [9] SNO Collaboration, “Measurement of the rate of  $\nu_e + d \rightarrow p + p + e^-$  interac-  
90 tions produced by  $^8B$  solar neutrinos at the Sudbury Neutrino Observatory,”  
91 *Phys. Rev. Lett.*, vol. 87, p. 071301, 2001. DOI: 10.1103/PhysRevLett.87.  
92 071301. arXiv: [nucl-ex/0106015](https://arxiv.org/abs/nucl-ex/0106015) [nucl-ex].

- 93 [10] SNO Collaboration, “Direct evidence for neutrino flavor transformation from  
94 neutral current interactions in the Sudbury Neutrino Observatory,” *Phys. Rev.*  
95 *Lett.*, vol. 89, p. 011301, 2002. DOI: 10.1103/PhysRevLett.89.011301. arXiv:  
96 nucl-ex/0204008 [nucl-ex].
- 97 [11] Particle Data Group, C. Patrignani, *et al.*, “Review of particle physics,” *Chin.*  
98 *Phys. C*, vol. 40, p. 100001, 2016. DOI: 10.1088/1674-1137/40/10/100001.
- 99 [12] N. Cabibbo, “Unitary symmetry and leptonic decays,” *Phys. Rev. Lett.*, vol.  
100 10, p. 531, 1963. DOI: 10.1103/PhysRevLett.10.531.
- 101 [13] M. Kobayashi and T. Maskawa, “CP-violation in the renormalizable theory  
102 of weak interaction,” *Prog. Theo. Phys.*, vol. 49, p. 652, 1973. DOI: 10.1143/  
103 PTP.49.652.
- 104 [14] J. H. Christenson, J. W. Cronin, V. L. Fitch, and R. Turlay, “Evidence for  
105 the  $2\pi$  decay of the  $K_2^0$  meson,” *Phys. Rev. Lett.*, vol. 13, p. 138, 4 Jul. 1964.  
106 DOI: 10.1103/PhysRevLett.13.138.
- 107 [15] KTeV Collaboration, “Observation of direct CP violation in  $K_{S,L} \rightarrow \pi\pi$   
108 decays,” *Phys. Rev. Lett.*, vol. 83, p. 22, 1999. DOI: 10.1103/PhysRevLett.  
109 83.22. arXiv: hep-ex/9905060 [hep-ex].
- 110 [16] NA48 Collaboration, “A new measurement of direct CP violation in two  
111 pion decays of the neutral kaon,” *Phys. Lett. B*, vol. 465, p. 335, 1999. DOI:  
112 10.1016/S0370-2693(99)01030-8. arXiv: hep-ex/9909022 [hep-ex].
- 113 [17] BaBar Collaboration, “Measurement of CP violating asymmetries in  $B^0$   
114 decays to CP eigenstates,” *Phys. Rev. Lett.*, vol. 86, p. 2515, 2001. DOI: 10.  
115 1103/PhysRevLett.86.2515. arXiv: hep-ex/0102030 [hep-ex].
- 116 [18] Belle Collaboration, “Observation of large CP violation in the neutral  $B$   
117 meson system,” *Phys. Rev. Lett.*, vol. 87, p. 091802, 2001. DOI: 10.1103/  
118 PhysRevLett.87.091802. arXiv: hep-ex/0107061 [hep-ex].
- 119 [19] LHCb Collaboration, “Observation of CP violation in  $B^\pm \rightarrow DK^\pm$  de-  
120 cays,” *Phys. Lett. B*, vol. 712, p. 203, 2012, [Corrigendum: DOI: 110.1016/j.  
121 physletb.2012.05.060]. DOI: 10.1016/j.physletb.2012.04.060. arXiv:  
122 1203.3662 [hep-ex].
- 123 [20] LHCb Collaboration, “First observation of CP violation in the decays of  
124  $B_s^0$  mesons,” *Phys. Rev. Lett.*, vol. 110, p. 221601, 2013. DOI: 10.1103/  
125 PhysRevLett.110.221601. arXiv: 1304.6173 [hep-ex].

- 126 [21] E. Noether, “Invariant variation problems,” trans. by M. A. Tavel, *Gott. Nachr.*, p. 235, 1918, [*Transp. Theory Statist. Phys.*, vol. 1, p. 186, 1971]. DOI: 10.1080/00411457108231446. arXiv: physics/0503066 [physics].
- 129 [22] M. Srednicki, *Quantum Field Theory*. Cambridge: Cambridge Univ. Press, 130 2007.
- 131 [23] S. L. Glashow, “Partial symmetries of weak interactions,” *Nucl. Phys.*, vol. 132 22, p. 579, 1961. DOI: 10.1016/0029-5582(61)90469-2.
- 133 [24] S. Weinberg, “A model of leptons,” *Phys. Rev. Lett.*, vol. 19, p. 1264, 1967. 134 DOI: 10.1103/PhysRevLett.19.1264.
- 135 [25] A. Salam, “Weak and electromagnetic interactions,” *Conf. Proc.*, vol. C680-136 519, p. 367, 1968.
- 137 [26] F. Englert and R. Brout, “Broken symmetry and the mass of gauge vector 138 mesons,” *Phys. Rev. Lett.*, vol. 13, p. 321, 9 Aug. 1964. DOI: 10.1103/ 139 PhysRevLett.13.321. <https://link.aps.org/doi/10.1103/PhysRevLett.13.321>.
- 141 [27] P. W. Higgs, “Broken symmetries and the masses of gauge bosons,” *Phys. 142 Rev. Lett.*, vol. 13, p. 508, 16 Oct. 1964. DOI: 10.1103/PhysRevLett.13.508. 143 <https://link.aps.org/doi/10.1103/PhysRevLett.13.508>.
- 144 [28] G. S. Guralnik, C. R. Hagen, and T. W. B. Kibble, “Global conservation 145 laws and massless particles,” *Phys. Rev. Lett.*, vol. 13, p. 585, 20 Nov. 1964. 146 DOI: 10.1103/PhysRevLett.13.585. <https://link.aps.org/doi/10.1103/PhysRevLett.13.585>.
- 148 [29] A. Alboteanu, W. Kilian, and J. Reuter, “Resonances and unitarity in weak 149 boson scattering at the LHC,” *JHEP*, vol. 11, p. 010, 2008. DOI: 10.1088/ 150 1126-6708/2008/11/010. arXiv: 0806.4145 [hep-ph].
- 151 [30] V. C. Rubin, “Dark matter in spiral galaxies,” *Scientific American*, vol. 248, 152 p. 96, 1983. DOI: 10.1038/scientificamerican0683-96.
- 153 [31] K. Garrett and G. Duda, “Dark matter: a primer,” *Adv. Astron.*, vol. 2011, 154 p. 968 283, 2011. DOI: 10.1155/2011/968283. arXiv: 1006.2483 [hep-ph].
- 155 [32] J. Ellis, “Searching for particle physics beyond the standard model at the 156 LHC and elsewhere,” *AIP Conf. Proc.*, vol. 1446, p. 9, 2012. DOI: 10.1063/ 157 1.4727987. arXiv: 1102.5009 [hep-ph].

- 158 [33] H. Georgi, H. R. Quinn, and S. Weinberg, “Hierarchy of interactions in  
159 unified gauge theories,” *Phys. Rev. Lett.*, vol. 33, p. 451, 1974. DOI: 10.1103/  
160 PhysRevLett.33.451.
- 161 [34] E. Gildener, “Gauge symmetry hierarchies,” *Phys. Rev. D*, vol. 14, p. 1667,  
162 1976. DOI: 10.1103/PhysRevD.14.1667.
- 163 [35] A. J. Buras, J. R. Ellis, M. K. Gaillard, and D. V. Nanopoulos, “Aspects of  
164 the grand unification of strong, weak and electromagnetic interactions,” *Nucl.  
165 Phys. B*, vol. 135, p. 66, 1978. DOI: 10.1016/0550-3213(78)90214-6.
- 166 [36] S. Mele, “The measurement of the number of light neutrino species at LEP,”  
167 *Adv. Ser. Direct. High Energy Phys.*, vol. 23, p. 89, 2015. DOI: 10.1142/  
168 9789814644150\_0004. <http://cds.cern.ch/record/2103251>.
- 169 [37] S. P. Martin, “A supersymmetry primer,” in *Perspectives on Supersymmetry  
170 II*. DOI: 10.1142/9789814307505\_0001. arXiv: hep-ph/9709356 [hep-ph].
- 171 [38] C. Autermann, “Experimental status of supersymmetry after the LHC run-  
172 I,” *Prog. Part. Nucl. Phys.*, vol. 90, p. 125, 2016. DOI: 10.1016/j.ppnp.2016.  
173 06.001. arXiv: 1609.01686 [hep-ex].
- 174 [39] H. Georgi and S. L. Glashow, “Unity of all elementary particle forces,” *Phys.  
175 Rev. Lett.*, vol. 32, p. 438, 1974. DOI: 10.1103/PhysRevLett.32.438.
- 176 [40] K. Hagiwara, R. D. Peccei, D. Zeppenfeld, and K. Hikasa, “Probing the weak  
177 boson sector in  $e^+e^- \rightarrow W^+W^-$ ,” *Nucl. Phys. B*, vol. 282, p. 253, 1987. DOI:  
178 10.1016/0550-3213(87)90685-7.
- 179 [41] G. J. Gounaris, J. Layssac, and F. M. Renard, “New and standard physics  
180 contributions to anomalous  $Z$  and  $\gamma$  self-couplings,” *Phys. Rev. D*, vol. 62,  
181 p. 073013, 2000. DOI: 10.1103/PhysRevD.62.073013. arXiv: hep-ph/  
182 0003143 [hep-ph].
- 183 [42] U. Baur and D. L. Rainwater, “Probing neutral gauge boson self-interactions  
184 in ZZ production at hadron colliders,” *Phys. Rev. D*, vol. 62, p. 113011, 2000.  
185 DOI: 10.1103/PhysRevD.62.113011. arXiv: hep-ph/0008063 [hep-ph].
- 186 [43] U. Baur and E. L. Berger, “Probing the weak boson sector in  $Z\gamma$  production  
187 at hadron colliders,” *Phys. Rev. D*, vol. 47, p. 4889, 1993. DOI: 10.1103/  
188 PhysRevD.47.4889.

- 189 [44] C. Degrande, N. Greiner, W. Kilian, O. Mattelaer, H. Mebane, T. Stelzer,  
 190 S. Willenbrock, and C. Zhang, “Effective field theory: a modern approach to  
 191 anomalous couplings,” *Annals Phys.*, vol. 335, p. 21, 2013. DOI: [10.1016/j.aop.2013.04.016](https://doi.org/10.1016/j.aop.2013.04.016). arXiv: [1205.4231](https://arxiv.org/abs/1205.4231) [hep-ph].
- 193 [45] O. J. P. Éboli, M. C. Gonzalez-Garcia, and J. K. Mizukoshi, “ $pp \rightarrow jje^\pm\mu^\pm\nu\nu$   
 194 and  $jje^\pm\mu^\mp\nu\nu$  at  $\mathcal{O}(\alpha_{\text{em}}^6)$  and  $\mathcal{O}(\alpha_{\text{em}}^4\alpha_s^2)$  for the study of the quartic electroweak  
 195 gauge boson vertex at LHC,” *Phys. Rev. D*, vol. 74, p. 073005, 2006. DOI:  
 196 [10.1103/PhysRevD.74.073005](https://doi.org/10.1103/PhysRevD.74.073005). arXiv: [hep-ph/0606118](https://arxiv.org/abs/hep-ph/0606118) [hep-ph].
- 197 [46] NNPDF Collaboration, “Parton distributions from high-precision collider  
 198 data,” 2017. arXiv: [1706.00428](https://arxiv.org/abs/1706.00428) [hep-ph].
- 199 [47] A. Lazopoulos, K. Melnikov, and F. Petriello, “QCD corrections to tri-boson  
 200 production,” *Phys. Rev. D*, vol. 76, p. 014001, 2007. DOI: [10.1103/PhysRevD.76.014001](https://doi.org/10.1103/PhysRevD.76.014001). arXiv: [hep-ph/0703273](https://arxiv.org/abs/hep-ph/0703273) [hep-ph].
- 202 [48] T. Binoth, G. Ossola, C. G. Papadopoulos, and R. Pittau, “NLO QCD  
 203 corrections to tri-boson production,” *JHEP*, vol. 06, p. 082, 2008. DOI: [10.1088/1126-6708/2008/06/082](https://doi.org/10.1088/1126-6708/2008/06/082). arXiv: [0804.0350](https://arxiv.org/abs/0804.0350) [hep-ph].
- 205 [49] V. Hankele and D. Zeppenfeld, “QCD corrections to hadronic WWZ pro-  
 206 duction with leptonic decays,” *Phys. Lett. B*, vol. 661, p. 103, 2008. DOI:  
 207 [10.1016/j.physletb.2008.02.014](https://doi.org/10.1016/j.physletb.2008.02.014). arXiv: [0712.3544](https://arxiv.org/abs/0712.3544) [hep-ph].
- 208 [50] F. J. Hasert *et al.*, “Search for elastic  $\nu_\mu$  electron scattering,” *Phys. Lett. B*,  
 209 vol. 46, p. 121, 1973. DOI: [10.1016/0370-2693\(73\)90494-2](https://doi.org/10.1016/0370-2693(73)90494-2).
- 210 [51] UA1 Collaboration, “Experimental observation of lepton pairs of invariant  
 211 mass around  $95\text{ GeV}/c^2$  at the CERN SPS collider,” *Phys. Lett. B*, vol. 126,  
 212 p. 398, 1983. DOI: [10.1016/0370-2693\(83\)90188-0](https://doi.org/10.1016/0370-2693(83)90188-0).
- 213 [52] SLD Electroweak Group, DELPHI Collaboration, ALEPH Collaboration,  
 214 SLD Collaboration, SLD Heavy Flavour Group, OPAL Collaboration, LEP  
 215 Electroweak Working Group, L3 Collaboration, “Precision electroweak mea-  
 216 surements on the Z resonance,” *Phys. Rept.*, vol. 427, p. 257, 2006. DOI: [10.1016/j.physrep.2005.12.006](https://doi.org/10.1016/j.physrep.2005.12.006). arXiv: [hep-ex/0509008](https://arxiv.org/abs/hep-ex/0509008) [hep-ex].
- 218 [53] J. M. Campbell and R. K. Ellis, “An update on vector boson pair production  
 219 at hadron colliders,” *Phys. Rev. D*, vol. 60, p. 113006, 1999. DOI: [10.1103/PhysRevD.60.113006](https://doi.org/10.1103/PhysRevD.60.113006). arXiv: [hep-ph/9905386](https://arxiv.org/abs/hep-ph/9905386) [hep-ph].

- 221 [54] J. M. Campbell, R. K. Ellis, and C. Williams, “Vector boson pair production  
222 at the LHC,” *JHEP*, vol. 07, p. 018, 2011. DOI: 10.1007/JHEP07(2011)018.  
223 arXiv: 1105.0020 [hep-ph].
- 224 [55] T. Melia, P. Nason, R. Röntsch, and G. Zanderighi, “ $W^+W^-$ ,  $WZ$  and  $ZZ$   
225 production in the POWHEG BOX,” *JHEP*, vol. 11, p. 078, 2011. DOI: 10.1007/  
226 JHEP11(2011)078. arXiv: 1107.5051 [hep-ph].
- 227 [56] F. Cascioli, T. Gehrmann, M. Grazzini, S. Kallweit, P. Maierhöfer, A. von  
228 Manteuffel, S. Pozzorini, D. Rathlev, L. Tancredi, and E. Weihs, “ $ZZ$  produc-  
229 tion at hadron colliders in NNLO QCD,” *Phys. Lett. B*, vol. 735, p. 311, 2014.  
230 DOI: 10.1016/j.physletb.2014.06.056. arXiv: 1405.2219 [hep-ph].
- 231 [57] F. Caola, K. Melnikov, R. Röntsch, and L. Tancredi, “QCD corrections to  
232  $ZZ$  production in gluon fusion at the LHC,” *Phys. Rev. D*, vol. 92, p. 094028,  
233 2015. DOI: 10.1103/PhysRevD.92.094028. arXiv: 1509.06734 [hep-ph].
- 234 [58] D. Rainwater, R. Szalapski, and D. Zeppenfeld, “Probing color-singlet ex-  
235 change in  $Z + 2$ -jet events at the CERN LHC,” *Phys. Rev. D*, vol. 54, p. 6680,  
236 11 Dec. 1996. DOI: 10.1103/PhysRevD.54.6680.
- 237 [59] Sjöstrand, Torbjörn and Ask, Stefan and Christiansen, Jesper R. and Corke,  
238 Richard and Desai, Nishita and Ilten, Philip and Mrenna, Stephen and Prestel,  
239 Stefan and Rasmussen, Christine O. and Skands, Peter Z., “An introduction  
240 to PYTHIA 8.2,” *Comput. Phys. Commun.*, vol. 191, p. 159, 2015. DOI: 10.  
241 1016/j.cpc.2015.01.024. arXiv: 1410.3012 [hep-ph].
- 242 [60] C. Bierlich and J. R. Christiansen, “Effects of color reconnection on hadron  
243 flavor observables,” *Phys. Rev. D*, vol. 92, p. 094010, 2015. DOI: 10.1103/  
244 PhysRevD.92.094010. arXiv: 1507.02091 [hep-ph].
- 245 [61] ALEPH Collaboration, “Measurement of the  $e^+e^- \rightarrow ZZ$  production cross-  
246 section at center-of-mass energies of 183 GeV and 189 GeV,” *Phys. Lett. B*,  
247 vol. 469, p. 287, 1999. DOI: 10.1016/S0370-2693(99)01288-5. arXiv: hep-  
248 ex/9911003 [hep-ex].
- 249 [62] OPAL Collaboration, “ $Z$  boson pair production in  $e^+e^-$  collisions at  $\sqrt{s} =$   
250 183 GeV and 189 GeV,” *Phys. Lett. B*, vol. 476, p. 256, 2000. DOI: 10.1016/  
251 S0370-2693(00)00197-0. arXiv: hep-ex/0003016 [hep-ex].
- 252 [63] L3 Collaboration, “ $Z$  boson pair production at LEP,” *Phys. Lett. B*, vol.  
253 572, p. 133, 2003. DOI: 10.1016/j.physletb.2003.08.023. arXiv: hep-  
254 ex/0308013 [hep-ex].

- 255 [64] DELPHI Collaboration, “ZZ production in  $e^+e^-$  interactions at  $\sqrt{s} = 183 -$   
256 209 GeV,” *Eur. Phys. J. C*, vol. 30, p. 447, 2003. DOI: 10.1140/epjc/s2003-  
257 01287-0. arXiv: hep-ex/0307050 [hep-ex].
- 258 [65] OPAL Collaboration, “Study of Z pair production and anomalous couplings  
259 in  $e^+e^-$  collisions at  $\sqrt{s}$  between 190 GeV and 209 GeV,” *Eur. Phys. J. c*, vol.  
260 32, p. 303, 2003. DOI: 10.1140/epjc/s2003-01467-x. arXiv: hep-ex/0310013  
261 [hep-ex].
- 262 [66] ALEPH Collaboration, “Measurement of Z-pair production in  $e^+e^-$  collisions  
263 and constraints on anomalous neutral gauge couplings,” *JHEP*, vol. 04, p. 124,  
264 2009. DOI: 10.1088/1126-6708/2009/04/124.
- 265 [67] CDF Collaboration, “First measurement of ZZ production in  $\bar{p}p$  collisions at  
266  $\sqrt{s} = 1.96$  TeV,” *Phys. Rev. Lett.*, vol. 100, p. 201801, 2008. DOI: 10.1103/  
267 PhysRevLett.100.201801. arXiv: 0801.4806 [hep-ex].
- 268 [68] D0 Collaboration, “ $ZZ \rightarrow \ell^+\ell^-\nu\bar{\nu}$  production in  $p\bar{p}$  collisions at  $\sqrt{s} =$   
269 1.96 TeV,” *Phys. Rev. D*, vol. 78, p. 072002, 2008. DOI: 10.1103/PhysRevD.  
270 78.072002. arXiv: 0808.0269 [hep-ex].
- 271 [69] D0 Collaboration, “Observation of ZZ production in  $p\bar{p}$  collisions at  $\sqrt{s} =$   
272 1.96 TeV,” *Phys. Rev. Lett.*, vol. 101, p. 171803, 2008, DOI: 10.1103/PhysRev  
273 Lett.101.171803. arXiv: 0808.0703 [hep-ex].
- 274 [70] D0 Collaboration, “Measurement of the ZZ production cross section in  $p\bar{p}$   
275 collisions at  $\sqrt{s} = 1.96$  TeV,” *Phys. Rev. D*, vol. 84, p. 011103, 2011. DOI:  
276 10.1103/PhysRevD.84.011103. arXiv: 1104.3078 [hep-ex].
- 277 [71] CDF Collaboration, “Measurement of ZZ production in leptonic final states  
278 at  $\sqrt{s}$  of 1.96 TeV at CDF,” *Phys. Rev. Lett.*, vol. 108, p. 101801, 2012. DOI:  
279 10.1103/PhysRevLett.108.101801. arXiv: 1112.2978 [hep-ex].
- 280 [72] CMS Collaboration, “Measurement of the ZZ production cross section and  
281 search for anomalous couplings in  $2\ell 2\ell'$  final states in pp collisions at  $\sqrt{s} =$   
282 7 TeV,” *JHEP*, vol. 01, p. 063, 2013. DOI: 10.1007/JHEP01(2013)063. arXiv:  
283 1211.4890 [hep-ex].
- 284 [73] CMS Collaboration, “Measurement of the  $pp \rightarrow ZZ$  production cross section  
285 and constraints on anomalous triple gauge couplings in four-lepton final states  
286 at  $\sqrt{s} = 8$  TeV,” *Phys. Lett. B*, vol. 740, p. 250, 2015, [Corrigendum: DOI: 10.  
287 1016/j.physletb.2016.04.010]. DOI: 10.1016/j.physletb.2014.11.059.  
288 arXiv: 1406.0113 [hep-ex].

- 289 [74] CMS Collaboration, “Measurements of the ZZ production cross sections in the  
290  $2\ell 2\nu$  channel in proton–proton collisions at  $\sqrt{s} = 7$  and 8 TeV and combined  
291 constraints on triple gauge couplings,” *Eur. Phys. J. C*, vol. 75, p. 511, 2015.  
292 DOI: 10.1140/epjc/s10052-015-3706-0. arXiv: 1503.05467 [hep-ex].
- 293 [75] CMS Collaboration, “Measurement of the differential cross sections for pairs  
294 of Z bosons produced in association with jets in pp collisions at  $\sqrt{s} = 8$  TeV,”  
295 CERN, Geneva, Tech. Rep. CMS-PAS-SMP-15-012, 2016. <https://cds.cern.ch/record/2209215>.
- 297 [76] ATLAS Collaboration, “Measurement of ZZ production in pp collisions at  
298  $\sqrt{s} = 7$  TeV and limits on anomalous ZZZ and ZZ $\gamma$  couplings with the ATLAS  
299 detector,” *JHEP*, vol. 03, p. 128, 2013. DOI: 10.1007/JHEP03(2013)128.  
300 arXiv: 1211.6096 [hep-ex].
- 301 [77] ATLAS Collaboration, “Measurements of four-lepton production in pp colli-  
302 sions at  $\sqrt{s} = 8$  TeV with the ATLAS detector,” *Phys. Lett. B*, vol. 753, p. 552,  
303 2016. DOI: 10.1016/j.physletb.2015.12.048. arXiv: 1509.07844 [hep-ex].
- 304 [78] ATLAS Collaboration, “Measurement of the ZZ production cross section  
305 in proton-proton collisions at  $\sqrt{s} = 8$  TeV using the ZZ  $\rightarrow \ell^-\ell^+\ell^-\ell^+$  and  
306 ZZ  $\rightarrow \ell^-\ell^+\nu\bar{\nu}$  channels with the ATLAS detector,” *JHEP*, vol. 01, p. 099,  
307 2017. DOI: 10.1007/JHEP01(2017)099. arXiv: 1610.07585 [hep-ex].
- 308 [79] CMS Collaboration, “Measurement of WZ and ZZ production in pp collisions  
309 at  $\sqrt{s} = 8$  TeV in final states with b-tagged jets,” *Eur. Phys. J. C*, vol. 74,  
310 p. 2973, 2014. DOI: 10.1140/epjc/s10052-014-2973-5. arXiv: 1403.3047  
311 [hep-ex].
- 312 [80] CMS Collaboration, “Measurement of the pp  $\rightarrow$  ZZ production cross section,  
313 Z  $\rightarrow 4\ell$  branching fraction and constraints on anomalous triple gauge couplings  
314 at  $\sqrt{s} = 13$  TeV,” 2017. <https://cds.cern.ch/record/2256100>.
- 315 [81] ATLAS Collaboration, “Evidence for electroweak production of W $^\pm$ W $^\pm$ jj  
316 in pp collisions at  $\sqrt{s} = 8$  TeV with the ATLAS detector,” *Phys. Rev. Lett.*,  
317 vol. 113, p. 141803, 2014. DOI: 10.1103/PhysRevLett.113.141803. arXiv:  
318 1405.6241 [hep-ex].
- 319 [82] CMS Collaboration, “Study of vector boson scattering and search for new  
320 physics in events with two same-sign leptons and two jets,” *Phys. Rev. Lett.*,  
321 vol. 114, p. 051801, 2015. DOI: 10.1103/PhysRevLett.114.051801. arXiv:  
322 1410.6315 [hep-ex].

- 323 [83] CMS Collaboration, “Measurement of the cross section for electroweak pro-  
324 duction of  $Z\gamma$  in association with two jets and constraints on anomalous quartic  
325 gauge couplings in proton–proton collisions at  $\sqrt{s} = 8$  TeV,” *Phys. Lett. B*, vol. 770, p. 380, 2017. DOI: 10.1016/j.physletb.2017.04.071. arXiv:  
326 1702.03025 [hep-ex].
- 328 [84] ATLAS Collaboration, “Studies of  $Z\gamma$  production in association with a high-  
329 mass dijet system in pp collisions at  $\sqrt{s} = 8$  TeV with the ATLAS detector,”  
330 *JHEP*, vol. 07, p. 107, 2017. DOI: 10.1007/JHEP07(2017)107. arXiv: 1705.  
331 01966 [hep-ex].
- 332 [85] CMS Collaboration, “Measurement of electroweak-induced production of  
333  $W\gamma$  with two jets in pp collisions at  $\sqrt{s} = 8$  TeV and constraints on anomalous  
334 quartic gauge couplings,” *JHEP*, vol. 06, p. 106, 2017. DOI: 10.1007/  
335 JHEP06(2017)106. arXiv: 1612.09256 [hep-ex].
- 336 [86] CMS Collaboration, “Evidence for exclusive  $\gamma\gamma \rightarrow W^+W^-$  production and  
337 constraints on anomalous quartic gauge couplings in pp collisions at  $\sqrt{s} = 7$   
338 and 8 TeV,” *JHEP*, vol. 08, p. 119, 2016. DOI: 10.1007/JHEP08(2016)119.  
339 arXiv: 1604.04464 [hep-ex].
- 340 [87] ATLAS Collaboration, “Measurement of exclusive  $\gamma\gamma \rightarrow W^+W^-$  production  
341 and search for exclusive Higgs boson production in pp collisions at  $\sqrt{s} = 8$  TeV  
342 using the ATLAS detector,” *Phys. Rev. D*, vol. 94, p. 032011, 2016. DOI:  
343 10.1103/PhysRevD.94.032011. arXiv: 1607.03745 [hep-ex].
- 344 [88] CMS Collaboration Collaboration, “Observation of electroweak production  
345 of same-sign W boson pairs in the two jet and two same-sign lepton final state  
346 in proton-proton collisions at 13 TeV,” CERN, Geneva, Tech. Rep. CMS-PAS-  
347 SMP-17-004, 2017. <https://cds.cern.ch/record/2264525>.
- 348 [89] ALEPH Collaboration, “Study of the four fermion final state at the Z reso-  
349 nance,” *Z. Phys. C*, vol. 66, p. 3, 1995. DOI: 10.1007/BF01496576.
- 350 [90] CMS Collaboration, “Observation of Z decays to four leptons with the  
351 CMS detector at the LHC,” *JHEP*, vol. 12, p. 034, 2012. DOI: 10.1007/  
352 JHEP12(2012)034. arXiv: 1210.3844 [hep-ex].
- 353 [91] ATLAS Collaboration, “Measurements of four-lepton production at the Z  
354 resonance in pp collisions at  $\sqrt{s} = 7$  and 8 TeV with ATLAS,” *Phys. Rev.*  
355 *Lett.*, vol. 112, p. 231806, 2014. DOI: 10.1103/PhysRevLett.112.231806.  
356 arXiv: 1403.5657 [hep-ex].

- 357 [92] LHC Higgs Cross Section Working Group Collaboration, “Handbook of LHC  
358 Higgs cross sections: 4. deciphering the nature of the Higgs sector,” 2016. DOI:  
359 10.23731/CYRM-2017-002. arXiv: 1610.07922 [hep-ph].
- 360 [93] OPAL Collaboration, DELPHI Collaboration, LEP Working Group for Higgs  
361 boson searches, ALEPH Collaboration, L3 Collaboration, “Search for the stan-  
362 dard model Higgs boson at LEP,” *Phys. Lett. B*, vol. 565, p. 61, 2003. DOI:  
363 10.1016/S0370-2693(03)00614-2. arXiv: hep-ex/0306033 [hep-ex].
- 364 [94] DELPHI Collaboration, OPAL Collaboration, ALEPH Collaboration, LEP  
365 Electroweak Working Group, L3 Collaboration, “A combination of prelimi-  
366 nary electroweak measurements and constraints on the standard model,” 2006.  
367 arXiv: hep-ex/0612034 [hep-ex].
- 368 [95] CDF Collaboration, D0 Collaboration, “Higgs boson studies at the Tevatron,”  
369 *Phys. Rev. D*, vol. 88, p. 052014, 2013. DOI: 10.1103/PhysRevD.88.052014.  
370 arXiv: 1303.6346 [hep-ex].
- 371 [96] CDF Collaboration, D0 Collaboration, “Evidence for a particle produced in  
372 association with weak bosons and decaying to a bottom-antibottom quark pair  
373 in Higgs boson searches at the Tevatron,” *Phys. Rev. Lett.*, vol. 109, p. 071804,  
374 2012. DOI: 10.1103/PhysRevLett.109.071804. arXiv: 1207.6436 [hep-ex].
- 375 [97] Tevatron Electroweak Working Group, CDF Collaboration, DELPHI Collab-  
376 oration, SLD Electroweak and Heavy Flavour Groups, ALEPH Collaboration,  
377 LEP Electroweak Working Group, SLD Collaboration, OPAL Collaboration,  
378 D0 Collaboration, L3 Collaboration, “Precision electroweak measurements and  
379 constraints on the standard model,” 2010. arXiv: 1012.2367 [hep-ex].
- 380 [98] CMS Collaboration, “Observation of a new boson at a mass of 125 GeV with  
381 the CMS experiment at the LHC,” *Phys. Lett. B*, vol. 716, p. 30, 2012. DOI:  
382 10.1016/j.physletb.2012.08.021. arXiv: 1207.7235 [hep-ex].
- 383 [99] ATLAS Collaboration, “Observation of a new particle in the search for the  
384 standard model Higgs boson with the ATLAS detector at the LHC,” *Phys.  
385 Lett. B*, vol. 716, p. 1, 2012. DOI: 10.1016/j.physletb.2012.08.020. arXiv:  
386 1207.7214 [hep-ex].
- 387 [100] CMS Collaboration, “Search for the standard model Higgs boson in the decay  
388 channel  $H \rightarrow ZZ \rightarrow 4$  leptons in pp collisions at  $\sqrt{s} = 7$  TeV,” *Phys. Rev. Lett.*,  
389 vol. 108, p. 111804, 2012. DOI: 10.1103/PhysRevLett.108.111804. arXiv:  
390 1202.1997 [hep-ex].

- 391 [101] ATLAS Collaboration, CMS Collaboration, “Combined measurement of the  
392 Higgs boson mass in pp collisions at  $\sqrt{s} = 7$  and 8 TeV with the ATLAS and  
393 CMS experiments,” *Phys. Rev. Lett.*, vol. 114, p. 191803, 2015. DOI: 10.1103/  
394 PhysRevLett.114.191803. arXiv: 1503.07589 [hep-ex].
- 395 [102] ATLAS Collaboration, CMS Collaboration, “Measurements of the Higgs  
396 boson production and decay rates and constraints on its couplings from a  
397 combined ATLAS and CMS analysis of the LHC pp collision data at  $\sqrt{s} = 7$   
398 and 8 TeV,” *JHEP*, vol. 08, p. 045, 2016. DOI: 10.1007/JHEP08(2016)045.  
399 arXiv: 1606.02266 [hep-ex].
- 400 [103] I. Ots, H. Uibo, H. Liivat, R. Saar, and R. K. Loide, “Possible anomalous ZZ $\gamma$   
401 and Z $\gamma\gamma$  couplings and Z boson spin orientation in  $e^+e^- \rightarrow Z\gamma$ ,” *Nucl. Phys.*,  
402 vol. B702, pp. 346–356, 2004. DOI: 10.1016/j.nuclphysb.2004.09.019.
- 403 [104] DELPHI Collaboration, “Study of triple-gauge-boson couplings ZZZ, ZZ $\gamma$   
404 and Z $\gamma\gamma$  at LEP,” *Eur. Phys. J. C*, vol. 51, p. 525, 2007. DOI: 10.1140/epjc/  
405 s10052-007-0345-0. arXiv: 0706.2741 [hep-ex].
- 406 [105] CDF Collaboration, D0 Collaboration, “Diboson physics at the Tevatron,”  
407 *EPJ Web Conf.*, vol. 28, p. 06001, 2012. DOI: 10.1051/epjconf/20122806001.  
408 arXiv: 1201.4771 [hep-ex].
- 409 [106] D0 Collaboration, “Search for ZZ and Z $\gamma^*$  production in p $\bar{p}$  collisions at  
410  $\sqrt{s} = 1.96$  TeV and limits on anomalous ZZZ and ZZ $\gamma^*$  couplings,” *Phys. Rev.*  
411 *Lett.*, vol. 100, p. 131801, 2008. DOI: 10.1103/PhysRevLett.100.131801.  
412 arXiv: 0712.0599 [hep-ex].
- 413 [107] ATLAS Collaboration, “Measurement of the ZZ production cross section  
414 and limits on anomalous neutral triple gauge couplings in proton-proton col-  
415 lisions at  $\sqrt{s} = 7$  TeV with the ATLAS detector,” *Phys. Rev. Lett.*, vol. 108,  
416 p. 041804, 2012. DOI: 10.1103/PhysRevLett.108.041804. arXiv: 1110.5016  
417 [hep-ex].
- 418 [108] ATLAS Collaboration, “Measurement of the ZZ production cross section in  
419 pp collisions at  $\sqrt{s} = 13$  TeV with the ATLAS detector,” *Phys. Rev. Lett.*,  
420 vol. 116, p. 101801, 2016. DOI: 10.1103/PhysRevLett.116.101801. arXiv:  
421 1512.05314 [hep-ex].
- 422 [109] L. Evans and P. Bryant, “LHC machine,” *JINST*, vol. 3, S08001, 2008. DOI:  
423 10.1088/1748-0221/3/08/S08001.

- 424 [110] O. Brüning, H. Burkhardt, and S. Myers, “The Large Hadron Collider,” *Prog.  
425 Part. Nucl. Phys.*, vol. 67, p. 7054, 2012. DOI: [https://doi.org/10.1016/j.  
426 ppnp.2012.03.001](https://doi.org/10.1016/j.ppnp.2012.03.001).
- 427 [111] CMS Collaboration, “The CMS experiment at the CERN LHC,” *JINST*, vol.  
428 3, S08004, 2008. DOI: [10.1088/1748-0221/3/08/S08004](https://doi.org/10.1088/1748-0221/3/08/S08004).
- 429 [112] C. Lefèvre, “The CERN accelerator complex. complexe des accélérateurs du  
430 CERN,” Dec. 2008, <https://cds.cern.ch/record/1260465>.
- 431 [113] ATLAS Collaboration, “The ATLAS experiment at the CERN Large Hadron  
432 Collider,” *JINST*, vol. 3, S08003, 2008. DOI: [10.1088/1748-0221/3/08/S08003](https://doi.org/10.1088/1748-0221/3/08/S08003).
- 434 [114] LHCb Collaboration, “The LHCb detector at the LHC,” *JINST*, vol. 3,  
435 S08005, 2008. DOI: [10.1088/1748-0221/3/08/S08005](https://doi.org/10.1088/1748-0221/3/08/S08005).
- 436 [115] ALICE Collaboration, “The ALICE experiment at the CERN LHC,” *JINST*,  
437 vol. 3, S08002, 2008. DOI: [10.1088/1748-0221/3/08/S08002](https://doi.org/10.1088/1748-0221/3/08/S08002).
- 438 [116] TOTEM Collaboration, “The TOTEM experiment at the CERN Large  
439 Hadron Collider,” *JINST*, vol. 3, S08007, 2008. DOI: [10.1088/1748-0221/3/08/S08007](https://doi.org/10.1088/1748-0221/3/08/S08007).
- 441 [117] LHCf Collaboration, “The LHCf detector at the CERN Large Hadron Col-  
442 linder,” *JINST*, vol. 3, S08006, 2008. DOI: [10.1088/1748-0221/3/08/S08006](https://doi.org/10.1088/1748-0221/3/08/S08006).
- 443 [118] MoEDAL Collaboration, “The physics programme of the MoEDAL exper-  
444 iment at the LHC,” *Int. J. Mod. Phys.*, vol. A29, p. 1430050, 2014. DOI:  
445 [10.1142/S0217751X14300506](https://doi.org/10.1142/S0217751X14300506). arXiv: [1405.7662](https://arxiv.org/abs/1405.7662) [hep-ph].
- 446 [119] M. Bajko *et al.*, “Report of the task force on the incident of 19th September  
447 2008 at the LHC,” CERN, Geneva, Tech. Rep. LHC-PROJECT-Report-1168.  
448 CERN-LHC-PROJECT-Report-1168, Mar. 2009. [http://cds.cern.ch/  
449 record/1168025](http://cds.cern.ch/record/1168025).
- 450 [120] M. Lamont, “Status of the LHC,” *Journal of Physics: Conference Series*,  
451 vol. 455, p. 012001, 2013. <http://stacks.iop.org/1742-6596/455/i=1/a=012001>.
- 453 [121] Y. Papaphilippou, H. Bartosik, G. Rumolo, and D. Manglunki, “Operational  
454 beams for the LHC,” 2014. arXiv: [1412.7857](https://arxiv.org/abs/1412.7857) [physics.acc-ph].

- 455 [122] F. Bordry and C. Pralavorio, “LHC smashes targets for 2016 run,” Nov.  
456 2016. <http://cds.cern.ch/record/2235979>.
- 457 [123] T. Sakuma and T. McCauley, “Detector and event visualization with Sketch-  
458 Up at the CMS experiment,” CERN, Geneva, Tech. Rep. CMS-CR-2013-379,  
459 Oct. 2013. arXiv: 1311.4942. <https://cds.cern.ch/record/1626816>.
- 460 [124] CMS Collaboration, “The magnet project: technical design report,” 1997.  
461 <https://cds.cern.ch/record/331056>.
- 462 [125] CMS Collaboration, “The CMS tracker system project: technical design  
463 report,” 1997. <http://cds.cern.ch/record/368412>.
- 464 [126] B. Isildak, “Measurement of the differential dijet production cross section  
465 in proton-proton collisions at  $\sqrt{s} = 7\text{ TeV}$ ,” PhD thesis, Bogazici U., 2011.  
466 arXiv: 1308 . 6064 [hep-ex]. <https://inspirehep.net/record/1251416/files/arXiv:1308.6064.pdf>.
- 468 [127] “The CMS muon project: technical design report,” 1997. <http://cds.cern.ch/record/343814>.
- 470 [128] CMS Collaboration, “The CMS muon system in Run2: preparation, status  
471 and first results,” *PoS*, vol. EPS-HEP2015, p. 237, 2015. arXiv: 1510 . 05424  
472 [physics.ins-det].
- 473 [129] CMS Collaboration, “CMS technical design report for the level-1 trigger up-  
474 grade,” Tech. Rep. CERN-LHCC-2013-011. CMS-TDR-12, Jun. 2013. <https://cds.cern.ch/record/1556311>.
- 476 [130] P. R. K. Chumney, S. Dasu, J. Lackey, M. Jaworski, P. Robl, and W. H.  
477 Smith, “Level-1 regional calorimeter trigger system for CMS,” *EConf*, vol.  
478 C0303241, THHT003, 2003. arXiv: [hep-ex/0305047](https://arxiv.org/abs/hep-ex/0305047) [hep-ex].
- 479 [131] B. Kreis and others, “Run 2 upgrades to the CMS level-1 calorimeter trigger,”  
480 *JINST*, vol. 11, p. C01051, 2016. DOI: [10.1088/1748-0221/11/01/C01051](https://doi.org/10.1088/1748-0221/11/01/C01051).  
481 arXiv: 1511 . 05855 [physics.ins-det].
- 482 [132] A. Svetek, M. Blake, M. Cepeda Hermida, S. Dasu, L. Dodd, R. Fobes, B.  
483 Gomber, T. Gorski, Z. Guo, P. Klabbers, A. Levine, I. Ojalvo, T. Ruggles, N.  
484 Smith, W. Smith, J. Tikalsky, M. Vicente, and N. Woods, “The calorimeter  
485 trigger processor card: the next generation of high speed algorithmic data  
486 processing at CMS,” *JINST*, vol. 11, p. C02011, 2016. DOI: [10.1088/1748-0221/11/02/C02011](https://doi.org/10.1088/1748-0221/11/02/C02011).  
487

- 488 [133] J. Ero *et al.*, “The CMS drift tube trigger track finder,” *JINST*, vol. 3,  
489 P08006, 2008. DOI: 10.1088/1748-0221/3/08/P08006.
- 490 [134] D. Acosta, A. Atamanchuk, V. Golovtsov, A. Madorsky, B. Razmyslovich,  
491 B. Scurlock, and S. Wang, “The track-finding processor for the level-1 trigger  
492 of the CMS endcap muon system,” 1999.
- 493 [135] J. Ero *et al.*, “The CMS level-1 trigger barrel track finder,” *JINST*, vol. 11,  
494 p. C03038, 2016. DOI: 10.1088/1748-0221/11/03/C03038.
- 495 [136] W. M. Zabolotny and A. Byszuk, “Algorithm and implementation of muon  
496 trigger and data transmission system for barrel-endcap overlap region of the  
497 CMS detector,” *JINST*, vol. 11, p. C03004, 2016. DOI: 10.1088/1748-0221/  
498 11/03/C03004.
- 499 [137] H. Sakulin and A. Taurok, “The level-1 global muon trigger for the CMS ex-  
500 periment,” CERN, Geneva, Tech. Rep. CMS-CR-2003-040, Oct. 2003. <https://cds.cern.ch/record/687846>.
- 502 [138] M. Jeitler, J. Lingemann, D. Rabady, H. Sakulin, and A. Stahl, “Upgrade  
503 of the CMS global muon trigger,” *IEEE Trans. Nucl. Sci.*, vol. 62, pp. 1104–  
504 1109, 2015. DOI: 10.1109/TNS.2015.2435060.
- 505 [139] M. Jeitler *et al.*, “The level-1 global trigger for the CMS experiment at LHC,”  
506 *JINST*, vol. 2, P01006, 2007. DOI: 10.1088/1748-0221/2/01/P01006.
- 507 [140] J. Wittmann, B. Arnold, H. Bergauer, M. Jeitler, T. Matsushita, D. Rabady,  
508 B. Rahbaran, and C.-E. Wulz, “The upgrade of the CMS global trigger,”  
509 *JINST*, vol. 11, p. C02029, 2016. [http://stacks.iop.org/1748-0221/11/  
510 i=02/a=C02029](http://stacks.iop.org/1748-0221/11/i=02/a=C02029).
- 511 [141] CMS Collaboration, “The CMS high level trigger,” *Eur. Phys. J. C*, vol. 46,  
512 p. 605, 2006. DOI: 10.1140/epjc/s2006-02495-8. arXiv: [hep-ex/0512077](https://arxiv.org/abs/hep-ex/0512077)  
513 [hep-ex].
- 514 [142] S. Van der Meer, “Calibration of the effective beam height in the ISR,” 1968.
- 515 [143] CMS Collaboration, “Beams scan based absolute normalization of the CMS  
516 luminosity measurement. CMS 2010 luminosity determination,” 2011. <https://cds.cern.ch/record/1357856>.

- 518 [144] CMS Collaboration, “CMS luminosity measurement for the 2015 data-taking  
519 period,” CERN, Geneva, Tech. Rep. CMS-PAS-LUM-15-001, 2017. <http://cds.cern.ch/record/2138682>.
- 521 [145] CMS Collaboration, “CMS luminosity measurements for the  
522 2016 data taking period,” CERN, Geneva, Tech. Rep. CMS-PAS-LUM-17-001,  
523 2017. <http://cds.cern.ch/record/2257069>.
- 524 [146] N. Metropolis and S. Ulam, “The Monte Carlo method,” *Journal of the  
525 American Statistical Association*, vol. 44, p. 335, 1949. DOI: 10.2307/2280232.  
526 <http://www.jstor.org/stable/2280232>.
- 527 [147] M. Matsumoto and T. Nishimura, “Mersenne Twister: A 623-dimensionally  
528 equidistributed uniform pseudo-random number generator,” *ACM Trans.  
529 Model. Comput. Simul.*, vol. 8, p. 3, 1998. DOI: 10.1145/272991.272995.  
530 <http://doi.acm.org/10.1145/272991.272995>.
- 531 [148] CTEQ Collaboration, “Handbook of perturbative QCD: version 1.0,” *Rev.  
532 Mod. Phys.*, vol. 67, p. 157, 1995. DOI: 10.1103/RevModPhys.67.157.
- 533 [149] J. Alwall, R. Frederix, S. Frixione, V. Hirschi, F. Maltoni, O. Mattelaer,  
534 H.-S. Shao, T. Stelzer, P. Torrielli, and M. Zaro, “The automated computation  
535 of tree-level and next-to-leading order differential cross sections, and their  
536 matching to parton shower simulations,” *JHEP*, vol. 07, p. 079, 2014. DOI:  
537 10.1007/JHEP07(2014)079. arXiv: 1405.0301 [hep-ph].
- 538 [150] P. Nason, “A new method for combining NLO QCD with shower Monte  
539 Carlo algorithms,” *JHEP*, vol. 11, p. 040, 2004. DOI: 10.1088/1126-6708/  
540 2004/11/040. arXiv: hep-ph/0409146 [hep-ph].
- 541 [151] S. Frixione, P. Nason, and C. Oleari, “Matching NLO QCD computations  
542 with parton shower simulations: the POWHEG method,” *JHEP*, vol. 11, p. 070,  
543 2007. DOI: 10.1088/1126-6708/2007/11/070. arXiv: 0709.2092 [hep-ph].
- 544 [152] S. Alioli, P. Nason, C. Oleari, and E. Re, “A general framework for im-  
545 plementing NLO calculations in shower Monte Carlo programs: the POWHEG  
546 BOX,” *JHEP*, vol. 06, p. 043, 2010. DOI: 10.1007/JHEP06(2010)043. arXiv:  
547 1002.2581 [hep-ph].
- 548 [153] T. Gleisberg, S. Hoeche, F. Krauss, M. Schonherr, S. Schumann, F. Siegert,  
549 and J. Winter, “Event generation with SHERPA 1.1,” *JHEP*, vol. 02, p. 007,  
550 2009. DOI: 10.1088/1126-6708/2009/02/007. arXiv: 0811.4622 [hep-ph].

- 551 [154] J. M. Campbell, R. K. Ellis, and W. T. Giele, “A multi-threaded version of  
552 MCFM,” *Eur. Phys. J. C*, vol. 75, p. 246, 2015. DOI: 10.1140/epjc/s10052-  
553 015-3461-2. arXiv: 1503.06182 [physics.comp-ph].
- 554 [155] R. Boughezal, J. M. Campbell, R. K. Ellis, C. Focke, W. Giele, X. Liu, F.  
555 Petriello, and C. Williams, “Color singlet production at NNLO in MCFM,”  
556 *Eur. Phys. J. C*, vol. 77, p. 7, 2017. DOI: 10.1140/epjc/s10052-016-4558-y.  
557 arXiv: 1605.08011 [hep-ph].
- 558 [156] G. P. Lepage, “A new algorithm for adaptive multidimensional integration,”  
559 *J. Comput. Phys.*, vol. 27, p. 192, 1978. DOI: 10.1016/0021-9991(78)90004-  
560 9.
- 561 [157] M. Bahr *et al.*, “Herwig++ physics and manual,” *Eur. Phys. J. C*, vol. 58,  
562 p. 639, 2008. DOI: 10.1140/epjc/s10052-008-0798-9. arXiv: 0803.0883  
563 [hep-ph].
- 564 [158] J. Bellm *et al.*, “Herwig 7.0/Herwig++ 3.0 release note,” *Eur. Phys. J.*  
565 *C*, vol. 76, p. 196, 2016. DOI: 10.1140/epjc/s10052-016-4018-8. arXiv:  
566 1512.01178 [hep-ph].
- 567 [159] B. Andersson, G. Gustafson, and C. Peterson, “A semiclassical model for  
568 quark jet fragmentation,” *Z. Phys. C*, vol. 1, p. 105, 1979. DOI: 10.1007/  
569 BF01450386.
- 570 [160] B. Andersson, G. Gustafson, and B. Soderberg, “A general model for jet  
571 fragmentation,” *Z. Phys. C*, vol. 20, p. 317, 1983. DOI: 10.1007/BF01407824.
- 572 [161] B. Andersson, S. Mohanty, and F. Soderberg, “The lund fragmentation  
573 process for a multigluon string according to the area law,” *Eur. Phys. J. C*,  
574 vol. 21, p. 631, 2001. DOI: 10.1007/s100520100757. arXiv: hep-ph/0106185  
575 [hep-ph].
- 576 [162] Sjöstrand, T. and Skands, Peter Z., “Transverse-momentum-ordered showers  
577 and interleaved multiple interactions,” *Eur. Phys. J. C*, vol. 39, p. 129, 2005.  
578 DOI: 10.1140/epjc/s2004-02084-y. arXiv: hep-ph/0408302 [hep-ph].
- 579 [163] J. Alwall *et al.*, “Comparative study of various algorithms for the merging  
580 of parton showers and matrix elements in hadronic collisions,” *Eur. Phys. J.*  
581 *C*, vol. 53, p. 473, 2008. DOI: 10.1140/epjc/s10052-007-0490-5. arXiv:  
582 0706.2569 [hep-ph].

- 583 [164] J. Alwall, S. de Visscher, and F. Maltoni, “QCD radiation in the production  
584 of heavy colored particles at the LHC,” *JHEP*, vol. 02, p. 017, 2009. DOI:  
585 10.1088/1126-6708/2009/02/017. arXiv: 0810.5350 [hep-ph].
- 586 [165] M. Rauch, “Vector-boson fusion and vector-boson scattering,” 2016. arXiv:  
587 1610.08420 [hep-ph].
- 588 [166] M. L. Mangano, M. Moretti, F. Piccinini, and M. Treccani, “Matching ma-  
589 trix elements and shower evolution for top-quark production in hadronic col-  
590 lisions,” *JHEP*, vol. 01, p. 013, 2007. DOI: 10.1088/1126-6708/2007/01/013.  
591 arXiv: hep-ph/0611129 [hep-ph].
- 592 [167] S. Catani, F. Krauss, R. Kuhn, and B. R. Webber, “QCD matrix elements  
593 + parton showers,” *JHEP*, vol. 11, p. 063, 2001. DOI: 10.1088/1126-6708/  
594 2001/11/063. arXiv: hep-ph/0109231 [hep-ph].
- 595 [168] R. Frederix and S. Frixione, “Merging meets matching in MC@NLO,” *JHEP*,  
596 vol. 12, p. 061, 2012. DOI: 10.1007/JHEP12(2012)061. arXiv: 1209.6215 [hep-  
597 ph].
- 598 [169] Sjöstrand, T. and Skands, Peter Z., “Multiple interactions and the structure  
599 of beam remnants,” *JHEP*, vol. 03, p. 053, 2004. DOI: 10.1088/1126-6708/  
600 2004/03/053. arXiv: hep-ph/0402078 [hep-ph].
- 601 [170] A. V. Manohar and W. J. Waalewijn, “A QCD analysis of double parton  
602 scattering: color correlations, interference effects and evolution,” *Phys. Rev.*  
603 *D*, vol. 85, p. 114009, 2012. DOI: 10.1103/PhysRevD.85.114009. arXiv:  
604 1202.3794 [hep-ph].
- 605 [171] S Banerjee, “CMS simulation software,” *Journal of Physics: Conference Se-  
606 ries*, vol. 396, p. 022003, 2012. %7Bhttp://stacks.iop.org/1742-6596/  
607 396/i=2/a=022003%7D.
- 608 [172] M Hildreth and V N Ivanchenko and D J Lange and M J Kortelainen, “CMS  
609 full simulation for run-2,” *Journal of Physics: Conference Series*, vol. 664,  
610 p. 072022, 2015. %7Bhttp://stacks.iop.org/1742-6596/664/i=7/a=  
611 072022%7D.
- 612 [173] S. Alioli, P. Nason, C. Oleari, and E. Re, “NLO vector-boson production  
613 matched with shower in POWHEG,” *JHEP*, vol. 07, p. 060, 2008. DOI: 10.  
614 1088/1126-6708/2008/07/060. arXiv: 0805.4802 [hep-ph].

- 615 [174] J. M. Campbell and R. K. Ellis, “MCFM for the Tevatron and the LHC,”  
616 *Nucl. Phys. Proc. Suppl.*, vol. 205, p. 10, 2010. DOI: 10.1016/j.nuclphysbps.  
617 2010.08.011. arXiv: 1007.3492 [hep-ph].
- 618 [175] A. Ballestrero, A. Belhouari, G. Bevilacqua, V. Kashkan, and E. Maina,  
619 “PHANTOM : a Monte Carlo event generator for six parton final states at  
620 high energy colliders,” *Comput. Phys. Commun.*, vol. 180, p. 401, 2009. DOI:  
621 10.1016/j.cpc.2008.10.005. arXiv: 0801.3359 [hep-ph].
- 622 [176] NNPDF Collaboration, “Parton distributions for the LHC Run II,” *JHEP*,  
623 vol. 04, p. 040, 2015. DOI: 10.1007/JHEP04(2015)040. arXiv: 1410.8849  
624 [hep-ph].
- 625 [177] CMS Collaboration, “Event generator tunes obtained from underlying event  
626 and multiparton scattering measurements,” *Eur. Phys. J. C*, vol. 76, p. 155,  
627 2016. DOI: 10.1140/epjc/s10052-016-3988-x. arXiv: 1512.00815 [hep-ex].
- 628 [178] GEANT4 Collaboration, “GEANT4: a simulation toolkit,” *Nucl. Instrum.  
629 Meth. A*, vol. 506, p. 250, 2003. DOI: 10.1016/S0168-9002(03)01368-8.
- 630 [179] R. Frühwirth, “Application of Kalman filtering to track and vertex fitting,”  
631 *Nucl. Instrum. Meth. A*, vol. 262, p. 444, 1987. DOI: 10.1016/0168-9002(87)  
632 90887-4.
- 633 [180] P. Billoir and S. Qian, “Simultaneous pattern recognition and track fitting  
634 by the Kalman filtering method,” *Nucl. Instrum. Meth. A*, vol. 294, p. 219,  
635 1990. DOI: 10.1016/0168-9002(90)91835-Y.
- 636 [181] W. Adam, B. Mangano, T. Speer, and T. Todorov, “Track reconstruction in  
637 the CMS tracker,” 2005.
- 638 [182] CMS Collaboration, “Description and performance of track and primary-  
639 vertex reconstruction with the CMS tracker,” *JINST*, vol. 9, P10009, 2014.  
640 DOI: 10.1088/1748-0221/9/10/P10009. arXiv: 1405.6569 [physics.ins-det].
- 641 [183] W. Adam, R. Frühwirth, A. Strandlie, and T. Todor, “Reconstruction of  
642 electrons with the Gaussian-sum filter in the CMS tracker at the LHC,” 2005.
- 643 [184] T. Speer, K. Prokofiev, R. Frühwirth, W. Waltenberger, and P. Vanlaer,  
644 “Vertex fitting in the CMS tracker,” 2006.

- 645 [185] K. Rose, “Deterministic annealing for clustering, compression, classification,  
646 regression, and related optimization problems,” *Proceedings of the IEEE*, vol.  
647 86, p. 2210, Nov. 1998, ISSN: 0018-9219. DOI: 10.1109/5.726788.
- 648 [186] CMS Collaboration, “Particle-flow event reconstruction in CMS and perfor-  
649 mance for jets, taus, and MET,” CERN, Geneva, Tech. Rep. CMS-PAS-PFT-  
650 09-001, Apr. 2009. <https://cds.cern.ch/record/1194487>.
- 651 [187] CMS Collaboration, “Commissioning of the particle-flow event reconstruction  
652 with the first LHC collisions recorded in the CMS detector,” Tech. Rep. CMS-  
653 PAS-PFT-10-001, 2010. <https://cds.cern.ch/record/1247373>.
- 654 [188] CMS Collaboration, “Particle-flow reconstruction and global event descrip-  
655 tion with the CMS detector,” 2017, Accepted by *JINST*. arXiv: 1706.04965  
656 [physics.ins-det].
- 657 [189] CMS Collaboration, “Performance of CMS muon reconstruction in pp colli-  
658 sion events at  $\sqrt{s} = 7 \text{ TeV}$ ,” *JINST*, vol. 7, P10002, 2012. DOI: 10.1088/1748-  
659 0221/7/10/P10002. arXiv: 1206.4071 [physics.ins-det].
- 660 [190] S. Baffioni, C. Charlot, F. Ferri, D. Futyan, P. Meridiani, I. Puljak, C. Rovelli,  
661 R. Salerno, and Y. Sirois, “Electron reconstruction in CMS,” *Eur. Phys. J. C*,  
662 vol. 49, p. 1099, 2007. DOI: 10.1140/epjc/s10052-006-0175-5.
- 663 [191] CMS Collaboration, “Performance of photon reconstruction and identifi-  
664 cation with the CMS detector in proton-proton collisions at  $\sqrt{s} = 8 \text{ TeV}$ ,”  
665 *JINST*, vol. 10, P08010, 2015. DOI: 10.1088/1748-0221/10/08/P08010.  
666 arXiv: 1502.02702 [physics.ins-det].
- 667 [192] G. P. Salam and G. Soyez, “A practical seedless infrared-safe cone jet algo-  
668 rithm,” *JHEP*, vol. 05, p. 086, 2007. DOI: 10.1088/1126-6708/2007/05/086.  
669 arXiv: 0704.0292 [hep-ph].
- 670 [193] G. P. Salam, “Towards jetography,” *Eur. Phys. J. C*, vol. 67, p. 637, 2010.  
671 DOI: 10.1140/epjc/s10052-010-1314-6. arXiv: 0906.1833 [hep-ph].
- 672 [194] M. Cacciari, G. P. Salam, and G. Soyez, “The anti- $k_T$  jet clustering algo-  
673 rithm,” *JHEP*, vol. 04, p. 063, 2008. DOI: 10.1088/1126-6708/2008/04/063.  
674 arXiv: 0802.1189 [hep-ph].
- 675 [195] M. Cacciari, G. P. Salam, and G. Soyez, “FastJet user manual,” *Eur. Phys.  
676 J. C*, vol. 72, p. 1896, 2012. DOI: 10.1140/epjc/s10052-012-1896-2. arXiv:  
677 1111.6097 [hep-ph].

- 678 [196] CMS Collaboration, “Study of pileup removal algorithms for jets,” 2014.
- 679 [197] CMS Collaboration, “Jet energy scale and resolution in the CMS experiment  
680 in pp collisions at 8 TeV,” *JINST*, vol. 12, P02014, 2017. DOI: 10.1088/1748-  
681 0221/12/02/P02014. arXiv: 1607.03663 [hep-ex].
- 682 [198] M. Cacciari, G. P. Salam, and G. Soyez, “The catchment area of jets,”  
683 *JHEP*, vol. 04, p. 005, 2008. DOI: 10.1088/1126-6708/2008/04/005. arXiv:  
684 0802.1188 [hep-ph].
- 685 [199] M. Cacciari and G. P. Salam, “Pileup subtraction using jet areas,” *Phys.  
686 Lett. B*, vol. 659, p. 119, 2008. DOI: 10.1016/j.physletb.2007.09.077.  
687 arXiv: 0707.1378 [hep-ph].
- 688 [200] CMS Collaboration, “Determination of jet energy calibration and transverse  
689 momentum resolution in CMS,” *JINST*, vol. 6, P11002, 2011. DOI: 10.1088/  
690 1748-0221/6/11/P11002. arXiv: 1107.4277 [physics.ins-det].
- 691 [201] CMS Collaboration, “Missing transverse energy performance of the CMS  
692 detector,” *JINST*, vol. 6, P09001, 2011. DOI: 10.1088/1748-0221/6/09/  
693 P09001. arXiv: 1106.5048 [physics.ins-det].
- 694 [202] CMS Collaboration, “Performance of the CMS missing transverse momentum  
695 reconstruction in pp data at  $\sqrt{s} = 8$  TeV,” *JINST*, vol. 10, P02006, 2015. DOI:  
696 10.1088/1748-0221/10/02/P02006. arXiv: 1411.0511 [physics.ins-det].
- 697 [203] CMS Collaboration, “Performance of missing energy reconstruction in 13 TeV  
698 pp collision data using the CMS detector,” CERN, Geneva, Tech. Rep. CMS-  
699 PAS-JME-16-004, 2016. <http://cds.cern.ch/record/2205284>.
- 700 [204] CMS Collaboration, “Electron reconstruction and identification at  $\sqrt{s} =$   
701 7 TeV,” CERN, Geneva, Tech. Rep. CMS-PAS-EGM-10-004, 2010. <https://cds.cern.ch/record/1299116>.
- 703 [205] CMS Collaboration, “Performance of electron reconstruction and selection  
704 with the CMS detector in proton-proton collisions at  $\sqrt{s} = 8$  TeV,” *JINST*,  
705 vol. 10, P06005, 2015. DOI: 10.1088/1748-0221/10/06/P06005. arXiv:  
706 1502.02701 [physics.ins-det].
- 707 [206] CMS Collaboration, “Measurement of the inclusive W and Z production  
708 cross sections in pp collisions at  $\sqrt{s} = 7$  TeV,” *JHEP*, vol. 10, p. 132, 2011.  
709 DOI: 10.1007/JHEP10(2011)132. arXiv: 1107.4789 [hep-ex].

- 710 [207] CMS Collaboration, “Measurement of the properties of a Higgs boson in the  
711 four-lepton final state,” *Phys. Rev. D*, vol. 89, p. 092007, 2014. DOI: 10.1103/  
712 PhysRevD.89.092007. arXiv: 1312.5353 [hep-ex].
- 713 [208] J. Butterworth *et al.*, “PDF4LHC recommendations for LHC Run II,” *J.  
714 Phys. G*, vol. 43, p. 023001, 2016. DOI: 10.1088/0954-3899/43/2/023001.  
715 arXiv: 1510.03865 [hep-ph].
- 716 [209] G. Bohm and G. Zech, *Introduction to statistics and data analysis for physi-  
717 cists*. DESY, 2010, ISBN: 9783935702416. <https://books.google.ch/books?id=aQBHcgAACAAJ>.
- 719 [210] G. D’Agostini, “A multidimensional unfolding method based on Bayes’ the-  
720 oreom,” *Nucl. Instrum. Meth. A*, vol. 362, p. 487, 1995. DOI: 10.1016/0168-  
721 9002(95)00274-X.
- 722 [211] A. P. Dempster, N. M. Laird, and D. B. Rubin, “Maximum likelihood from  
723 incomplete data via the EM algorithm,” *J. R. Stat. Soc. B*, vol. 39, p. 1, 1977,  
724 ISSN: 00359246. <http://www.jstor.org/stable/2984875>.
- 725 [212] L. B. Lucy, “An iterative technique for the rectification of observed distri-  
726 butions,” *Astron. J.*, vol. 79, p. 745, Jun. 1974. DOI: 10.1086/111605.
- 727 [213] W. H. Richardson, “Bayesian-based iterative method of image restoration,”  
728 *J. Opt. Soc. Am.*, vol. 62, p. 55, Jan. 1972. DOI: 10.1364/JOSA.62.000055.  
729 <http://www.osapublishing.org/abstract.cfm?URI=josa-62-1-55>.
- 730 [214] L. A. Shepp and Y. Vardi, “Maximum likelihood reconstruction for emission  
731 tomography,” *IEEE Transactions on Medical Imaging*, vol. 1, p. 113, Oct.  
732 1982, ISSN: 0278-0062. DOI: 10.1109/TMI.1982.4307558.
- 733 [215] T. Adye, “Unfolding algorithms and tests using RooUnfold,” in *Proceedings,  
734 PHYSTAT 2011 Workshop on Statistical Issues Related to Discovery Claims  
735 in Search Experiments and Unfolding*, CERN, Geneva, Switzerland 17–20 January  
736 2011, CERN, Geneva: CERN, 2011, p. 313. DOI: 10.5170/CERN-2011-  
737 006.313. arXiv: 1105.1160 [physics.data-an]. <https://inspirehep.net/record/898599/files/arXiv:1105.1160.pdf>.
- 739 [216] Y. Vardi, “Empirical distributions in selection bias models,” *Ann. Statist.*,  
740 vol. 13, p. 178, Mar. 1985. DOI: 10.1214/aos/1176346585. <http://dx.doi.org/10.1214/aos/1176346585>.

- 742 [217] F. Pedregosa, G. Varoquaux, A. Gramfort, V. Michel, B. Thirion, O. Grisel,  
743 M. Blondel, P. Prettenhofer, R. Weiss, V. Dubourg, J. Vanderplas, A. Pas-  
744 soss, D. Cournapeau, M. Brucher, M. Perrot, and E. Duchesnay, “Scikit-learn:  
745 Machine learning in Python,” *J. Mach. Learn. Res.*, vol. 12, p. 2825, 2011.
- 746 [218] CMS Collaboration Collaboration, “Performance of quark/gluon discrimina-  
747 tion in 8 TeV pp data,” CERN, Geneva, Tech. Rep. CMS-PAS-JME-13-002,  
748 2013. <https://cds.cern.ch/record/1599732>.
- 749 [219] G. Cowan, K. Cranmer, E. Gross, and O. Vitells, “Asymptotic formulae for  
750 likelihood-based tests of new physics,” *Eur. Phys. J. C*, vol. 71, p. 1554, 2011,  
751 [Erratum: DOI: 10.1140/epjc/s10052-013-2501-z]. DOI: 10.1140/epjc/  
752 s10052-011-1554-0. arXiv: 1007.1727 [physics.data-an].
- 753 [220] CMS Collaboration and ATLAS Collaboration, “Combination of results from  
754 the ATLAS and CMS experiments on anomalous triple gauge couplings in ZZ  
755 production from pp collisions at a centre-of-mass energy of 7 TeV at the LHC,”  
756 CERN, Geneva, Tech. Rep. CMS-PAS-SMP-15-001. ATLAS-CONF-2016-036,  
757 2016. <https://cds.cern.ch/record/2202807>.
- 758 [221] CMS Collaboration, “Measurement of the ZZ production cross section in  
759  $\ell\ell\ell'\ell'$  decays in pp collisions at  $\sqrt{s} = 13$  TeV,” 2015. [https://cds.cern.ch/](https://cds.cern.ch/record/2114822)  
760 record/2114822.
- 761 [222] CMS Collaboration, “Measurement of the ZZ production cross section and  
762  $Z \rightarrow \ell^+\ell^-\ell'^+\ell'^-$  branching fraction in pp collisions at  $\sqrt{s} = 13$  TeV,” *Phys.*  
763 *Lett. B*, vol. 763, p. 280, 2016. DOI: 10.1016/j.physletb.2016.10.054.  
764 arXiv: 1607.08834 [hep-ex].
- 765 [223] CMS Collaboration, “Measurements of differential cross sections and search  
766 for the electroweak production of two Z bosons produced in association with  
767 jets,” 2017. <https://cds.cern.ch/record/2264556>.
- 768 [224] CMS Collaboration, “Measurement of vector boson scattering and constraints  
769 on anomalous quartic couplings from events with four leptons and two jets in  
770 proton-proton collisions at  $\sqrt{s} = 13$  TeV,” 2017, Submitted to *Phys. Lett. B*.  
771 arXiv: 1708.02812 [hep-ex].
- 772 [225] CMS Collaboration, “Studies of Higgs boson production in the four-lepton  
773 final state at  $\sqrt{s} = 13$  TeV,” 2016. <https://cds.cern.ch/record/2139978>.

- 774 [226] CMS Collaboration, “Measurements of properties of the Higgs boson and  
775 search for an additional resonance in the four-lepton final state at  $\sqrt{s} =$   
776 13 TeV,” 2016. <https://cds.cern.ch/record/2204926>.
- 777 [227] CMS Collaboration, “Measurements of properties of the Higgs boson decay-  
778 ing into the four-lepton final state in pp collisions at  $\sqrt{s} = 13$  TeV,” 2017,  
779 Submitted to *JHEP*. arXiv: 1706.09936 [hep-ex].
- 780 [228] R. Gavin, Y. Li, F. Petriello, and S. Quackenbush, “FEWZ 2.0: a code  
781 for hadronic Z production at next-to-next-to-leading order,” *Comput. Phys.  
782 Commun.*, vol. 182, p. 2388, 2011. DOI: 10.1016/j.cpc.2011.06.008. arXiv:  
783 1011.3540 [hep-ph].
- 784 [229] ATLAS Collaboration, “ $ZZ \rightarrow \ell^+ \ell^- \ell'^+ \ell'^-$  cross-section measurements and  
785 aTGC search in 13 TeV pp collisions with the ATLAS detector,” 2017. <http://cds.cern.ch/record/2263045>.
- 787 [230] K. Arnold *et al.*, “VBFNLO: a parton level Monte Carlo for processes with  
788 electroweak bosons,” *Comput. Phys. Commun.*, vol. 180, p. 1661, 2009. DOI:  
789 10.1016/j.cpc.2009.03.006. arXiv: 0811.4559 [hep-ph].